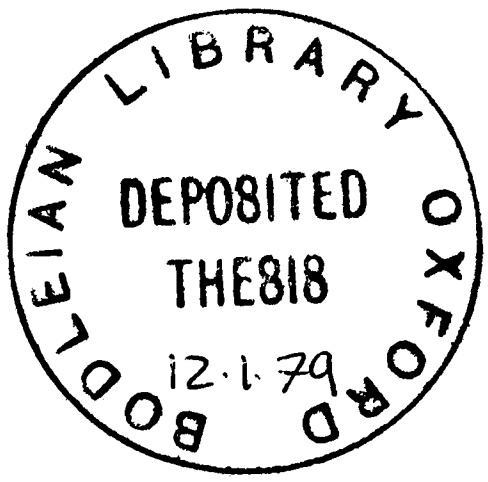
FAILURE ANALYSIS OF PRESSURE VESSELS

WITH DEFECTS

by

PAULINE H. HODKINSON

Somerville College, Oxford



A thesis submitted for the degree of Doctor of Philosophy

at the University of Oxford, Trinity Term 1978.

ABSTRACT

A combined theoretical and experimental study of the criteria governing the failure analysis of pressure vessels with defects has been performed.

The fields of fracture mechanics (linear elastic and elastic-plastic behaviour), failure governed by large scale plastic deformation and energy balance methods are critically reviewed. All three approaches are shown to have relevance in the complete failure analysis of a structure with defects.

An experimental study of the failure mechanisms of precracked polycarbonate and maraging steel plates and model polycarbonate vessels is presented. Room temperature, static loading tests are performed on 85 mm wide, 5 mm thick compact specimens of polycarbonate ($0.013 \leqslant \frac{a}{W} \leqslant 0.810$). For comparison, 51 mm wide maraging steel compact specimens are monotonically loaded at room temperature. The influence of through-thickness constraint on the fracture toughness and slow crack growth characteristics of the steel is investigated using plates of varying thickness (3.1 mm - 25.4 mm) and initial crack length ($0.386 \leqslant \frac{a}{W} \leqslant 0.766$ for 3.1 mm thick sheet); various ancillary studies (scanning electron microscopy, surface deformation studies) complement the results.

The crack growth behaviour of longitudinal through ($0.704 \leqslant c \,/\, \sqrt{DT/2} \leqslant 1.434$) and deep part-through ($\frac{d}{T}$ = 0.700 and 0.878) cracks in 50.8 mm and 102 mm diameter (5 mm and 6 mm wall thickness) polycarbonate cylinders is also studied.

Dowling and Townley's two-criteria approach to failure i.e. LEFM on the one hand and limit analysis on the other, is shown to provide a useful method for assessing the relative importance of crack initiation, in the presence of limited crack tip plasticity and general yield as failure criteria for a given sized defect. Thus, for crack tip plasticity fully

contained by an outer elastic field i.e. not general yield, the LEFM parameter, K_{Ic} (with the possibility of a plasticity correction factor for thin sheet) can be used to predict crack initiation. For the low strain-hardening maraging steel, Irwin's plane strain plasticity correction, $\frac{1}{6\pi}(K_{Ic/\sigma_y})^2$ is shown to be applicable to sheet thicknesses comparable to $\frac{1}{\pi}(K_{Ic/\sigma_y})^2$ i.e. twice Irwin's plane stress plastic zone radius.

CONTENTS

		Page
TITLE		i
ABSTRACT		ii
CONTENTS		iv
GENERAL NOTATION		vii
ACKNOWLEDGEMENTS		xii
CHAPTER 1	GENERAL INTRODUCTION	1.1
1.1	Traditional Methods of Failure Analysis	1.1
1.2	Current Design Code Practice for the Safety of Pressure Vessels with Defects	1.5
1.3	Objectives of the Present Study	1.10
1.4	Scope of the Present Study	1.11
	References	1.12
CHAPTER 2	FRACTURE MECHANICS	2.1
2.1	Linear Elastic Fracture Mechanics	2.1
2.2	LEFM and the Plasticity Correction Factor	2.5
2.3	Fracture Mechanics and Elastic-Plastic Behaviour	2.7
2.4	Summary	2.15
	References	2.16
	Figures	2.19
CHAPTER 3	FAILURE GOVERNED BY LARGE SCALE PLASTIC DEFORMATION	3.1
3.1	Stress Intensification and Plastic Constraint	3.1
3.2	Solutions for Failure by General Yield and Plastic Collapse before Crack Initiation	3.6
3.3	Solutions for Failure by General Yield after Crack Initiation	3.8
3.4	Summary	3.10
	References	3.11

		Page
	Figures	3.14
CHAPTER 4	ENERGY BALANCE APPROACH TO FAILURE ANALYSIS	4.1
4.1	Energy Balance Approach to Crack Growth	4.1
4.2	The Fracture Toughness Parameter, R	4.8
4.3	Application of Energy Balance Approach in Design	4.11
4.4	Advantages and Limitations of the Energy Balance Approach	4.13
4.5	Summary	4.14
	References	4.15
	Figures	4.17
CHAPTER 5	INTRODUCTION TO EXPERIMENTAL STUDY	5.1
5.1	Materials Selection	5.1
5.2	Model Configurations	5.3
5.3	Experimental Programme	5.18
	References	5.20
	Figures	5.23
CHAPTER 6	CRACK GROWTH IN MODEL PLATES OF POLYCARBONATE	6.1
6.1	Material Characterisation	6.1
6.2	Experimental Procedure	6.3
6.3	Results and Analysis of Results	6.6
6.4	Discussion	6.15
6.5	Conclusions	6.26
	References	6.28
	Tables	6.30
	Figures	6.38
CHAPTER 7	CRACK GROWTH IN MARAGING STEEL PLATE SPECIMENS	7.1
7.1	Material Characterisation	7.1

		Page
7.2	Experimental Procedure	7.4
7.3	Results and Analysis of Results	7.8
7.4	Discussion	7.16
7.5	Conclusions	7.30
	References	7.33
	Tables	7.35
	Figures	7.43
CHAPTER 8	CRACK GROWTH IN MODEL VESSELS OF POLYCARBONATE	8.1
8.1	Preparation of Model Vessels	8.1
8.2	Experimental Procedure	8.3
8.3	Results and Analysis of Results	8.4
8.4	Discussion	8.13
8.5	Conclusions	8.19
	References	8.21
	Tables	8.23
	Figures	8.27
CHAPTER 9	SUMMARY AND CONCLUSIONS	9.1
CHAPTER 10	SUGGESTIONS FOR FUTURE WORK	10.1
APPENDICES		
	Appendix 1	A.1
	Appendix 2	A.5
	Appendix 3	A.6
	Appendix 4	A.9
	Appendix 5	A.10
	Appendix 6	A.11
	Appendix 7	A.14
	References	A.15

GENERAL NOTATION

(other symbols are defined as they occur)

a	Crack half-length of internal crack, crack length of surface crack
Δa	Crack extension
A_e, A_b	Extensional and bending components of the stress intensity coefficient for a longitudinal through-thickness crack in a cylindrical shell
B, B_c, B_n	Thickness, critical thickness for plane strain crack initiation and net sectional thickness, respectively
$2c$	Longitudinal crack length in a cylindrical shell
C, C_{sp}, C_m	Elastic compliance, u/p with subscripts $_{sp}$ and $_m$ for specimen and machine, respectively
d	Crack depth
D	Mean diameter of cylindrical shell, (I.D. + O.D.)/2
E	Young's modulus
$2F$	Free length of cylindrical shell
$\mathcal{G}$	Elastic strain energy release rate
$\mathcal{G}_Q$	Conditional plane strain energy release rate
J	J-contour integral
k	LEFM geometrical parameter, stress intensity coefficient
K	Elastic stress intensity factor
$\dot{K}$	Rate of increase of stress intensity
ΔK	Stress intensity range of fatigue cracking
$K_f(max)$	Maximum value of stress intensity of the fatigue cycle
K_I, K_{II}, K_{III}	Elastic stress intensity factors for modes I, II and III, respectively
K_{Ic}	Plane strain fracture toughness

K_Q	Conditional plane strain fracture toughness
L	Plastic constraint, $P_{gy}/2\tau_y.2(W-a)B$
LEFM	Linear elastic fracture mechanics
M	Bending moment
n	Strain-hardening exponent
P	Load, Internal pressure
P_Q	5% offset load
$p\phi$	Dimensionless failure parameter (see sections 5.2.a.i, 5.2.b)
Q	Stress intensification, $\sigma_{yy}(max)/2\tau_y$
r,θ	Polar coordinates
r_y	Plasticity correction factor
r_{y1}, r_{y2}	Irwin's plastic zone radius for plane stress and plane strain, respectively
R	Fracture toughness parameter, work done against resistance of the material per unit crack growth area
R_{mc}	Best conservative estimate of R corresponding to a load maximum
R_{stable}	Fracture toughness corresponding to finite stable crack extension
S	Stretch zone width
T	Wall thickness
u, u_{ll}, u_{lp}	Displacement with subscripts $_{ll}$ and $_{lp}$ for load line and load pin, respectively
U, U_{ll}	Strain energy, total and due to the presence of the crack alone, respectively
U_e	Linear elastic strain energy component
U_p	Fully plastic strain energy component
U^*	Complementary energy

$-\frac{1}{B}\left(\frac{\partial U}{\partial a}\right)_u$	Strain energy rate at fixed displacement
$\frac{1}{B}\left(\frac{\partial U^*}{\partial a}\right)_p$	Complementary energy rate at fixed load
$\frac{1}{B}\ \frac{\Delta U_p}{\Delta a}$	Plastic strain energy rate associated with shear lip formation
v	Crack tip displacement
w	Maximum surface displacement in the through-thickness direction
W	Plate half-width for internal crack of length, 2a, plate width for surface crack of length, a
Y	Stress intensity coefficient for the compact specimen
α	Relative crack length, a/W
α_o	Relative crack length after precracking, a_o/W
$\Delta\alpha$	Relative crack extension, $\frac{\Delta a}{W}$
$\gamma,\ \gamma_p$	Theoretical surface tension and plastic work contribution to surface energy, respectively.
δ	Crack opening displacement, COD = 2v
ε	Tensile strain
$\dot{\varepsilon}_{nom}$	Nominal applied strain rate across the net section
ε_{tip}	Crack tip strain
$\dot{\varepsilon}_{tip}$	Crack tip strain rate
ε_{tm}	True strain at plastic instability, nominal strain-hardening exponent
ε_y	Tensile yield strain
$\bar{\varepsilon}_z$	Average through-thickness crack tip strain, 4w/B
λ	$\sqrt[4]{12(1-\nu^2)}.\rho$
ν	Poisson's ratio
ρ	$c\ /\ \sqrt{DT/2}$

$\rho_{mod.}$	$\rho / \cos \frac{\pi}{2} \frac{\sigma_h}{\sigma_y}$
ρ'	Plastic zone size
ρ'_x	Surface plastic zone size along the line of the crack (see Fig. 7.20.c)
σ	Nominal applied stress across the gross section
σ_1, σ_2, σ_3	Principal stresses
σ_{flow}	Flow stress, $(\sigma_y + \sigma_u)/2$
σ_h	Hoop stress, PD/2T
σ_u	Ultimate tensile strength
σ_{xx}, σ_{yy}, σ_{zz}	Tensile stress components in the x, y and z directions, respectively
σ_y	Uniaxial yield stress
$\sigma_{\infty\ plate}$	Nominal applied stress corresponding to an infinite plate
τ_{xy}, τ_{xz}, τ_{yz}	Shear stress components
τ_y	Shear yield stress
ϕ	Geometrical parameter, $-(1-\alpha)\left(\frac{\partial U}{\partial \alpha}\right)_u / U$
ϕ_e	Linear elastic geometrical parameter, $-(1-\alpha)\, C \left(\frac{\partial \frac{1}{C}}{\partial \alpha}\right)_u$
ϕ_p	Fully plastic geometrical parameter, $-\frac{(1-\alpha)}{P_{gy}}\left(\frac{\partial P_{gy}}{\partial \alpha}\right)_u$
Φ_o	Elliptical integral, $\int_o^{\frac{\pi}{2}} \left[1 - \left(\frac{c^2-d^2}{c^2}\right)\sin^2\theta\right]^{\frac{1}{2}} d\theta$

The following subscripts are used throughout unless otherwise stated:

arr	Crack arrest
c	Crack instability
f	Final crack position
gy	General yield

i	Crack initiation
icb	Initial craze breakdown
Ic	Critical plane strain value, mode I
m	Load maximum
pop-in	"Pop-in" mode
s-t	"Snap-through"
u	Ultimate collapse
∞	Steady-state limit

ACKNOWLEDGEMENTS

The author wishes to express her thanks to Dr. C. Ruiz for all his guidance and encouragement with this work.

Thanks are also due to Firth Brown Limited, Sheffield for donating the steel plate and to Mr. R. J. Smurthwaite, Mr. G. N. Roger and the Department of Engineering Science Workshop staff for their assistance with equipment and model preparation.

Financial assistance from the Central Electricity Generating Board is gratefully acknowledged.

CHAPTER 1

GENERAL INTRODUCTION

An unavoidable feature of all structural components is the presence of defects which may have a deleterious effect on load-bearing capacity. For, in addition to pre-existing flaws that the material may contain, flaws or defects are produced during fabrication of welded structures. These flaws are usually in the form of gouges, scratches or pits in the surface of the base metal and as surface or buried cracks in weld zones, the latter the result of incomplete penetration, porous blow holes, inclusions or residual stresses following thermal treatment. The majority of such defects are known to occur in the vicinity of large structural discontinuities such as a nozzle or opening in a pressure vessel.

The two principal types of failure of a technical pressure-retaining component in the presence of defects such as sharp notches are unstable fracture, characterised by small local plastic deformation and general yield across the net or gross section, accompanied by large permanent deformations. In a pressure vessel, those defects opening up under the action of hoop stresses in the main shell are most likely to be responsible for any subsequent failure of the structure (1) (2).

In critical applications, such as a reactor pressure vessel, the estimation of the severity of defects is of utmost importance to designers and inspectors since failure would result in considerable economic loss in addition to the risk to human life. Thus, the failure analysis of pressure vessels with defects is of great technological importance as well as scientific interest.

1.1 Traditional Methods of Failure Analysis

Classical engineering design criteria have been based upon the mater-

ial's yield stress or ultimate tensile strength. An effectively flawless material is assumed for which the fracture strength is always greater than the yield stress and equal to or greater than the ultimate strength. A design code is then followed which ensures that the applied design stresses in the structure nowhere exceed the material's yield or ultimate strength, the code incorporating a safety factor to allow for some ignorance of local stress conditions, such as residual stresses resulting from fabrication. For designs based on yield stress this safety factor is normally 1.5 - 2.0, although a safety factor of approximately 3.0 may be used with the ultimate strength.

The adequacy of this design approach has been demonstrated by the relatively small number of failures that have occurred in the past. However, with the increasing use of welded structures and the availability of higher strength materials in the last forty years, it has become apparent that such classically designed structures are particularly susceptible to failure by fast fracture. The fracture of the Liberty Ship "Schenectady" in the early 1940's was the first of a series of catastrophic failures of a few large structures at stresses below the nominal yield stress and the design limit. Other notable examples of bridges, steam turbine and generator rotors and gas pipe-lines are given in references (3) (4). More recently in the early 1960's, the catastrophic failure of several thick-walled boilers and pressure vessels during proof testing caused considerable concern in the nuclear industry (5)-(8). All of these failures were found to emanate from a defect, a necessary condition for failure below the yield stress, the ensuing fractures continuing to propagate with a brittle or ductile fracture mode at nominal stresses less than yield.

During the late 1940's and 1950's engineering design procedures were developed to prevent the occurrence of fast fracture in structural grades of carbon and alloy steels. These procedures depend upon the fairly sharp

transition from low energy brittle fracture to high energy ductile fracture with increasing temperature exhibited by low-to-medium strength steels (all those which have a body-centred cubic lattice atomic structure) when notched or sharply cracked specimens are broken. The majority of these tests are performed under impact loading as representing the most severe testing condition, the Charpy V-notch and the Pellini drop weight test being among the most commonly used for the purpose. Using a series of specimens, plots of temperature versus energy absorbed to fracture or percentage crystallinity are constructed from which material quality is defined either by the amount of energy absorbed at a particular temperature or by a transition temperature corresponding to the change in fracture mode. Various definitions of transition temperature have been used including that corresponding to a specific energy level and that at which the fracture appearance exhibits a specific crystallinity or shear called the fracture appearance transition temperature, $FATT_n$ where n is the percentage shear. Of these definitions $FATT_{50}$ for 50% crystallinity, 50% shear is most frequently specified. In the Pellini drop weight test the nil ductility temperature, NDT is defined as the highest temperature at which the material remains brittle.

The information obtained from impact tests has been applied in design either by specifying that a minimum amount of energy, say 20J, must be absorbed by the structural material at a given operating temperature or by allowing loading of the structure only at temperatures a given increment, say 30°C, above the transition temperature. Unfortunately, the impact energy transition curve is not a material property in the same sense as the yield stress or ultimate tensile strength but depends very much on the actual test conditions of notch geometry, section thickness and straining rate. Therefore, before applying small notched or precracked specimen test results to large structural components, intermediate model tests and correlations with service experience are necessary. The high cost of such

tests has meant that correlations between small and large scale configurations have only been performed in a few cases.

For example, as a result of extensive tests carried out on the Liberty Ship hulls after the Second World War, it was suggested that any steel used at sub-zero temperatures should exhibit a minimum absorbed energy to fracture of 20J at 10°C; 20J representing a transition energy level below which the ship's plates failed by brittle cleavage fracture.

More recently, extensive work has been undertaken by Pellini and his associates using the drop weight test, the dynamic tear test and the Robertson crack arrest test, the results being developed into their well-known Fracture Analysis Diagram, FAD which reflects service failure correlations (9)-(11). In the FAD, material behaviour in the presence of a defect is described graphically by the three variables, nominal stress, temperature relative to NDT and defect length. The transition temperature procedure of the FAD later became the basis of material toughness requirements and operational criteria stipulated in Section III of the ASME Boiler and Pressure Vessel Code. The latter is, perhaps, the most widely used code in the world for pressure vessel design and up to 1972 the ASME requirement was that primary pressure-retaining components be operated above the NDT in the ductile regime.

Unfortunately, although simple to use, several major criticisms have been made of design criteria established on the basis of the transition temperature procedure. For example, although thick sections are known to produce a degree of constraint at a notch or crack tip resulting in a shift in transition temperature to higher values, the exact quantitative influence of this effect has not been clarified. Expensive tests on representative sections of material of the appropriate thickness are not always possible.

In addition, even if the resources are available for measuring a full-scale transition temperature such a value has little relevance except under

fast loading conditions. The results of full-scale tests on 762 mm diameter pipe (12) have shown that conventional impact tests (Charpy V-notch, Pellini drop weight test) have no direct relationship with a fracture initiation transition temperature, although the Charpy V-notch and the Battelle drop weight tear test (a development of a drop weight tear test concept originated by Pellini) can be used to predict a full- scale fracture propagation transition temperature. These same results indicate that the propagation transition temperature for low-to-medium strength structural steels commonly used in pressure vessels and piping, averages about 30°C above the initiation transition temperature so that on this basis, the design philosophy based on a propagation transition temperature has been deemed conservative. However, as pointed out by Duffy (12) in 1969 and contrary to a commonly held view at the time, ductile crack initiation and propagation is possible at temperatures above the (propagation) transition temperature and designing on this basis merely ensures that if fracture occurs it is of the high energy absorbing, shear type. Although such a design philosophy has relevance in a pipe-line where subsequent crack arrest is possible, it is difficult to justify for a one-off pressure vessel where even a shear fracture can destroy the vessel.

Finally, although the information obtained from standard impact tests is obviously useful in material selection and quality control, it does not allow quantitative evaluation of the load-carrying capacity and crack propagation resistance of a structural material in the presence of defects i.e. the precise conditions under which failure occurs cannot be specified.

1.2 Current Design Code Practice for the Safety of Pressure Vessels with Defects

In comparison to classical engineering design, current design code practice for the safety of pressure vessels assumes that the vessel contains defects no matter how strict the production and inspection procedures. The

aim is then to limit the defect size to acceptable levels having due regard to material toughness, section thickness, operating temperature and loading conditions as well as fabrication and inspection techniques.

Current regulations for fracture-safe assurance of pressure vessels in America were first embodied in Section III, Appendix G of the ASME Boiler and Pressure Vessel Code in the Summer Addenda, 1972 (13). These rules are based upon the concepts of linear elastic fracture mechanics, developed during the 1950's and 1960's as an alternative to the transition temperature approach to failure analysis. In comparison with the latter, linear elastic fracture mechanics is a stress-analysis based approach concerned with the mathematical treatment of elastic stress field conditions at the crack tip, thereby allowing evaluation of applied stress levels to failure.

Briefly, the linear elastic fracture mechanics approach assumes that the stresses in the structural component, including the crack tip region, follow linear elastic behaviour. With this assumption it can be shown that the crack tip stress field may be characterised by a single parameter called the "stress intensity factor," K which is a function of crack size, structural dimensions and shape and applied load. For loadings which produce an opening mode of displacement between the crack surfaces, the subscript $_I$ is normally used i.e. K_I. A basic premise of linear elastic fracture mechanics is that unstable crack propagation from an existing defect occurs when K_I attains a critical value, designated K_{Ic}, the latter being called the plane strain (thick sections) fracture toughness of the material at the temperature of interest.

For normal and upset conditions in shell or head regions remote from discontinuities, the current ASME B.and P.V. Code (14) postulates the existence of a sharp, surface defect normal to the maximum stress direction. The defect is assumed to be semi-elliptical with a length six times its depth; a depth of one quarter the section thickness being assumed for

sections 102-305 mm thick, with a constant depth of 25 mm and 76 mm for sections less than 102 mm and greater than 305 mm thick, respectively. For shell and head regions remote from discontinuities, the only significant loadings should be components due to the pressure or primary membrane stress, K_{Ip} and to the thermal stress during startup and shutdown, K_{It}. Then, the requirement for startup, shutdown and normal and upset operating conditions is given by:

$$2K_{Ip} + K_{It} \leqslant K_{IR} \qquad 1.1$$

throughout the life of the component at each temperature, where K_{IR} is a lower bound value of K_{Ic} and the factor, 2 represents a safety factor on the primary stress level. K_{Ip} and K_{It} are either calculated or obtained graphically from figures presented in the Code. For nuclear pressure vessel steels, correlations of static, dynamic and crack arrest critical K_I values have been used to define a lower bound curve for K_{Ic} as a function of temperature and an analytical approximation to the curve is given in the Code for use with ferritic steels meeting certain yield strength requirements.

In the absence of fatigue or high temperature creep, the complete design criteria for the safety of shell or head regions away from discontinuities is then provided by application of equation 1.1 in combination with criteria based upon classical engineering design. Thus, to prevent failure by gross section yield, the applied design stress level, σ is limited to values below the yield stress, σ_y or the ultimate tensile strength, σ_u i.e.

$$\sigma = \frac{\sigma_{y(min)}}{1.5} \quad \text{or} \quad \frac{\sigma_{u(min)}}{3} \qquad 1.2$$

whichever is the lower, where the subscript $_{(min)}$ refers to the minimum specified value at the temperature of interest.

The same general procedure for shell and head regions may be used

for areas where more complicated stress distributions occur and recommendations are made as to allowable loadings and safety factors. For example, close to a flange or nozzle where bending stresses may be an important contribution to K_I, a safety factor of 2.0 is suggested for the primary bending stress. The Code also recommends the use of linear elastic fracture mechanics principles for emergency conditions but the formulation of criteria for this situation is left to the user.

At present the most serious problem with the ASME B. and P.V. Code relatesto limitations in its application. For example, values of K_I are only given for relatively simple geometric configurations such as the semi-elliptical surface flaw in a thick plate. For more complex situations such as a longitudinal flaw at the toe of a nozzle or an internal nozzle corner crack in the longitudinal plane of symmetry, both serious possibilities in a pressure vessel (1) (2), no guidelines for the quantitative evaluation of K_I are given.

In addition, plane strain fracture toughness values for materials other than the nuclear pressure vessel steels considered in the Code may be difficult to obtain for low-to-medium strength materials for which the standard specimen size requirements (15) are prohibitively large. In fact, this is the main reason why the reference material toughness, K_{IR} for the ferritic steels given in the Code was determined by correlations.

Finally, the Code is only applicable to situations where the concepts of linear elastic fracture mechanics have some validity. An investigation of the boundaries of applicability of linear elastic fracture mechanics forms a major part of the present study.

In comparison with the ASME B. and P.V. Code, more traditional material notch toughness requirements have been incorporated into the British Standard 5500 for "Unfired Fusion Welded Pressure Vessels" (16) as part of the design criteria for the operation of carbon and carbon manganese steel

vessels at low temperatures. The specifications are based upon wide plate test data and require that the material exhibits a minimum Charpy V energy at a test temperature determined by the operating design temperature and section thickness. For example, materials with an ultimate tensile strength less than 450 N. mm^{-2} require a Charpy V energy level of at least 27 J; for higher strength materials with an ultimate strength in excess of 450 N. mm^{-2}, a minimum energy absorption of 40 J is specified. Temperature-thickness limits are presented graphically for selection of the correct impact test temperature, allowance being made for components in the unwelded, welded or post-welded heat treated condition. The applied design stress is also limited by criteria similar to equation 1.2, although the safety factor for designs based on the ultimate tensile strength is limited to 2.35 for carbon and carbon manganese steels.

Unfortunately, no comparisons of the degree of conservatism built into the ASME B.and P.V. Code and B.S. 5500 for the fracture-safe assurance of pressure vessels with defects, have been made. However, it is clear that both Codes depend upon a minimum specified material toughness being achieved at the operating temperature, this specified toughness level varying according to the section thickness and the uniaxial tensile properties of the material.

Another procedure for fracture-safe design which has been receiving considerable attention in the U.K., is based on a different concept of material toughness called "crack opening displacement." In this approach a critical crack opening displacement is evaluated for the section thickness of material at the operating temperature and related to the nominal strain applied to the structure by means of an empirically derived design curve (17):

$$\left.\begin{aligned} \Phi = \frac{\delta}{2\pi\varepsilon_y a} &= \left(\frac{\varepsilon}{\varepsilon_y}\right)^2 \quad \text{for } \frac{\varepsilon}{\varepsilon_y} \leqslant 0.5 \\ \Phi = \frac{\delta}{2\pi\varepsilon_y a} &= \frac{\varepsilon}{\varepsilon_y} - 0.25 \quad \text{for } \frac{\varepsilon}{\varepsilon_y} \geqslant 0.5 \end{aligned}\right\} \quad 1.3$$

Equations 1.3 were established primarily from results obtained for centre and edge-cracked plates loaded in tension (18) where δ represents the crack opening displacement, ε, the nominal tensile strain, ε_y, the tensile yield strain of the material and a, the crack half-length. For a design strain, $\frac{\varepsilon}{\varepsilon_y}$ a "safe" value of Φ is determined using equation 1.3, from which either the critical crack opening displacement or defect size is obtained from knowledge of the other. Reference (17) also describes procedures for accounting for stress concentrations and residual stresses, although the basis on which the design strain, $\frac{\varepsilon}{\varepsilon_y}$ should be assessed is not clear.

A further attempt to establish guidelines for the assessment of the severity of defects in structures in the U.K. has also been made by the C.E.G.B. (19).

1.3 Objectives of the Present Study

The main aim of the present work is to study the fundamental principles underlying quantitative assessments of the severity of defects in structural components, in general, in order to determine criteria for the failure analysis of pressure vessels with defects. This study divides naturally into two parts.

Chapters 2, 3 and 4 consist of a critical review of the fields of fracture mechanics (linear elastic and elastic-plastic behaviour), failure governed by large scale plastic deformation and energy balance methods, respectively. It is shown that all three approaches have relevance in the complete failure analysis of a structure with defects and that these approaches are complementary rather than competing. Particular problem areas are pointed out in the text, some of which are investigated in the

experimental programme.

Chapters 6, 7 and 8 are an experimental study of the failure mechanisms of precracked model specimens of polycarbonate and maraging steel and model cylindrical vessels of polycarbonate with longitudinal defects. Of particular interest are the phenomena of crack initiation and stable crack growth and these results are presented in a form similar to the one suggested by Dowling and Townley (20). A major part of the experimental investigation is concerned with the determination of the geometry dependence of the general fracture toughness parameter, R and R_i for crack initiation; the latter being related to the plane strain fracture toughness, K_{Ic}. An introduction to the experimental study is given in chapter 5.

1.4 Scope of the Present Study

In order to understand the fundamental concepts of failure analysis techniques and to study actual failure mechanisms experimentally, the emphasis of the present work has been placed on simplicity. Thus, both the theoretical and experimental programmes are restricted to the simplest possible condition of static loading of configurations with single, isolated defects at ambient temperature. Arrays of cracks and their interaction are not considered and the influence of variations in strain rate and temperature are not studied explicitly. In addition, cyclic loading (fatigue), environmental attack (corrosion) and high temperature effects (creep) are also very important but are beyond the scope of the present study.

References

(1) J. Deacock, Proc. 1st Int. Conf. Pres. Ves. Tech., Delft, paper II-58, 1969.

(2) J.L. Mershon, Welding Research Council, Bulletin No. 77, 1962.

(3) C.F. Tipper, "The Brittle Fracture Story," Cambridge Univ. Press, 1962.

(4) G.M. Boyd, "Brittle Fracture in Steel Structures," Butterworths, London, 1970.

(5) "Special Report on Failure of a Boiler during Hydrostatic Test at Sizewell Nuclear Power Station," West of Scotland Iron and Steel Institute, 1964.

(6) BWRA, Bulletin, 7, No. 6, June 1966.

(7) "Report on the Brittle Fracture of a High-Pressure Boiler Drum at Cockenzie Power Station," Welding Research Abroad, Oct. 1967.

(8) A.B. Holt, Nuclear Eng. and Design, 28, p. 239, 1974.

(9) W.S. Pellini and P.P. Puzak, Welding Research Council, Bulletin No. 88, 1963.

(10) W.S. Pellini, Welding Research Council, Bulletin No. 130, 1968.

(11) W.S. Pellini and F.J. Loss, NRL Report No. 6900, April 1969.

(12) A.R. Duffy, R.J. Eiber, G.M. McClure and W.A. Maxey, "Fracture — an Advanced Treatise," Vol. V, Ed. H. Liebowitz, Academic Press, New York, p. 159, 1969.

(13) ASME Boiler and Pressure Vessel Code, Section III, Nuclear Power Plant Components, Summer Addenda, 1972.

(14) ASME Boiler and Pressure Vessel Code, Section III, Division 1 — Nuclear Power Plant Components, 1974 and Section VIII, Pressure Vessels — Division 2 — Alternative Rules, 1974.

(15) "Plane Strain Fracture Toughness of Metallic Materials," A.S.T.M. E399-72 Part 31, 1972.

(16) "Specifications for Unfired Fusion Welded Pressure Vessels," B.S. 5500: 1976, B.S.I., London.

(17) I.I.S./I.I.W., Commission X, Working Group on Significance of Defects, "Proposed Acceptance Standards for Flaws with Respect to Failure by Brittle Fracture," Document X-WGSD-13, 1974.

(18) F.M. Burdekin and D.E.W. Stone, J. Strain Analysis, 1, p. 145, 1966.

(19) R.P. Harrison, K. Loosemore and I. Milne, C.E.G.B. Report No. R/H/R6 - Rev. 1, Aug. 1976, revised April 1977.

(20) A.R. Dowling and C.H.A. Townley, Int. J. Pres. Ves. and Piping, 3, p. 77, 1975.

CHAPTER 2

FRACTURE MECHANICS

Fracture mechanics developed from the study of brittle fracture as a result of accidental failures of engineering structures at stress levels well below the yield strength and in particular below the design limits. In most cases the origin of failure was found at existing flaws which became critical as the stress was increased, or which grew to critical size during operation of the structure. Fracture mechanics, based on a generalised continuum approach to fracture, provides an analytical basis for the study of the crack growth process at the macroscopic level.

In general, there are considered to be two approaches to fracture mechanics, the stress intensity approach and the energy balance approach; only the former will be presented here, the latter being treated more fully in chapter 4.

2.1 Linear Elastic Fracture Mechanics - Stress Intensity Factor Approach

Irwin's concept of stress intensity stems from the Westergaard equations for the stress distribution ahead of a sharp crack in a linear elastic material (1). For example, the elastic stress field corresponding to the opening mode of crack surface displacement is, referring to Fig. 2.1 for notation:

$$\sigma_{xx} = k\,\sigma\sqrt{\frac{a}{2r}}\,.\,\cos\frac{\theta}{2}\left(1 - \sin\frac{\theta}{2}\,.\,\sin\frac{3\theta}{2}\right) + \ldots. \qquad 2.1$$

$$\sigma_{yy} = k\,\sigma\sqrt{\frac{a}{2r}}\,.\,\cos\frac{\theta}{2}\left(1 + \sin\frac{\theta}{2}\,.\,\sin\frac{3\theta}{2}\right) + \ldots. \qquad 2.2$$

$$\sigma_{zz} = \nu\,(\sigma_{xx} + \sigma_{yy}) \qquad \text{plane strain} \qquad 2.3$$

$$\text{or}\quad \sigma_{zz} = 0 \qquad \text{plane stress} \qquad 2.4$$

$$\tau_{xy} = k\,\sigma\,\sqrt{\frac{a}{2r}}\,.\,\sin\frac{\theta}{2}\,.\,\cos\frac{\theta}{2}\,.\,\cos\frac{3\theta}{2} + \ldots. \qquad 2.5$$

$$\tau_{xz} = \tau_{yz} = 0 \qquad 2.6$$

where .... refers to terms of the order of r^0, k is a constant and a function of body and crack geometry, σ is the applied stress, a is the crack half-length and ν is Poisson's ratio.

Irwin (2) noted that the stresses in the vicinity of the crack tip could be rewritten in the form:

$$\begin{bmatrix}\sigma_{xx}\\ \sigma_{yy}\\ \tau_{xy}\end{bmatrix} = \frac{K_I \cos\frac{\theta}{2}}{\sqrt{2\pi r}} \begin{bmatrix}1 - \sin\frac{\theta}{2}\,.\,\sin\frac{3\theta}{2}\\ 1 + \sin\frac{\theta}{2}\,.\,\sin\frac{3\theta}{2}\\ \sin\frac{\theta}{2}\,.\,\cos\frac{3\theta}{2}\end{bmatrix} + \text{terms of order } r^0 \qquad 2.7$$

where K_I is defined as the elastic stress intensity factor (opening mode) and characterises the elastic stress field at the tip of the crack. Comparison with the Westergaard equations yields:

$$K_I = k\,\sigma\,\sqrt{\pi a} \qquad \text{for} \quad r << a \qquad 2.8$$

i.e. K_I is solely a function of body and crack geometry, applied stress and crack length.

With the elastic stress field equations in this form the stresses are always proportional to the square root of the distance from the crack tip. Thus, for a particular loading mode the stress intensity factors due to different loadings can be superimposed by algebraic addition or, if several different loading modes are present the individual stress components and displacements can be superimposed.

However, the basic requirement of a successful analysis is to have an effective criterion of fracture. For a crack to grow under static loading two distinct conditions must be satisfied (3). Firstly, the crack must be

sufficiently sharp for the stress to be available to operate a fracture mechanism. The second condition, concerned with the thermodynamics of the fracture process, was originally treated by Griffith (4) who showed that the work done by the applied forces must be sufficient to supply the surface energy of the crack. Restated by Irwin in fracture mechanics terms:

$$\mathcal{G} \geqslant \mathcal{G}_c \qquad 2.9$$

where $\mathcal{G}$ is the elastic strain energy release rate and $\mathcal{G}_c$ is the effective surface energy (two surfaces) and is understood to include both the theoretical surface energy and the plastic work contribution.

The importance of this inequality was established after Irwin (2) demonstrated by virtual work arguments the equivalence between the strain energy release rate, $\mathcal{G}$ and the stress intensity factor, K:

$$\mathcal{G} = \frac{K^2}{E'} \qquad 2.10$$

where $E' = E/(1-\nu^2)$, plane strain

$E' = E$, plane stress

Thus, if fracture can be characterised by the attainment of a critical strain energy release rate, $\mathcal{G}$ it can also be characterised by a critical stress environment, K. It follows that both conditions concerning the stress and energy or thermodynamic requirements for crack growth are satisfied when:

$$K \geqslant K_c \qquad 2.11$$

Therefore, for the failure of an elastically loaded body containing a crack of initial half-length, a:

$$K_c \leqslant k\,\sigma\,\sqrt{\pi a} \qquad 2.12$$

This equation forms the basis of the fracture mechanics approach to the design and inspection of structures once the geometrical parameter or stress

intensity coefficient k is known and the material parameter, K_c called the "fracture toughness" has been determined by means of tests on small specimens.

The main advantage of linear elastic or Griffith-Irwin fracture mechanics is that it is based on a linear elastic analysis. Thus, K should not be regarded as a parameter solely associated with stress but rather as a parameter characterising the mechanical environment as a whole, whether this be in terms of the stress, strain, displacement or strain energy density of the near-tip elastic stress field. The fact that the analysis admits application of the principle of superposition is of secondary importance; for, although stress components and displacements due to different loading modes can be superimposed, in practice this is not done since it is difficult to justify a fracture criterion based on the attainment of critical values of K_{II} or K_{III} where crack extension is non-planar. Most practical cases are concerned with loading that is symmetric with respect to the crack plane and in these circumstances the variables with subscript $_I$ apply. For the purposes of future discussion, crack surface displacements of the opening mode, only will be considered unless otherwise specified.

The main limitations of the analysis as presented so far, in addition to the obvious one of linear elastic behaviour, are those inherent in the use of the Westergaard simplified treatment of the stress field. These include the use of a two-dimensional stress analysis and its breakdown at very small and large values of r.

The third dimension is not accounted for explicitly in the use of the K concept. A body is considered to be under conditions of plane stress or plane strain, depending on the third dimension and with either of these assumptions, the stress-strain analysis is greatly simplified, being reduced to a two-dimensional problem. Within the context of this two-dimensional analysis the conditions of plane stress and plane strain should

be regarded merely as upper and lower bounds on K with a maximum variation between the two given by Poisson's ratio through the term, $(1-\nu^2)$.

The form of the Westergaard equations implies that the stresses are infinite at the crack tip as r tends to zero. This conclusion is, of course, incorrect and results from the assumption of a true continuum. Normally, such difficulties are rationalised by regarding the discrete nature of the crack tip as a disturbance in the continuum and, by invoking St. Venant's principle, the effect of the disturbance is negligible at large distances with respect to the size disturbance. Thus, the real stress fields should approach those given by the Westergaard equations at sufficiently large distances compared with the crack tip radius.

In summary, despite the inherent defects of linear elastic fracture mechanics, LEFM the analysis is found to give reliable results when applied to high strength materials, glassy plastics and thick sections of commercial alloys for which the assumption of linear elastic behaviour is valid. Standard test procedures now exist for determining the "plane strain fracture toughness," K_{Ic} (5) (6) and a compendium of stress intensity factors has recently been published for direct application of these values to complex geometrical situations (7).

2.2 LEFM and the Plasticity Correction Factor

It may seem surprising that thick sections of commercial alloys display constant K_{Ic} values since it is well known that most alloys of practical interest yield and relax plastically at the crack tip; also, the Westergaard equations do not describe the stresses in an elastic-plastic material. Hahn and Rosenfield (8) point out, however, that the general features of LEFM are also displayed by elastic-plastic solutions. For example, K continues to express the equivalence between applied stress and crack length for stress levels up to 0.7 times the general yield stress, σ_{gy}. In addition, such features as the plastic zone size, ρ', the crack

tip displacement, v and the crack tip strain, ε_{tip} are monotonic — though not linear — functions of K so that a fracture criterion based on a constant limiting value of v_c or ε_c must lead to a constant value of K_{Ic}.

Irwin (9) has shown that provided the plastic zone size is small, very much smaller than the radius over which K can be considered to characterise the stress field, then the elastic stress field beyond the yield zone is practically unaffected by plastic deformation and the formulae for K remain valid. At present, standard specimen size requirements (5) (6) demand that the plastic zone size, ρ' be less than 0.02a to allow linear elastic analyses to be used.

For plastic zones larger than 0.02a a linear elastic analysis may still be used but now a correction factor is required to account for the deviation of the single valued parameter, K from the full series expression at increasing distances from the crack tip (10) (11). To rationalise this apparent increase in K, Irwin (9) introduced the concept of an "equivalent elastic crack." His equivalent model is shown in Fig. 2.2 where it can be seen that the plastic zone is bounded by the surface on which the stress is equal to the uniaxial yield stress, σ_y. Using the Westergaard equations for the elastic stress field, Irwin showed that the plastic zone could be represented by a cylinder of radius:

$$r_{y1} = \frac{1}{2\pi}\left(\frac{K}{\sigma_y}\right)^2 \qquad \text{plane stress} \qquad 2.13$$

$$r_{y2} = \frac{1}{6\pi}\left(\frac{K}{\sigma_y}\right)^2 \qquad \text{plane strain} \qquad 2.14$$

the plane strain expression being obtained by imposing an average stress intensification of $\sqrt{2\sqrt{2}} = 1.68$ on the uniaxial yield stress. The governing equation is then modified:

$$K_{Ic} \leqslant k\,\sigma\sqrt{\pi\,(a+r_y)} \qquad \frac{\sigma}{\sigma_{gy}} < 0.7 \qquad 2.15$$

Thus, the distribution of stress remains as $r^{-1/2}$; it is only the

apparent position of the crack border which has changed.

In real situations the size and shape of the plastic zone depends upon the plastic flow properties of the material, but it is proportional to $(K/\sigma_y)^2$; Irwin's elastic solution being a good approximation for certain materials with high strain-hardening exponents (8) (12).

2.3 Fracture Mechanics and Elastic-Plastic Behaviour

An interesting feature in the behaviour of thin sections of many commercial alloys is the production of extremely large crack tip plastic zones which may be accompanied by sustained slow crack growth of significant proportions prior to crack instability. Unfortunately, if the plastic zone becomes too large which generally occurs when the applied stress exceeds $0.7\sigma_{gy}$, LEFM is no longer applicable. General elastic-plastic analysis is needed to describe crack growth under such conditions but due to the mathematical difficulties, no satisfactory analytical treatment suitable for fracture toughness evaluation is at present available.

Attempts have been made to resolve the problem by extending the concepts of LEFM into situations where moderate to extensive plastic deformation may be accommodated at the crack tip. Of particular note are the crack opening displacement, the J-integral and the crack growth resistance curve.

2.3.a Crack Opening Displacement, COD

It is now well established that for elastic-plastic crack tip deformation a singularity still exists (13) and it has been proposed that the crack opening displacement near the crack tip reflects the nature of this singularity (14). Wells (14) suggested that the amount by which the crack opens is a measure of the work done in extending the crack and under linear elastic conditions this opening, termed COD, was shown to be compatible with the K and $\mathcal{J}$ concepts used in LEFM.

Several different crack tip models have been used to represent the

COD. These include Irwin's equivalent elastic model as well as mixed elastic-plastic stress field models for plane stress (15) and anti-plane strain (mode III) configurations (16) (17). Only the Dugdale-Muskhelishvili model for plane stress relaxation will be considered here, however, since the analysis yields similar results as an analysis based on a continuous distribution of dislocations (16) (17).

The Dugdale model (15), shown in Fig. 2.3, consists of an isolated slit of length, 2a in a thin infinite sheet (plane stress) subjected to a remotely applied uniform stress, σ. Although the plastic zone shape i.e. very narrow bands of thickness comparable to the dimension of the slit opening, are assumed *a priori,* such yield zones have been observed in very thin sheet material with mild strain-hardening (18). The size of ρ' is chosen such that the stress singularity disappears. The real crack with plastic zones is replaced by a hypothetical crack of half-length, $a + \rho'$ acted on over the region ρ' by internal tractions of yield magnitude. Using Muskhelishvili stress function methods for the elastic analysis of a sheet with an end-loaded extended crack a relationship between the crack length, applied stress and plastic zone size is obtained:

$$\frac{a}{a+\rho'} = \cos\left(\frac{\pi}{2}\frac{\sigma}{\sigma_y}\right) \qquad \text{plane stress, no strain-hardening} \quad a > 0 \qquad 2.16$$

With this model it can be shown (19) (20) that the amount by which the real crack opens at its ends, the COD, is:

$$\delta = 8\frac{\sigma_y a}{\pi E} \ln \sec\left(\frac{\pi}{2}\cdot\frac{\sigma}{\sigma_y}\right) \qquad 2.17$$

In terms of a series expansion:

$$\delta = 8\frac{\sigma_y a}{\pi E}\left[\frac{1}{2}\left(\frac{\pi}{2}\cdot\frac{\sigma}{\sigma_y}\right)^2 + \frac{1}{12}\left(\frac{\pi}{2}\cdot\frac{\sigma}{\sigma_y}\right)^4 + \ldots.\right] \qquad 2.18$$

For small values of σ, only the first term need be retained:

$$\delta = \pi \frac{\sigma^2 a}{E\sigma_y} \qquad \frac{\sigma}{\sigma_y} < 0.1,\ \rho' < 0.01a \qquad 2.19$$

The LEFM expression for a cracked infinite sheet in plane stress is:

$$K^2 = E\mathcal{G} = \sigma^2 \pi a \qquad 2.20$$

and substitution into 2.19 yields:

$$\delta = \frac{K^2}{E\sigma_y} = \frac{\mathcal{G}}{\sigma_y} \qquad \text{plane stress, no strain-hardening} \qquad 2.21$$
$$\frac{\sigma}{\sigma_y} < 0.1,\ \rho' < 0.01a$$

Thus, in the case of crack growth under plane stress conditions at low applied stress levels, the COD is totally consistent with LEFM.

To extend this expression to crack growth at higher applied stress levels and consequently to allow increased plasticity at the crack tip, requires consideration of the higher order terms of the series expansion, equation 2.18. However, a similar result is obtained using Irwin's equivalent elastic model for the plastic zone (21), Fig. 2.2:

$$\left.\begin{aligned} \delta &= \frac{4}{\pi} \cdot \frac{K^2}{E\sigma_y} = \frac{4}{\pi} \cdot \frac{\mathcal{G}}{\sigma_y} && \text{plane stress} \\ \delta &= \frac{4}{\pi}\sqrt{3} \cdot \frac{K^2}{E\sigma_y} = \frac{4}{\pi}\sqrt{3}\,(1-\nu^2) \cdot \frac{\mathcal{G}}{\sigma_y} && \text{plane strain} \end{aligned}\right\} \frac{\sigma}{\sigma_{gy}} < 0.7 \qquad 2.22$$

These expressions indicate that the overall relationship between the COD and K or $\mathcal{G}$ remains essentially the same even up to applied stress levels of 0.7 σ_{gy} and may be accounted for by means of a constant parameter. Thus, if a constant critical value of COD, independent of geometry, can be measured in a small specimen for which crack growth occurs at stress levels below 0.7 σ_{gy}, then the possibility exists for this COD to be related to a constant critical K or $\mathcal{G}$ and thereby to be used in the failure analysis of large structures, equation 2.12. This is the essence of the COD approach which has received considerable support, particularly in the U.K. At the present time there is evidence that the COD at the initiation of fibrous fracture (microvoid coalescence), defined as δ_i, is constant

for a given crack tip stress state (22) (23) and can be related to the plane strain fracture toughness, K_{Ic} (24). Values of δ taken at maximum load in a generally yielded specimen, however, are sensitive to the loading conditions (25) (26) and geometry (27)-(29). With this experimental evidence in mind several important points should be considered.

Firstly, the limits of applicability of the COD approach appear to be identical to those of LEFM with a plasticity correction factor. Therefore, the only advantage in using the COD must lie in the possibility of obtaining values of K_{Ic} or $\mathcal{Y}_{Ic}$ by means of small specimens, for which the applied stress does not exceed $0.7\sigma_{gy}$ prior to crack initiation and for which there is no change in fracture made at specimen mid-section between large and small specimens.

Difficulties may arise in the experimental determination of reliable values of COD. These difficulties mainly relate to the choice of the rotational factor, r which enables conversion of values of on-load clip gauge displacement to mid-section COD. Experimental results have shown that r is itself a function of the COD (24) and the test piece geometry (30) so that knowledge of the particular relationship between r and COD for the geometry of interest is required before reliable values of COD may be obtained. The British Standard Institution Draft for Development, DD19: 1972 (31) recommends the use of the three point bend test configuration for determining values of COD.

Finally, opinions differ as to the exact form of the relationship between COD and K or $\mathcal{Y}$, depending upon the theoretical analysis used (24). Recent results (32) indicate that it is material dependent, possibly being controlled by the strain-hardening rate. This is equivalent to the case of LEFM with a plasticity correction factor, r_y, the latter being a function of the plastic flow properties of the material.

2.3.b J-Contour Integral, J-Integral[a]

The energy line integral, J as originally proposed by Rice (33) is applicable to an elastic or deformation-type elastic-plastic material. It is defined for two-dimensional problems by:

$$J = \int_{\Gamma} \left[W dy - T_i \frac{\partial u_i}{\partial x} \right] ds \qquad 2.23$$

where x and y are rectangular coordinates normal to the crack front, y being perpendicular to the crack surface for a crack aligned in the x direction; ds is an increment of arc length along any contour, Γ from the lower crack surface anticlockwise around the crack tip to the upper face; W is the strain energy density of the form $\int_0^{\varepsilon} \sigma_{ij} \, d\varepsilon_{ij}$ and $T_i \, du_i$ are work terms when components of surface tractions on the contour path, T_i move through displacements, du_i.

Rice (33) has proven the path independence of the J-contour integral and has further shown (34) that for the elastic or deformation-type elastic-plastic material, J may be interpreted as the potential energy difference between two identically loaded bodies of thickness, B having neighbouring crack sizes a and a + Δa:

$$J = -\frac{1}{B}\left(\frac{\partial U}{\partial a}\right)_u \qquad \begin{array}{l}\text{elastic or}\\ \text{deformation-type}\\ \text{elastic-plastic material}\end{array} \qquad 2.24$$

where the potential energy equals the strain energy, U for loading by imposed displacements, u only.

For small scale yielding J reduces to the fracture mechanics parameter $\mathcal{G}$ (33):

$$J = \frac{K^2}{E'} = \mathcal{G} \qquad \begin{array}{l}\text{small scale}\\ \text{yielding}\end{array} \qquad 2.25$$

---

[a] In the American literature, the expression "J-integral" refers to the quantity obtained experimentally from load-displacement curves, $-\frac{1}{B}\left(\frac{\partial U}{\partial a}\right)_u$. This should be distinguished from Rice's contour integral, called the "J-contour integral."

where $E' = E/(1-\nu^2)$, plane strain

$E' = E$, plane stress

It is this equivalence between $\mathcal{Y}$ and J in small scale yielding which has made the J-contour integral appear attractive as a possible fracture criterion for elastic-plastic behaviour.

A major assumption in deformation plasticity is that plastic strains are of the same small order as elastic strains and are uniquely determined by the final stress state, independent of loading history (35). Such behaviour may be followed by non-linear elastic materials but real materials generally obey incremental laws for which the final state does depend on the loading history. It is thus argued by proponents of the "J-integral" that the J-contour integral may be used as a parameter characterising the singular near tip stress and strain field around any elastic-plastic crack provided that only simple monotonic loading occurs, there is no unloading at the crack tip and the remote stress field is still elastic; conditions for which, it is argued, there should be little difference between deformation or incremental plastic behaviour.

Certainly, the J-contour integral cannot be applied generally to describe the behaviour of elastic-plastic materials after crack initiation (at which point some elements of material must be unloaded) or where complex loading may occur since, under such circumstances, deformation plasticity is no longer applicable and the line integral is path dependent (36) (37). If relevant at all, Rice's contour integral, J must relate to small scale yielding under monotonic loading up to the onset of crack growth.

There is an increasing body of experimental evidence indicating that the value of the experimentally determined parameter, $-\frac{1}{B}\left(\frac{\partial U}{\partial a}\right)_u$ at crack initiation is, subject to certain size limitations, independent of the degree of plasticity in the test piece (32) (38)-(42). Further, it appears that these critical values are related to the plane strain fracture

toughness, K_{Ic}:

$$-\frac{1}{B}\left(\frac{\partial U}{\partial a}\right)_{u_i} = \frac{(1-\nu^2)}{E} K_{Ic}^2 = \mathcal{J}_{Ic} \quad \text{plane strain} \qquad 2.26$$

On the basis of this relationship the experimental parameter, $-\frac{1}{B}\left(\frac{\partial U}{\partial a}\right)_u$ termed the "J-integral," has been proposed (40) as a method for obtaining valid measurements of K_{Ic} from small specimens in a manner analogous to the COD approach. However, it remains to be proved that, for crack initiation in elastic-plastic materials, the parameter $-\frac{1}{B}\left(\frac{\partial U}{\partial a}\right)_u$ can be identified with Rice's contour integral or that crack initiation in such materials occurs under small scale yielding conditions.

2.3.c Crack Growth Resistance Curve, R-Curve

The concept of a crack growth resistance curve, R-curve was first introduced by Krafft (43) to account for the observed increase in load necessary to maintain crack growth in cracked thin metal sheet prior to catastrophic failure. The situation is represented in Fig. 2.4, where load-displacement and load-crack length curves for an elastic-plastic material (thin sheet, ductile material) are compared with the corresponding curves for a linear elastic material (thick section, frangible material). The rising load-displacement and load-crack length curves for the elastic-plastic material after crack initiation are due to the increase in the plastic zone size with crack length and also to the strain-hardening property of the material (37).

On the basis of an earlier energy balance approach (44), Krafft (43) postulated that a continuous energy balance exists between the strain energy release rate, $\mathcal{J}$ and the rate of resistance of the material to crack extension, termed R, at all stages of slow crack growth up to the point of crack instability. A schematic representation of this energy balance is shown in Fig. 2.5, where stable crack growth occurs when:

$$\mathcal{J} = R \qquad \text{stable crack growth} \qquad 2.27$$

and the point of tangency between the $\mathcal{G}$ and R curves is taken as the point at which crack instability occurs:

$$\mathcal{G}_c = R_c \quad \text{and} \quad \left(\frac{d\mathcal{G}}{dA}\right)_c = \left(\frac{dR}{dA}\right)_c \qquad \text{crack instability} \qquad 2.28$$

Krafft further postulated that the curve of crack growth resistance versus absolute crack extension, termed the R-curve, is a material property independent of specimen geometry, for a given sheet thickness. On the basis of this assumption all changes in geometry are accounted for by changes in the geometry dependent $\mathcal{G}$-curve and hence, $\mathcal{G}_c$ is geometry dependent; Krafft was thereby able to account for the observed increase of fracture toughness, $\mathcal{G}_c$ with specimen width for remote-loaded specimens.

Two major criticisms of the validity of R-curve methods have been made (37). Firstly, the size of the plastic zone ahead of the crack front in thin sheet material may be extremely large so that the use of the fracture mechanics parameter, $\mathcal{G}$ valid only for small scale yielding is questionable. Also, the work rate of the applied forces is not accounted for explicitly in the energy balance expressions generally used for $\mathcal{G}$ (see section 4.1.a); conditions of either "fixed grip", where the work rate is zero, or "fixed load", where the work rate is twice the elastic energy release rate, are assumed but such conditions are only applicable at the onset of crack growth i.e. crack initiation. Therefore, unless the contribution of the work rate of the applied forces during slow crack growth under rising load is estimated, $\mathcal{G}$ cannot be applied to the crack extension process after crack initiation.

In spite of the foregoing, considerable interest has developed in R-curve techniques (45). A standard method for their determination has been proposed (46) although experimentally the postulate that an R-curve is a material characteristic, depending only on section thickness has not been fully substantiated (47)-(50).

Of particular interest is an observation by Mai (51) that R-curves

obtained from different thickness specimens of 4340 steel emanated from a common R_o at crack initiation, the only region in which experimental measurements of R have some analytical validity. Mai suggests that this value of R_o may be related to the plane strain fracture toughness, K_{Ic}.

2.4 Summary

To summarise, equation 2.15 defines the limit of applicability of fracture mechanics in the failure analysis of engineering structures at applied stress levels below general yield. At higher stress levels elastic-plastic or fully plastic behaviour develops depending on the extent of yielding and alternative analytical methods of failure analysis are necessary.

References

(1) H.M. Westergaard, J. Appl. Mech., 61, A49, 1939.

(2) G.R. Irwin, J. Appl. Mech., 24, p. 361, 1957.

(3) A.H. Cottrell, Proc. Symp. Crack Propagation, Cranfield, p. 1, 1961.

(4) A.A. Griffith, Phil. Trans. Roy. Soc., A221, p. 163, 1920.

(5) "Methods for Plane Strain Fracture Toughness (K_{Ic}) of Metallic Materials," B.S. 5447: 1977, B.S.I., London.

(6) "Plane Strain Fracture Toughness of Metallic Materials," A.S.T.M. E399-72 Part 31, 1972.

(7) D.P. Rooke and D.J. Cartwright, "Compendium of Stress Intensity Factors," Procurement Executive, M.D., H.M.S.O. Books, London, 1976.

(8) G.T. Hahn and A.R. Rosenfield, A.S.T.M. S.T.P. 432, "Applications Related Phenomena in Titanium Alloys," Am. Soc. for Testing and Materials, p. 5, 1968.

(9) G.R. Irwin, Proc. 7th Sagamore Conf., Syracuse Univ., p IV-63, 1960.

(10) J. Eftis and H. Liebowitz, Eng. Fract. Mechs., 7, p. 101, 1975.

(11) J.F. Knott, J. Strain Analysis, 10, p. 201, 1975.

(12) W.W. Gerberich, Expt. Mechs., 4, p. 335, 1964.

(13) J.R. Rice and G.F. Rosengren, J. Mech, Phys. Solids, 16, p. 1, 1968.

(14) A.A. Wells, Proc. Symp. Crack Propagation, Cranfield, p. 210, 1961.

(15) D.S. Dugdale, J. Mech. Phys. Sol., 8, p. 100, 1960.

(16) B.A. Bilby, A.H. Cottrell and K.H. Swinden, Proc. Roy. Soc., A272, p. 304, 1963.

(17) B.A. Bilby and K.H. Swinden, Proc. Roy. Soc., A285, p. 22, 1965.

(18) A.R. Rosenfield, P.K. Dai and G.T. Hahn, Proc. 1st Int. Conf. Fracture, Sendai, Japan, 1, p. 223, 1965.

(19) G.T. Hahn and A.R. Rosenfield, Acta Metallurgica, 13, p. 293, 1965.

(20) F.M. Burdekin and D.E.W. Stone, J. Strain Analysis, 1, p. 145, 1966.

(21) G.R. Egan, Eng. Fract. Mechs., 5, p. 167, 1973.

(22) R.F. Smith and J.F. Knott, Conf. Practical Application of Fracture Mechanics to Pressure Vessel Technology, Inst. Mech. Engs., p. 65, 1971.

(23) G.D. Fearnehough, G.M. Lees, J.M. Lowes and R.T. Weiner, Conf. Practical Application of Fracture Mechanics to Pressure Vessel Technology, Inst. Mech. Engs., p. 119, 1971.

(24) J.N. Robinson and A.S. Tetelman, A.S.T.M. S.T.P. 559, "Fracture Toughness and Slow-Stable Cracking," Am. Soc. for Testing and Materials, p. 139, 1974.

(25) G. Green, R.F. Smith and J.F. Knott, British Steel Corp. Conf. on Mechanics and Mechanisms of Crack Growth, Cambridge, paper 5, 1973.

(26) C.G. Chipperfield, J.F. Knott and R.F. Smith, 3rd Int. Conf. Fracture, Munich, 1, paper 233, 1973.

(27) T.C. Harrison and G.D. Fearnehough, Int. J. of Fract. Mechs., 5, p. 348, 1969.

(28) G. Green and J.F. Knott, J. Mech. Phys. Sol., 23, p. 167, 1975.

(29) G. Green and J.F. Knott, Metals Technology, 2, p. 422, 1975.

(30) T. Ingham, G.R. Egan, D. Elliott and T.C. Harrison, Conf. Practical Application of Fracture Mechanics to Pressure Vessel Technology, Inst. Mech. Engrs., p. 200, 1971.

(31) "Methods for Crack Opening Displacement (COD) Testing," D.D.19: 1972, B.S.I. London.

(32) J.N. Robinson, Int. J. of Fracture, 12, p. 723, 1976.

(33) J.R. Rice, J. Appl. Mech., 35, p. 379, 1968.

(34) J.R. Rice, "Fracture – An Advanced Treatise," Vol. II, Ed. H. Liebowitz, Academic Press, New York, p. 191, 1968.

(35) R. Hill, "The Mathematical Theory of Plasticity," Oxford Univ. Press, 1950.

(36) B.K. Neale, C.E.G.B. Report No. RD/B/N3253, 1975.

(37) J. Eftis and H. Liebowitz, Eng. Fract. Mechs., 7, p. 101, 1975.

(38) J.A. Begley and J.D. Landes, A.S.T.M. S.T.P. 514, "Fracture Toughness," Am. Soc. for Testing and Materials, p. 1, 1972.

(39) J.D. Landes and J.A. Begley, A.S.T.M. S.T.P. 514, "Fracture Toughness," Am. Soc. for Testing and Materials, p. 24, 1972.

(40) J.D. Landes and J.A. Begley, A.S.T.M. S.T.P. 560, "Fracture Analysis," Am. Soc. for Testing and Materials, p. 170, 1974.

(41) C.A. Griffis, Trans. A.S.M.E., Series J, J. Pres. Ves. Tech., 97, p. 278, 1975.

(42) K. Markström, Eng. Fract. Mechs., 9, p. 637, 1977.

(43) J.M. Krafft, A.M. Sullivan and R.W. Boyle, Proc. Symp. Crack Propagation, Cranfield, p. 8, 1961.

(44) G.R. Irwin and J.A. Kies, Welding Journal Research Supplement, 19, p. 193, 1954.

(45) A.S.T.M. S.T.P. 527, "Fracture Toughness Evaluation by R-Curve Methods", Am. Soc. for Testing and Materials, 1973.

(46) "A Recommended Procedure for R-Curve Determination," A.S.T.M. Book of Standards, No. 10, p. 811, 1975.

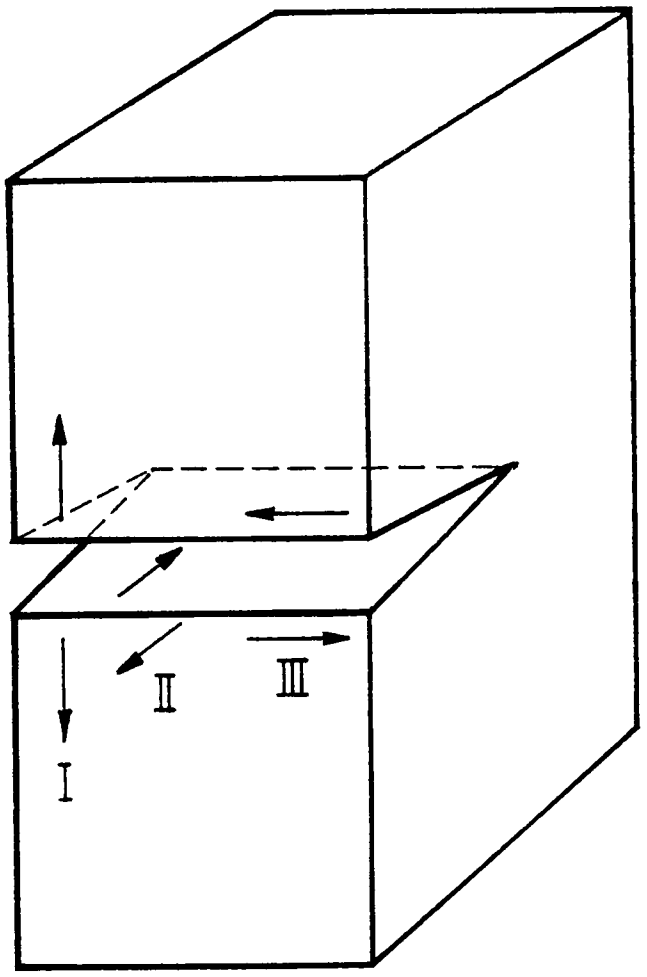
(47) R.H. Heyer and D.E. McCabe, Eng. Fract. Mechs., 4, p. 413, 1972.

(48) R.W. Judy, Jr., and R.J. Goode, A.S.T.M. S.T.P. 527, "Fracture Toughness Evaluation by R-Curve Methods," Am. Soc. for Testing and Materials, p. 48, 1973.

(49) A.M. Sullivan, C.N. Freed and J. Stoop, A.S.T.M. S.T.P. 527, "Fracture Toughness Evaluation by R-Curve Methods," Am. Soc. for Testing and Materials, p. 85, 1973.

(50) C.M. Carman, D.F. Armiento and H. Markus, Proc. 1st Int. Conf. Fracture, Sendai, Japan, 2, p. 995, 1965.

(51) Y.W. Mai, A.G. Atkins and R.M. Caddell, Int. J. of Fracture, 12, p. 391, 1976.



I OPENING MODE

II EDGE SLIDING MODE

III SHEAR MODE

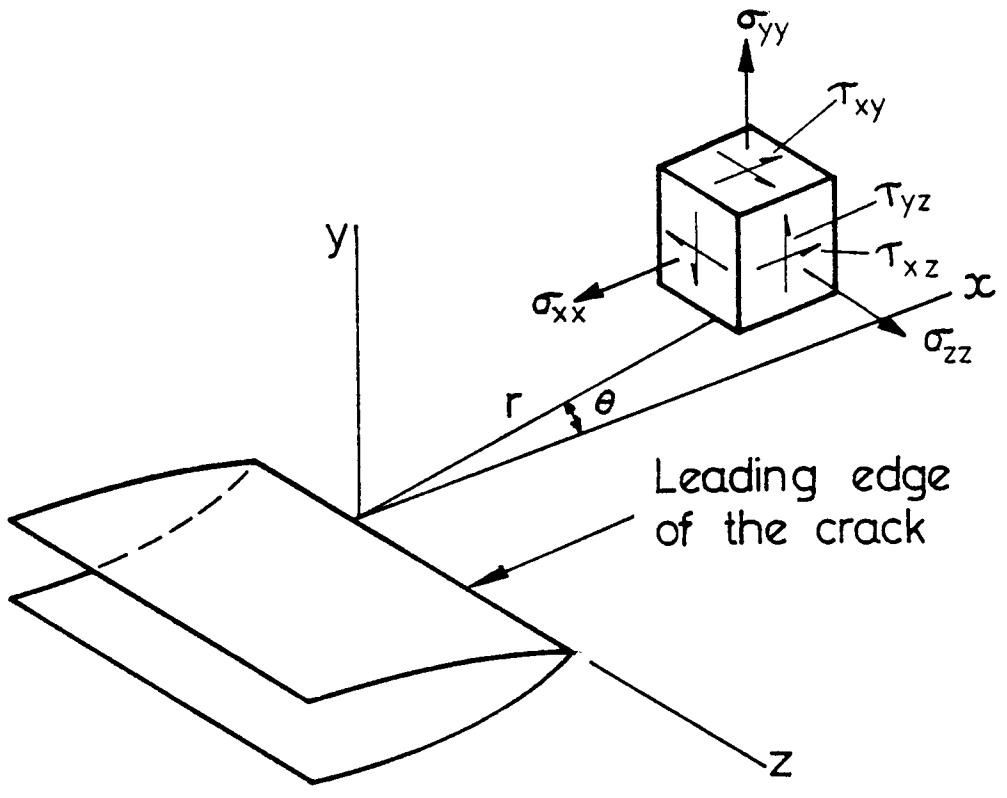


Fig. 2.1 Basic modes of crack surface displacement and coordinates measured from the leading edge of a crack and the stress components at the crack tip stress field

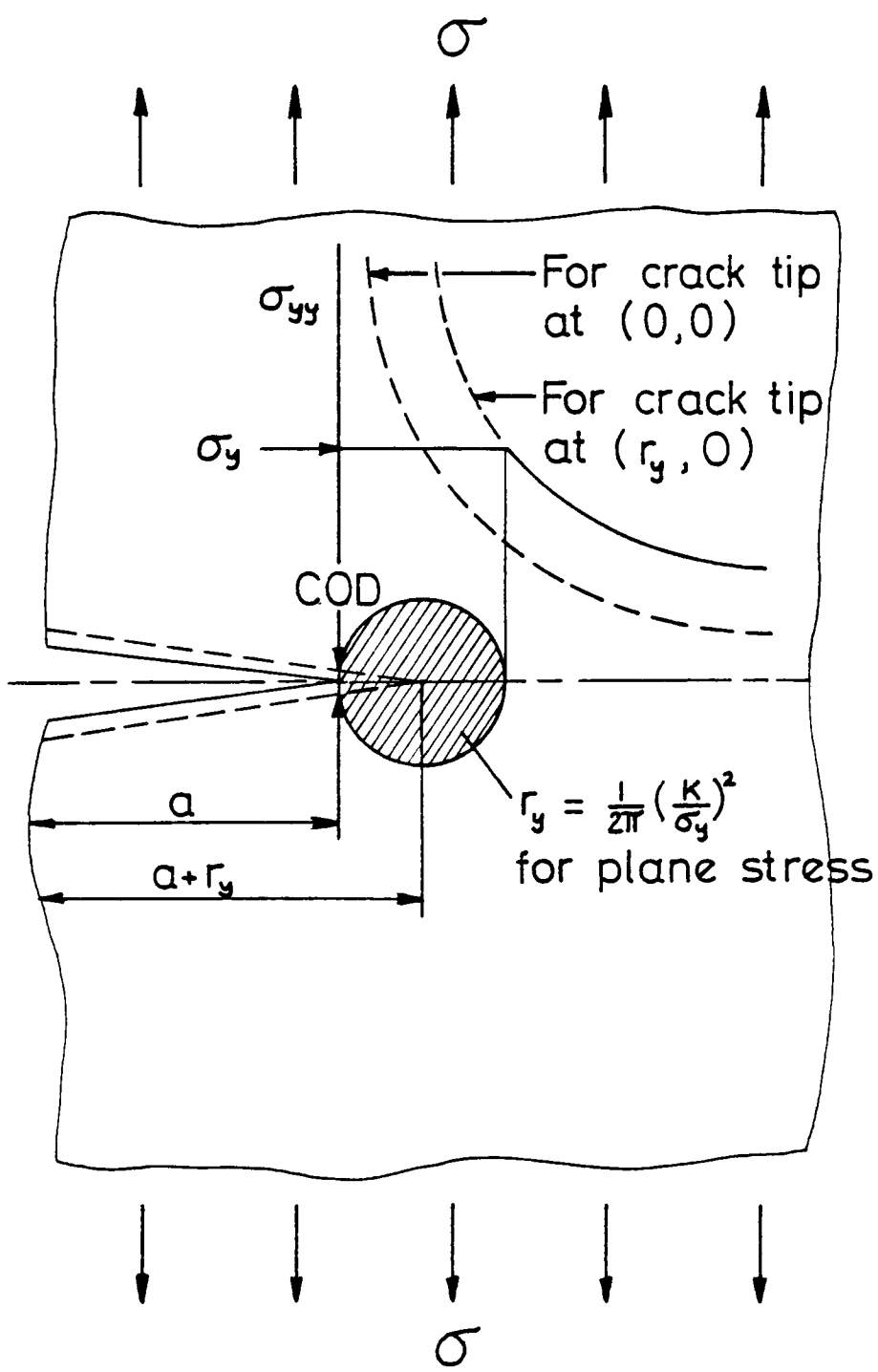


Fig. 2.2 Irwin's plastic zone correction

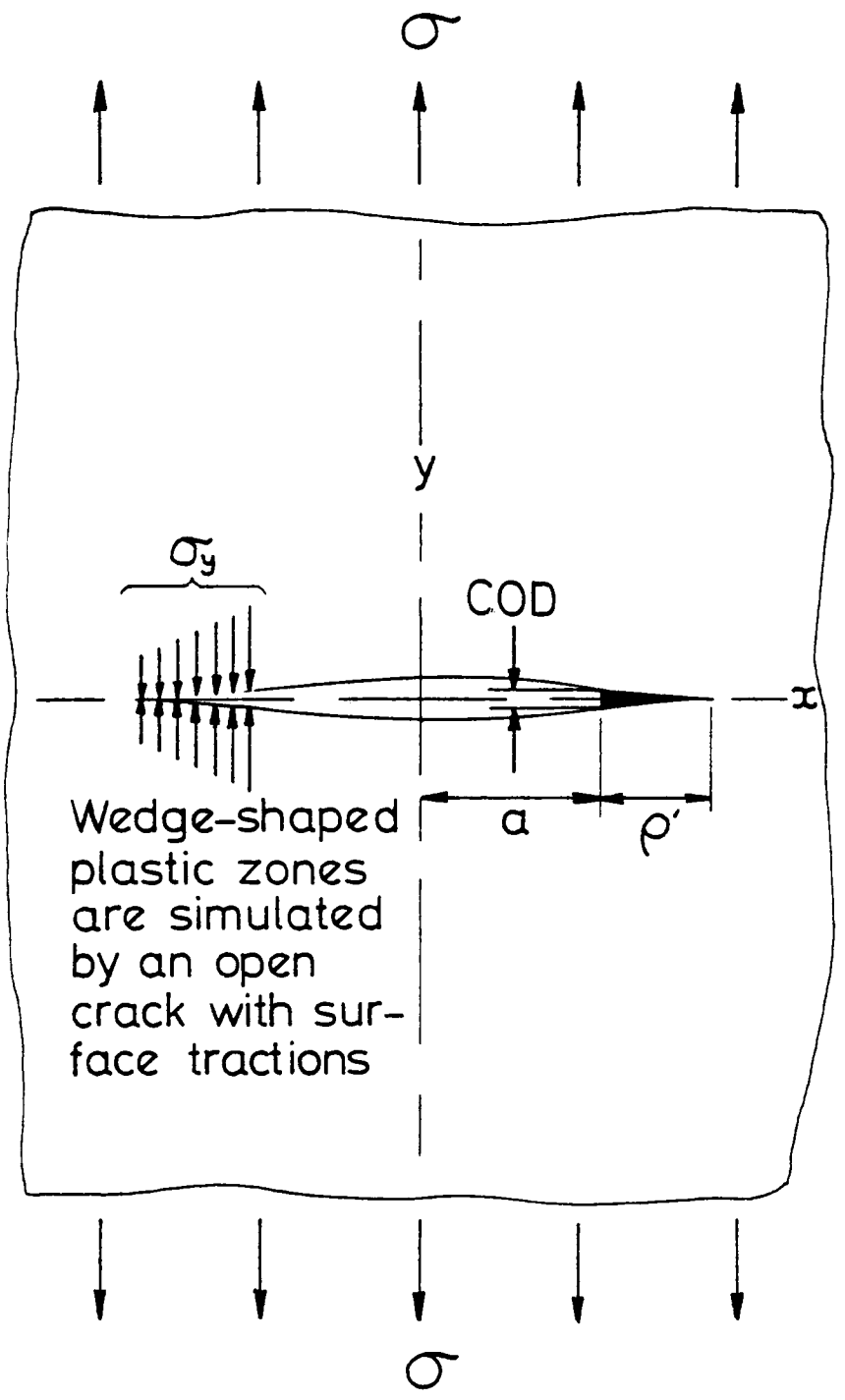
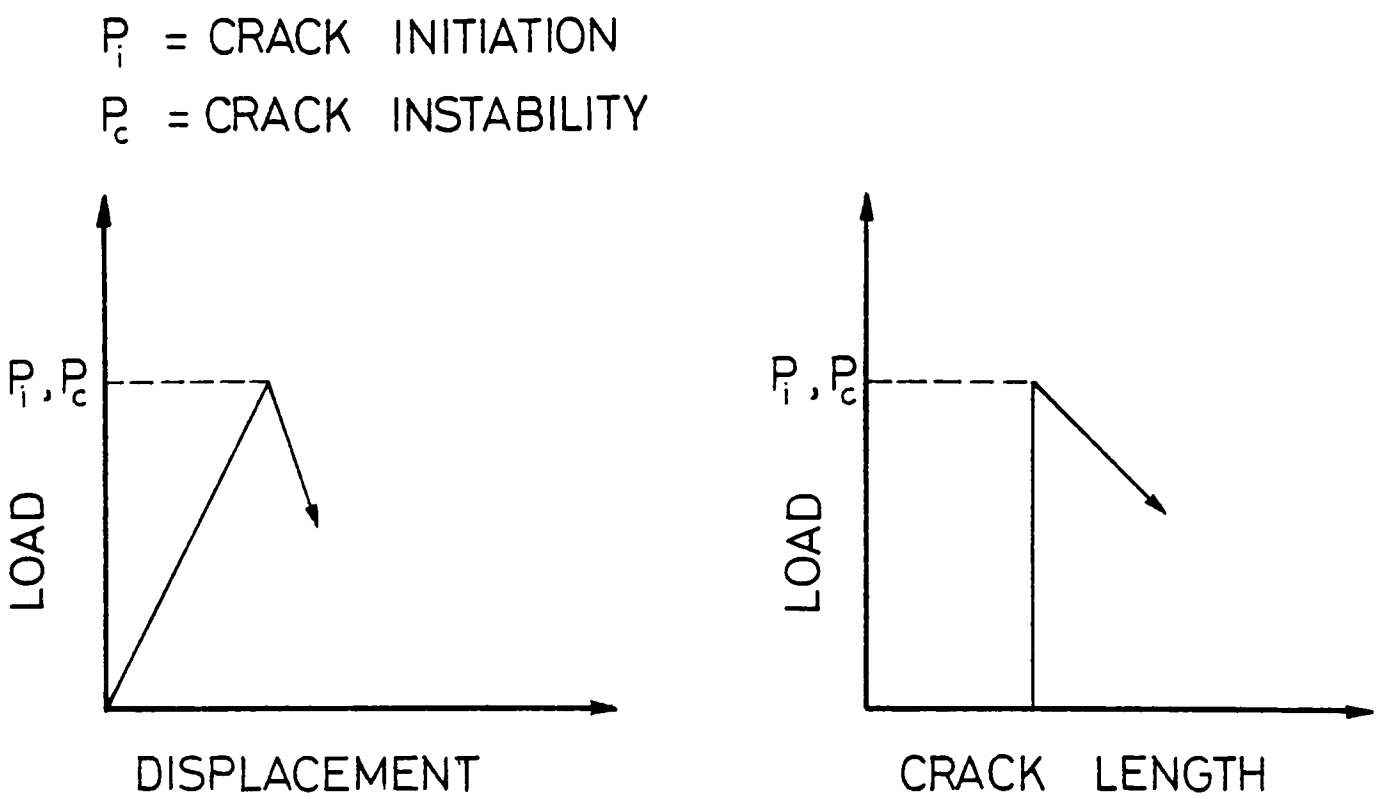
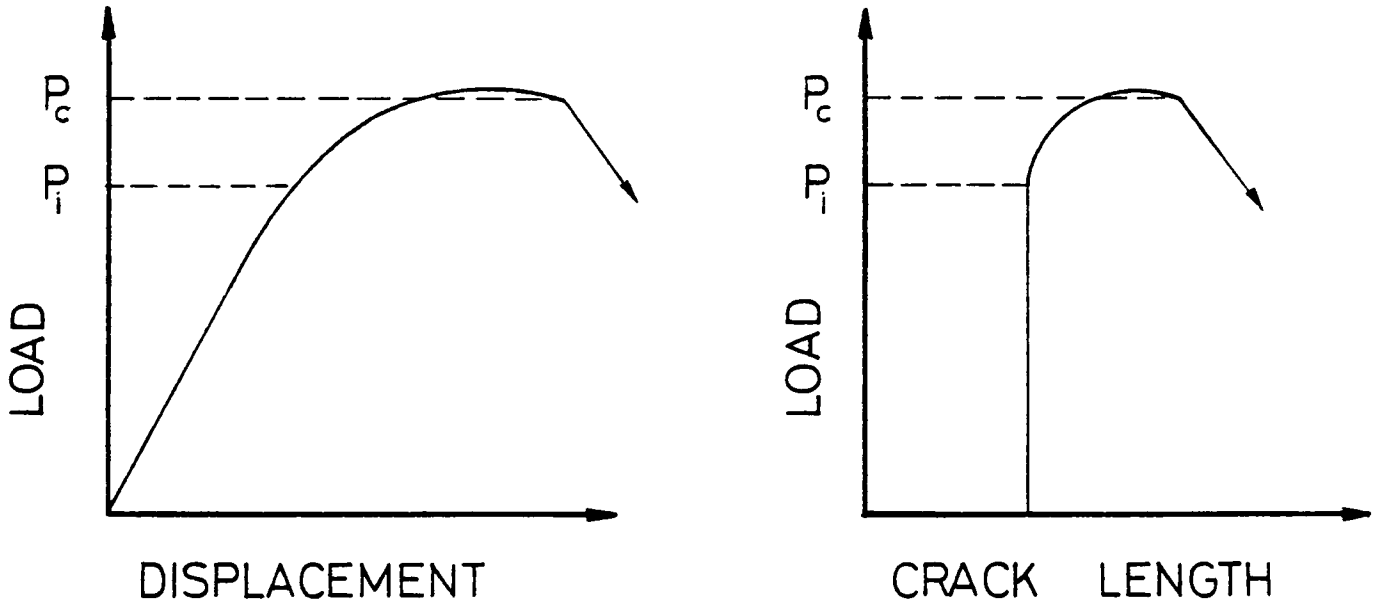


Fig. 2.3 Dugdale's strip yield model of the plastic zone



a. Linear elastic material (thick section, frangible material)



b. Elastic-plastic material (thin sheet, ductile material)

Fig. 2.4 Load-displacement and load-crack length curves for a linear elastic and an elastic-plastic material

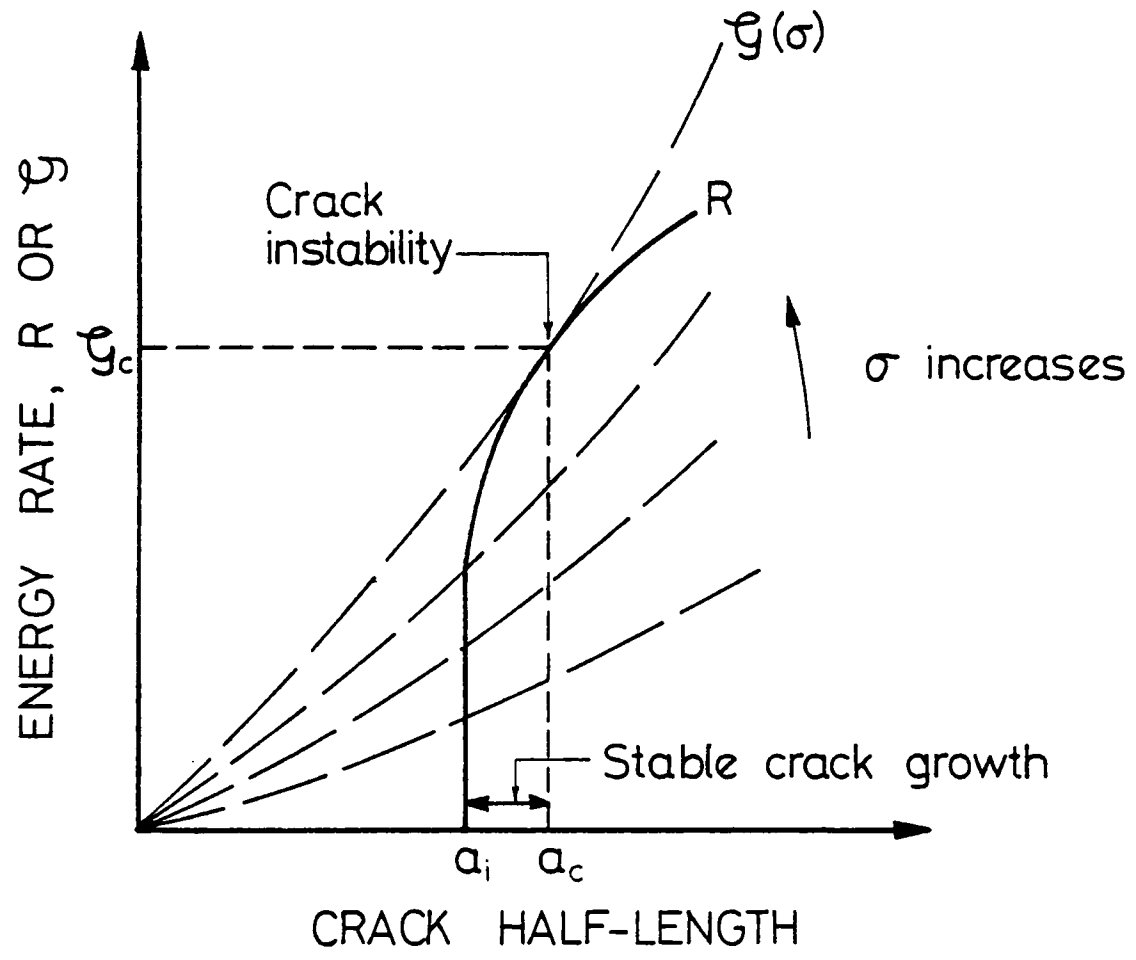


Fig. 2.5 Schematic representation of Krafft's crack growth resistance curve for an elastic-plastic material

CHAPTER 3

FAILURE GOVERNED BY LARGE SCALE PLASTIC DEFORMATION

Failure of a cracked component or structure in the presence of large scale plastic deformation occurs by the development of general yield across the net section accompanied by crack extension and/or large permanent deformations. Such failures require a significant interaction between the crack tip plastic zone and the far free boundary and, under such circumstances, the term fully plastic behaviour is justified.

General yield may develop either before or after crack initiation during the loading of a cracked structural component, although in practice it may be difficult to distinguish which occurs first. For example, for very long or deep cracks with a short remaining ligament, crack initiation may be closely followed by general yield across the remaining ligament. The actual behaviour depends on the material flow properties, the geometrical configuration and the loading system; the probability of crack instability increasing under load-controlled conditions i.e. "soft" loading system. The influence of material properties and geometry in determining the occurrence of general yield is discussed next; the importance of the nature of the loading system is left to the following chapter (see section 4.1.b).

3.1 Stress Intensification and Plastic Constraint

The extent of yielding and thereby the failure mechanism for a particular geometry and material depends upon the stress intensification ahead of the crack tip, Q and the degree of plastic constraint across the net section, L. Following Knott's definition for Q and L (1):

$$Q = \frac{\sigma_{yy}}{2\tau_y}^{(max)} \qquad 3.1$$

$$L = \frac{P_{gy}}{2\tau_y \; 2(W-a)B} \qquad 3.2$$

where σ_{yy} (max) is the maximum normal stress, τ_y, the shear yield stress[a] and P_{gy}, the general yield load of the net section of width, 2(W-a) and thickness, B.

The distinction between stress intensification and plastic constraint is important. Q relates to local effects in the crack tip region which result in stress elevation and is extremely sensitive to crack tip geometry as well as material properties such as yield stress and strain-hardening exponent, which markedly influence the shape of the stress singularity in the vicinity of the crack tip. In comparison, L represents the general elevation of the applied load across the net section by the triaxial stresses and the presence of finite boundaries and material yield stress and strain-hardening capacity are of prime importance.

It is well known that hydrostatic tension is a direct driving force for void nucleation and growth (2) and for various micro-mechanisms of brittle fracture (3). Therefore, in the presence of high local hydrostatic stress elevation ahead of the crack and high plastic constraint across the net section, crack initiation occurs at low nominal stress levels by the initiation and growth of internal voids, brittle cracking or some combined micro-mechanism such as quasi-cleavage. Provided crack instability does not occur after crack initiation (see section 4.1.a) subsequent crack growth behaviour is governed by the change in Q with plastic zone size and any variation in L with crack length or depth.

On the other hand, if there is no local stress intensification nor plastic constraint then the opportunity exists for general yield across the net section when the stress over the net cross-sectional area averages the uniaxial yield stress.

---

[a] On the Tresca yield criterion, $2\tau_y = \sigma_y$; on the von Mises yield criterion, $2\tau_y = \frac{2}{\sqrt{3}} \sigma_y = 1.15 \; \sigma_y$.

Unfortunately, the problem of constrained plastic flow embedded in an elastic matrix is difficult to treat analytically since both elastic and plastic compatibility must be satisfied. No analytical solutions for the increase in Q with plastic zone size, with or without slow crack growth, have been developed for sharp cracks although results have been obtained for reasonably sharp hyperbolic notches under plane strain up to general yield (4) (5) and, more recently, finite element methods have been applied to the problem of a notched bar subjected to pure bending in plane strain (6). However, the majority of estimates of stress intensification and plastic constraint have been determined for notched plates and bars using the method of slip line fields based on rigid plastic theory and some examples are shown in Fig. 3.1.

The influence of geometric configuration and stress state on plastic constraint is clearly seen. For pure bending, the plastic constraint factor is necessarily referred to bending moments i.e.

$$L = \frac{2M_{gy}}{\tau_y (W-a)^2 B} \qquad 3.3$$

where M_{gy} is the bending moment for general yield of the notched bar and $M = \tau_y (W-a)^2 B/2$ is the bending moment for general yield on the net section[b].

It would also appear that the local stress intensification, Q is sensitive to geometry and stress state but the current view is that crack tip blunting would be an overriding effect for plane strain deformation (12).

Crack tip geometry effects have been considered by Rice (13) for the case of a plane strain stress state with small scale yielding. The slip line field solution for a sharp crack tip in plane strain (Fig. 3.2.a)

---

[b] Due to the stress gradient from tension to compression across the width, this differs from the moment required for initial yield in the outer tensile and compressive faces of the bar i.e. $M = \tau_y (W-a)^2 B/3$.

results in a large hydrostatic stress elevation directly ahead of the crack, $Q = 1 + \frac{\pi}{2}$ and intense shear concentrations above and below the tip where the slip lines are curved, but no concentration directly ahead of the crack where the lines are straight. However, there is a displacement discontinuity at the crack tip so that the end region must open up into a blunted shape. Slip line fields for a blunted crack in plane strain (Fig. 3.2.b) lead to a fan region which is now non-centred and focuses into a region ahead of the tip comparable in size to the opening displacement, causing intense strain concentrations ahead of the crack as well as above and below the tip. Hydrostatic stress elevation ahead of the crack remains large increasing from a value, $Q = 1$ at the tip (plane stress state, $\sigma_{xx} = 0$ at the free surface) to $Q = 1 + \frac{\pi}{2}$ at the furthest extent of the logarithmic spiral. The effect of strain-hardening is to raise the peak value of the stress intensification and to move it closer to the crack tip (14) (15).

It is important to realise that the region dominated by the crack tip singularity, termed the "process zone" (16) (17) is very much smaller than the macroscopic plastic zone and the maximum stress, σ_{yy} (max) occurs well behind the elastic-plastic interface in the x direction (18). Under constrained yielding this macroscopic plastic zone must be sufficiently large to accommodate the displacements involved at the same time being contained within an elastic matrix; experiments indicate that local strain concentrations are more easily dispersed in materials with high strain-hardening exponents and that the plastic zones are more widespread in such materials (19) (20).

Geometric dimensions of prime importance are the crack length, a or depth, d, the sectional thickness, B and the net sectional width or remaining ligament, 2(W-a). The crack length or depth may influence the failure mechanism since with shallow cracks gross sectional yielding may occur before the constrained yielding can cross the net section. In fact,

longer cracks are required to maintain constrained yielding when the plastic constraint is high (21) and high constraint in the double-edge-notched panel in plane strain is only assured in the presence of very long cracks, $W/(W-a) \sim 9$ (22), although a similar panel in plane stress is not crack length sensitive.

It is the sectional thickness which largely affects the stress state at the crack tip, thin sections favouring a plane stress state where relaxation of the through-thickness stress, σ_{zz} can occur. By analogy with small scale yielding, Paris (23) estimated that full transverse constraint would be achieved in the elastic-plastic and fully plastic case when the sectional thickness lies within the limits:

$$25\ \delta_{Ic} \leqslant B \leqslant 50\ \delta_{Ic} \qquad 3.4$$

where δ_{Ic} is the critical crack opening displacement for plane strain conditions. There is some experimental support for this condition (24) (25) but further work is necessary before it can be fully validated.

Even if a condition of plane strain exists in the interior of a section, there is always a plane state of stress at the surface and the through-thickness stress, σ_{zz} must increase from zero (at the surface) to the plane strain value in the interior. A consequence of this is that if crack initiation occurs prior to general yield, the crack front tunnels forward in the mid-section where the strain gradient immediately ahead of the crack tip in the process zone is steep; for crack extension under increasing load the crack tip plastic zone increases in size relaxing σ_{zz} so that there is a geometry dependent transition from plane strain type constraint to less constrained conditions such as plane stress with increasing crack growth. The extent of this stress transition depends on the section thickness, the net sectional width and the crack extension. Thus, in-plane plastic deformation and mode I crack extension (Fig. 3.3.a) are promoted in thick sections when B is larger than 2(W-a) (26).

Conversely, 45° out-of-plane plastic deformation and mode III crack extension (Fig. 3.3.b) are promoted in thin sheets for which B << 2(W-a) (27). Intermediate thickness sections are of "mixed mode" with a region of square fracture in the mid-thickness and shear lips at the surface[c]. However, the influence of specimen dimensions on the extent of slow crack growth is not yet understood.

Finally, the role played by the temperature and strain rate is of considerable importance in materials exhibiting a thermal and strain rate sensitive yield stress and strain-hardening exponent; high strain rates and low temperatures favouring strain localisation and hydrostatic stress elevation (28). In addition to any rate dependence of the flow properties, local heat generation by plastic deformation may significantly increase the crack tip ductility in rapid loading situations (29).

3.2 Solutions for Failure by General Yield and Plastic Collapse before Crack Initiation

The concept of fracture toughness has little significance in situations where failure occurs by general yielding across the net section with negligible crack extension. Under such circumstances structural integrity is determined by the ability of a material to undergo large permanent deformations and this may be reasonably assessed by means of the upper and lower bound theorems of slip line fields (30) and limit analysis (31).

A stress, strain or displacement field constitutes a lower bound to the slip line field solution or general yield load when internal equilibrium is satisfied, the external forces are balanced by the internal stresses and the state of stress is everywhere within the yield locus. On the other hand, a stress, strain or displacement field constitutes an upper bound when the boundary conditions are satisfied, the yield criterion including

---

[c] The planes of maximum shear stress shown in Fig. 3.3 are for the elastic case, however, this probably still holds in the elastic-plastic case.

the flow rule is satisfied everywhere where yielding is taking place and the rate of working obtained from the external forces and external velocities is equal to or exceeds the rate of internal energy dissipation obtained from internal forces and velocities. These upper and lower bound theorems were first presented by Gvozdev in 1938 but proofs can be found in many text books on plasticity.

A complete solution, which is both statically and kinematically admissible, is obtained if the upper and lower bound solutions are made compatible by the choice of the appropriate slip line field. In slip line field theory, this solution consists of two sets of orthogonal slip lines (lines of constant shear stress or velocity discontinuities) which satisfy the equilibrium, compatibility and boundary conditions and examples were shown in Fig. 3.1. It assumes the plastically deformed material moves in rigid blocks so shaped by the loading system as to slide over one another along the lines of maximum shear stress. Alternatively, the plastically deformed material may be considered to rotate in rigid blocks about plastic hinges which form at the focus of the lines of maximum shear stress (32) (33).

The latter physical interpretation of fully plastic behaviour is extremely useful in the analysis of more complex geometries for which general yield of a particular section does not necessarily imply plastic collapse of the whole structure. For plastic collapse the structure must become a mechanism and plastic hinge formation is a simple means of determining possible collapse mechanisms for very general structures. Upper and lower limits to the true collapse load may then be obtained in a manner analogous to the methods used for slip line fields. The complete solution or true collapse load, which may be obtained for fairly simple geometries such as frames by choice of the appropriate plastic hinge mechanism, will be both statically and kinematically acceptable. Examples of lower bound solutions for complex geometries such as a pressure vessel

include the spherical shell with a circular hole (34) and the cylindrical shell with various shapes of unreinforced hole (35) (36) and part- through notches (37) (38).

Both slip line fields and limit analysis are based on a rigid-perfectly plastic model, neglecting elasticity and work-hardening and provide a two-dimensional description of the deformed shape at the onset of widespread yielding. For fully plastic behaviour where the elastic displacements are negligible compared with the total displacements, the use of a rigid-plastic model is reasonably justified. In fact, one of the main advantages of limit analysis is that a stress distribution is not sought when calculating the collapse loads of complex structures so that results can be readily scaled. Suitable allowance for work-hardening is sometimes made by assuming that the extreme of fully plastic behaviour corresponds to some stress higher than the uniaxial yield stress, σ_y. In slip line field analysis the von Mises yield condition, 1.15 σ_y is frequently used. However, for more practical applications such as pressure vessel analysis, it has been suggested that failure or ultimate collapse may be predicted more accurately by basing the limit analysis on the ultimate tensile strength of the material; the yield stress based limit load representing a good lower bound to experimental results (39).

Finally, the two dimensional nature of the upper and lower bound analysis is a major limitation. Limit analysis assumes a plane state of stress, restricting the validity of the analysis to thin plates and shells. However, plane strain solutions, for thick plates, based on slip line fields have been derived for relatively simple geometries and attempts are being made to apply this technique to more complex configurations such as a pressurised cylindrical shell containing a long part-through notch (38).

3.3 Solutions for Failure by General Yield after Crack Initiation

In sharp contrast to fully plastic behaviour, fracture toughness does have some significance for elastic-plastic materials undergoing slow crack

growth up to the onset of general yield, although it is not clear to what extent any measure of fracture toughness after crack initiation will depend upon geometry. A three-dimensional analysis is required to study the crack growth process from crack initiation to general yield taking into account such features as crack tip blunting, plastic unloading during slow crack growth, ductile shape changes and the transition from contained to uncontained plasticity; however, the mathematics are formidable.

For elastic-plastic behaviour it is no longer possible to neglect the elastic displacements and solutions, whether analytical or numerical (polynomial stress functions, finite differences or finite elements) must be based on an elastic-plastic model. Several attempts have been made to obtain a solution to the problem of a steadily moving crack in an elastic-plastic material. Assuming isotropy, two-dimensional analytical solutions have been found for cracks in anti-plane strain (mode III) (9) (40) (41) and plane stress tension (42) (43). A two-dimensional finite element treatment of a uniformly moving elastic-plastic crack tip in anti-plane strain and plane stress tension has been performed (17) and from this, Broberg (16) has developed an approximate analytical procedure for estimating slow crack growth in plane stress or plane strain tension. However, no shape change like crack tip blunting is possible and the effect of triaxiality on stress intensification during slow crack growth is not predicted. In fact, fracture mode transitions from plane strain to less constrained crack tip conditions cannot be treated and the connection between contained crack tip plasticity and full plasticity across the net section without catastrophic fracture, has not been developed.

Up to now, the analysis of failures by net section yielding has been restricted to estimates of general yield loads based on original crack sizes using slip line field and limit analysis techniques, regardless of crack initiation and any subsequent slow crack extension. Only recently, has slow crack growth been shown to be much more common than had previously been

thought to be the case (16)(17). Thus, failure analysis techniques for designing against the onset of general yield after significant slow crack extension can only be developed after a thorough study of the slow crack growth phenomenon has been made.

3.4 Summary

For materials which are reasonably isotropic on a macroscopic scale and for which the uniaxial yield stress is fully representative of material macrostructure, slip line field and limit analysis methods may be used to estimate general yield loads of individual sections or the plastic collapse load of an entire structure in the absence of slow crack extension. The possibility of basing limit loads on the ultimate tensile strength of a material requires investigation.

At present there is no means of designing against general yield after significant crack extension and under such circumstances a study of the phenomenon of slow crack growth is warranted. However, when slow crack extension occurs after crack initiation a measure of fracture toughness is still required to ensure that crack instability does not occur prior to the onset of general yield and this is discussed in the following chapter.

References

(1) J.F. Knott, "Fundamentals of Fracture Mechanics," Butterworths, London, p. 34 et seq., 1973.

(2) J.W. Hancock and A.C. MacKenzie, J. Mech. Phys. Solids, 24, p. 147, 1976.

(3) Ref. (1), p. 176 et seq.

(4) J.A. Hendrickson, D.S. Wood and D.S. Clark, Trans. Am. Soc. Metals, 50, p. 656, 1958.

(5) F.W. Barton and W.J. Hall, Ship Structure Committee Report SSC-147, U.S. Coast Guard H.Q., Washington D.C., 1963.

(6) J.R. Griffiths and D.R.J. Owen, J. Mech. Phys. Solids, 19, p. 419, 1971.

(7) E. Orowan, Trans. Inst. Engrs. Shipbuilders Scotland, 89, p. 165, 1945.

(8) R. Hill, J. Mech. Phys. Solids, 1, p. 19, 1952.

(9) F.A. McClintock and G.R. Irwin, A.S.T.M. S.T.P. 381, "Fracture Toughness Testing and its Applications," Am. Soc. for Testing and Materials, p. 84, 1965.

(10) A.P. Green and B.B. Hundy, J. Mech. Phys. Solids, 4, p. 128, 1956.

(11) G. Lianis and H. Ford, J. Appl. Math. Phys. (ZAMP), 8, p. 360, 1957.

(12) J.A. Begley and J.D. Landes, A.S.T.M. S.T.P. 514, "Fracture Toughness," Am. Soc. for Testing and Materials, p.1, 1972.

(13) J.R. Rice and M.A. Johnson in "Inelastic Behaviour of Solids," Ed. by M.F. Kanninen, W.F. Adler, A.R. Rosenfield and R.I. Jaffee, McGraw-Hill, p. 641, 1970.

(14) J.R. Rice and G.F. Rosengren, J. Mech. Phys. Solids, 16, p. 1, 1968.

(15) J.W. Hutchinson, J. Mech. Phys. Solids, 16, p. 13 and p. 337, 1968.

(16) K.B. Broberg, J. Mech. Phys. Solids, 23, p. 215, 1975.

(17) H. Andersson, J. Mech. Phys. Solids, 22, p. 285, 1974.

(18) Ref. (1), p. 86 et seq.

(19) W.W. Gerberich, Expt. Mechs., 4, p. 335, 1964.

(20) G.T. Hahn and A.R. Rosenfield, A.S.T.M. S.T.P. "Applications Related Phenomena in Titanium Alloys," Am. Soc. for Testing and Materials, p. 5, 1968.

(21) J.F. Knott, Proc. 2nd Int. Conf. Fracture, Brighton, p. 205, 1969.

(22) D.J.F. Ewing and R. Hill, J. Mech. Phys. Solids, 15, p. 115, 1967.

(23) P.C. Paris, A.S.T.M. S.T.P. 514, "Fracture Toughness," Am. Soc. for Testing and Materials, p. 21, 1972.

(24) R.F. Smith and J.F. Knott, Conf. Practical Application of Fracture Mechanics to Pressure Vessel Technology, Inst. Mech. Engrs., p. 65, 1971.

(25) J.N. Robinson and A.S. Tetelman, Int. J. of Fracture, 11, p. 453, 1975.

(26) R.H. Sailors, TAM Report No. 367, Univ. of Illinois, April 1973.

(27) R.H. Heyer and D.E. McCabe, Eng. Fract. Mechs., 4, p. 393 and p. 413, 1972.

(28) H.C. Rogers in "Fundamentals of Deformation Processing," Ed. by W.A. Backofen et al., Syracuse Univ. Press, p. 199, 1964.

(29) J. Eftis and J.M. Krafft, Trans. A.S.M.E., Series D, J. Basic Eng., 87, p. 257, 1965.

(30) R. Hill, "The Mathematical Theory of Plasticity", Oxford Univ. Press, 1950.

(31) P.G. Hodge, Jr., "Plastic Analysis of Structures," McGraw-Hill, New York, 1959.

(32) D.J.F. Ewing and C.E. Richards, J. Mech. Phys. Solids, 22, p. 27, 1974.

(33) J.R. Haigh and C.E. Richards, C.E.R.L. Report No. RD/L/M 461, May 1974.

(34) S.S. Gill, Int. J. Mech. Sc., 6, p. 105, 1964.

(35) R. Kitching, J.K. Davis and S.S. Gill, J. Mech. Eng. Sc., 12, p. 313, 1970.

(36) I. W. Goodall, "On the Design of Intersections in Pressure Vessels," Ph.D. dissertation, Univ. of Cambridge, 1967.

(37) C. Ruiz, O.U.E.L. Report No. 1200, 1977.

(38) B. Dodd, M. Shiratori and C. Ruiz, O.U.E.L. Report No. 1199, 1977.

(39) A. R. Dowling and C.H.A. Townley, Int. J. Pres. Ves. and Piping, 3, p. 77, 1975.

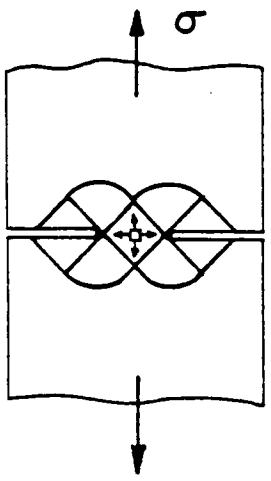
(40) A.D. Chitaley and F.A. McClintock, J. Mech. Phys. Solids, 19, p. 147, 1971.

(41) J.R. Rice, "Fracture — an Advanced Treatise," Vol. II, Ed. H. Liebowitz, Academic Press, New York, p. 191, 1968.

(42) M.P. Wnuk, A.S.T.M. S.T.P. 536, "Progress in Flaw Growth and Fracture Toughness Testing," Am. Soc. for Testing and Materials, p. 64, 1973.

(43) D.C. Drucker and J.R. Rice, Eng. Fract. Mechs., 1, p. 577, 1970.

PLANE STRAIN

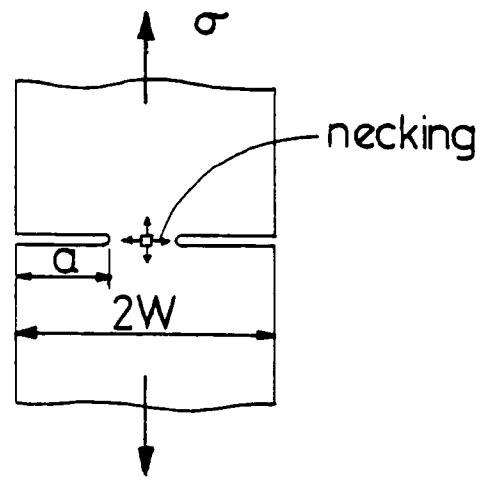


$Q = 1 + \frac{\pi}{2}$

$L = 1 + \frac{\pi}{2}$

Prandtl (7)

PLANE STRESS

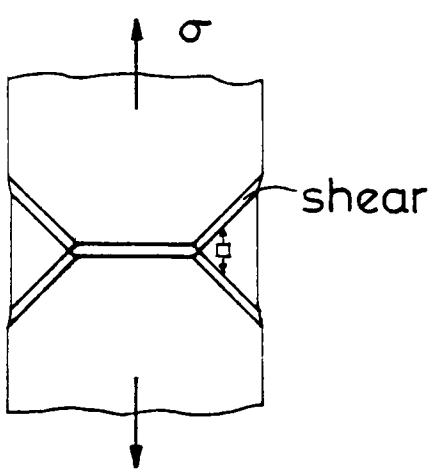


$Q = 1$

$L = 1$

Hill (8)

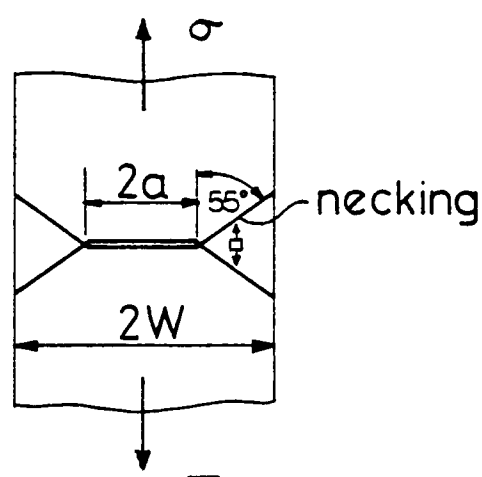
a. Double-edge-notched panels



$Q = 1$

$L = 1$

McClintock and Irwin (9)

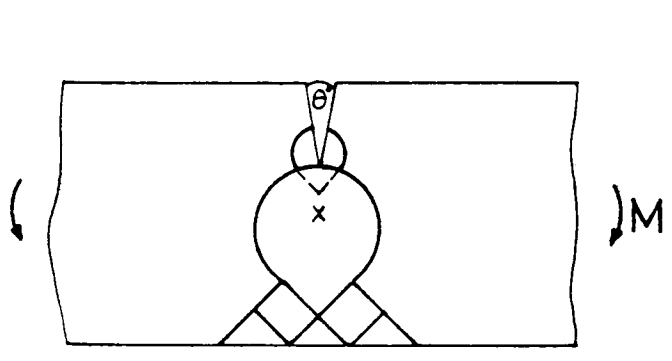


$Q = \frac{\sqrt{3}}{2}$

$L = \frac{\sqrt{3}}{2}$

Hill (8)

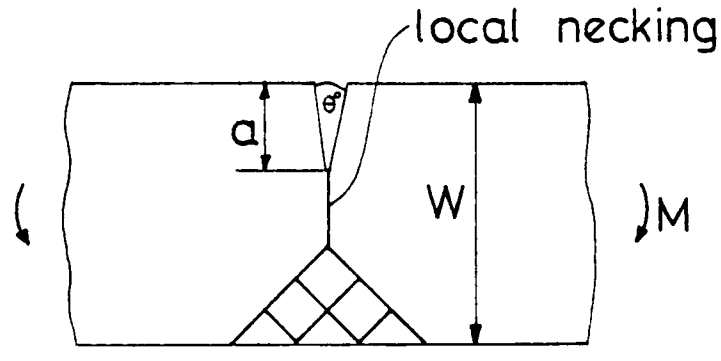
b. Centre-notched panels



$Q_x = 1 + \frac{\pi}{2} - \frac{\theta}{2} \quad (\theta° > 6.4°)$

$L = 1.26$

Green and Hundy (10)



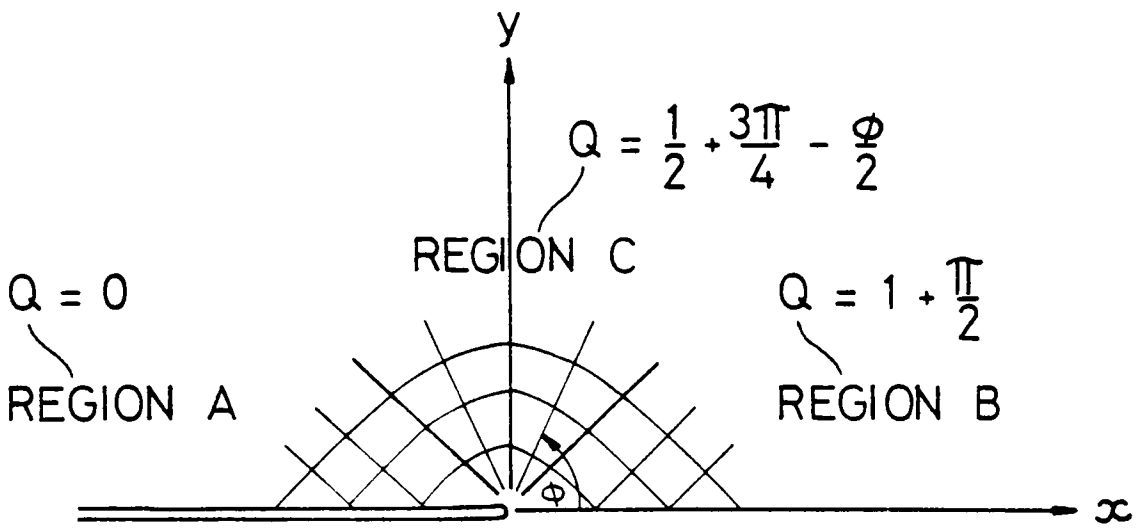
$Q = 1 \quad (0° \leq \theta° \leq 141°4')$

$L = 1$

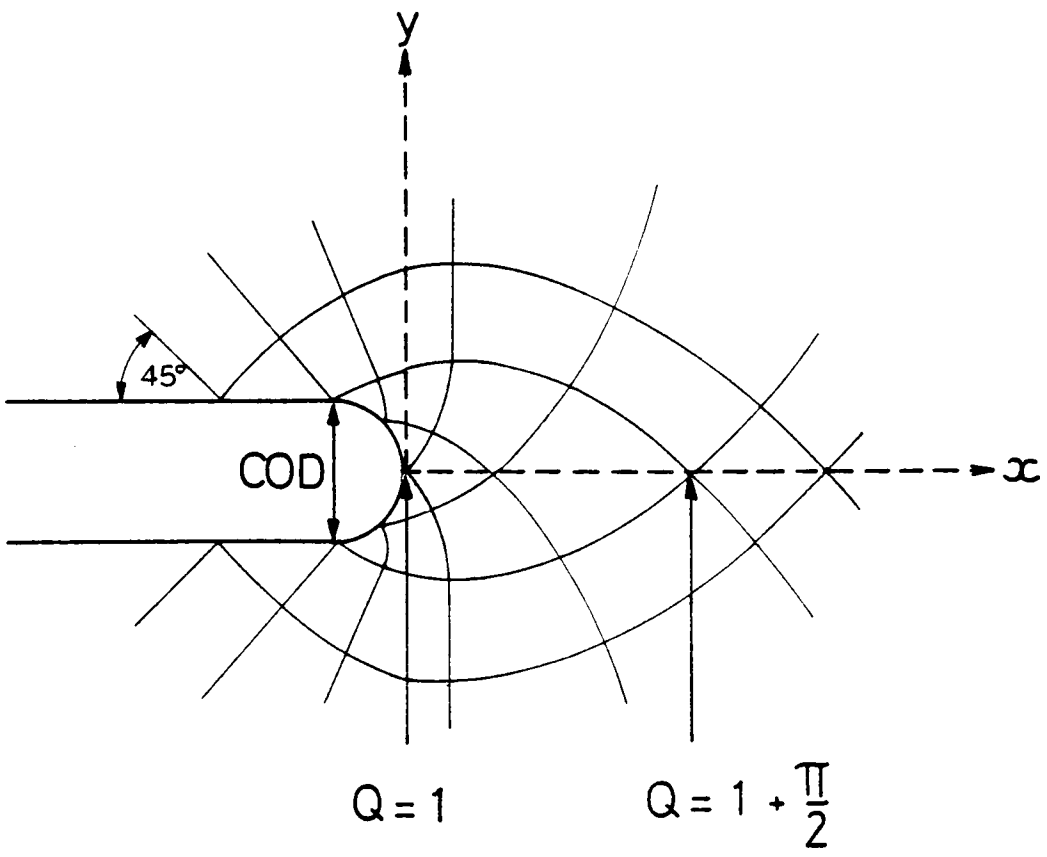
Lianis and Ford (11)

c. Pure bending notched bars

Fig. 3.1 Examples of slip line field solutions for fully plastic opening modes

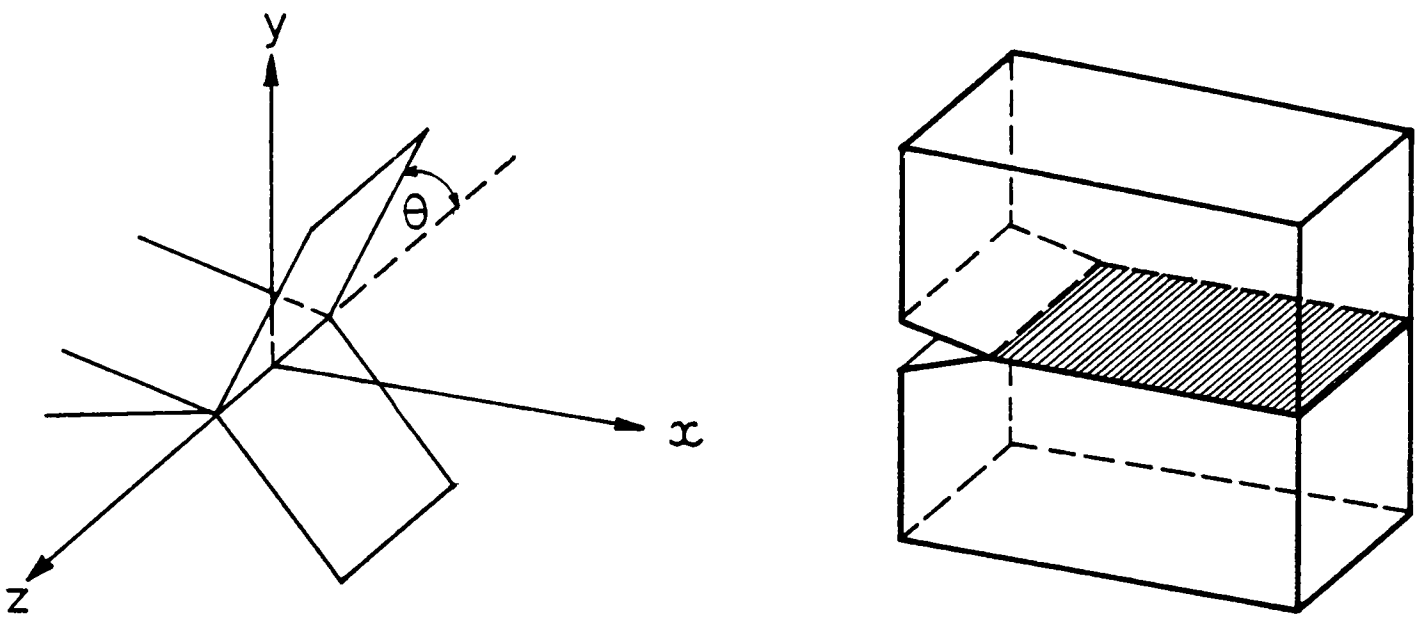


a. Sharp crack tip

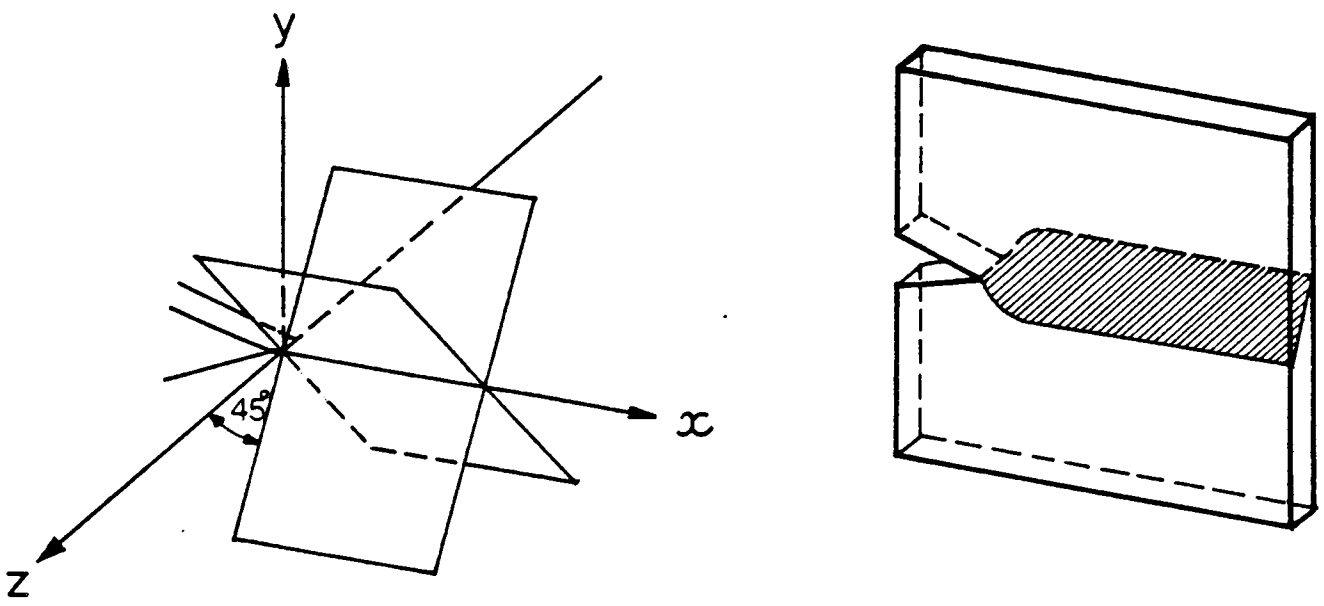


b. Blunted crack tip

Fig. 3.2 Slip line fields for a sharp crack tip and for a blunted crack tip in plane strain (13)



a. Plane strain. In-plane plastic deformation and mode I crack extension



b. Plane stress. 45^{o} out-of-plane plastic deformation and mode III crack extension

Fig. 3.3 Planes of maximum shear stress and fracture surfaces for plane strain and plane stress failures

CHAPTER 4

ENERGY BALANCE APPROACH TO FAILURE ANALYSIS

An energy balance approach to failure analysis is concerned only with the thermodynamics of the fracture process; no consideration is given to crack tip acuity and possible fracture mechanisms. Therefore, a major assumption in all energy approaches is that an effective atomic mechanism of fracture can operate once the thermodynamic requirements are met.

The following two-dimensional generalised energy balance approach is based on Griffith's treatment of the brittle fracture of a cracked infinite sheet (1) but as presented here it is applicable to both elastic and elastic-plastic material behaviour. More rigorous analyses of quasi-static crack extension have been given by Havner and Glassco (2) and by Eftis and Liebowitz (3).

4.1 Energy Balance Approach to Crack Growth

4.1.a General Model

Consider an isotropic, homogeneous plate of thickness, B and width, 2W containing a crack of length, 2a (Fig. 4.1.a). On loading to a load, P the load-displacement record for the two crack half-lengths, a follows the path OPO_1 (Fig. 4.1.b). If the load is applied slowly or quasi-statically there is no appreciable heat input and, in the absence of body forces, an energy conservation equation may be written:

$$\left.\begin{array}{lcccc} \text{External} & = & \text{Initial Stored Elastic} & + & \text{Initial Stored Plastic} \\ \text{Work} & & \text{Strain Energy} & & \text{Strain Energy} \\ W_{ext,i} & = & U_{e,i} & + & U_{p,i} \\ \text{or} \quad \text{Area OPS} & = & \text{Area } O_1PS & + & \text{Area } OPO_1 \end{array}\right\} \quad 4.1$$

where the subscript, $_i$ refers to the initial loading state and it is assumed that no plastic deformation occurs except in the immediate vicinity

of the crack front.

On reloading to a load, P + ΔP, the crack extends to a + Δa along the path O_1PQO_2. For the total energy to be conserved:

External Work	= Final Stored Elastic Strain Energy	+ Initial Stored Plastic Strain Energy	+ Work Required to Extend Crack	+ Kinetic Energy	4.2
$W_{ext,f}$	= $U_{e,f}$	+ $U_{p,i}$	+ RBΔa	+ ΔT	
or Area OPQR	= Area O_2QR	+ Area OPO_1	+ RBΔa	+ ΔT	

where the subscript, $_f$ refers to the final loading state and R is a fracture toughness parameter defined as the work done against the resistance of the material per unit crack growth area.

Substituting the initial stored plastic strain energy from equation 4.1 into equation 4.2:

$$\left.\begin{aligned} \Delta W_{ext} - \Delta U_e &= RB\Delta a + \Delta T \\ \text{or} \quad \text{Area } O_1PQO_2 &= RB\Delta a + \Delta T \end{aligned}\right\} \quad 4.3$$

With the load quasi-statically applied, all changes with time are due to a progressive change in the crack growth area and the kinetic energy released by the crack faces is negligible i.e.

$$\left.\begin{aligned} \frac{\Delta W_{ext} - \Delta U_e}{B\Delta a} &= R \\ \text{or} \quad \frac{\text{Area } O_1PQO_2}{B\Delta a} &= R \end{aligned}\right\} \quad \text{stable crack growth} \qquad 4.4$$

Therefore, the work rate of the applied forces which is not taken up as change in the stored elastic strain energy is available to promote slow stable crack extension; this being a completely general solution for any shaped cracked body under quasi-statically applied loads.

Let us now consider the four critical conditions of crack initiation, crack instability, steady-state and the onset of general yield.

i) Crack Initiation

Crack initiation always requires finite load applications so that the general energy balance equation 4.4 may be rewritten:

$$\frac{\Delta W_{ext} - \Delta U_e}{B\Delta a} \geqslant R_i \qquad \text{crack initiation} \qquad 4.5$$

where R_i is a minimum fracture toughness corresponding to crack initiation.

ii) Crack Instability

When crack instability occurs equation 4.4 is no longer valid as there is now a significant increase in the kinetic energy released which may appear in the form of heat. Under such circumstances, $\frac{1}{B}\frac{\Delta T}{\Delta a} > 0$:

$$\frac{\Delta W_{ext} - \Delta U_e}{B\Delta a} > R_c \qquad \text{unstable crack growth} \qquad 4.6$$

where R_c is a fracture toughness corresponding to crack instability.

Following Griffith (1), crack instability occurs when the external work term W_{ext} achieves a stationary maximum i.e. $\frac{1}{B}\frac{\Delta W_{ext}}{\Delta a} = 0$ and $\frac{1}{B}\frac{\Delta^2 W_{ext}}{\Delta a^2} < 0$:

$$\left.\begin{aligned} -\frac{1}{B}\frac{\Delta U_e}{\Delta a} &= R_c \\ \text{and} \quad -\frac{1}{B}\frac{\Delta^2 U_e}{\Delta a^2} &> \frac{1}{B}\left(\frac{\Delta R}{\Delta a}\right)_c \end{aligned}\right\} \quad \text{crack instability} \qquad 4.7$$

iii) Steady-State

For a sufficiently wide plate, R approaches an upper limiting value associated with the achievement of an equilibrium-maximum plastic zone size (4). Under constant strain rate conditions, R remains constant at this steady-state value, R_∞ i.e. $\frac{1}{B}\frac{\Delta R}{\Delta a} = 0$:

$$\frac{\Delta^2 (W_{ext} - U_e)}{B\Delta a^2} = 0 \qquad \text{steady-state} \qquad 4.8$$

iv) General Yield

When general yield spreads across the remaining ligament, less plastic work is dissipated to the crack tip as the ligament decreases and, under constant strain rate conditions, R decreases (5). Thus, the condition for the onset of general yield is that $\frac{1}{B}\frac{\Delta R}{\Delta a} < 0$ shows a maximum i.e. $\frac{1}{B}\frac{\Delta^2 R}{\Delta\, a^2} = 0$ and $\frac{1}{B}\frac{\Delta^3 R}{\Delta\, a^3} < 0$:

$$\left.\begin{aligned} \frac{\Delta^3(W_{ext} - U_e)}{B\Delta a^3} &= 0 \\ \text{and} \quad \frac{\Delta^4(W_{ext} - U_e)}{B\Delta a^4} &< 0 \end{aligned}\right\} \quad \text{onset of general yield} \qquad 4.9$$

Theoretically, therefore, if an effective fracture mechanism can operate and if ΔW_{ext}, ΔU_e and R are known as functions of a, it should be possible to determine the critical conditions and failure mode of a loaded structure. In practice, however, this is extremely difficult especially if an attempt is made to account for any time-dependent effects. In addition, there is no information concerning the external work required to maintain slow stable crack extension even under simple loading conditions. Thus, at present, the use of the energy balance approach in design is limited to determination of the critical conditions of crack initiation and crack instability.

4.1.b Crack Stability

Stability is defined according to equation 4.7 which effectively states that if an increment of crack extension causes the change in fracture toughness to be positive with respect to the change in the elastic strain energy rate, the crack will be arrested and is defined as stable. Further crack extension then requires an increase of applied load i.e. external work. However, if the increment of crack extension causes the change in R to be negative with respect to the change in the elastic strain energy

rate, the crack will continue to propagate and is defined as unstable. Under such circumstances the "crack driving force" is no longer supplied by the external work but stems from within the body at the expense of the stored elastic strain energy.

Gurney and Hunt (6) and Clausing (7) independently formulated the criteria on fracture stability according to chosen constraints of the loading rate as follows.

In linear elastic-plastic materials the elastic strain energy may be expressed in terms of the compliance, $C = {}^{u}/_{p}$ i.e. $U_e = \frac{P^2C}{2}$ or $\frac{u^2}{2C}$. Differentiating U_e twice with respect to a under fixed loading and fixed grip conditions and substituting into equation 4.7, the following conditions are obtained for crack instability:

$$\left.\begin{aligned} \left\{ \frac{\Delta^2 C}{\Delta a^2} \Big/ \frac{\Delta C}{\Delta a} \right\}_p &> \frac{1}{B}\frac{\Delta R}{\Delta a} \Big/ R \\ \left\{ \frac{\Delta^2 (\frac{1}{C})}{\Delta a^2} \Big/ \frac{\Delta (\frac{1}{C})}{\Delta a} \right\}_u &> \frac{1}{B}\frac{\Delta R}{\Delta a} \Big/ R \end{aligned}\right\} \begin{array}{l} \text{crack} \\ \text{instability} \end{array} \qquad 4.10$$

The left hand side of the equations may be called "geometric stability factors" ($\frac{n_x}{a}$, $\frac{n_u}{a}$ and f_2, f_2-f_3 in Gurney and Hunt's and Clausing's notation, respectively) and it can be seen that the smaller their algebraic value the more stable is the cracking with negative values making the crack particularly stable. In general, the geometric stability factors depend upon the geometric size and configuration of the cracked body as well as the flexibility of the loading system. Thus, crack stabilisation is easier to achieve in small crackline-loaded edge-cracked specimens under stiff loading conditions than in large centre-cracked tension or edge-cracked bend specimens under similar loading conditions. The influence of the flexibility of the applied loading system is easily demonstrated.

Let the total compliance be separated into contributions due to the cracked component or specimen, C_{sp} and the applied loading system or machine, C_m so that the total displacement, u is $(C_{sp} + C_m)$ P and the

instability conditions may be rewritten (6):

$$\left\{ \frac{\Delta^2 C_{sp}}{\Delta a^2} \Big/ \frac{\Delta C_{sp}}{\Delta a} \right\}_p > \frac{1}{B} \frac{\Delta R}{\Delta a} \Big/ R \qquad \text{crack instability}$$

$$\left\{ \left(\frac{\Delta^2}{\Delta a^2} \left(\frac{1}{C_{sp}} \right) \Big/ \frac{\Delta}{\Delta a} \left(\frac{1}{C_{sp}} \right) \right) + \left(2\, C_m \frac{\Delta}{\Delta a} \left(\frac{1}{C_{sp}} \right) \Big/ 1 + \frac{C_m}{C_{sp}} \right) \right\}_u > \frac{1}{B} \frac{\Delta R}{\Delta a} \Big/ R \qquad 4.11$$

Since $\frac{\Delta}{\Delta a}\left(\frac{1}{C_{sp}}\right)$ is negative the stability is decreased by the flexibility of the loading system and crack instability is most probable under soft loading conditions i.e. dead weight loading. From the point of view of design it is probably necessary to assume load-controlled conditions in the absence of a knowledge of the compliance of the loading system, since these yield conservative estimates of crack instability.

4.1.c Simplified Model for Crack Initiation

The form of equation 4.5 is such that crack initiation cannot be predicted in the general case without knowledge of the external work term. However, a simplified model for crack initiation can be used which is applicable in situations with limited crack tip plasticity.

Figs. 4.1.c and 4.1.d show typical load-displacement diagrams for an elastic-plastic material undergoing crack growth at a fixed load, P_i and at a fixed displacement, u_i. It is assumed that the initial stored plastic strain energy prior to crack extension is small and that the unloading and reloading curves for a crack of length $a + \Delta a$ are identical so that the origins 0, 0_1 and 0_2 coincide. This imposes the condition that the plasticity is limited and unloading is confined to a small region near the crack tip i.e. crack initiation with limited plasticity.

Considering Fig. 4.1.c:

$$\text{Area } 0_1PQ0_2 = \int_0^{P_i} u\,(P, a + \Delta a)\, dP - \int_0^{P_i} u(P, a)\, dP$$

$$= \int_0^{P_i} \left(\frac{\partial u}{\partial a} \right)_P \Delta a.\, dP$$

Denoting $\int_0^P u\,dP$ by U^* (complementary energy), the general equation for crack initiation, equation 4.5 becomes:

$$\text{In the limit as } \Delta a \to 0 \qquad \frac{1}{B}\left(\frac{\partial U^*}{\partial a}\right)_p \geqslant R_i \qquad \text{crack initiation limited plasticity} \qquad 4.12$$

Considering Fig. 4.1.d:

$$\text{Area } O_1PQO_2 = \int_0^{u_i} P(u,a)\,du - \int_0^{u_i} P(u,a+\Delta a)\,du$$

$$= -\int_0^{u_i} \left(\frac{\partial P}{\partial a}\right)_u \Delta a \,.\, du$$

Denoting $\int_0^u P\,du$ by U (strain energy), the condition for crack initiation becomes:

$$\text{In the limit as } \Delta a \to 0 \qquad -\frac{1}{B}\left(\frac{\partial U}{\partial a}\right)_u \geqslant R_i \qquad \text{crack initiation limited plasticity} \qquad 4.13$$

Therefore, equations 4.12 and 4.13 may be considered as the equations governing crack initiation in an elastic-plastic material with limited crack tip yield, the latter requiring experimental investigation.

This loss in generality in the use of the energy balance approach is unfortunate but, as shown later, it is probably outweighed by the advantages of an analytical treatment which is useful in design.

4.1.d Comparison between R_i and other Fracture Mechanics Parameters

For linear elastic materials, the energy may be expressed in terms of the elastic compliance, C. Equations 4.12 and 4.13 then give the single condition:

$$\text{In the limit as } \Delta a \to 0 \qquad \frac{1}{2}\frac{P^2}{B}\left(\frac{\partial C}{\partial a}\right) \geqslant R_i \qquad 4.14$$

The elastic strain energy release rate, $\mathcal{G}$ is defined by:

$$\text{In the limit as } \Delta a \to 0 \qquad \mathcal{G} = \frac{1}{2}\frac{P^2}{B}\left(\frac{\partial C}{\partial a}\right) \qquad 4.15$$

giving the following condition for crack initiation:

$$\text{In the limit as } \Delta a \to 0 \qquad \mathcal{J}_i = R_i \qquad \text{linear elastic material} \qquad 4.16$$

i.e. R is consistent with the LEFM parameter, $\mathcal{J}$ in the elastic regime.

In addition, inspection of equations 2.24 and 2.25 show that for elastic or deformation-type elastic-plastic materials R_i at crack initiation may be identified with Rice's contour integral:

$$\text{In the limit as } \Delta a \to 0 \qquad J_i = R_i \qquad \text{elastic or deformation-type elastic-plastic material} \qquad 4.17$$

and for elastic-plastic materials with small scale yielding:

$$\text{In the limit as } \Delta a \to 0 \qquad \mathcal{J}_i = J_i = R_i \qquad \text{small scale yielding} \qquad 4.18$$

However, for crack initiation under moderate to large scale yielding conditions and for finite stable crack extension and subsequent crack instability in elastic-plastic materials, R cannot be identified with either $\mathcal{J}$ or J and under such circumstances general equations 4.5, 4.4 and 4.7 apply, respectively.

4.2 The Fracture Toughness Parameter, R

4.2.a General Definition

For the general case of an elastic-plastic material, the fracture toughness parameter, R may be defined by:

$$R = 2\gamma + 2\gamma_p + \frac{1}{B}\frac{\Delta U_p}{\Delta a} \qquad 4.19$$

where $2\gamma + 2\gamma_p$ is the fracture surface energy associated with the two newly created surfaces and includes both the theoretical surface tension, γ and the plastic work contribution, γ_p . $\frac{1}{B}\frac{\Delta U_p}{\Delta a}$ is the plastic strain energy rate associated with shear lip formation.

In ideal brittle fracture equation 4.19 reduces to:

$$R = 2\gamma \qquad 4.20$$

and R corresponds to a purely cleavage separation of the atomic planes. On the other hand, for a flat fibrous fracture with negligible shear lips:

$$\left.\begin{aligned} &R = 2\gamma + 2\gamma_p \\ &\text{or } R = 2\gamma_p \quad \text{since} \quad 2\gamma << 2\gamma_p \end{aligned}\right\} \qquad 4.21$$

and the fracture surface now includes both cleavage and slip micromodes of separation. There is substantial evidence to indicate that γ and γ_p are material constants at a given temperature and strain rate so that under such circumstances R may be considered a material constant depending only on the temperature and loading rate.

However, in all other situations R will not be a material constant due to the contribution of the plastic energy rate, $\frac{1}{B}\frac{\Delta U_p}{\Delta a}$. The extent of the plastic zone and consequently the plastic strain energy rate depends on the stress state in the vicinity of the crack front and it is therefore influenced by the geometric size and configuration as well as temperature and strain rate. Also, since the processes that cause $\frac{1}{B}\frac{\Delta U_p}{\Delta a}$ to change are irreversible, for a particular material, geometry and environment R will not be a unique function of crack extension and time but will depend on the loading history. Examples of this have been presented by Gurney and Hunt (6) and Broek (8) who showed that if during quasi-static crack extension the load is reduced and then subsequently increased, crack growth under rising load takes place at a lower load than it did before the load was reduced. An extreme case would be stable crack extension under cyclic loading conditions i.e. fatigue.

In spite of the foregoing, Krafft (4) and Rice (9) have both postulated that (under monotonic loading) the curve of R versus absolute crack extension is a material property, independent of geometry and initial crack

length for a given section thickness, temperature and strain rate.

4.2.b Determination of R

The inappropriateness of equating the LEFM parameter, $\mathcal{J}$ with R during slow stable crack extension in order to determine the fracture toughness of an elastic-plastic material was discussed previously in section 2.3.c and has been clearly demonstrated in section 4.1.d.

At present, analytical determination of the general fracture toughness parameter, R is not possible but experimentally R may be obtained from the general energy balance equation 4.4 (5) or by direct evaluation of the plastic strain energy rate, $\frac{1}{B}\frac{\Delta U_p}{\Delta a}$ from shear lip dimensions (4) and plastic enclave strain measurements (10).

The former method requires the use of wide test pieces which promote stable cracking and avoid general yield so that a continuous load-displacement record is obtained during quasi-static crack extension. If the crack length is accurately monitored during crack extension and the load-displacement curve represents a real energy input, values of R may be computed directly after subtracting elastic strain energy contributions. Unfortunately, results of such experiments have only been reported recently (5) partly due to the practical difficulties involved in performing such tests.

The design of the experimental test piece needs careful consideration for, in addition to questions of crack stability and plastic stability, yielding at regions remote from the crack tip must be avoided. If such irreversibilities do occur then it is impossible to distinguish between the work done against the resistance of the material and the work of yielding and anomalously high values of R are obtained (5).

A further consideration in the determination of R is the method of monitoring crack extension. Surface crack extension measurements generally underestimate real crack extensions due to crack front tunnelling at the mid-section, which may result in an overestimate in R; only for very large crack extensions, when an equilibrium-maximum plastic zone has been

achieved, may surface crack measurements be used with any confidence. In fact, alternative techniques are required to determine crack initiation at the mid-section and small amounts of stable crack growth.

In comparison, determination of the crack initiation parameter, R_i [a] has received considerable attention due to the observed relationship between plane strain values of R_i and the plane strain fracture toughness, K_{Ic}. The original technique of Begley and Landes (11) (12) involved experimental determination of the calibration function , $-\frac{1}{B}\left(\frac{\partial U}{\partial a}\right)_u$ from load-displacement records of a series of notched specimens. Values of R for crack initiation were then obtained directly from knowledge of the critical displacement for precracked specimens.

Subsequently, methods were developed for measuring the function $-\frac{1}{B}\left(\frac{\partial U}{\partial a}\right)_u$ from single specimen tests (13)-(15). These methods use deeply cracked bend type specimens for which a linear relationship exists between the strain energy, U and $-\frac{1}{B}\left(\frac{\partial U}{\partial a}\right)_u$ in the linear elastic and fully plastic regimes. However, crack extension monitoring and detection of the crack initiation point still remain a problem.

4.3 Application of Energy Balance Approach in Design

Application of the energy balance approach in design is limited to the two critical conditions of crack initiation, in the presence of limited crack tip plasticity and crack instability, in the presence of large scale contained crack tip plasticity.

4.3.a Design Against Crack Instability

In order to use the energy balance approach the geometrical parameter, $\frac{1}{B}\frac{\Delta U_e}{\Delta a}$ of the cracked component or structure and the material parameter, R

---

[a] Although the term "J-integral" is generally used for the crack initiation parameter, $-\frac{1}{B}\left(\frac{\partial U}{\partial a}\right)_u$ in the American literature, the notation R_i is retained here for consistency with the general fracture toughness parameter, R.

are required as functions of crack length and crack extension, respectively. As discussed previously in section 4.1.b, in the absence of a knowledge of the flexibility of the loading system, an elastic strain energy rate, $\frac{1}{B}\left(\frac{\Delta U_e}{\Delta a}\right)_p$ under load-controlled conditions should be used. Assuming that the hypothesis of a universal R-curve is correct i.e. independent of geometry and initial crack size for a given thickness, temperature and strain rate, a conservative estimate of crack instability can be determined by the construction procedure illustrated in Fig. 4.2.a. At the point of tangency of the two curves:

$$\left.\begin{aligned} \frac{1}{B}\left(\frac{\Delta U_e}{\Delta a}\right)_{p,t} &= R_t \leqslant R_c \\ \text{and } \frac{1}{B}\left(\frac{\Delta^2 U_e}{\Delta a^2}\right)_{p,t} &= \frac{1}{B}\left(\frac{\Delta R}{\Delta a}\right)_t \geqslant \frac{1}{B}\left(\frac{\Delta R}{\Delta a}\right)_c \end{aligned}\right\} \quad 4.22$$

The similarity between Fig. 4.2.a and Fig. 2.5 is obvious. However, in the former case the construction method is used merely as an aid in design to obtain a conservative estimate of crack instability; it is not used as a method for the determination of R during stable crack extension.

4.3.b Design Against Crack Initiation

To design against crack initiation the geometrical parameter, $\frac{1}{B}\left(\frac{\partial U^*}{\partial a}\right)_p$ or $-\frac{1}{B}\left(\frac{\partial U}{\partial a}\right)_u$ of the cracked component or structure and the material parameter, R_i are needed for the initial crack size under consideration. This requires some judgement as to the nature of the loading system, since overly conservative estimates may be obtained on the basis of load-controlled conditions. Perhaps, a more useful and physically more meaningful situation is when crack initiation occurs along a line defined by the hyperbola, Pu = constant (Fig. 4.2.b). Under these circumstances:

$$U^* + U = Pu = \text{constant}$$

$$dU^* + dU = 0$$

$$\text{and} \quad \frac{1}{B}\left(\frac{\partial U^*}{\partial a}\right) = -\frac{1}{B}\left(\frac{\partial U}{\partial a}\right)$$

Therefore, if either the complementary energy, U^* or the strain energy, U of the configuration can be determined as a function of its derivative with respect to crack length analytically or by means of finite elements, it should be possible to limit the complementary energy or the stored strain energy within design limits imposed by a knowledge of R_i since at crack initiation:

$$\text{In the limit as } \Delta a \to 0 \qquad \frac{1}{B}\left(\frac{\partial U^*}{\partial a}\right) = -\frac{1}{B}\left(\frac{\partial U}{\partial a}\right) \geqslant R_i \ (Pu = \text{constant}) \qquad 4.23$$

4.4 Advantages and Limitations of the Energy Balance Approach

The most important advantage of the energy balance approach is that it deals with slow crack extension and extensive plasticity ahead of the crack tip, being of greater applicability than LEFM which is limited to crack initiation under small scale yielding only.

The simplified model for crack initiation provides an analytical basis for the determination of the fracture toughness, R_i which should prove useful in design. In addition, results reported so far indicate that R_i for crack initiation is, subject to certain size requirements, related to the plane strain fracture toughness, K_{Ic} (11) (12) (15) - (18) i.e.

$$R_{Ic} = \frac{(1-\nu^2)}{E} K_{Ic}^2 \qquad \text{plane strain} \qquad 4.24$$

where R_{Ic} corresponds to the critical value of R_i under plane strain crack tip conditions, thus, providing a possible method of determination of K_{Ic} using small specimens.

Unfortunately, the main advantage of the energy balance approach may be outweighed by some of the disadvantages in its application. At present

the determination of R values, other than perhaps R_i, is difficult and costly even for one material, section thickness and environment and the hypothesis of a universal R-curve, which would reduce the task considerably, has not yet been validated. According to one theoretical analysis of quasi-static crack extension in a rate-sensitive Tresca solid (19), such an hypothesis is valid but only in the limiting case of a rate-insensitive elastic-plastic solid. Certainly, the application of an R-curve obtained under monotonic uniaxial loading conditions to the complex loading situation in a structure should be treated with caution.

In addition, with the quasi-two-dimensional general model only thickness average values of R, $\frac{1}{B}\left(\frac{\Delta U_e}{\Delta a}\right)_p$ and $-\frac{1}{B}\left(\frac{\partial U}{\partial a}\right)_u$ have been considered. In the case of R this is unavoidable due to the method of determination. However, the crack front configuration may be quite complex and it is known that $\frac{1}{B}\left(\frac{\Delta U_e}{\Delta a}\right)_p$ and $-\frac{1}{B}\left(\frac{\partial U}{\partial a}\right)_u$ have, in general, a different value at each position along the crack border (20) - (22). Such aspects of crack growth behaviour must be considered before energy balance methods can be used with any degree of confidence.

Finally, the energy balance approach cannot be used when yielding occurs at locations other than the crack tip, for example, in a reinforcement or at a bolt hole. Although, the true limits of applicability of energy balance techniques have yet to be determined.

4.5 Summary

An energy balance approach to failure analysis appears useful as a means of designing against crack initiation, in the presence of limited crack tip plasticity, and crack instability, after slow crack extension accompanied by considerable crack front plastic yield. However, it is not possible to design against the onset of general yield due to the lack of information concerning the work rate of the applied forces.

References

(1) A.A. Griffith, Phil. Trans. Roy. Soc., A221, p. 163, 1920.

(2) K.S. Havner and J.B. Glassco, Int. J. of Fract. Mechs., 2. p. 506, 1966.

(3) J. Eftis and H. Liebowitz, Eng. Fract. Mechs., 7, p. 101, 1975.

(4) J.M. Krafft, A.M. Sullivan and R.W. Boyle, Proc. Symp. Crack Propagation, Cranfield, p. 8, 1961.

(5) H.C. van Elst, H. Wildschut, M.A. Lont and F.H. Toneman, 4th Int. Conf. Fracture, Waterloo, 3, p. 155, 1977.

(6) C. Gurney and J. Hunt, Proc. Roy. Soc., A299, p. 508, 1967.

(7) D.P. Clausing, Int. J. of Fract. Mechs., 5, p. 211, 1969.

(8) D. Broek, Aerospace Proc., p. 811, 1966.

(9) J.R. Rice, "Fracture — An Advanced Treatise," Vol. II, Ed. H. Liebowitz, Academic Press, New York, p. 191, 1968.

(10) D.P. Rooke and F.J. Bradshaw, Proc. 2nd Int. Conf. Fracture, Brighton, p. 46, 1969.

(11) J.A. Begley and J.D. Landes, A.S.T.M. S.T.P. 514, "Fracture Toughness," Am. Soc. for Testing and Materials, p. 1, 1972.

(12) J.D. Landes and J.A. Begley, A.S.T.M. S.T.P. 514, "Fracture Toughness," Am. Soc. for Testing and Materials, p. 24, 1972.

(13) R.J. Bucci, P.C. Paris, J.D. Landes and J.R. Rice, A.S.T.M. S.T.P. 514, "Fracture Toughness," Am. Soc. for Testing and Materials, p. 40, 1972.

(14) J.R. Rice, P.C. Paris and J.G. Merkle, A.S.T.M. S.T.P. 536, "Progress in Flaw Growth and Fracture Toughness Testing," Am. Soc. for Testing and Materials, p. 231, 1973.

(15) J.D. Landes and J.A. Begley, A.S.T.M. S.T.P. 560, "Fracture Analysis," Am. Soc. for Testing and Materials, p. 170, 1974.

(16) C.A. Griffis, Trans. A.S.M.E., Series J, J. Pres. Ves. Tech., 97, p. 278, 1975.

(17) J.N. Robinson, Int. J. of Fracture, 12, p. 723, 1976.

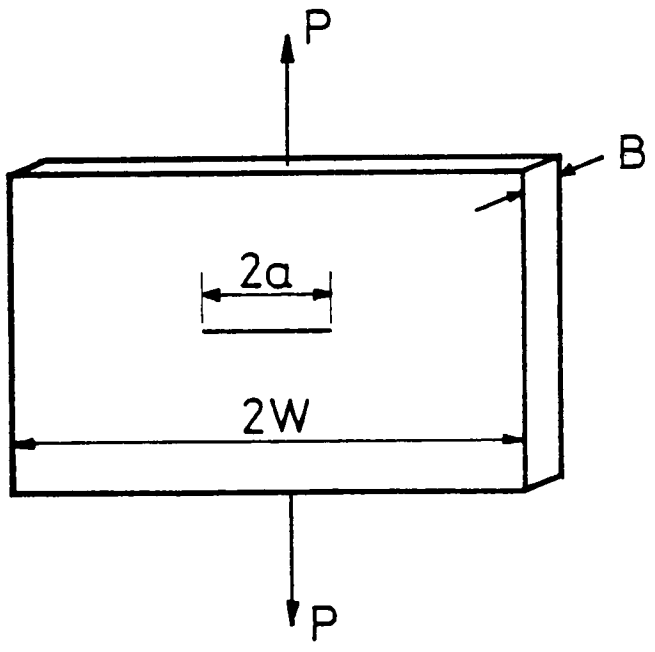
(18) K. Markström, Eng. Fract. Mechs., 9, p. 637, 1977.

(19) M.P. Wnuk, A.S.T.M. S.T.P. 536, "Progress in Flaw Growth and Fracture Toughness Testing," Am. Soc. for Testing and Materials, p. 64, 1973.

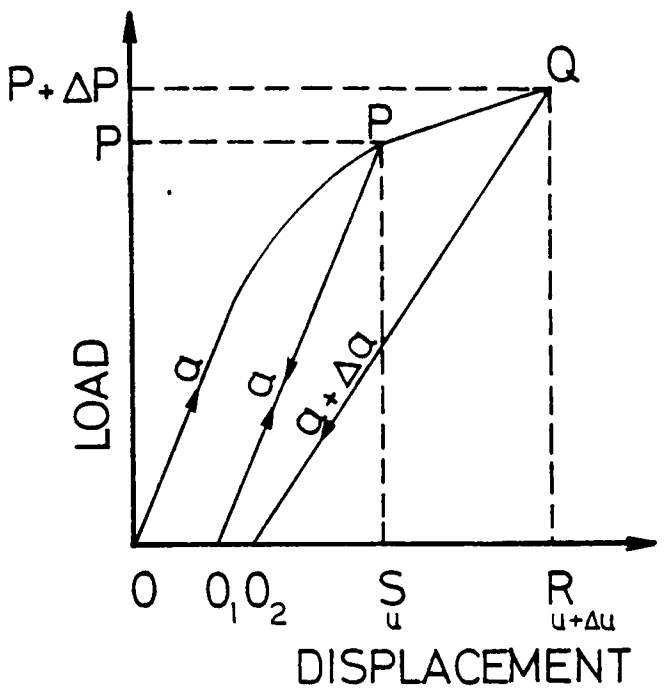
(20) J.L. Swedlow and M.A. Ritter, A.S.T.M. S.T.P. 513, "Stress Analysis and Growth of Cracks," Part 1, Am. Soc. for Testing and Materials, p. 79, 1972.

(21) M.A. Schroedl and C.W. Smith, A.S.T.M. S.T.P. 560, "Fracture Analysis," Am. Soc. for Testing and Materials, p. 69, 1974.

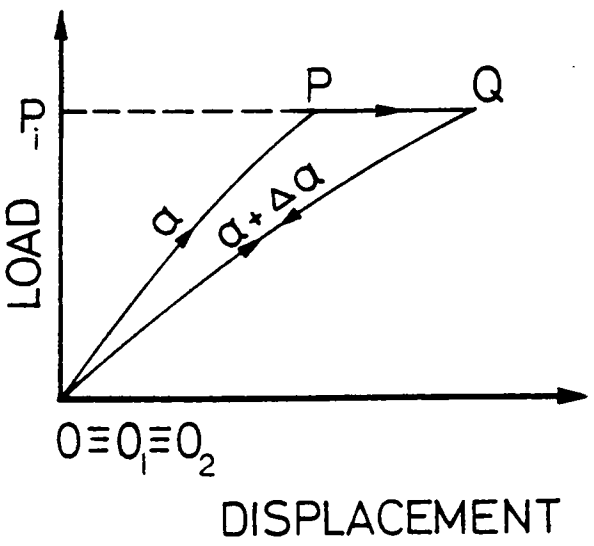
(22) B.K. Neale, Int. J. of Fracture, 12, p. 499, 1976.



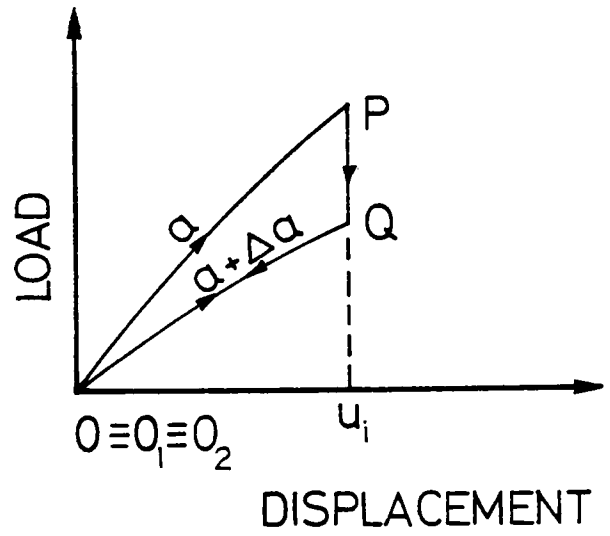
a. A crack in a wide plate



b. Typical stress (load) - strain (displacement) diagram

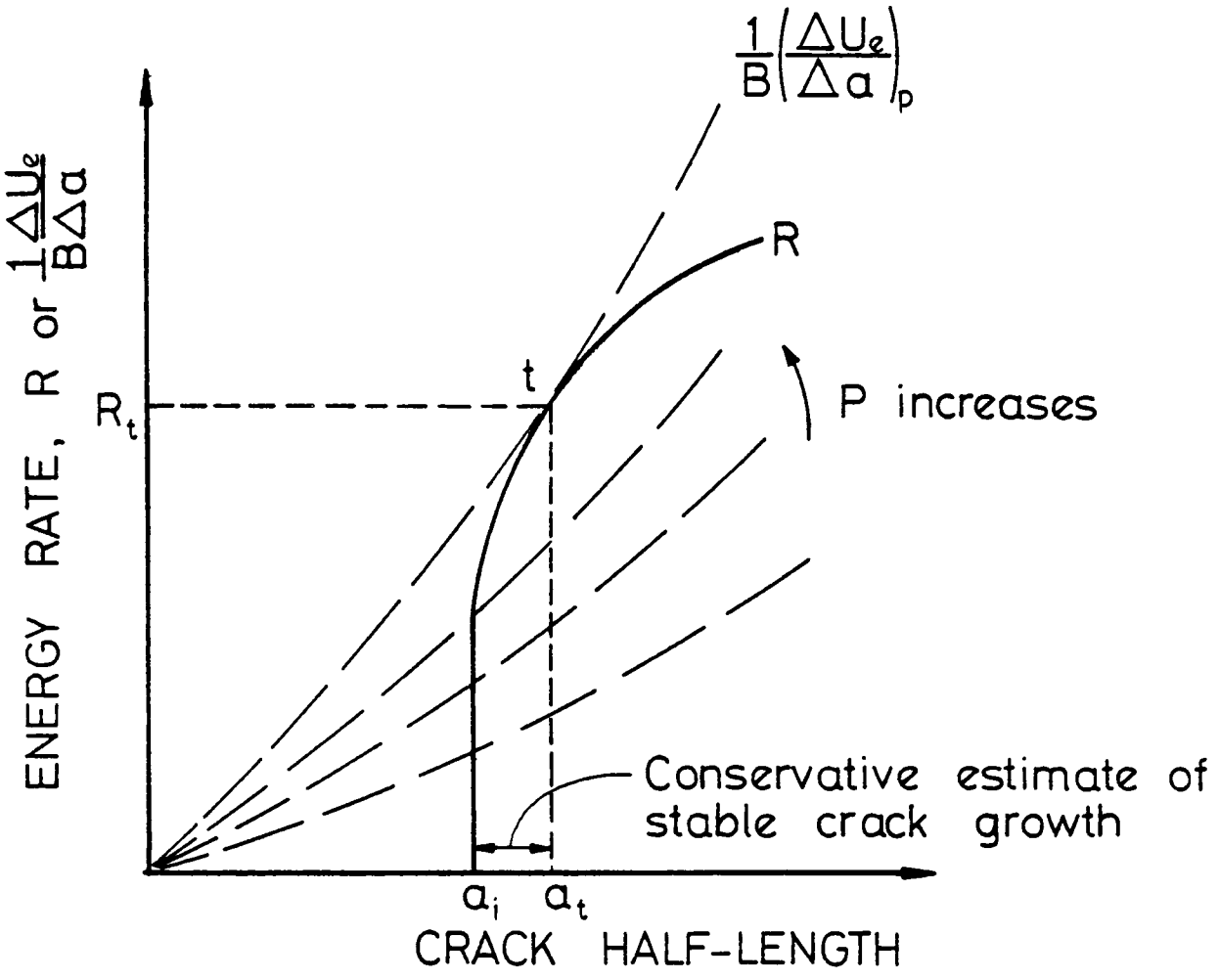


c. Load-controlled test

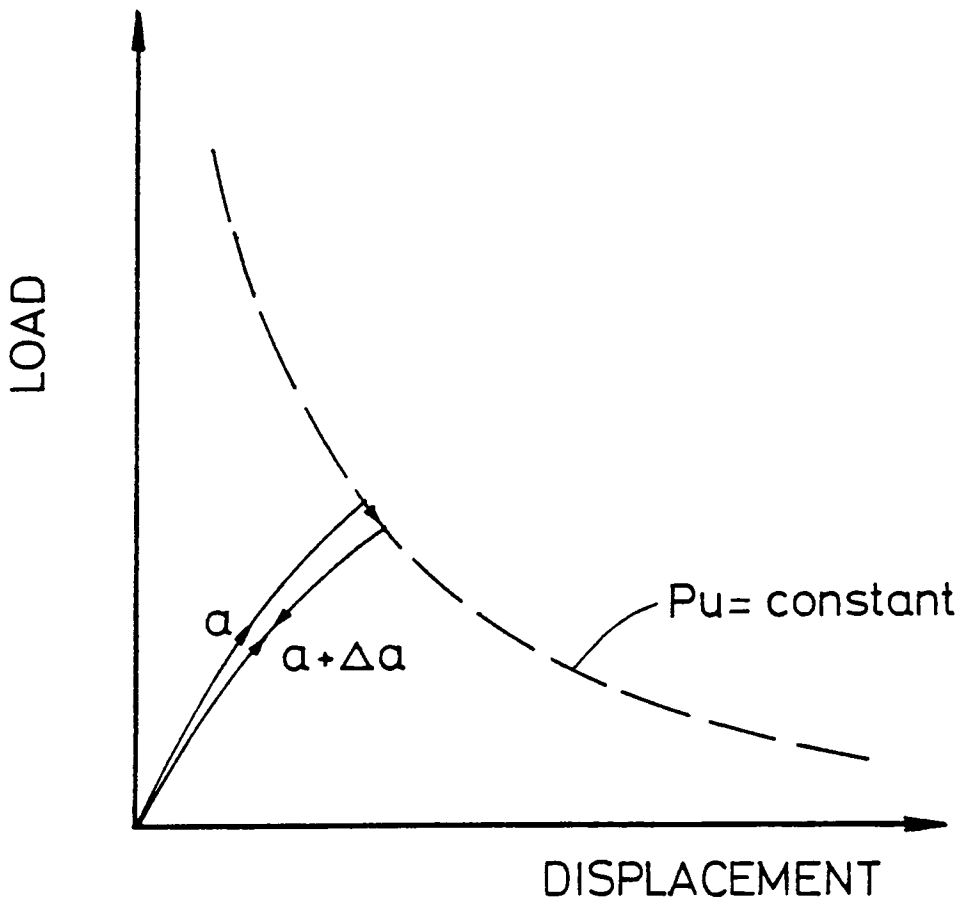


d. Displacement-controlled test

Fig. 4.1 Energy balance approach to crack growth



a. Crack instability



b. Crack initiation

Fig. 4.2 Application of energy balance approach in design

CHAPTER 5

INTRODUCTION TO EXPERIMENTAL STUDY

The main aim of the experimental programme is to study the failure mechanisms of precracked model specimens and vessels in order to determine criteria for the failure analysis of pressure vessels with defects. With this in mind, the results are presented in a form similar to the one suggested by Dowling and Townley in their two-criteria approach to failure (1).

5.1 Materials Selection

The first step in the investigation must be to characterise as completely as possible the model material. Considering first the possibility of brittle [a] fracture, the toughness and yielding characteristics of pressure vessel steel would require extremely large specimens well above the testing capacity of the laboratory making it unsuitable as a model material. This is apparent from the specimen size requirements for a valid plane strain fracture toughness test (2) (3):

$$a,\ W-a,\ B \geqslant 2.5\left(\frac{K_{Ic}}{\sigma_y}\right)^2 \qquad 5.1$$

where a is the crack length, W is the test piece width, B, the thickness and σ_y, the yield stress of the material. In order to obtain meaningful results from small specimens a material was required with a low fracture toughness-to-yield strength ratio; an 18% Ni 200-grade maraging steel was finally selected having the additional property of a strain rate insensit-

---

[a] In Dowling and Townley's two-criteria approach to failure (1) and in the following chapters "brittle" is used in the engineering sense and refers to an unstable, low stress fracture which occurs when the stress intensity factor achieves the critical plane strain value, K_{Ic}.

ive fracture toughness (4) and a structure not unlike pressure vessel steel.

The use of plastics in the experimental study was also considered. From a testing standpoint plastics offer some obvious advantages including transparency for observation of crack extension during loading, low elastic moduli for large and more accurately measurable displacements, reduced loading requirements and easy machinability.

In particular, the use of glassy plastics to model the macroscopic yield and fracture behaviour of metals has been discussed by several authors (5)-(7). Significant differences exist between the time-dependent elastic and yield behaviour of polymers and the elastic-plastic behaviour of metals. However, glassy plastics generally present small time-dependent phenomena in short term tests at ambient temperature and the use of such materials in modelling the elastic-plastic behaviour of metals at room temperature can be justified if all that is required is a qualitative study for the purpose of design.

Of the various plastics available, the polycarbonate Makrolon made by Bayer was the most suitable due to the similarity of behaviour to many steels. For example, the size and shape of the crack tip plastic zones developed in thin and intermediate thickness sheet undergo a transition from plane strain to plane stress with rising load, approaching those given by the Dugdale model at high applied stress levels (6) (8) (9). At low temperatures, polycarbonate exhibits a sharp ductile-to-brittle fracture transition which is sensitive to thermal history of the polycarbonate, degree of transverse constraint, strain rate and environment (10)-(13). These similarities between steel and polycarbonate imply that the experimental results may be adapted to the study of the failure of steel structures, bearing in mind the obvious differences due to microstructure, strain

rate sensitivity and surface energy. The simple tests with maraging steel specimens overlapping some of the configurations of the polycarbonate should help in this adaptation.

5.2 Model Configurations

Model configurations were required which promote stable crack growth and for which linear elastic and limit analysis solutions are readily available. Thus, the compact specimen under displacement-controlled loading was chosen for the plate tests having the additional advantage of being a standard fracture toughness specimen. Model cylindrical vessels containing longitudinal defects and tested under hard loading conditions i.e. pressurised hydraulically with water for stable cracking, were also selected. These model configurations are shown in Fig. 5.1.

5.2.a The Compact Specimen

The compact specimen is a combined tension and bending specimen specifically designed for economical material testing with the bending component producing considerable reductions in machine load capacity requirements.

A two-dimensional linear elastic analysis has been produced for this configuration by the method of boundary collocation for a relative crack length range, α $(= \frac{a}{W})$ from 0.3 to 0.7 (14). More recently, this analysis has been extended over a wider range of α (15) (16) and further improved to account for the effects of pin-loading (17) (18). However, for this specimen LEFM analysis has to be restricted to the α range of 0.2 to 1.0 due to the proximity of the loading holes to the crackline which causes the stress intensity factor to be sensitive to small variations in dimensions when α is small. This is a penalty inherently associated with the compactness of the specimen.

Stress intensity factors for the compact specimen are normally presented

in the form:

$$K = \frac{P}{\sqrt{W}\,B} \cdot Y \qquad 5.2$$

where P is the nominal applied load and Y is the stress intensity coefficient for the compact specimen and a function of α. Therefore, the critical average gross cross-sectional stress at failure normalised with respect to the unixial yield stress, σ_y is:

$$\frac{P_{Ic}}{\sigma_y\, WB} = \frac{K_{Ic}}{\sigma_y\, \sqrt{W}\, Y} \qquad 5.3$$

i.e. a function of the material parameters, K_{Ic} and σ_y as well as the geometry through the parameters $\sqrt{W}$ and α.

As a first approximation of the deformation behaviour of the pin-loaded compact specimen, a simple limit analysis may be performed based solely on the equilibrium requirements, ignoring the stress triaxiality at the crack tip and assuming a linear elastic-perfectly plastic material response. The model is illustrated in Fig. 5.2 and developed in Appendix 1. It is assumed that the neutral axis occurs at the point of stress reversal, C which acts as a hinge; material beneath the crack tip is then subjected to a tensile stress whilst material between C and the far free surface is subjected to a compressive stress.

Under increasing load, the yield point is first reached over a region in the vicinity of the crack front as shown in Fig. 5.2.b. Assuming a linear elastic stress distribution across the remaining ligament and that the material obeys Tresca's yield criterion, an elastic limit load, P_{el} may be estimated:

$$\frac{P_{el}}{\sigma_y\, WB} = \frac{(1 - \alpha)^2}{2\,(2 + \alpha)} \qquad 5.4$$

with a corresponding extensional strain at the loading point:

$$\frac{E\varepsilon_{el}}{\sigma_y} = \frac{(2 + 2\alpha + 2\alpha^2)}{(1 - \alpha)(2 + \alpha)} \qquad 5.5$$

At higher applied load levels the tensile yield zone spreads across the remaining ligament leading gradually to yielding in compression at the back of the specimen. The load corresponding to initial yield at the back surface may be given by:

$$\frac{P_{by}}{\sigma_y WB} = -(\tfrac{1}{2} + \alpha) + \tfrac{1}{2}\sqrt{3(1 + 2\alpha^2)} \qquad 5.6$$

with a notional elastic strain at the loading point of:

$$\frac{E\varepsilon_{by}}{\sigma_y} = \frac{1 + \sqrt{3(1 + 2\alpha^2)}}{3 - \sqrt{3(1 + 2\alpha^2)}} \qquad 5.7$$

During the transitional stress state represented by Fig. 5.2.d the width of the internal stress block required to equilibrate the applied load, 2x decreases until finally the whole specimen yields in tension or compression, Fig. 5.2.e. A lower bound limit analysis estimate for the transition state is:

$$\frac{E\varepsilon_p}{\sigma_y} = \frac{[\,1 + \alpha + (P_p/\sigma_y WB)\,]}{\sqrt{3(1-\alpha)^2 - 3(P_p/\sigma_y WB)^2 - 6(P_p/\sigma_y WB)(1+\alpha)}} \qquad 5.8$$

where P_p and ε_p are the corresponding load and notional elastic strain at the loading point, respectively and, in the limit as ε_p tends to infinity, the general yield load is obtained:

$$\frac{P_{gy}}{\sigma_y WB} = -(1 + \alpha) + \sqrt{2(1 + \alpha^2)} \qquad 5.9$$

It should be noted that the "constraint factors," $P/\sigma_y WB$ or alternatively "weakening factors" since they are all less than unity, are defined with respect to the gross cross-sectional area rather than the net cross-sectional area as suggested by equation 3.2. In addition, these values are obtained by comparison with the tensile yielding of an uncracked specimen, whereas the cracked specimen deforms in a manner characteristic of

almost pure bend especially at longer crack lengths. The concept of an average gross cross-sectional stress is retained here solely for compatibility with the general form of the LEFM equation 5.3.

5.2.a.i Failure Analysis Diagram

Following Dowling and Townley (1), a failure analysis diagram may be constructed by plotting the parameter, $P/\sigma_y WB$ versus the relative crack length, α. This is demonstrated in Fig. 5.3 where, for clarity, only the two extremes of linear elastic fracture, equation 5.3 and fully plastic yield, equation 5.9 are shown. An upper bound plane strain slip line field solution for the compact specimen configuration (19), a generalisation of Green's field for the pure bending of a plate, is also included.

In Dowling and Townley's two-criteria approach to failure (1) it is assumed that failure occurs when the applied load reaches the lower of the load to cause brittle fracture or the general yield load. A failure analysis diagram then indicates the applied load levels and defect size range over which failure is governed predominantly by brittle fracture or general yield. The influence of the variables K_{Ic}, σ_y, $\sqrt{W}$ is to alter the relative position of the LEFM failure line only, the general yield load remaining constant for a given defect size. Fig. 5.3 demonstrates for the compact specimen that a reduction in the plane strain fracture toughness or an increase in the uniaxial yield stress or specimen width increases the probability of brittle fracture at intermediate crack lengths.

The failure analysis diagram is obviously an oversimplification since no attempt has been made to account for the effects of work-hardening nor the complex transition regions at relatively short and long crack lengths. However, the method should prove useful in the presentation and analysis of slow crack growth results.

Although attempts to account for the effects of work-hardening when applying limit analysis techniques may be questionable, correlations

between experimental results and theory have sometimes been improved by taking the value of the yield stress as the ultimate tensile strength of the material or some intermediate, arbitrary value between yield and ultimate collapse called the "flow stress". However, the problem is frequently compounded by inconsistencies in the definition of an experimental limit load. In the following experimental study the lower bound limit analysis solutions are based on the ultimate tensile strength of the material i.e. an ultimate collapse load is defined such that:

$$\frac{P_u}{\sigma_u WB} = -(1+\alpha) + \sqrt{2(1+\alpha^2)} \qquad 5.10$$

$$\left(= -1 + \sqrt{2} \text{ when } \alpha = 0 \right)$$

Following Dowling and Townley, a dimensionless failure parameter, P^{ϕ} may then be defined for the compact specimen by normalising the average gross cross-sectional stress with respect to the ultimate collapse load for an uncracked specimen i.e.

$$P^{\phi} = \frac{P}{0.4142\ \sigma_u WB} \qquad 5.11$$

$$\text{and } P^{\phi}_{Ic} = \frac{K_{Ic}}{0.4142\ \sigma_u \sqrt{W}\, Y} \qquad 5.12$$

$$P^{\phi}_{gy} = \frac{\sigma_y}{\sigma_u} \frac{\left[-(1+\alpha) + \sqrt{2(1+\alpha^2)}\right]}{0.4142} \qquad 5.13$$

$$P^{\phi}_{u} = \frac{\left[-(1+\alpha) + \sqrt{2(1+\alpha^2)}\right]}{0.4142} \qquad 5.14$$

Thus, P^{ϕ}_{gy} represents a dimensionless failure parameter for the initiation of widespread yielding with P^{ϕ}_{u} attempting to account for the influence of work-hardening prior to ultimate collapse; the validity of such an approach requiring experimental investigation. Equations 5.11-5.14 will be used to analyse the results obtained from the polycarbonate and maraging

steel plate tests.

5.2.a.ii Energy Balance Approach

For the compact specimen it is possible to determine the strain energy, U and the complementary energy, U^* as functions of their derivatives with respect to crack length, $-\frac{1}{B}\left(\frac{\partial U}{\partial a}\right)_u$ and $\frac{1}{B}\left(\frac{\partial U^*}{\partial a}\right)_p$ by means of the simple model.

Under linear elastic loading conditions, the load-displacement relationship may be obtained from the dimensionless compliance expression of Adams and Munro (20):

$$\frac{EBu_{lp}}{P} = 2.2 + 1752\,[0.50\,\alpha^2 - 4.177\,\alpha^3 + 20.894\,\alpha^4 - 69.272\,\alpha^5 + 160.75\,\alpha^6 - 256.1\,\alpha^7 + 267.09\,\alpha^8 - 164.8\,\alpha^9 + 46.588\,\alpha^{10}] \quad 5.15$$

where u_{lp} refers to the total or load pin displacement for a well defined energy input and plane stress conditions are assumed throughout. The linear elastic load-displacement relationships are then made compatible with the simple lower bound solution for general yield, equation 5.9, by means of the transitional equation 5.8, with a gauge length, W arbitrarily selected for the best fit. The resultant load-displacement curves are shown in Fig. 5.4.

The improvement in the model resulting from the use of Adams and Munro's linear elastic analysis is apparent in Appendix 2, where the dimensionless compliance expressions corresponding to the elastic limit, equations 5.4 and 5.5, and to initial yield at the back of the specimen, equations 5.6 and 5.7, are compared with equation 5.15. At all relative crack lengths, $EBW\varepsilon_{el/P_{el}}$ and $EBW\varepsilon_{by/P_{by}}$ are almost identical but the

agreement with Adams and Munro's calibration is poor especially for a gauge length equal to the distance between the loading pins, 0.55 W. Selection of a gauge length, W does improve the fit at short crack lengths.

The dimensionless energies $\frac{U}{B}\left(\frac{E}{\sigma_y^2 W^2}\right)$ and $\frac{U^*}{B}\left(\frac{E}{\sigma_y^2 W^2}\right)$ may be obtained by integration of Fig. 5.4 and it is clear that in the presence of large plastic deformations, at loads approaching the limiting value, displacement-controlled tests are more relevant to actual practice than load-controlled tests. Taking derivatives with respect to α, the curves of Fig. 5.5 and 5.6 are obtained where the complementary energy curves extend over a smaller range of the load than the strain energy curves.

Originally Begley and Landes (21) and subsequently Neale and Townley (22) noted a linear relation between the strain energy and its derivative with respect to crack length for the compact specimen in the range $0.3 < \alpha < 0.8$. From Fig. 5.6 it is seen that this observation is in agreement with the derived results. On the basis of this linear relation it has been suggested (23) that, for a deeply cracked compact specimen, the function $-\frac{1}{B}\left(\frac{\partial U}{\partial a}\right)_u$ may be estimated from a single load-load line displacement record using the following equation:

$$-\frac{1}{B}\left(\frac{\partial U}{\partial a}\right)_u = \frac{2U_{11}}{(W-a)B} \qquad \alpha \geqslant 0.6 \qquad 5.16$$

where U_{11} denotes the total strain energy (elastic and plastic) due to the presence of the crack (see Appendix 3). R_i for crack initiation is then obtained from knowledge of the critical displacement.

However, such relationships still require direct experimental confirmation by comparison with results determined from experimental load-load pin displacement records. One of the aims of the polycarbonate and maraging steel plate tests will be to study such relationships experimentally.

5.2.b Cylindrical Model with Longitudinal Defects

Under linear elastic conditions the failure criteria based on energy coincide with the LEFM approach so that both methods give the same assessment of the severity of a defect in an elastic brittle material. Thus, from a knowledge of the appropriate LEFM geometrical shape factor, the dimensionless failure parameter, P^{ϕ} for a cylindrical model can be determined as a function of crack length; the relative crack length, α now being replaced by ρ defined as $c/\sqrt{DT/2}$ for a model of mean diameter D, wall thickness, T containing a longitudinal crack of length, 2c.

When plastic deformation occurs the problem becomes considerably more complex than for a model specimen and, while it is possible to find a limiting pressure for general yield, a satisfactory mathematical model for the calculation of the energy in the elastic-plastic region is not available. This means that for the moment the analysis is limited to LEFM at one extreme and to limit analysis at the other.

5.2.b.i Longitudinal Through-Thickness Defects

A longitudinal through-thickness defect in a cylindrical shell not only interrupts the hoop stress along its length causing the tensile force to be redistributed at its ends but also breaks the continuity of the cylinder such that the radial pressure tends to bulge the unsupported wall adjacent to the defect. The latter effect has no counterpart in a flat plate test but in a cylindrical shell bulging can raise the stress intensity in the vicinity of the crack tip to values considerably larger than the equivalent flat plate value.

The linear elastic analysis of cylindrical shells with longitudinal through-thickness cracks has been treated by Folias (24). He considered the bending and stretching of thin shallow[b] shells which could be described

---

[b] Folias defines a shell as shallow if the radius of curvature is one order of magnitude greater than the linear dimensions i.e. $4c/_D \leqslant 0.1$ and thin if $2T/_D \leqslant 0.1$.

by traditional two-dimensional linear theory and, after obtaining two coupled singular integral equations for the cylinder, gave asymptotic expressions for the stress intensity factors. These expressions were functions of the shell geometry through the parameter, λ $(= \sqrt[4]{12(1-\nu^2)}.\rho)$.

More recently, Erdogan and Kibler (25) improved the analysis by solving the integral equations numerically and they present stress intensity factors said to be valid up to $\lambda = 8$ for cylindrical shells. For a longitudinal through-thickness crack of length, 2c the solution takes the form:

$$\left.\begin{aligned} K &= \sigma_h (A_e + A_b) \sqrt{\pi c} \qquad \text{outer surface} \\ \text{and } K &= \sigma_h (A_e - A_b) \sqrt{\pi c} \qquad \text{inner surface} \end{aligned}\right\} \qquad 5.17$$

where σ_h is the hoop stress, $PD/_{2T}$ and A_e, A_b are the extensional and bending components of the stress intensity, respectively and are functions of the shell parameter, λ. A_e, A_b account for the stress amplification due to outward bulging of the crack edges by the internal pressure; this effect decreasing with decreasing crack length and increasing shell diameter and wall thickness until, in the limit as λ approaches zero, the flat plate solution is recovered.

At the mid-thickness, where the bending moment is zero, the above solution can be simplified to:

$$K = \sigma_h A_e \sqrt{\pi c} \qquad \text{mid-thickness} \qquad 5.18$$

Under such circumstances, the critical hoop stress at brittle failure normalized with respect to the uniaxial yield stress, σ_y is:

$$\frac{\sigma_h}{\sigma_y} = \frac{K_{Ic}}{\sigma_y A_e \sqrt{\pi c}} \qquad 5.19$$

i.e. a function of the material parameters, K_{Ic} and σ_y as well as the shell geometry, λ and the crack length, 2c. The form of this equation is represented in the generalised failure analysis diagram of Fig. 5.7 for $\nu = 0.33$.

In comparison with the linear elastic solution, a lower bound to the limit pressure for a thin cylindrical shell with a circular cutout is also shown. This limit analysis solution was determined by Goodall (26) using a circumscribing yield surface and takes the form:

$$\frac{\sigma_h}{\sigma_y} = \text{fn } (\rho) \qquad 5.20$$

Several lower bounds are available including Kitching, Davis and Gill's (27) solution for cylinders containing various shapes of unreinforced hole. However, the latters' expressions considerably underestimate experimental results obtained from thin cylindrical pressure vessels with circular cut-outs (28) and with unreinforced openings of various shapes (27); on the other hand, Goodall's analysis provides an excellent lower bound.

From Fig. 5.7 it is apparent that a reduction in the plane strain fracture toughness or an increase in the uniaxial yield stress or crack length increases the probability of brittle fracture especially for large diameter, thick-walled cylinders. However, no consideration is given to finite boundary effects nor to the restraining effects of cylindrical end caps.

As for the case of the compact specimen, some degree of work-hardening may be accounted for by basing the lower bound solution on the ultimate tensile strength of the material i.e. a hoop stress corresponding to ultimate collapse is defined such that:

$$\frac{\sigma_h}{\sigma_u} = \text{fn } (\rho) \qquad 5.21$$

$$(= 1 \quad \text{when } \rho = 0)$$

A dimensionless failure parameter, P^{ϕ} may then be defined for a thin cylindrical shell by normalising the hoop stress with respect to the hoop stress corresponding to ultimate collapse of an uncracked cylinder:

$$P^{\phi} = \frac{\sigma_h}{\sigma_u} \qquad 5.22$$

$$\text{and} \quad P^{\phi}_{Ic} = \frac{K_{Ic}}{\sigma_u A_e \sqrt{\pi c}} \qquad 5.23$$

$$P^{\phi}_{gy} = \frac{\sigma_y}{\sigma_u} \cdot fn(\rho) \qquad 5.24$$

$$P^{\phi}_{u} = fn(\rho) \qquad 5.25$$

Equations 5.22 - 5.25 will be used to analyse results from the polycarbonate cylindrical models with through-thickness defects.

5.2.b.ii Longitudinal Part-Through-Thickness Defects

A longitudinal part-through-thickness defect in a cylindrical shell interrupts the hoop stress along its length in proportion to its depth and also produces outward bulging, although to a much lesser extent than through-thickness defects of the same length. Under such circumstances, failure occurs either by crack extension through the wall to produce a through-thickness defect or by general yield across the remaining ligament.

The most elementary part-through defect is that of infinite length and Emery and Segedin (29) have studied the case of an infinitely long external radial edge crack in a tube with a uniform internal pressure. Using a relaxation method they calculated the stress intensity factors for various ratios of internal to external radii up to a relative crack depth, $d/_T$ of 0.6.

For short part-through defects the situation is much more complex since the influence of the crack shape on the stress field must be taken into account. The majority of studies of part-through defects have been on surface-flawed tension plates for which the stress intensity factor is of the general form:

$$K = k \sigma \sqrt{\pi d} \qquad 5.26$$

where σ is the nominal applied stress, d is the crack depth and k is the stress intensity coefficient which depends upon the flaw shape, the finite boundaries of the front and back free surfaces and, in certain cases, the crack front position at which K is calculated. In particular, solutions for k have been obtained for the semi-elliptical (30)-(32) and part-circular (33) surface flaw as functions of the aspect ratio, $d/_c$, the relative crack depth, $d/_T$ and crack front position. Rice and Levy (34) also determined k for a semi-elliptical surface flaw in a plate subject to combined tension and bending; however, since the solution does not account for the strong influence of the back free surface, it is only applicable for $d/_T < 0.7$ and is not considered further.

The application of such values to cylindrical models has been studied experimentally by Derby (35), testing eleven thick-walled ($2T/_D = 0.2$) epoxy cylinders with longitudinal part-through cracks in the outer wall. Taking σ as the hoop stress, experimentally determined shape factors were compared with theoretical estimates based on the Irwin (30), Paris-Sih (31) and Kobayashi-Moss (32) equations for k at the maximum depth of a semi-elliptical surface flaw. Although no crack failed at the exact middle, Derby found that within the range $0.36 < d/_T < 0.88$ experimentally determined values of k were within 10% of those predicted by the Paris-Sih equation; the Irwin and Kobayashi-Moss values showing good agreement only for cracks approximately half as deep as the model wall.

The Paris-Sih expression for the stress intensity factor at the end of the semi-minor axis of a semi-elliptical surface flaw is:

$$K = \frac{\left[1 + 0.12\ (1-{}^{d}/_{c})\right]\left[\frac{2T}{\pi d}.\ \tan\ ({}^{\pi d}/_{2T})\right]^{1/2}\sigma\sqrt{\pi d}}{\Phi_o} \qquad 5.27$$

where the first and second terms are the front and back free surface magnification factors, respectively and Φ_o is an elliptical integral:

$$\Phi_o = \int_0^{\frac{\pi}{2}} \left[1 - \left(\frac{c^2-d^2}{c^2} \right) . \sin^2 \theta \right]^{1/2} d\theta \qquad 5.28$$

Thus, on the basis of Derby's results, the critical hoop stress at brittle failure of a cylindrical model with a longitudinal part-through defect normalised with respect to the uniaxial yield stress, σ_y may be given by:

$$\frac{\sigma_h}{\sigma_y} = \frac{K_{Ic}}{\sigma_y \sqrt{\pi d}} \frac{\Phi_o}{\left[1 + 0.12 \left(1-d/c\right) \right] \left[2T/\pi d . \tan \left(\pi d/2T\right) \right]^{1/2}} \qquad 5.29$$

i.e. it is a function of the material parameters, K_{Ic} and σ_y as well as the geometrical parameters, d/c, d/T and the crack depth, d. The form of this equation is represented in the generalised failure analysis diagram of Fig. 5.8 where it can be seen that σ_h/σ_y is not particularly sensitive to the aspect ratio, d/c but is extremely sensitive to the presence of the back free surface.

Fully plastic analyses of cylindrical shells with longitudinal part-through defects are extremely limited. Infinitely long part-through flaws are normally assumed to increase the average hoop stress across the remaining ligament in proportion to the ligament ratio so that, on the basis of Tresca's yield criterion, general yield occurs when:

$$\frac{\sigma_h}{\sigma_y} = (1 - d/T) \qquad 5.30$$

An upper bound plane strain slip line field solution (36), which is a generalisation of Green's field for the pure bending of a flat notched plate, has been obtained for an infinitely long external part-through notch of zero root radius for various ratios of wall thickness to internal radius and for notch flank angles between 60^o and 90^o. These results indicate that once the curvature and the bending moment caused by the internal pressure are taken into account, the hoop stress at general yield

is considerably lower than that predicted by equation 5.30 for intermediate and large values of d/T, although the curvature has a secondary effect for thin shells when $2T/D \leqslant 0.1$. However, neither solution accounts for the biaxial stress state in the remaining ligament which should considerably raise the general yield pressure.

In comparison, the yielding characteristics of a short part-through defect will be very different due to the constraining influence at the ends of the flaw where it meets the surface of the cylinder. A simple limit analysis of a cylindrical shell with a longitudinal part-through notch of finite length has been performed (37); being based on a limited interaction criterion in which the onset of yielding corresponds to the formation of yield hinges at the centre and ends of the notch when the average hoop stress across the reduced notch section equals the uniaxial yield stress. The resultant equation is:

$$\frac{\sigma_h}{\sigma_y} = \frac{1 + \rho^2 \ (1-d/T)}{0.5 + \rho^2} \qquad 5.31$$

In spite of considerable scatter, Ruiz (37) obtained reasonable agreement between experimental failure pressures for widespread yielding taken from the literature and theoretical estimates based on equation 5.31, after introducing the Dugdale plasticity correction factor to the notch length. It was argued that, for short notch lengths, the position of the yield hinges would not coincide with the ends of the notch but would lie at a distance $(c_{mod.} - c)$ ahead of these such that:

$$c_{mod.} = \frac{c}{\cos \frac{\pi}{2} \left(\frac{\sigma_h}{\sigma_y} \right)_{mod.}} \qquad 5.32$$

The modified form of equation 5.31 is then:

$$\rho^2 = \frac{\left[1 - 0.5\left(\frac{\sigma_h}{\sigma_y}\right)_{mod.}\right]\left[\cos\frac{\pi}{2}\left(\frac{\sigma_h}{\sigma_y}\right)_{mod.}\right]^2}{\left[\left(\frac{\sigma_h}{\sigma_y}\right)_{mod.} - (1 - d/T)\right]} \qquad 5.33$$

Comparison of equations 5.31 and 5.33 indicates that the plasticity correction factor modifies the latter such that $(\sigma h/\sigma_y)_{mod.}$ approaches unity as ρ tends to zero; at large ρ, however, it has little effect as $\sigma h/\sigma_y$ and $(\sigma h/\sigma_y)_{mod.}$ approach the same value.

The modified equation 5.33 is shown in the generalised failure analysis diagram of Fig. 5.8 where it is apparent that $\sigma h/\sigma_y$ is extremely sensitive to notch length and curvature at intermediate and large values of d/T. Comparison of the limit analysis and LEFM solutions indicates that a reduction in the plane strain fracture toughness or an increase in the uniaxial yield stress or crack depth for a particular defect length and curvature, increases the probability of brittle fracture especially for thick-walled cylinders.

By analogy with the case for a longitudinal through-thickness defect, a hoop stress corresponding to ultimate collapse may be defined such that:

$$\left(\frac{\sigma_h}{\sigma_u}\right)_{mod.} = \frac{1 + \rho^2_{mod.}\,(1 - d/T)}{0.5 + \rho^2_{mod.}} \qquad 5.34$$

where the lower bound solution for a longitudinal part-through defect is now based on the ultimate tensile strength of the material to allow for a certain amount of work-hardening. Since $(\sigma h/\sigma_u)_{mod.} = 1$ when $\rho_{mod.} = 0$, the dimensionless failure parameters for a cylindrical shell with a longitudinal part-through defect are:

$$P^{\phi}_{Ic} = \frac{K_{Ic}}{\sigma_u\sqrt{\pi d}}\,\frac{\Phi_o}{\left[1 + 0.12\,(1-d/c)\right]\left[2T/\pi d \cdot \tan(\pi d/2T)\right]^{1/2}} \qquad 5.35$$

$$P_{gy}^{\phi} = \frac{\sigma_y}{\sigma_u} \cdot \frac{[\,1 + \rho^2_{mod.}\,(1 - d/T)\,]}{[\,0.5 + \rho^2_{mod.}\,]} \qquad 5.36$$

$$P_{u}^{\phi} = \frac{[\,1 + \rho^2_{mod.}\,(1 - d/T)\,]}{[\,0.5 + \rho^2_{mod.}\,]} \qquad 5.37$$

Equations 5.35-5.37 will be used in the analysis of the polycarbonate cylinder results for part-through defects.

5.3 Experimental Programme

Chapters 6, 7 and 8 describe experiments performed on model compact specimens of polycarbonate, compact specimens of maraging steel and model cylindrical vessels of polycarbonate with longitudinal defects, respectively.

In the first series of tests, 85 mm wide, 5 mm thick plates of as-received polycarbonate ($0.013 \leqslant \alpha_o \leqslant 0.810$) are statically loaded at room temperature under displacement-controlled conditions. R_{stable} corresponding to finite stable crack extension is determined using the general energy balance equation 4.4 and R_i for crack initiation is obtained by evaluation of the calibration function, $-\frac{1}{B}\left(\frac{\partial U}{\partial a}\right)_u$ using the method developed by Begley and Landes (38). The failure analysis diagram (1) is used to interpret variations in fracture behaviour.

For comparison with the model material polycarbonate, 51 mm wide standard compact specimens of 18% Ni heat treated maraging steel are monotonically loaded at room temperature under displacement-controlled conditions. The influence of through-thickness constraint on the fracture toughness of the steel is investigated using plates of varying thickness (3.1 mm, 6.3 mm, 12.7 mm and 25.4 mm) in addition to initial crack length ($0.386 \leqslant \bar{\alpha}_o \leqslant 0.766$ for the 3.1 mm thick specimens). Landes and Begley's approximate method for a deeply cracked compact specimen, equation 5.16 (23) is used to measure the fracture toughness, R_i for crack initiation. However, for the 3.1 mm thick specimens, R_i is also determined by evaluation of the calibration function,

$-\frac{1}{B}\left(\frac{\partial U}{\partial a}\right)_u$ using the method developed by Begley and Landes (38). Conservative estimates of the more general fracture toughness parameter, R are also obtained for the thinnest specimens. Finally, the overall crack growth behaviour is interpreted by means of the failure analysis diagram and various ancillary studies (scanning electron microscopy, surface deformation measurements) are also performed to complement the experimental results.

In the final experiments, a study is made of the crack growth behaviour of longitudinal through-thickness ($0.704 \leqslant \rho_o \leqslant 1.434$) and deep part-through-thickness cracks ($^d/_T$ = 0.700 and 0.878) in 50.8 mm and 102 mm diameter polycarbonate cylinders (5 mm and 6 mm wall thickness). These model vessels are pressurised hydraulically with water to maintain stable crack growth and the crack extension monitored as a function of pressure. Again, the results are interpreted with the aid of the failure analysis diagram.

References

(1) A.R. Dowling and C.H.A. Townley, Int. J. Pres. Ves. and Piping, 3, p. 77, 1975.

(2) "Methods for Plane Strain Fracture Toughness (K_{Ic}) of Metallic Materials," B.S. 5447: 1977, B.S.I., London.

(3) "Plane Strain Fracture Toughness of Metallic Materials," A.S.T.M. E399-72 Part 31, 1972.

(4) P.B. Crosley and E.J. Ripling, Nuclear Eng. and Design, 17, p. 32, 1971.

(5) P.L. Key and Y. Katz, Int. J. of Fract. Mechs., 5, p. 63, 1969.

(6) H.F. Brinson, Expt. Mechs., 10, p. 72, 1970.

(7) P.S. Theocaris, Int. J. of Mech. Sci., 18, p. 171, 1976.

(8) N.J. Mills, Eng. Fract. Mechs., 6, p. 537, 1974.

(9) P.S. Theocaris and E.E. Gdoutos, Expt. Mechs., 15, p. 169, 1975.

(10) D.Hull and T.W. Owen, J. Polymer Sci. Phys., 11, p. 2039, 1973.

(11) F.A. Johnson, A.P. Glover and J.C. Radon, Proc. 1973 Symp. on Mech. Behaviour of Materials, The Society of Materials Science, Japan, p. 141, 1974.

(12) M. Parvin and J.G. Williams, Int. J. of Fracture, 11, p. 963, 1975.

(13) N.J. Mills, J. Mats. Sc., 11, p. 363, 1976.

(14) E. Roberts, Jr., Materials Research and Stds., MTRSA, 9, No. 2, p. 27, 1969.

(15) W.K. Wilson, Eng. Fract. Mechs., 2, p. 169, 1970.

(16) J.E. Srawley and B. Gross, Eng. Fract. Mechs., 4, p. 587, 1972.

(17) J.C. Newman, Jr., A.S.T.M. S.T.P. 560," Fracture Analysis," Am. Soc. for Testing and Materials, p. 105, 1974.

(18) J.E. Srawley, Int. J. of Fracture, 12, p. 455, 1976.

(19) M. Shiratori and B. Dodd, O.U.E.L. Report No. 1207, 1977.

(20) N.J.I. Adams and H.G. Munro, Eng. Fract. Mechs., 6, p. 119, 1974.

(21) J.A. Begley and J.D. Landes, A.S.T.M. S.T.P. 536, "Progress in Flaw Growth and Fracture Toughness Testing," Am. Soc. for Testing and Materials, p. 246, 1973.

(22) B.K. Neale and C.H.A. Townley, C.E.G.B. Report No. RD/B/N3358, May 1975.

(23) J.D. Landes and J.A. Begley, A.S.T.M. S.T.P. 560, "Fracture Analysis," Am. Soc. for Testing and Materials, p. 170, 1974.

(24) E.S. Folias, Int. J. of Fract. Mechs., 1, p. 20, 1965.

(25) F.Erdogan and J.J. Kibler, Int. J. of Fract. Mechs., 5, p. 229, 1969.

(26) I.W. Goodall, "On the Design of Intersections in Pressure Vessels," Ph.D. dissertation, Univ. of Cambridge, 1967.

(27) R. Kitching, J.K. Davis and S.S. Gill, J. Mech. Eng. Sc., 12, p. 313, 1970.

(28) C.R. Calladine and I.W. Goodall, J. Mech. Eng. Sc., 11, p. 351, 1969.

(29) A.F. Emery and C.M. Segedin, J. Basic Eng., Series D, 94, p. 387, 1972.

(30) G.R. Irwin, J. Appl. Mech., 29, p. 651, 1962.

(31) P.C. Paris and G.C. Sih, A.S.T.M. S.T.P. 381, "Fracture Toughness Testing and its Applications," Am. Soc. for Testing and Materials, p. 30, 1965.

(32) A.S. Kobayashi and W.L. Moss, Proc. 2nd Int. Conf. Fracture, Brighton, p. 31, 1969.

(33) F.W. Smith and M.J. Alavi, Proc. 1st Int. Conf. Pres. Ves. Tech., Delft, paper II-69, 1969.

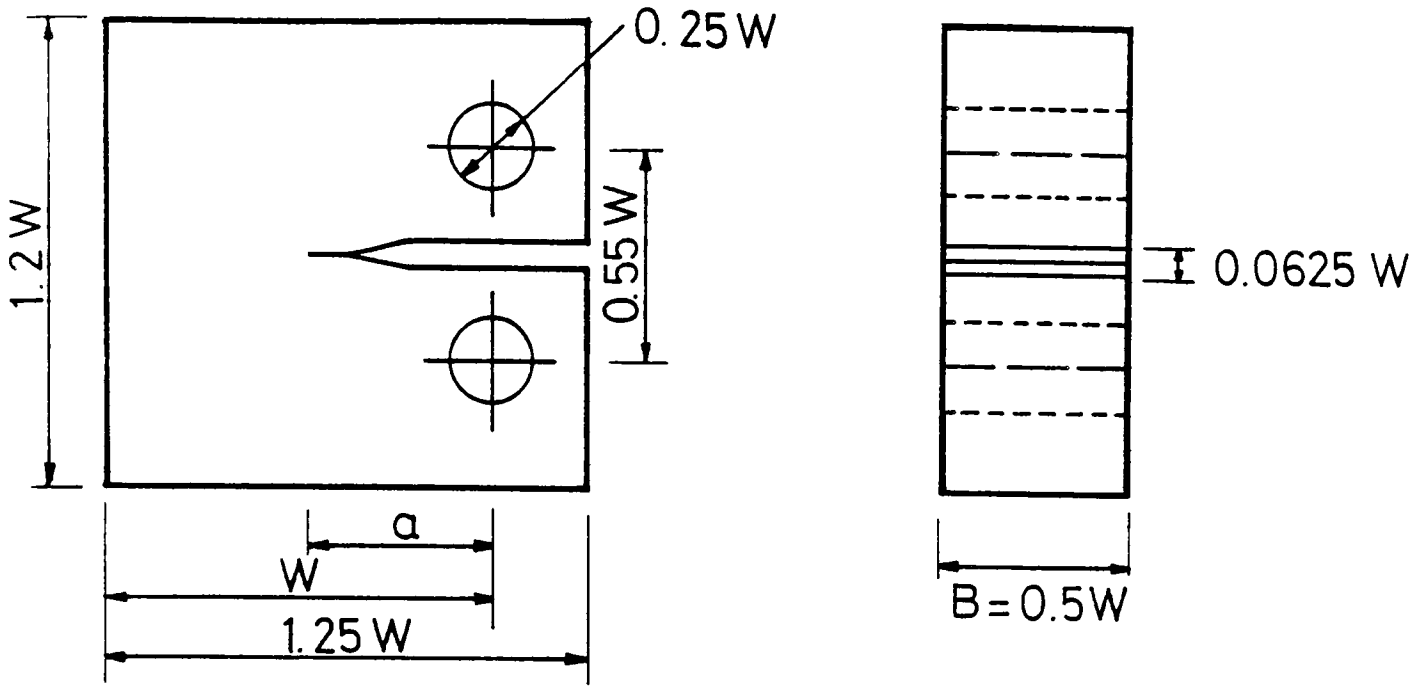
(34) J.R. Rice and N. Levy, J. Appl. Mechs., 39, p. 185, 1972.

(35) R.W. Derby, A.S.T.M. S.T.P. 536, "Progress in Flaw Growth and Fracture Toughness Testing," Am. Soc. for Testing and Materials, p. 482, 1973.

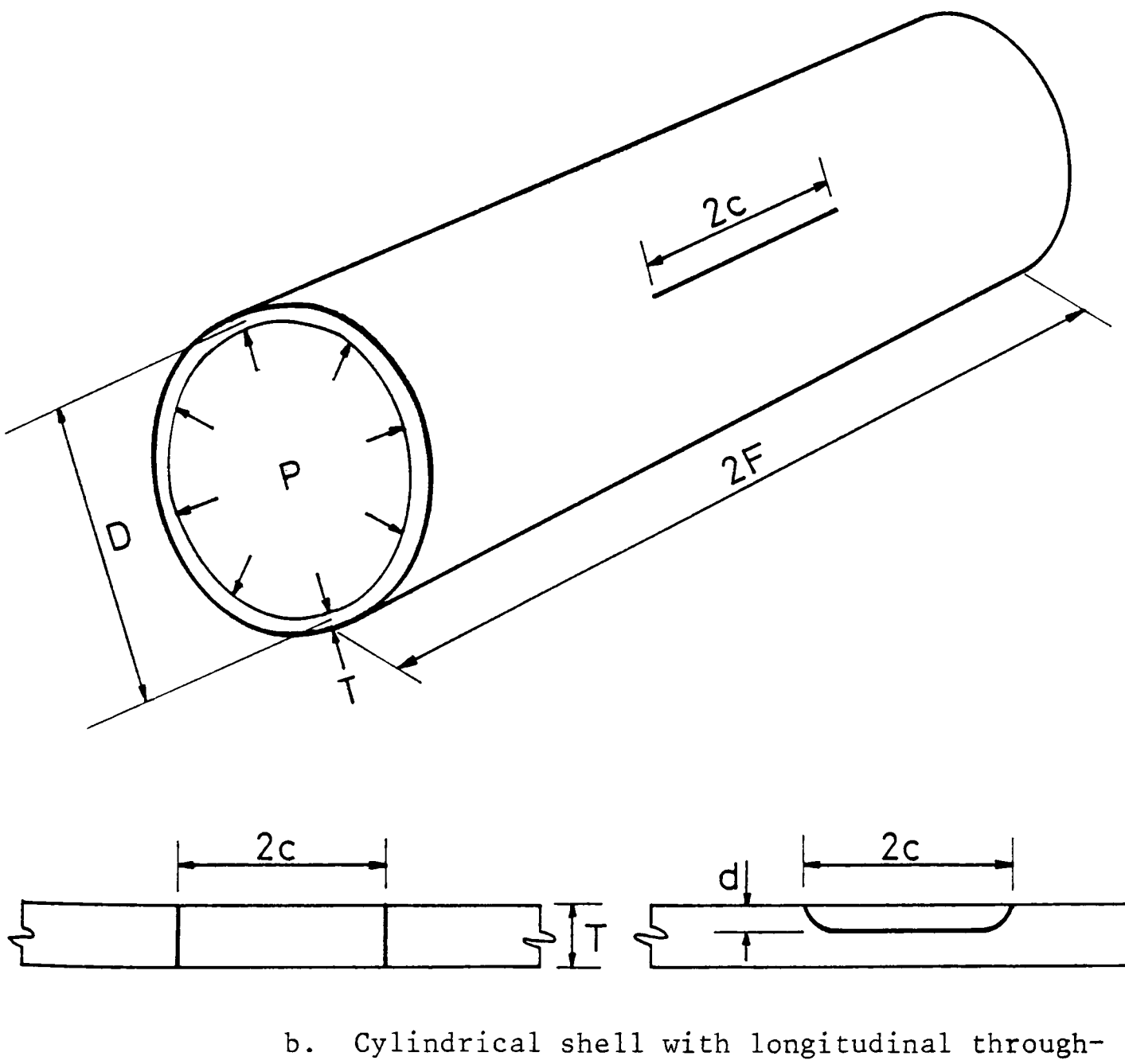
(36) B. Dodd, M. Shiratori and C. Ruiz, O.U.E.L. Report No. 1199, 1977.

(37) C. Ruiz, O.U.E.L. Report No. 1200, 1977, to be published in Int. J. of Mech. Sci.

(38) J.A. Begley and J.D. Landes, A.S.T.M. S.T.P. 514, "Fracture Toughness," Am. Soc. for Testing and Materials, p. 1, 1972.



a. Standard compact specimen



b. Cylindrical shell with longitudinal through-thickness and part-through-thickness cracks

Fig. 5.1 Model configurations

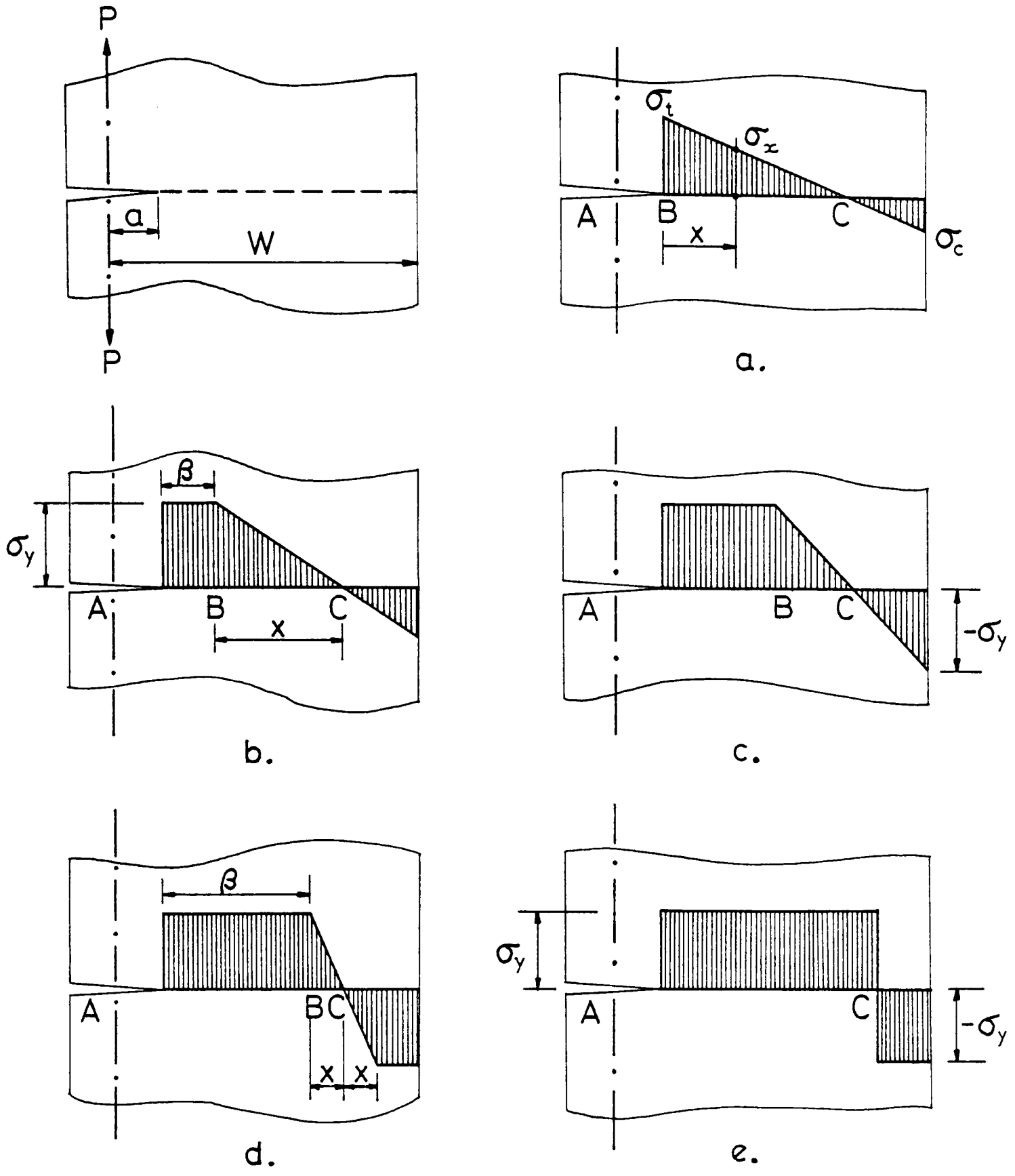


Fig. 5.2 Successive stages in the yielding of a compact specimen

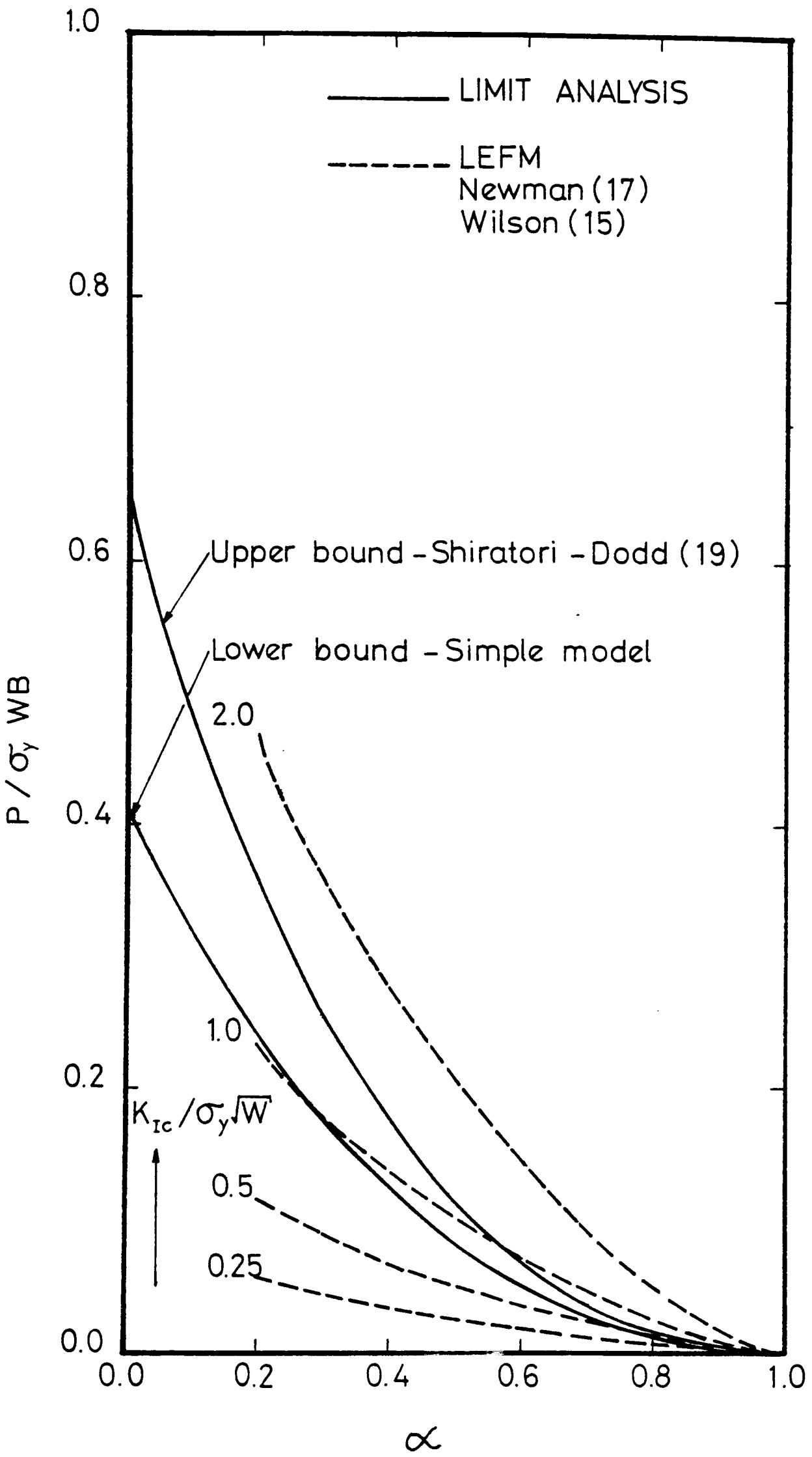


Fig. 5.3 Generalised failure analysis diagram for the standard compact specimen

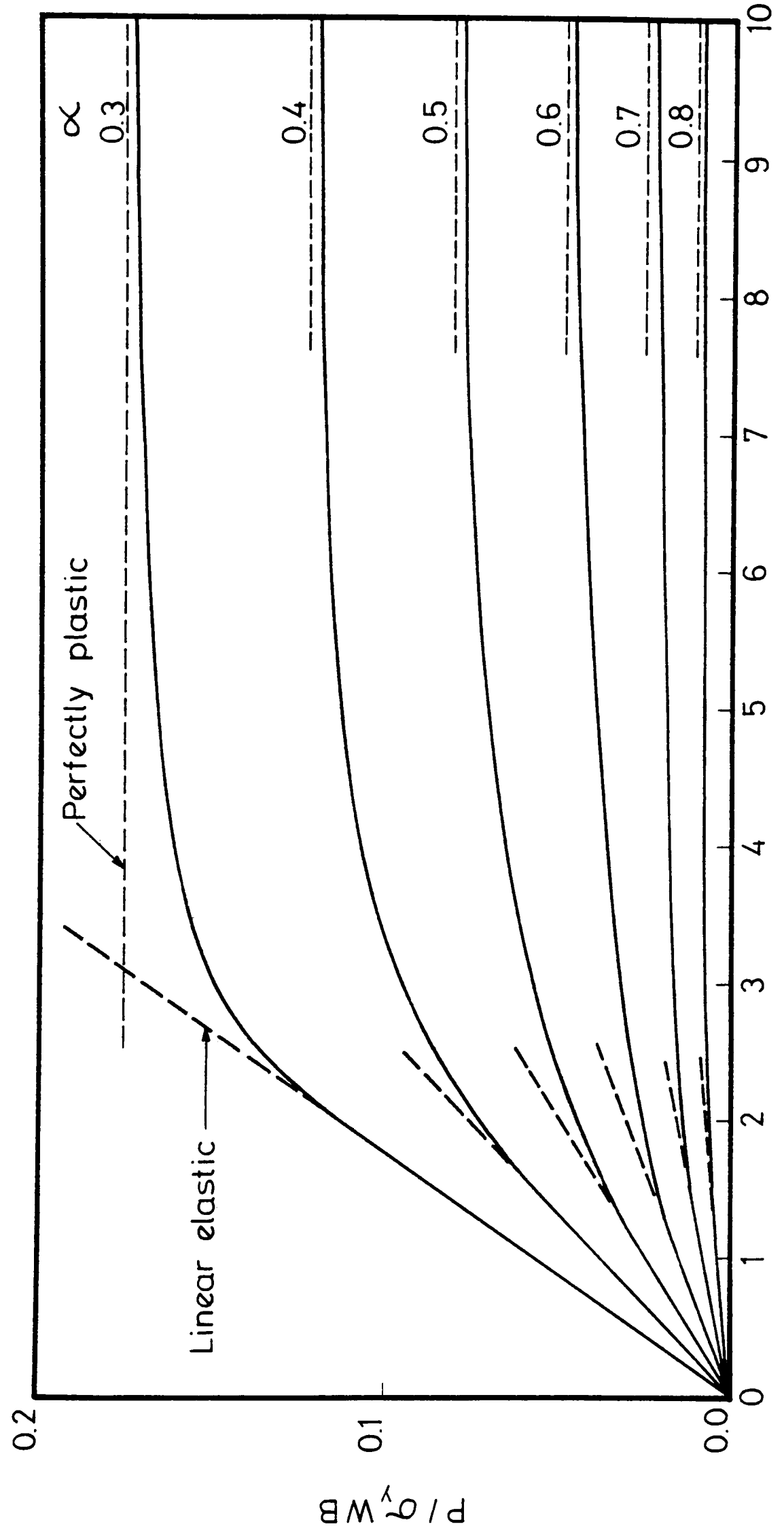


Fig. 5.4 Generalised load-displacement curves for the standard compact specimen

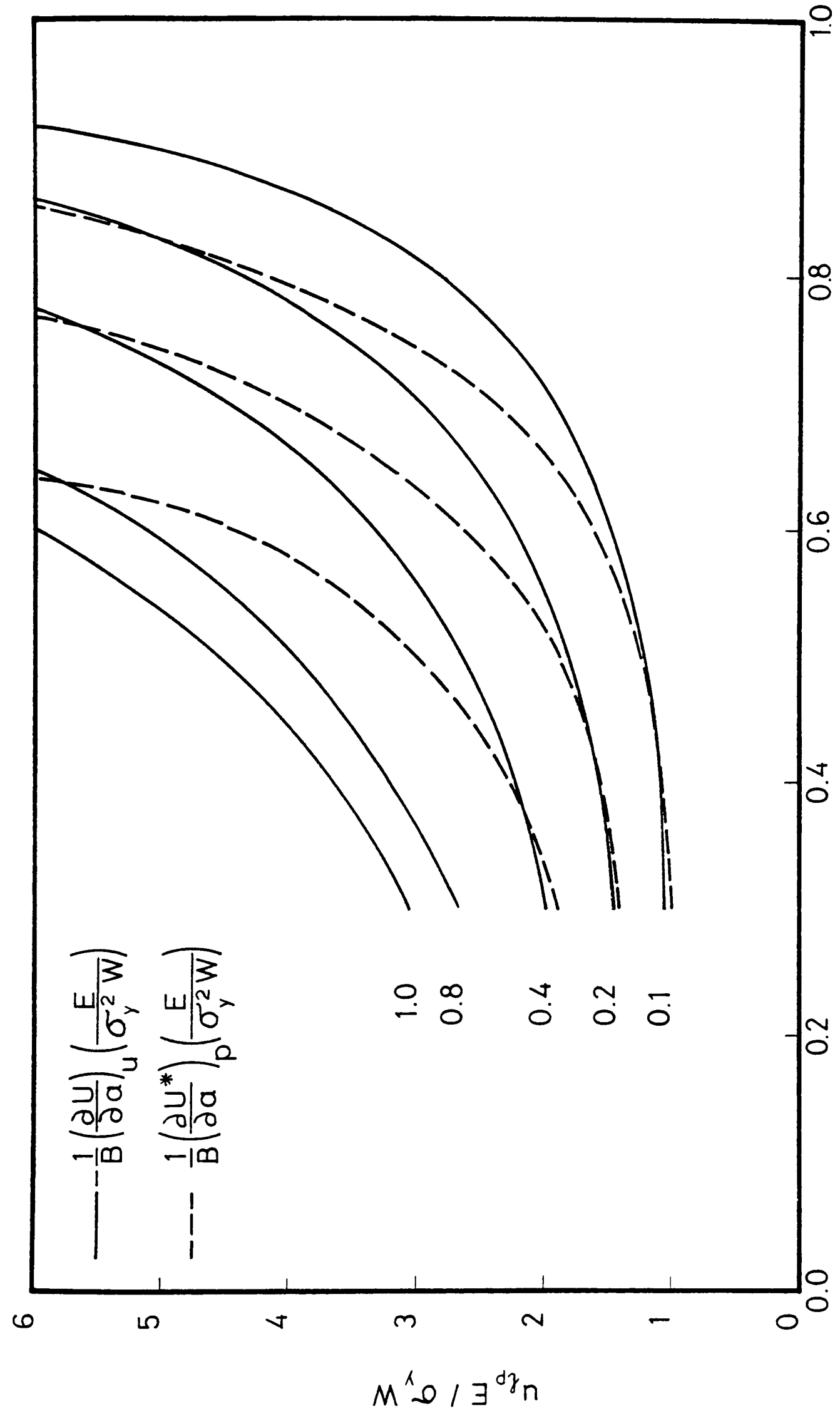


Fig. 5.5 Curves of dimensionless energy slope versus dimensionless displacement for the standard compact specimen

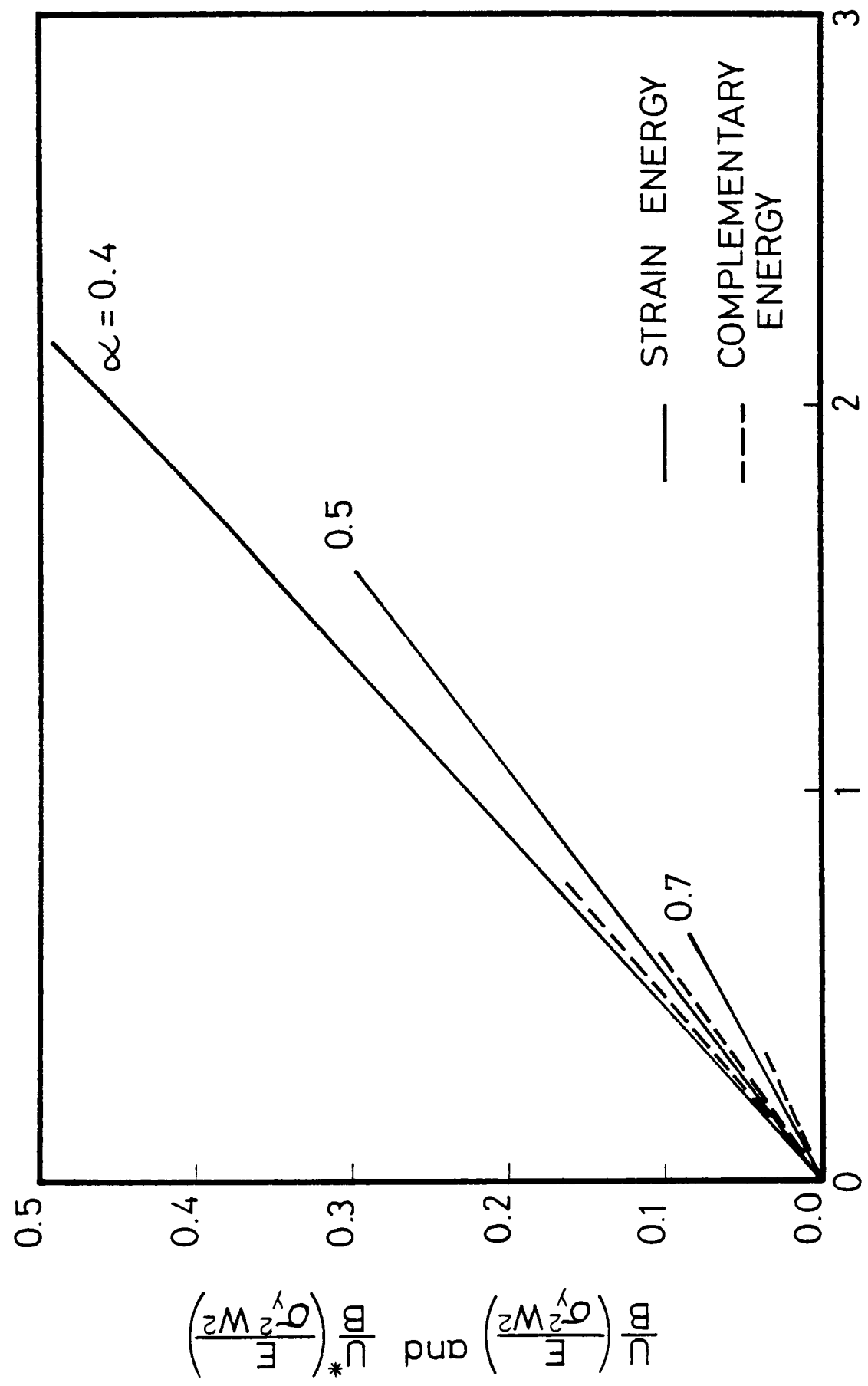


Fig. 5.6 Curves of dimensionless energy versus dimensionless energy slope for the standard compact specimen

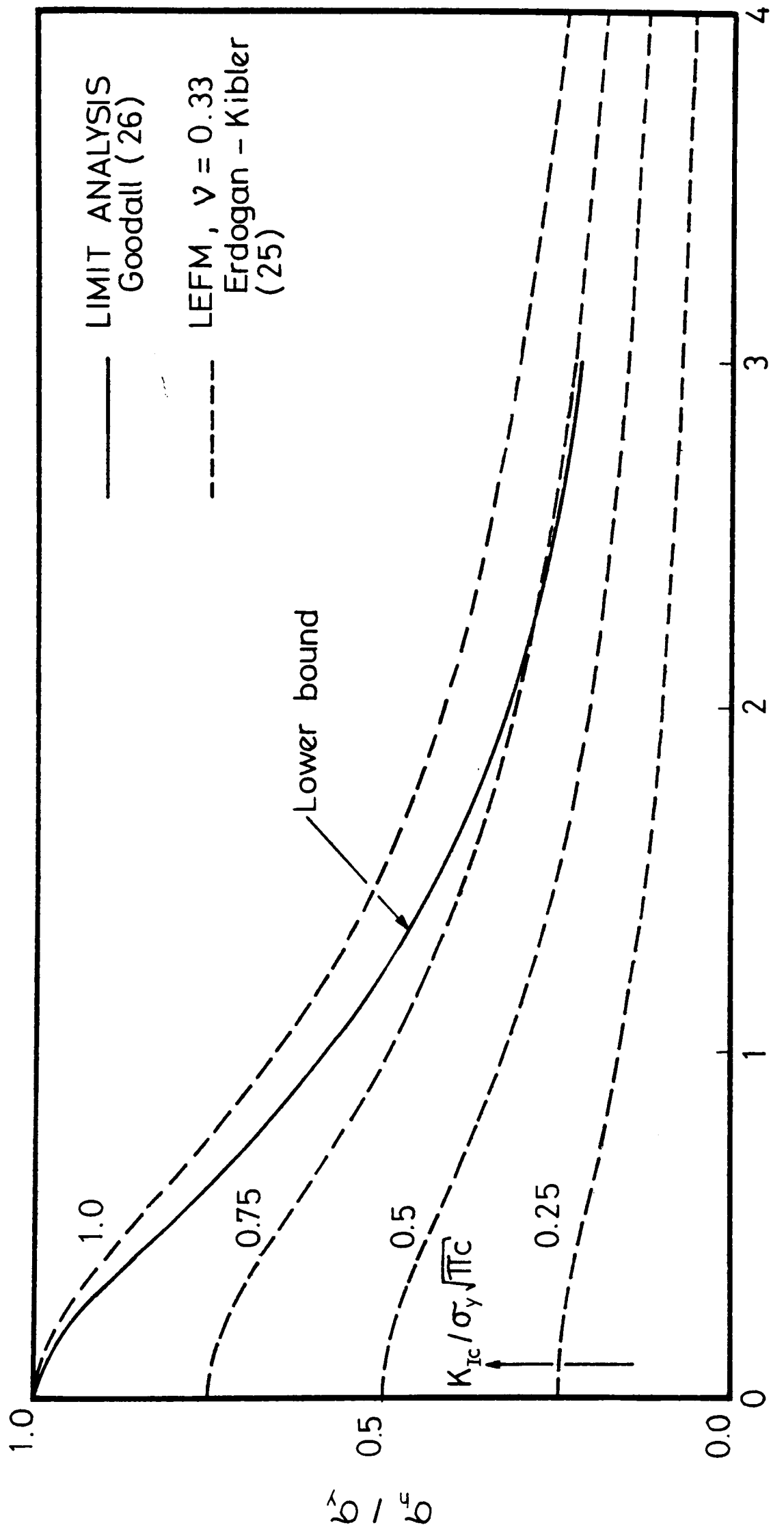


Fig. 5.7 Generalised failure analysis diagram for cylindrical shells with longitudinal through-thickness defects

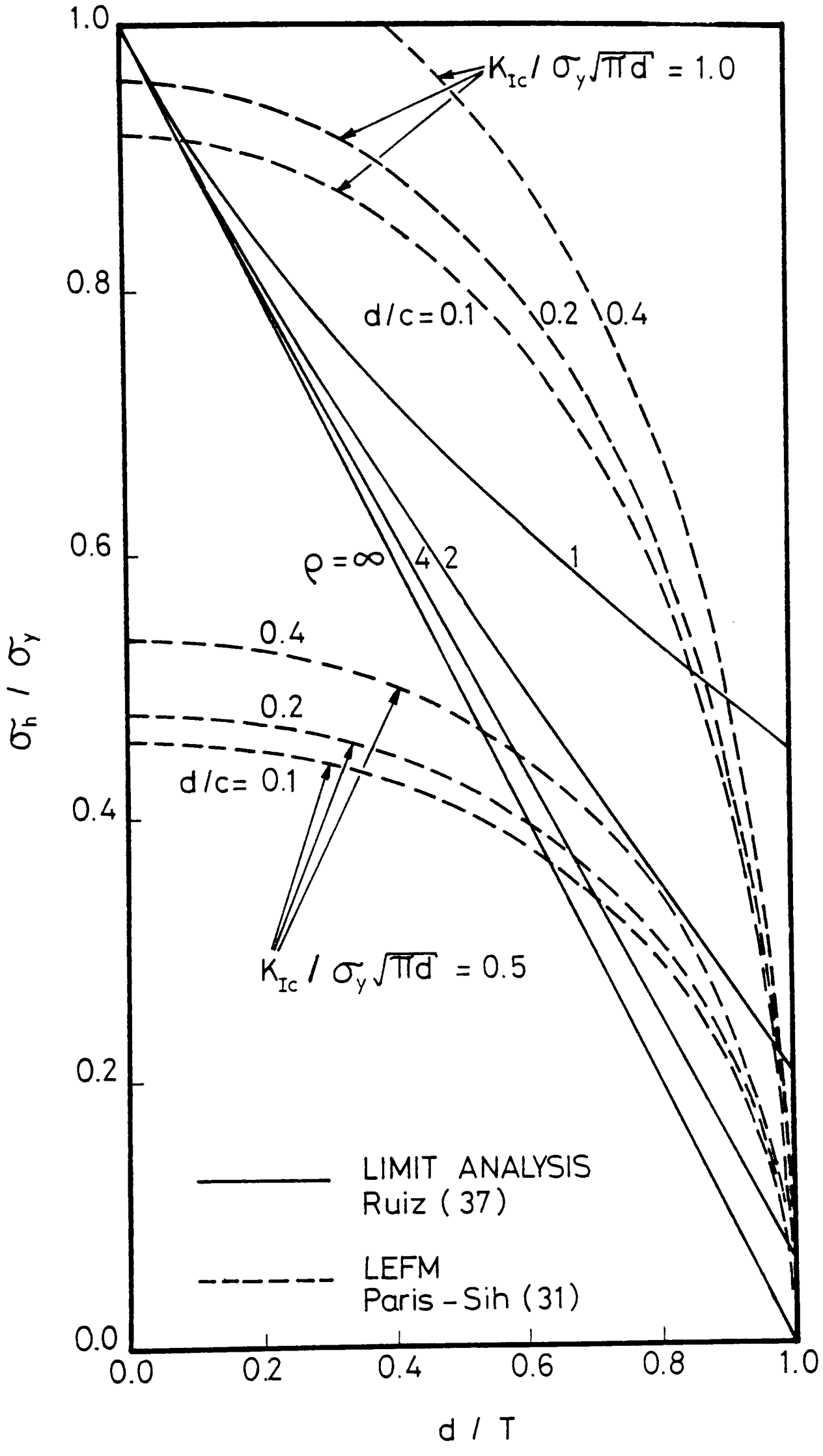


Fig. 5.8 Generalised failure analysis diagram for cylindrical shells with longitudinal part-through-thickness defects

CHAPTER 6

CRACK GROWTH IN MODEL PLATES OF POLYCARBONATE

The Bayer "Makrolon" polycarbonate was supplied in the form of 5 mm thickness transparent sheet made from the high molecular weight 3203 grade by an extrusion process. The material specifications are listed in Table 6.1.

6.1 Material Characterisation

In order to determine the mechanical properties of the as-received material four enlarged end uniaxial tensile specimens were machined with a cross-sectional area of 15 x 5 mm^2, a parallel length of 40 mm and a minimum shoulder radius of 15 mm. Two specimens were cut in each of the two principal sheet directions to check for any residual orientation as a result of the extrusion process. The specimens were tested at room temperature in an Instron universal testing machine at a crosshead speed of 0.5 in. min^{-1}, corresponding to a nominal strain rate, $\dot{\varepsilon}_{nom}$ of 2.3 x 10^{-3} sec^{-1}, and the crosshead displacement recorded as a function of the applied load. In one case a 25.4 mm gauge length extensometer (0-50% strain) was attached to the specimen and the true extension monitored up to the onset of necking. The resultant true stress-true strain curve is shown in Fig. 6.1.

The polycarbonate exhibited an unusual tensile instability. After an initial region of linear and non-linear behaviour up to 6% strain, a highly localised neck formed across the specimen width at approximately 55^{o} to the tensile direction accompanied by a 25% drop in the applied load. This necked region was entirely stable and propagated along the specimen length under constant load, the angle of the neck changing rapidly from 55^{o} to perpendicular to the tensile direction. The overall elongation of the

specimen during the expansion of the neck was approximately 80% of the initial parallel length. Failure eventually occurred after the necked region had expanded all over and the material strain-hardened until small cracks or crazes appeared at the surface and propagated catastrophically across the reduced section at about 95% strain.

Plastic yielding is conventionally defined as the onset of permanent or irrecoverable deformation. However, this is much more difficult to define in time-dependent polymeric materials where recovery processes may be more significant than in crystalline solids such as metals where plastic recovery occurs infrequently. Various criteria have been used to define a yield point for polymers and these include the proportional limit, the 1% proof stress, the maximum true stress (intrinsic yield point) and the maximum engineering stress (extrinsic yield point); the extrinsic yield point approaching the intrinsic yield point when the rate at which the tensile instability develops is slow.

In the literature it has generally been accepted that the yield point for polycarbonate corresponds to the initiation of necking in the specimen and the similarity of the tensile instability to a Lüders band instability in mild steel is frequently mentioned in support of this. Thus, both instabilities consist of an inclined neck on planes at 55^{o} to the tensile direction, planes for which one component of the strain is zero and yield can occur without constraint from the surrounding medium (1).

However, for mild steel the Lüders strain represents only a small non-uniform strain perturbation of 2-3% compared with a region of large uniform plastic deformation which follows up to 20-30% strain. This is in contrast to polycarbonate where at the onset of necking the remaining material outside the neck relaxes elastically (2) and further deformation is accomplished by successive zones of material being inserted into the necking zone as it propagates along the specimen; the region of non-uniform strain

extending up to 80% of the total deformation of the material. In this case the real uniform plastic deformation occurs only over a relatively small region up to 6-7% strain. Therefore, the true stress-true strain curve of Fig. 6.1 should provide an adequate description of the uniform elastic-plastic deformation of polycarbonate for the purposes of modelling the elastic-plastic behaviour of metals.

A summary of the room temperature properties to be used for the as-received material are listed in Table 6.2. The uniaxial yield stress was arbitrarily defined as the engineering stress where the $\frac{d\sigma}{d\varepsilon} = fn(\varepsilon)$ curve presents an inflection point (3) and the ultimate tensile strength as the maximum engineering stress (extrinsic yield point); such definitions being compatible with those used for metals and encompassing the major part of the non-linear region of the stress-strain curve. The precision in the specimen dimensions was $\pm$ 0.03 mm giving a total estimated error in the engineering stress of 1.3%. Thus, comparison of the ultimate tensile strength of the sheet measured in the x and y directions indicates that the polycarbonate was reasonably isotropic since the variation, 0.5% was less than the experimental uncertainty of the measurements.

No attempt was made to define a true strain-hardening exponent, n since the polycarbonate did not conform to the standard parabolic relationship, $\sigma = C\varepsilon^n$ where C is a constant. However, the true strain at plastic instability, 0.067 may be considered as a nominal strain-hardening exponent valid in the region of 6.7% strain.

6.2 Experimental Procedure

Plate tests were performed on compact specimens of as-received polycarbonate at room temperature, 295 $\pm$ 2^{o}K and about 45% relative humidity $\pm$ 5%. Each specimen was machined to the dimensions shown in Fig. 6.2, a 1.59 mm wide notch machined and a line scribed along the axis of symmetry on each side of the specimen to guide the crack. Prior to testing a starter crack

was introduced at the end of the notch with a 0.10 mm thick razor blade, a fresh part of the blade being used for each specimen to produce a planar crack front.

A list of all specimens tested is given in Table 6.3. In addition, to prevent adventitious yielding at the loading holes during testing, it was necessary to reinforce specimens 2P-4P by means of 0.65 mm thick slices (25.4 mm external diameter) of polycarbonate; these were bonded each side of the plates at the loading holes with dichloroethane solvent, increasing the effective plate thickness in that area to 6.25 mm and the nominal loading capacity to 3,970N. Specimens 3P and 4P, tested to 4340N, were carefully inspected afterwards but showed no signs of permanent deformation in regions other than the crack tip.

A photograph of the experimental set-up is shown in Fig. 6.3, the apparatus being positioned between the crosshead and a "D" tensile load cell (1,000 lb. capacity) in an Instron testing machine. The presence of the two steel clamping plates was necessary to prevent lateral buckling of the polycarbonate during loading, however these were lined with perspex to minimise any frictional constraint and to allow free movement of the specimens during testing. The central section of each steel plate was cut away for observation of the crack front through the perspex.

It was anticipated that the low elastic modulus and large displacements of polycarbonate would ensure that the load versus crosshead displacement record represented a well defined energy input which could be used directly in the evaluation of the energy parameter, R. However, to check this a compliance calibration was performed using specimen 1P. Previously, it had been ascertained that the compliance of the machine and linkages became negligible at loads greater than 89N so that specimen 1P was loaded at a crosshead speed of 0.5 in. min^{-1} to between 133N and 445N and the compliance measured from the slope of the load-crosshead displacement record. Specimen 1P was notched, the notch length being successively

increased after each test. The resultant dimensionless compliance calibration, Fig. 6.4, is in excellent agreement with Adams and Munro's analytical expression (4), lying between the plane strain and plane stress limits. Thus, the chart read-out does appear to represent a real energy input in terms of crack tip conditions, provided the initial non-linearity due to settling effects is ignored.

In the first series of tests the fracture toughness, R_{stable} corresponding to finite stable crack extension was determined using general equation 4.4. Precracked specimens were loaded at a crosshead speed of 0.5 in. min^{-1} at which speed stable crack growth can take place in polycarbonate. Each specimen was loaded until crack extension occurred and the load attained a maximum, after which the crosshead was stopped to allow the crack to arrest under constant displacement. Finally, after about ten minutes when the load had relaxed the specimen was unloaded. This procedure, illustrated schematically in Fig. 6.5.a, was repeated several times with each specimen until the crack traversed the entire width. Specimens 5P, 10P and 12P with different initial precrack lengths, α_o were all tested in this way.

For the determination of R_i, for crack initiation, additional tests were carried out using specimens 3P and 4P. These were loaded and unloaded incrementally at a crosshead speed of 0.5 in. min^{-1} until the load passed through a maximum, after which the same procedure of crack growth and arrest under constant displacement was followed as before. This incremental loading procedure, Fig. 6.5.b, was continued until the crack had traversed the net section.

Initially the crack extension was monitored by photographing the crack front position after each loading step with the aid of oblique illumination. The high reflectivity of the internal surface enabled very small crack

extensions to be observed. However, examination of the fracture surfaces after testing revealed a series of elliptical profiles which photographic comparison confirmed were successive positions of the arrested crack front between loading increments. Afterwards, crack growth increments were obtained directly from the fracture surfaces using a low magnification travelling microscope, crack lengths being measured at their furthest extent along the mid-section to $\pm$ 0.01 mm.

The final schematic load-displacement curve, Fig. 6.5.c, was obtained for specimens 2P, 6P-9P and 11P. The polycarbonate showed an unusual duplex behaviour in that, on loading these specimens under identical loading conditions to those described previously, the crack front started to bow but, before a stable crack could develop, the crack accelerated rapidly across the remaining ligament. In order to analyse such failures both the initial precrack length, α_o and the crack length up to the onset of rapid crack propagation, α_c were measured from the fracture surfaces with the travelling microscope.

6.3 Results and Analysis of Results

Examples of fracture surfaces for the as-received polycarbonate compact specimens are shown in Fig. 6.6. These optical macrographs were obtained after evaporating a thin film ($\sim$ 600 Å) of aluminium onto the surface in vacuo in order to reduce surface reflections.

From Fig. 6.6.a, the successive positions of the crack front under incremental loading are easily identified. Failure was initiated by the formation of crazes (regions of highly oriented polymer with a void content of 40-60% (5)) ahead and in the plane of the precrack tip. A crack then formed from the crazes with a roughly elliptical shape leaving behind a tongue-shaped region of craze material. This crack extension was accompanied by the development of a through-thickness surface yield zone resembling that of the Dugdale wedge model and of equilibrium height

approximately equal to the sheet thickness, 5 mm. The resultant "mixed mode" fracture surfaces (3P-5P, 10P, 12P) consisted of approximately 70% square fracture in the mid-thickness with 15% shear yield at the two surfaces.

In comparison, Fig. 6.6.b illustrates the case when unstable fracture occurs with the crack accelerating rapidly from the initial region of craze material producing a square fracture with negligible shear yield. One of the most striking features was the display of interference colours along a portion of the fast fracture region close to the fracture origin. Such failures (2P, 6P-9P, 11P) were classified as brittle.

The results for specimen 3P loaded incrementally are shown in Fig. 6.7 where the load is plotted as the dimensionless failure parameter, P^{ϕ} = $P/0.4142\ \sigma_u\ WB$, equation 5.11. The initial increase in crack length at a low applied load reflects the formation of the tongue-shaped region of craze material as the crack grew from the precrack. Under increasing load, however, the rate of increase of crack length decreased as the surface plastic zones developed. Extensive crack growth occurred only at higher loads close to a maximum with further crack extension continuing rapidly under decreasing load until crack arrest at constant displacement.

On reloading in the presence of prior plasticity the initial region of craze material was absent and crack initiation did not occur until a higher applied load level than previously. Subsequent crack growth, however, exhibited the same characteristics as before and this was repeated for all succeeding loading sequences, the extent of slow crack growth up to a load maximum decreasing with decreasing ligament size. At a relative crack length, α of approximately 0.88 the surface plastic zones impinged on the far free surface and a state of general yield was achieved with the polycarbonate sustaining very large permanent deformations with negligible crack extension. A plastic hinge formed and final rupture occurred only

by a tearing form of crack propagation.

The question arises as to the significance of interrupted load tests in failure analysis. Interrupted tests on thin centre-cracked sheets of aluminium alloys have been performed by Broek (6) and his results showed that in the presence of significant crack tip deformation and after unloading from a given stress level, crack extension was reinitiated at a lower stress level on reloading. This was due to the unloading not being fully elastic and a zone of reversed plastic flow being formed at the crack tip; on subsequent reloading the crack tip stress achieved the previous unloaded value at a lower nominal stress. However, after the crack had grown through the small region of reversed plastic flow the unloading was no longer effective and the behaviour was similar to that in a continuous test with a slight reduction in the maximum stress level achieved presumably due to the increased crack length.

Therefore, it was anticipated that interrupted load tests on polycarbonate would increase the slow crack extension between load increments compared with continuous loading but that the general features of finite stable crack growth behaviour would remain the same. This was found to be the case as demonstrated in the following figure.

Fig. 6.8 summarises results for all the polycarbonate specimens tested where again the load is plotted as the dimensionless failure parameter, P^{ϕ}. Considering those specimens undergoing ductile failure and neglecting the first loading sequence with craze remnants, there are three characteristic failure levels corresponding to crack initiation in the presence of prior plasticity (0.1% crack extension, see section 6.3.b.i), load maximum and crack arrest. The results were obtained from specimens with different initial crack lengths and loading sequence and it is apparent from the reproducibility of the curves that all three failure levels depend only on the instantaneous crack size and are independent of the extent of prior

slow crack extension leading to that failure level. Thus, interrupted load tests have no influence upon the three characteristic failure levels, increased crack extension between loading increments merely displacing experimental failure loads to longer crack lengths. The influence of interrupted tests on the determination of R_i and R_{stable} is more important and this is discussed later.

Finally, considering those specimens which failed by a brittle fracture mode, two additional failure levels may be defined which characterise initial craze breakdown and subsequent crack instability, both failure levels considerably below that necessary for crack initiation in the presence of prior plasticity.

6.3.a LEFM Approach to Unstable, Brittle Fracture

Examination of Fig. 6.5.c indicates the essentially linear nature of the loading of those specimens which failed by an unstable, brittle fracture mode, the small deviation from linearity at the load, P_{icb} corresponding to initial craze breakdown. In addition, 0.75-1.00 mm of craze material fractured prior to crack instability at the load, P_c representing an increase in the initial crack length of 1.2-2.7% depending upon α_o; values close to the 2% effective crack extension criterion recommended in the standard plane strain fracture toughness (K_{Ic}) test for metallic materials (7) (8). Although no standard K_{Ic} test has been established for polymeric materials, these features of the polycarbonate brittle fracture tests make them particularly attractive for analysis by LEFM techniques.

Critical stress intensity factors corresponding to initial craze breakdown, K_{icb} and crack instability, K_c were calculated for specimens 6P-9P and 11P on the basis of the loads, P_{icb} and P_c and the relative crack lengths, α_o and α_c, respectively using equation 5.2, $K = PY/\sqrt{W}\,B$. The results are summarised in Table 6.4 where values of the stress intensity coefficient, Y for the compact specimen were taken from Newman (9).

The fracture toughness parameters, R_{icb} and R_c corresponding to the two failure levels were also calculated assuming plane strain crack tip conditions. The validity of this assumption is discussed later.

Mean values of 70 ± 1 $N.mm^{-3/2}$ and 130 ± 2 $N.mm^{-3/2}$ were obtained for K_{icb} and K_c, respectively for the as-received polycarbonate for a nominal strain rate between 1.7×10^{-4} sec^{-1} (6P) and 5.5×10^{-5} sec^{-1} (11P). These results are in excellent agreement with those of Parvin and Williams (10) who, using 3 mm and 5 mm thick single-edge-notched specimens of polycarbonate and a range of crosshead speeds between 0.05-50 cm. min^{-1}, report values of 71 N. $mm^{-3/2}$ and 127 N. $mm^{-3/2}$ for crack initiation and brittle fracture, respectively independent of loading rate.

6.3.b Energy Balance Approach to Stable, Ductile Failure

Stable crack extension in polycarbonate specimens loaded at a crosshead speed of 0.5 in. min^{-1} proceeded in a ductile manner at velocities sufficiently low (maximum velocity of 1.0 mm. sec^{-1} just beyond a load maximum) that at each moment the load was able to adjust itself quasi-statically to the increased compliance; a system ideal for analysis by energy balance methods. Unfortunately, the crack growth behaviour of polycarbonate was such that in order to use it as a model elastic-plastic material it was necessary to grow the crack out of the initial region of craze material. Therefore, R_i for crack initiation and R_{stable} for finite stable crack extension were determined for an equilibrium system in which the crack had achieved an elliptical profile with an associated plastic zone; initial preambulary loading sequences in which tongue-shaped regions of craze remnants were produced were ignored.

6.3.b.i R_i for Crack Initiation

The fracture toughness, R_i was determined by evaluation of the calibration function, $-\frac{1}{B}\left(\frac{\partial U}{\partial a}\right)_u$ from load-displacement records of specimens

with differing crack lengths using the method developed by Begley and Landes (11).

Some examples of experimental load-displacement curves for polycarbonate compact specimens are shown in Fig. 6.9 where the experimental records are compared with analytical curves derived from the simple model (see section 5.2.a). Using Adams and Munro's plane strain compliance calibration (4), agreement between the two sets of curves in the linear elastic regime is excellent. This is confirmed in Table 6.5 where the elastic compliance for the elliptical crack front with an associated plastic zone is compared with values taken from Fig. 6.4 for the planar notch. It is apparent that a crack length measurement taken at the end of the semi-major axis at the mid-section represents an average apparent crack length for the elliptical shaped crack, any overestimate due to crack front curvature being compensated by the underestimate due to crack tip plasticity.

Considering the fully plastic regime of Fig. 6.9, at first glance the agreement between experiment and analysis is very poor; analytical limit loads being calculated on the basis of the ultimate tensile strength, σ_u rather than the yield stress, σ_y to allow for a certain amount of work-hardening (see section 5.2.a.i.). However, on closer examination the experimental limit loads do approach the analytical values corresponding to an infinite displacement at longer crack lengths where slow crack extension becomes negligible. This points out one of the major defects of the simple model, its inability to predict limit load failure at finite strains.

Experimental curves of strain energy, $U/_{WB}$ versus relative crack length, α, Fig. 6.10 were obtained by areal measurement of the experimental load-displacement records from specimens 3P-5P, 10P and 12P at constant displacement using a planimeter, the results covering a displacement range of 2-10 mm. The calibration function, $-\frac{1}{B}\left(\frac{\partial U}{\partial a}\right)_u$ was then determined

as a function of displacement by measuring the slopes of these curves graphically at selected values of α. The resultant curves are given in Fig. 6.11 where the values of α_i selected correspond to specimen 3P which had been loaded incrementally.

The $-\frac{1}{B}\left(\frac{\partial U}{\partial a}\right)_u$ values associated with increments of crack extension, $\Delta\alpha$ produced in specimen 3P were then computed from Fig. 6.11 according to the initial crack size, α_i and the measured displacement, u_{lp} corresponding to the instantaneous crack length, $\alpha_i + \Delta\alpha$. Plots of $-\frac{1}{B}\left(\frac{\partial U}{\partial a}\right)_u$ versus crack growth increment, $\Delta\alpha$ are shown in Fig. 6.12. In spite of considerable scatter ar large values of $\Delta\alpha$, the curves overlap quite well for initial crack sizes, α_i up to 0.7; at large α_i, however, the curves fall with increasing crack length.

The data scatter at large $\Delta\alpha$ arises from two sources: an increasing random error associated with measurements of large values of the energy slope (maximum uncertainty in $-\frac{1}{B}\left(\frac{\partial U}{\partial a}\right)_u$ of 10% at the largest displacements); an increasing systematic error due to overestimates in crack growth increments as a result of the incremental loading sequence. The reduction in the level of the $-\frac{1}{B}\left(\frac{\partial U}{\partial a}\right)_u$ versus $\Delta\alpha$ curves as a result of the latter is difficult to estimate since it obviously depends upon the loading history. However, in the present case inexact values of $-\frac{1}{B}\left(\frac{\partial U}{\partial a}\right)_u$ at large $\Delta\alpha$ are only required for extrapolation to determine a critical value at crack initiation and the proximity of these values at low $\Delta\alpha$ indicates that the use of an incremental loading procedure for such purposes is valid.

To evaluate R_i as an initiation criterion a definition of crack initiation is required. Previous studies indicate that an absolute measurement of crack extension is necessary since a measurement point taken relative to specimen size can result in significant size effects (12) (13). Landes and Begley (12) have suggested a measurement point taken at the intersection of the $-\frac{1}{B}\left(\frac{\partial U}{\partial a}\right)_u$ versus Δa curves with a stretch zone line

defined by:

$$-\frac{1}{B}\left(\frac{\partial U}{\partial a}\right)_u = 2\sigma_{flow}\,\Delta a \qquad 6.1$$

where $\sigma_{flow} = (\sigma_y + \sigma_u)/2$. However, as demonstrated in Fig. 6.12 such a definition has no significance in the present case where crack extension occurs in the presence of prior plasticity and crack front geometry changes do not follow equation 6.1. Therefore, an absolute measurement point was arbitrarily selected at a crack extension of 0.085 mm corresponding to a crack growth increment of 0.1% for a constant specimen width of 85 mm. The resultant R_i values are plotted as a function of α_i in Fig. 6.13 and the results summarised in Table 6.6.

A mean value of 26 ± 1 N mm^{-1} was obtained for R_i within the range $0.263 \leqslant \alpha_i \leqslant 0.664$ for a nominal strain rate between 2.7 x 10^{-4} sec^{-1} (α_i = 0.263) and 8.2 x 10^{-5} sec^{-1} (α_i = 0.664); R_i decreasing to 15.6 N mm^{-1} at α_i of 0.902 for a nominal strain rate of 2.5 x 10^{-5} sec^{-1}. This result reflects the variation in the $-\frac{1}{B}\left(\frac{\partial U}{\partial a}\right)_u$ versus $\Delta\alpha$ curves and selection of a slightly different measurement point for crack initiation would not alter the general behaviour of R_i. A stress intensity factor, K_i for crack initiation was also calculated using $K_i = \sqrt{ER_i/(1-\nu^2)}$; the reason for this is discussed later.

Experimental curves of strain energy, U/WB versus strain energy slope, $-\frac{1}{B}\left(\frac{\partial U}{\partial a}\right)_u$ for the polycarbonate compact specimens are shown in Fig. 6.14 as a function of α. It is apparent that a linear relationship exists between the two functions within the crack initiation locus over the range $0.3 \leqslant \alpha \leqslant 0.9$, deviations occurring only at higher energy levels. Thus, as pointed out by Begley and Landes (14) and Neale and Townley (15), the relationship is of the form:

$$-\frac{1}{B}\left(\frac{\partial U}{\partial a}\right)_u = \phi\,\frac{U}{(W-a)B} = \phi\,\frac{U}{(1-\alpha)WB} \qquad 6.2$$

Values of the function $\phi = (1-\alpha)$ slope were calculated and these are shown in the figure. Comparison with the table in Appendix 3 indicates that the results follow closely the general relationships for ϕ predicted by the linear elastic - fully plastic model. In addition, the use of the approximate relation, equation 5.16 i.e. $\phi = 2.0$ for $\alpha \geqslant 0.6$ would appear to be valid for polycarbonate, underestimating values of $-\frac{1}{B}\left(\frac{\partial U}{\partial a}\right)_u$ by only 7½% at $\alpha = 0.6$ and by 4% at $\alpha = 0.7$.

6.3.b.ii R_{stable} for Finite Stable Crack Extension

The fracture toughness, R_{stable} should be determined from general equation 4.4 by measuring the areal difference between loading and unloading load-displacement curves for cracks of length, a_i and a_f, respectively. However, the load-displacement records for polycarbonate, Fig. 6.5.a, exhibited considerable non-linearity on unloading due to hysterisis and, more significantly, interference of the plastically deformed crack surfaces. Therefore, after measuring the total area under the load-displacement curve for a crack of length a_i with a planimeter, the recoverable elastic contribution was accounted for by subtraction of $\frac{1}{2} P_{arr}^2 C_f$ where P_{arr} is the final arrest load and C_f, the elastic compliance corresponding to the final crack position. The results are shown in Table 6.7 and plotted as a function of α_{mean} in Fig. 6.13.

The reproducibility of the experimental data (maximum deviation from the solid line of 10% at $\alpha_{mean} = 0.728$) indicates that the crack extensions, Δa were sufficiently large to negate any influence of the initial loading when the crack grows through regions of residual plasticity. Under such circumstances the use of interrupted load tests to determine R_{stable} is justified, R_{stable} being independent of crack extension increment, Δa.

It is apparent that the energy required for finite stable crack extension is considerably larger than that necessary for crack initiation. This

is to be expected in a material showing considerable through-thickness yield during crack growth as R increases with plastic zone size until the latter attains an equilibrium-maximum. Thus, R_{stable} represents an average for the entire process of finite stable crack extension and arrest. However, R_{stable} shows a strong dependence on α at all crack sizes decreasing continuously from 226N mm^{-1} (α_{mean} = 0.221) to 89 N mm^{-1} (α_{mean} = 0.892).

6.4 Discussion

6.4.a Unstable, Brittle Fracture

The occurrence of both ductile and brittle failures in 5 mm thick polycarbonate sheet indicates that the model material was near a transition between the two fracture modes sensitive to slight variations in precracking procedure, the propensity towards square fracture presumably arising from poor precrack tip acuity. Under such circumstances so much energy must be used in producing individual crazes at the initial razor cut that when the crack finally grows through one of the crazes the system has more than enough energy to propagate the crack and a fast, unstable fracture occurs. Such duplex behaviour of 5 mm thick polycarbonate has been observed before (10).

However, although initial crack tip geometry seems to be a major factor in determining final fracture mode, values of K_{icb} for initial craze breakdown and K_c for crack instability appear to be insensitive to slight variations in initial crack tip sharpness showing an experimental variation of only 3%; in strong contrast to metals where spuriously large values of K_{Ic} are generally obtained when cracks are insufficiently sharp. The reason for this may be due to the generation of microscopic cracks at the base of the precrack during introduction with the razor blade, these cracks acting as nuclei for craze formation and subsequent crack growth. Once the crack has grown through the initial region of craze material, of

course, the subsequent level of K_c would not be affected by the initial state of the crack tip. Agreement between critical stress intensity factors for polycarbonate specimens containing machined notches and sharp precracks supports this (10) (16).

Room temperature K_{Ic} values of 70-140 N mm$^{-3/2}$ have been reported previously for polycarbonate (10) (16)-(18). This wide variation appears to stem from the complex crack growth dissipative process (crazing) which occurs prior to final instability since differences in material fabrication, orientation and strain rate can account only for small changes in critical stress intensity factor. For example, on the basis of the K_{Ic} specimen size requirement for metallic materials, equation 5.1, K_{icb} for initial craze breakdown, but not K_c for crack instability, constitutes a valid plane strain fracture toughness for polycarbonate of 70 N mm$^{-3/2}$ (a, W-a, $B \geqslant 2.5\ (K/\sigma_y)^2$ = 4.9 mm and 16.9 mm for K_{icb} and K_c, respectively). However, apart from the specimen thickness requirement, the majority of the evidence is in favour of K_c representing a plane strain fracture toughness of 130 N mm$^{-3/2}$; crack instability never occurring at stress intensity levels significantly below K_c irrespective of initial crack length and geometric configuration (10).

The existence of two plane strain failure levels characterising unstable brittle fracture in polycarbonate is open to question. An increase in load-bearing capacity, and thereby apparent fracture toughness, after initial crack front bowing might be anticipated on the basis of crack front curvature effects, for it is known that if a thumbnail crack grows from a straight crack the stress intensity coefficient, Y decreases (19) (20). Using a finite element analysis of a compact specimen Neale (20) has shown that for an initial planar crack (α = 0.535) growing into a parabolic crack (α = 0.550) the stress intensity coefficient for the average straight crack (α = 0.548) overestimates K_{Ic} for the parabolic crack

by 9%. Such errors are obviously a function of initial crack length, however in the present case for polycarbonate the magnitude of this effect should be no larger than this since the maximum extent of crack front curvature, $\Delta\alpha$ at crack instability was only 0.011.

An alternative explanation for the observed toughening effect is that there is a reduction in crack tip constraint as a result of crack growth through the initial region of craze material. Certainly, a predominantly square fracture with negligible shear yield does not, of itself, constitute evidence of a fully plane strain fracture since the through-thickness stress at the mid-plane may induce sufficient triaxiality to produce a square fracture mode without reaching its full plane strain value (21). Under such circumstances, testing specimens of increasing thickness should result in a reduction in the critical stress intensity factor. In fact, results obtained for 5 mm and 6 mm thick heat treated polycarbonate (see section 8.3) indicate that K_c is independent of thickness and thus, K_c may be considered as a fully plane strain value.

Therefore, it appears that the two plane strain failure levels associated with initial craze breakdown and crack instability are real and calculation of the corresponding energy parameters, R_{icb} and R_c under such circumstances is justified.

Fracture in glassy polymers generally occurs by a multiple cavitation process which involves the formation and breakdown of crazes (22). These are narrow wedge-shaped zones of highly deformed and voided polymer which resemble real cracks as they normally form under hydrostatic tension at right angles to the major principal axis and are highly light reflecting. However, unlike true cracks, crazes are not complete discontinuities and are capable of supporting large stresses comparable to the normal yield stress of the bulk polymer (23). Crazes may be distinguished from cracks by direct illumination since the latter totally internally reflect light

at all angles of incidence but crazes transmit light at high angles and reflect light only at low angles of incidence to the polymer-craze interface; the refractive index of craze material being intermediate between that of air and the bulk polymer (24).

Evidence of craze formation in the present tests was provided by the highly fragmented region of material oriented in the crack growth direction close to the precrack tip and the negligible lateral contraction. The large void content of crazes (between 40-60% (5)) allows the highly stressed material at the crack tip to deform in the direction of the applied stress without lateral contraction, the latter normally being prevented under plane strain conditions by the elastic constraint of the surrounding undeformed polymer. In addition, the presence of interference colours in the fast fracture region indicated the formation of a thin layer of material and hence refractive index, different from that of the substrate. Again, only the large void content of crazes can account for the reduction in the refractive index of the bulk polymer necessary to produce such fringes.

Following Kambour (25) R may be considered to be made up of a number of energy absorbing processes:

$$R = 2\gamma_f + 2\gamma_v + 2\gamma_e \qquad 6.3$$

where $2\gamma_f$ is the energy required for craze formation from undeformed polymer being associated with polymer chain orientation, $2\gamma_v$ is the surface energy for void formation within a craze and $2\gamma_e$ is the viscoelastic energy for craze breakdown. Estimates by Kambour (25) indicate that the first two terms account for only 16% and 1.5% of the total energy, respectively so that the largest contribution to R is necessary for the breakdown of craze material which can sustain very large viscoelastic deformation. For example, because of the negligible lateral contraction, the longitudinal strain associated with a craze consisting of 50% voids must be of the order of

100% (void content $\approx \varepsilon_{yy}/1 + \varepsilon_{yy}$).

It might be expected that fracture associated with the thick crazes formed in the subcritical region would give higher values of the energy parameter, R but the results appear to contradict this, R_{icb} and R_c having values of 1.9 N mm^{-1} and 6.4 N mm^{-1}, respectively. From the foregoing the difference in magnitude of R necessary for initial craze breakdown and fast fracture from a single craze would appear to be due mostly to an increase in the viscoelastic contribution, $2\gamma_e$. However, such increases are difficult to quantify since factors such as size and shape of craze material ahead of the crack tip, mutual interference of crazes and rate of craze and crack growth at instability require consideration.

6.4.b Stable, Ductile Failure

Stable crack growth occurred in the polycarbonate specimens when shear yield was no longer suppressed. The plastic zone then developed under increasing load in a manner similar to that observed for metals (26), the zone size increasing with transition from plane strain to less constrained crack tip conditions as the crack tunnelled forward. The final equilibrium height of the surface plastic zone corresponded roughly to the sheet thickness as it does in some metals under plane stress crack tip conditions (26). Under such circumstances polycarbonate provides a good model for the elastic-plastic behaviour of metals undergoing mixed mode failure.

The compliance of the elliptical shaped crack with an associated plastic zone was in excellent agreement with linear elastic analysis (Table 6.5 and Fig. 6.4) so that the use of load-displacement curves based on this configuration for establishing relationships between strain energy, $\frac{U}{WB}$ and strain energy slope, $-\frac{1}{B}\left(\frac{\partial U}{\partial a}\right)_u$ is justified. For this system crack initiation (0.1% crack extension) occurs at loads well below a maximum close to the linear elastic regime, as indicated in Fig. 6.9, so that it is not surprising that a linear relation exists between U/WB and $-\frac{1}{B}\left(\frac{\partial U}{\partial a}\right)_u$ up to crack

initiation (Fig. 6.14) as predicted by Begley and Landes (14) and Neale and Townley (15). Perhaps of greater interest, is the fact that such relationships are maintained beyond crack initiation into the elastic-plastic transition region, deviations occurring only at higher energy levels presumably as a result of significant slow crack extension.

For the crack size range, $0.263 \leqslant \alpha_i \leqslant 0.664$, R_i for crack initiation has been shown to be a constant. By analogy with metals, equation 4.19, this fracture toughness may be considered to be made up of two terms:

$$R_i = 2\gamma_p + \frac{1}{B}\left(\frac{\Delta U_p}{\Delta a}\right)_i = R_c + \frac{1}{B}\left(\frac{\Delta U_p}{\Delta a}\right)_i \qquad 6.4$$

where $2\gamma_p$ or R_c is the deformation energy necessary for the formation and breakdown of craze material and $\frac{1}{B}\left(\frac{\Delta U_p}{\Delta a}\right)_i$ is the plastic strain energy rate associated with initial shear yield; the theoretical surface tension, 2γ being negligible. For a constant R_i of 26 N mm^{-1} and assuming R_c takes a value of 6.4 N mm^{-1} for identical loading conditions, the implication is that the shear yield process constitutes approximately 75% of the initial energy expenditure for mixed mode failure. Such a large contribution may seem surprising but unlike metals where plastic deformation occurs by dislocation motion in a polycrystalline structure, the shear yield energy in polycarbonate is used in re-orientation of the chain-like molecules by stretching, sliding and the breakdown of entanglements and under the unconstrained plane stress conditions at the surface these large scale molecular motions might be expected to show much stronger viscoelastic behaviour than under the more constrained conditions at the mid-thickness.

At longer crack lengths, $\alpha_i > 0.7$, R_i decreased significantly below 26 N mm^{-1} although this does not appear to be due to any strain rate effect since the latter decreased continuously throughout the crack size range, $\alpha_i = 0.263\text{-}0.902$.

In comparison with R_i, R_{stable} for finite stable crack extension

decreased continuously over the entire crack size range, $\alpha = 0.221 - 0.892$ from 226 N mm^{-1} to 89 N mm^{-1}. As before, R_{stable} may be defined in terms of energy absorbing processes by:

$$R_{stable} = R_c + \frac{1}{B}\left(\frac{\Delta U_p}{\Delta a}\right)_{eqm} \approx \frac{1}{B}\left(\frac{\Delta U_p}{\Delta a}\right)_{eqm} \qquad 6.5$$

where the deformation energy required for the formation and breakdown of craze material, R_c is now negligible in comparison with the plastic strain energy rate associated with the equilibrium shear yield process, $\frac{1}{B}\left(\frac{\Delta U_p}{\Delta a}\right)_{eqm}$. Therefore, the reduction in R_{stable} with increasing crack length would appear to be due to a decrease in the plastic strain energy contribution.

Using 3 mm thick polycarbonate sheet at room temperature, Mai has clearly demonstrated that the plane stress or shear yield contribution to R is a function of crack front speed (27). In the present case, however, the reduction in R_{stable} cannot be accounted for on the basis of variations in crack velocity since, although the crack speed in any one test increased from zero to a maximum of 1 mm sec^{-1}, the mean crack velocity showed no systematic change with crack length but varied randomly within the range $0.9 \pm 0.2 \times 10^{-2}$ mm sec^{-1} for all tests.

Thus, it appears that the variation of R_{stable}, and R_i at longer crack lengths, is a real geometrical effect and arises from the applied load exceeding the general yield level in narrow specimens. This effect is most easily demonstrated by invoking LEFM principles, substituting the general yield load given by equation 5.9 into equation 5.2:

$$K_{gy} = \sigma_y \sqrt{W}\ Y \left[-(1+\alpha) + \sqrt{2(1+\alpha^2)} \right] = \sqrt{ER_{gy}} \qquad 6.6$$

where K_{gy} is a pseudo-elastic stress intensity factor and R_{gy}, a pseudo-elastic fracture toughness corresponding to the general yield level. The variation of R_{gy} with crack length, α for the polycarbonate compact specimens is shown in Fig. 6.13. It is apparent that R_{stable} decreases in a

manner similar to R_{gy}, the latter representing a pseudo-elastic and therefore, extremely conservative estimate of R_{stable}. In comparison, R_i remains constant at energy levels considerably below R_{gy} at short and intermediate crack lengths, only decreasing at longer crack lengths when R_i exceeds 76% R_{gy}.

Of course, the fact that the applied load exceeds the general yield level does not imply the onset of full net section yield at the limit load but merely that a state of local plastic instability develops ahead of the crack tip in a manner directly analogous to the tensile instability at a load maximum in a uniaxial test piece. The form of equation 6.6 indicates that a constant value of R_{stable} is only likely to be achieved in wide specimens for which the general yield level, R_{gy} is raised above R_{stable} and local plastic instability does not occur.

6.4.c Failure Analysis Diagram

For stable ductile failure only the crack initiation parameter, R_i has been shown to be relevant, R_{stable} for finite stable crack extension exhibiting a geometry dependence over the entire crack size range. Normally, an elastic-plastic analysis would be required to determine the dimensionless failure parameter, P_i^{ϕ} for crack initiation from a knowledge of R_i. However, with the present tests on polycarbonate the situation is considerably simplified by the occurrence of crack initiation (0.1% crack extension) at relatively low load levels close to the linear elastic region (Fig. 6.9). Under such circumstances the use of the elastic functions derived from LEFM is appropriate and by redefining the failure criterion as $\sqrt{ER_i/(1-\nu^2)}$ i.e. K_i, P_i^{ϕ} for crack initiation may be calculated by means of equation 5.12[a].

---

[a]The use of a stress intensity factor, $K_i = \sqrt{ER_i/(1-\nu^2)}$ does not, of itself, imply plane strain crack tip conditions. In fact, the crack tip stress state is known to be mixed plane strain, plane stress. The term, $(1-\nu^2)$, is used only to ensure compatibility with the elastic compliance calibration of Table 6.5 and Fig. 6.4.

Therefore, in order to test the applicability of the two-criteria approach to failure (28) described in section 5.2.a.i, a failure analysis diagram was constructed for the polycarbonate compact specimens based solely on a knowledge of the stress intensity factors, K_{icb}, K_c and K_i and the uniaxial tensile properties, σ_y and σ_u using equations 5.12-5.14. The result is shown in Fig. 6.15 where the analytical LEFM and limit analysis curves are compared with the experimental results.

For unstable, brittle fracture agreement between the LEFM curves based on K_{icb} and K_c and the experimental loads for initial craze breakdown and crack instability is excellent, within the 3% scatter band determined for the stress intensity factors.

For stable, ductile crack growth the locus for crack initiation based on K_i of 259 N $mm^{-3/2}$ is in excellent agreement with the experimental loads for 0.1% crack extension obtained by interpolation for short and intermediate size cracks. This is clearly demonstrated in Table 6.8 where the experimental loads are within 2% of the predicted values for crack lengths, α up to 0.7. However, at longer crack lengths the experimental loads decrease significantly below the predicted values achieving only 75% of the calculated load at $\alpha = 0.902$.

For longer crack lengths the failure loads based on the limit analysis solution for yield predict lower values than those corresponding to the LEFM K_i analysis so that a change in failure mode to one of increased plasticity might be anticipated. This is in keeping with the observation that R_i and P_i^{ϕ} decreased at $\alpha > 0.7$ although full net section yield did not take place until a relative crack length of approximately 0.88 when the surface plastic zones impinged on the far free surface. Thus, there appears to be a transition from contained to uncontained plasticity over the crack size range, $\alpha = 0.7 - 0.88$ where, as shown in Table 6.8, the crack initiation loads are intermediate between the LEFM K_i solution and the limit analysis

solution for yield.

In order to analyse failure after significant slow crack extension, the experimental plastic instability loads or load maxima, P_m^{ϕ} have been included in Fig. 6.15 for comparison with the limit analysis solution for yield and ultimate collapse; the crack arrest loads, P_{arr}^{ϕ}, lying significantly below P_m^{ϕ} (Fig. 6.8) due to the time-dependent recovery processes occurring within the crack tip deformation zone, are not represented as they require consideration of time-dependent mechanical properties. From Fig. 6.15 it is apparent that the experimental loads are in reasonable agreement with the limit analysis solution for yield on the basis of the instantaneous crack size for crack lengths within the range, α = 0.300 - 0.444. At longer crack lengths, however, the experimental results deviate significantly from the locus for yield but are in good agreement with the limit analysis solution for ultimate collapse prior to full net section yield at α = 0.88. This is confirmed in Table 6.9 where all the experimental loads are within 14% of the predicted values of P_m^{ϕ} up to α = 0.9; the accuracy of the load measurement being open to question at higher α values due to the compliance of the linkages.

The agreement between the experimental values of P_m^{ϕ} and the limit analysis solution may seem surprising since the latter is only based on a simple one-dimensional model. As shown by Dixon (29), the development of a curved crack front modifies the stress distribution such that the maximum longitudinal stress is shifted to the boundary regions. Therefore, it is reasonable to assume that, at high load levels, mixed mode failure is governed by the load-bearing capacity of the boundary regions undergoing plane stress shear yield. For a material obeying the maximum shear stress or Tresca's yield criterion, a simple one-dimensional solution should provide a good lower bound.

Unlike metals, glassy polymers generally obey a pressure-dependent

von Mises yield criterion (30) which may take the form:

$$\frac{1}{6}\left[(\sigma_1-\sigma_2)^2 + (\sigma_2-\sigma_3)^2 + (\sigma_3-\sigma_1)^2\right] = \tau_m^2 = (\tau_m^0-\mu\sigma_p)^2 \qquad 6.7$$

where $\sigma_1 > \sigma_2 > \sigma_3$ are the principal stresses, τ_m is the Mises shear stress, τ_m^0 the Mises pure shear stress, μ the coefficient of internal friction and σ_p the hydrostatic stress. However, Christiansen (31) reports a value of only 0.07 for μ of polycarbonate so that equation 6.7 reduces to the usual von Mises yield criterion for metals. In this case a simple one-dimensional model is no longer adequate to represent a plane stress state since by definition, Mises criterion requires a knowledge of all three principal stresses to determine the shear stress, τ_m.

The deviation of the experimental plastic instability loads, P_m^ϕ from the limit analysis solution for yield at $\alpha > 0.444$ may be due to the tendency of polycarbonate to follow von Mises yield criterion. On the other hand, some work-hardening may also occur. In the absence of an elastic-plastic finite element analysis, however, the yield and work-hardening characteristics of the crack tip deformation zone appear to be adequately accounted for by basing the lower bound solution on the ultimate tensile strength of the material.

More difficult to explain is the apparent reduction in work-hardening capacity and subsequent inadequacy of the lower bound solution at short crack lengths. This does not appear to be due to any strain rate sensitivity of the polycarbonate, in fact, quite the reverse. The nominal strain rate applied to the specimens has been stated to increase with decreasing crack length from 2.5×10^{-5} sec^{-1} ($\alpha_i = 0.902$) to 2.7×10^{-4} sec^{-1} ($\alpha_i = 0.263$) and according to Bauwens-Crowet (32) an order of magnitude increase in strain rate should raise the plastic instability stress, σ_u of polycarbonate at room temperature by 2.9 N mm^{-2} or 4% of σ_u. When calculated on the basis of the initial crack tip strain rate, $\dot{\varepsilon}_{tip}$ (see Appendix 4) this

possible increase in σ_u is even less i.e. 1.6N mm^{-2} or 2% of σ_u as $\dot{\varepsilon}_{tip}$ increases from 2.4 x 10^{-2} sec^{-1} (α_i = 0.902) to 8.3 x 10^{-2} sec^{-1} (α_i = 0.263). Thus, the reduction in the experimental failure loads, P_m^{ϕ} below the simple lower bound solution occurs despite any possible increase in the uniaxial tensile properties, σ_y or σ_u at short crack lengths.

6.5 Conclusions

a. Static loading experiments on compact specimens of as-received polycarbonate at room temperature have shown that 5 mm thick sheet fails either by unstable, brittle fracture or by stable, ductile crack extension.

b. Unstable, brittle fracture in polycarbonate may be characterised by two critical stress intensity factors, K_{icb} and K_c corresponding to initial craze breakdown and crack instability, respectively. Under static loading conditions, the value of these parameters have been found to be independent of initial crack length, geometric configuration and thickness, thereby constituting fully plane strain values of fracture toughness.

c. When polycarbonate undergoes stable, ductile crack extension it may be used as a model elastic-plastic material for mixed mode failure in metals. Under such circumstances, a linear relationship has been shown to exist between the strain energy, $U/_{WB}$ and its derivative with respect to crack length, $-\frac{1}{B}\left(\frac{\partial U}{\partial a}\right)_u$ as predicted by Begley and Landes (14) and Neale and Townley (15), this relationship being maintained even after initial crack extension.

d. Mixed mode failure in polycarbonate may be characterised by two fracture toughness parameters, R_i for crack initiation and R_{stable} for finite stable crack extension. $R_i = -\frac{1}{B}\left(\frac{\partial U}{\partial a}\right)_{u_i}$ has been shown to be a constant independent of initial crack length and prior plasticity

up to energy levels corresponding to 76% of the pseudo-elastic general yield level, R_{gy}. However, R_{stable}, determined by the general energy balance equation 4.4, exhibited a geometry dependence at all crack lengths as a result of local plastic instability ahead of the crack tip in the narrow specimens.

e. Dowling and Townley's two-criteria approach to failure (28) has been shown to provide good estimates of the failure loads for 5 mm thick polycarbonate compact specimens undergoing both unstable, brittle fracture and stable, ductile crack extension.

Failure loads corresponding to initial craze breakdown, crack instability and crack initiation in the presence of prior plasticity were within 3% of LEFM estimates. In the transitional region between contained and uncontained plasticity where R_i exceeded 76% of the pseudo-elastic general yield level, R_{gy}, crack initiation loads were intermediate between LEFM and limit analysis estimates; the latter providing more conservative predictions.

Finally, on the basis of the instantaneous crack size, plastic instability loads were within 11% of the limit analysis solution for yield at short crack lengths, $\alpha = 0.300 - 0.444$ and within 14% of the limit analysis solution for ultimate collapse for intermediate and long crack lengths, $\alpha = 0.444 - 0.900$. However, the apparent variation in work-hardening capacity with crack size is not understood.

References

(1) A. Nadai, "Theory of Flow and Fracture of Solids," vol. 1, McGraw-Hill, New York, p. 320, 1950.

(2) H.F. Brinson and A. DasGupta, Expt. Mechs., 15, p. 458, 1975.

(3) P.S. Theocaris and E.E. Gdoutos, Expt. Mechs., 15, p. 169, 1975.

(4) N.J.I. Adams and H.G. Munro, Eng. Fract. Mechs., 6, p. 119, 1974.

(5) R.P. Kambour, J. Polymer Sci., A2, p. 4159, 1964.

(6) D. Broek, Aerospace Proc., p. 811, 1966.

(7) "Methods for Plane Strain Fracture Toughness (K_{Ic}) of Metallic Materials," B.S. 5447: 1977, B.S.I., London.

(8) "Plane Strain Fracture Toughness of Metallic Materials," A.S.T.M. E399-72 Part 31, 1972.

(9) J.C. Newman, Jr., A.S.T.M. S.T.P. 560, "Fracture Analysis," Am. Soc. for Testing and Materials, p. 105, 1974.

(10) M. Parvin and J.G. Williams, Int. J. of Fracture, 11, p. 963, 1975.

(11) J.A. Begley and J.D. Landes, A.S.T.M. S.T.P. 514, "Fracture Toughness," Am. Soc. for Testing and Materials, p. 1, 1972.

(12) J.D. Landes and J.A. Begley, A.S.T.M. S.T.P. 560, "Fracture Analysis," Am. Soc. for Testing and Materials, p. 170, 1974.

(13) C.A. Griffis and G.R. Yoder, NRL Report No. 7676, April 1974.

(14) J.A. Begley and J.D. Landes, A.S.T.M. S.T.P. 536, "Progress in Flaw Growth and Fracture Toughness Testing," Am. Soc. for Testing and Materials, p. 246, 1973.

(15) B.K. Neale and C.H.A. Townley, C.E.G.B. Report No. RD/B/N3358, May 1975.

(16) F.A. Johnson, A.P. Glover and J.C. Radon, Proc. 1973 Symp. on Mechanical Behaviour of Materials, Soc. of Materials Science, Japan, p. 141, 1974.

(17) P.L. Key and Y. Katz, Int. J. of Fract. Mechs., 5, p. 63, 1969.

(18) R.P. Kambour and S. Miller, J. Mats. Sc., 11, p. 823, 1976.

(19) J.L. Swedlow and M.A. Ritter, A.S.T.M. S.T.P. 513, "Stress Analysis and Growth of Cracks," Part 1, Am. Soc. for Testing and Materials, p. 79, 1972.

(20) B.K. Neale, Int. J. of Fracture, 12, p. 499, 1976.

(21) J.F. Knott, "Fundamentals of Fracture Mechanics," Butterworths, London, p. 125, 1973.

(22) J.P. Berry, J. Polymer Sci., 50, p. 107 and p. 313, 1961.

(23) R.P. Kambour, Polymer Eng. Sci., 8, p. 281, 1968.

(24) R.P. Kambour, Polymer, 5, p. 143, 1964.

(25) R.P. Kambour, Appl. Polymer Symp., 7, p. 215, 1968.

(26) G.T. Hahn and A.R. Rosenfield, Acta Metallurgica, 13, p. 293, 1965.

(27) Y.W. Mai, Int. J. of Fracture, 9, p. 349, 1973.

(28) A.R. Dowling and C.H.A. Townley, Int. J. Pres. Ves. and Piping, 3, p. 77, 1975.

(29) J.R. Dixon, Proc. Conf. on Physical Basis of Yield and Fracture, Oxford, p. 6, 1966.

(30) P.B. Bowden in "The Physics of Glassy Polymers," Ed. by R.N. Haward, Appl. Sci. Publ. Ltd., London, p. 321, 1973.

(31) A.W. Christiansen, E. Baer and S.V. Radcliffe, Phil. Mag., 24, p. 451, 1971.

(32) C. Bauwens-Crowet, J.C. Bauwens and G. Homès, J. Polymer Sci., Part A-2, 7, p. 735, 1969.

Table 6.1 Specifications for As-Received 3203 Makrolon Polycarbonate Sheet

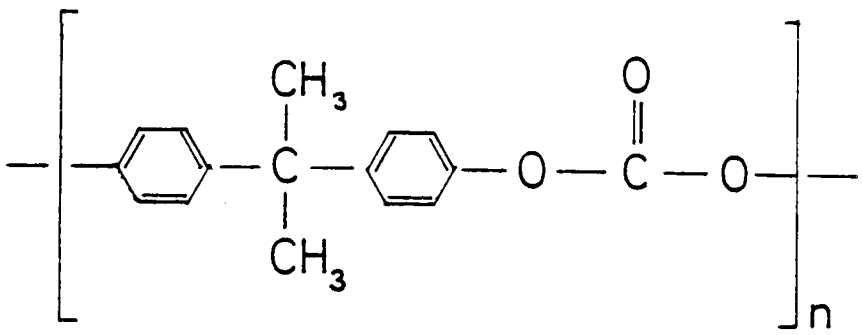
Structural formula	 from bisphenol A and carbon dioxide
Physical structure	partially crystalline
Density	1.2×10^{-6} Kg mm^{-3}
Refractive index	1.584
Coefficient of linear thermal expansion (-50°C - + 90°C)	$60 - 70 \times 10^{-6}$ °K^{-1}
Water absorption at room temperature (60% rel. humidity)	0.15 - 0.19% by weight
Deflection temperature	135 - 145°C
Melt temperature	220 - 230°C

Table 6.2 Mechanical Properties of As-Received Polycarbonate ($295°K$, $\dot{\varepsilon}_{nom} = 2.3 \times 10^{-3}$ sec^{-1})

Uniaxial yield stress, σ_y	50 N mm^{-2} [1]*
Ultimate tensile strength, σ_u	
"x" direction	65.95 ± 0.02N mm^{-2} [2]
"y" direction	65.37 ± 0.02 N mm^{-2} [2]
mean	65.7 ± 0.3 N mm^{-2} [4]
True strain at plastic instability, ε_{tm}	0.067 [1]
Static Young's modulus, E	2.27×10^3 N mm^{-2} [1]
Poisson's ratio, ν	0.37 (manuf.)

* No. of measurements

± 1 Standard deviation

Table 6.3 Compact Specimen Dimensions for As-received Polycarbonate

	B mm	B_n mm	W mm	α_o	Failure mode	Load-displacement curve
1P	4.95	4.95	84.89	Variable	—	Compliance calib.
2P	4.95	4.77	84.68	0.013	U-B*	c
3P	4.95	4.83	85.27	0.040	S-D †	b
4P	4.95	4.80	84.92	0.041	S-D	b
5P	4.95	4.78	84.90	0.338	S-D	a
6P	4.95	4.81	84.34	0.405	U-B	c
7P	4.95	4.77	84.52	0.407	U-B	c
8P	4.95	4.87	84.87	0.428	U-B	c
9P	4.95	4.86	84.71	0.503	U-B	c
10P	4.95	4.83	84.70	0.610	S-D	a
11P	4.95	4.82	84.89	0.696	U-B	c
12P	4.95	4.80	84.61	0.810	S-D	a

* U-B, Unstable, brittle fracture

† S-D, Stable, ductile failure

Table 6.4 Analysis of Elastic Brittle Fractures of As-Received Polycarbonate Compact Specimens

	α_o	P_{icb} N	$K_{icb} = P_{icb} Y/\sqrt{WB}$ N mm$^{-3/2}$	$R_{icb} = K_{icb}^2 (1-\nu^2)/E$ N mm^{-1}	α_c	P_c N	$K_c = P_c Y/\sqrt{WB}$ N mm$^{-3/2}$	$R_c = K_c^2 (1-\nu^2)/E$ N mm^{-1}	$\Delta\alpha/\alpha_o$
6P	0.405	423	70.7	1.90	0.416	743	128	6.23	0.027
7P	0.407	423	71.4	1.94	0.417	747	130	6.43	0.025
8P	0.428	400	70.1	1.87	0.435	716	128	6.23	0.016
9P	0.503	311	68.0	1.76	0.509	600	134	6.83	0.012
11P	0.696	156	71.8	1.96	0.704	274	131	6.52	0.012
Mean			70 $\pm$ 1	1.9 $\pm$ 0.1			130 $\pm$ 2	6.4 $\pm$ 0.2	

Table 6.5 Comparison of Elastic Compliances for Cracks and Notches in Polycarbonate Compact Specimens

	α	$\frac{EBu_1}{P}_p$ a. Elliptical crack front with associated plastic zone, 3P, 4P, 5P.	b. Planar notch front, 1P, Fig. 6.4	$\frac{C_{elliptical}}{C_{planar}}$
3P	0.178	10.3	10.2	1.01
	0.327	17.8	18.2	0.98
	0.444	29.3	29.5	0.99
	0.527	43.1	43.2	1.00
	0.618	65.0	68.0	0.96
	0.695	111	120	0.93
4P	0.182	10.9	10.6	1.03
	0.300	16.1	16.1	1.00
	0.416	26.0	26.0	1.00
	0.508	39.0	39.6	0.98
	0.618	66.4	68.0	0.98
5P	0.423	26.8	26.7	1.00
	0.455	31.0	31.0	1.00
	0.521	41.6	42.1	0.99
	0.606	63.0	63.6	0.99
	0.650	80.7	84.0	0.96

Table 6.6 Determination of R_j for Crack Initiation Using Specimen 3P

α_i	$\Delta\alpha$	u_{lp} mm	$-\frac{1}{B}\left(\frac{\partial U}{\partial a}\right)_u$ N mm^{-1}	$R_i = -\frac{1}{B}\left(\frac{\partial U}{\partial a}\right)_{u_i}$ N mm^{-1}	$K_i = \sqrt{ER_i/(1-\nu^2)}$ N mm$^{-3/2}$
0.263	0.0003	2.28	15.2	25.0	256
	0.0009	2.73	23.6		
	0.0047	3.39	37.3		
	0.0165	4.06	52.2		
0.403	0.0004	3.08	19.8	26.2	263
	0.0026	4.10	35.0		
	0.0150	5.33	58.5		
0.498	0.0010	3.95	24.7	24.7	255
	0.0044	4.78	38.0		
0.587	0.0009	4.71	26.6	26.8	265
	0.0080	6.12	44.7		
0.664	0.0002	4.31	16.7	25.1	257
	0.0010	5.24	25.1		
	0.0043	6.10	33.7		
Mean				26 ± 1	259 ± 4
0.760	0.0004	5.30	16.8	21.5	-
	0.0014	6.38	24.0		
	0.0038	7.20	30.3		
0.823	0.0013	7.06	20.2	19.5	-
	0.0052	9.15	31.9		
0.902	0.0004	8.43	13.9	15.6	-
	0.0018	9.90	17.8		

Table 6.7 Determination of R_{stable} for Finite Stable Crack Extension

	α_i	Δa	$R_{stable} = \frac{\Delta W_{ext} - \Delta U_e}{B_n \Delta a}$	α_{mean}
		mm	N mm^{-1}	
3P	0.178	7.24	226	0.221
	0.327	6.43	202	0.365
	0.444	4.65	196	0.471
	0.527	5.16	177	0.557
	0.618	3.94	158	0.641
	0.695	5.61	131	0.728
	0.773	4.26	119	0.798
	0.828	6.27	85.5	0.865
4P	0.182	7.73	218	0.228
	0.300	7.16	207	0.342
	0.416	5.17	199	0.447
	0.508	5.37	185	0.540
	0.618	4.28	164	0.643
	0.726	3.91	138	0.749
5P	0.423	2.70	193	0.439
	0.455	5.60	190	0.488
	0.521	7.21	182	0.564
	0.606	3.75	169	0.628
	0.650	9.60	149	0.707
10P	0.720	4.78	130	0.749
	0.777	2.39	131	0.791
	0.805	2.35	125	0.819
	0.832	2.11	107	0.845
	0.857	2.14	97.7	0.870
12P	0.881	1.85	89.0	0.892

Table 6.8 Comparison of Experimental and Calculated Values of the Failure Parameter, P_i^{ϕ} for Crack Initiation

	α_i	P_i^{ϕ}				
		a. Expt.	b. LEFM	c. L.A. - Yield	$\frac{a}{b}$	$\frac{a}{c}$
3P	0.263	0.202	0.202	-	1.00	-
	0.403	0.139	0.140	-	0.99	-
	0.498	0.106	0.107	-	0.99	-
	0.587	0.080	0.079	-	1.01	-
	0.664	0.056	0.057	-	0.98	-
	0.760	0.031	0.033	0.030	0.94	1.03
	0.823	0.018	0.021	0.016	0.86	1.13
	0.902	0.006	0.008	0.005	0.75	1.20
4P	0.273	0.198	0.197	-	1.01	-
	0.392	0.145	0.145	-	1.00	-
	0.477	0.113	0.115	-	0.98	-
	0.571	0.086	0.084	-	1.02	-
	0.772	0.028	0.031	0.027	0.90	1.04
	0.865	0.011	0.013	0.009	0.85	1.22

Table 6.9 Comparison of Experimental and Calculated Values of the Failure Parameter, P_m^{ϕ} for Load Maximum

	α_m	P_m^{ϕ} a. Expt.	b. L.A. - Yield	c. L.A. - U.C.	$\frac{a}{b}$	$\frac{a}{c}$
3P	0.306	0.298	0.318	0.417	0.94	(0.71)
	0.444	0.211	0.190	0.249	1.11	(0.85)
	0.527	0.157	0.132	0.173	(1.19)	0.91
	0.618	0.108	0.082	0.107	(1.32)	1.01
	0.695	0.071	0.050	0.066	(1.42)	1.08
	0.773	0.040	0.027	0.035	(1.48)	1.14
	0.828	0.021	0.015	0.020	(1.40)	1.05
	0.906	0.007	0.004	0.006	(1.75)	1.17
4P	0.300	0.299	0.323	0.425	0.93	(0.70)
	0.416	0.226	0.213	0.279	1.06	(0.81)
	0.508	0.172	0.144	0.189	(1.19)	0.91
	0.618	0.109	0.082	0.107	(1.33)	1.02
	0.668	0.084	0.060	0.079	(1.40)	1.06
	0.726	0.059	0.040	0.052	(1.48)	1.13
	0.784	0.034	0.024	0.031	(1.42)	1.10
	0.828	0.020	0.015	0.020	(1.33)	1.00
	0.870	0.011	0.008	0.011	(1.38)	1.00
	0.898	0.006	0.005	0.007	(1.20)	0.86
	0.924	0.004	0.003	0.004	(1.33)	1.00
	0.935	0.004	0.002	0.003	(2.00)	1.33

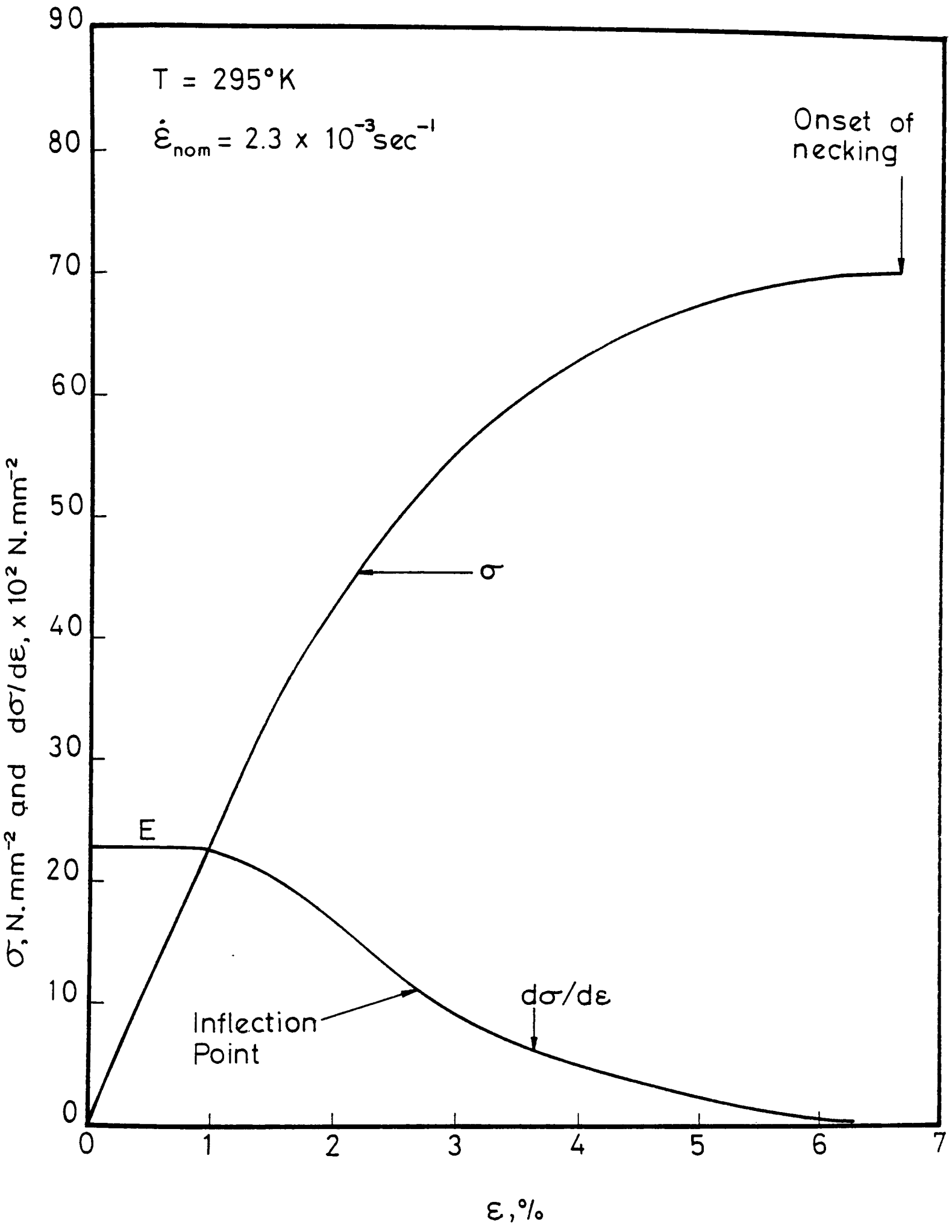
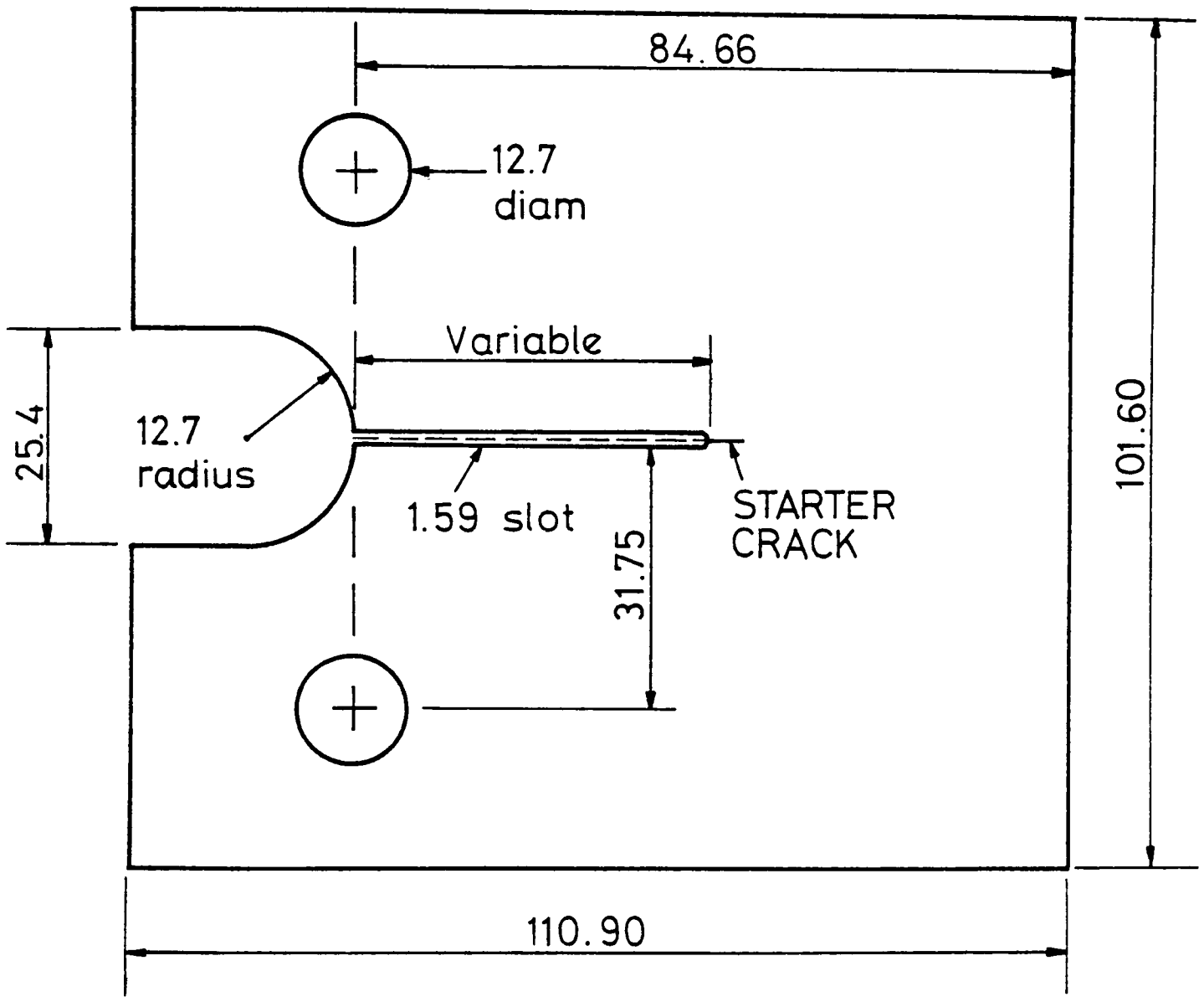


Fig. 6.1 True stress versus true strain for as-received polycarbonate at room temperature



(Dimensions in mm)

Fig. 6.2 Compact specimen configuration for polycarbonate plate tests

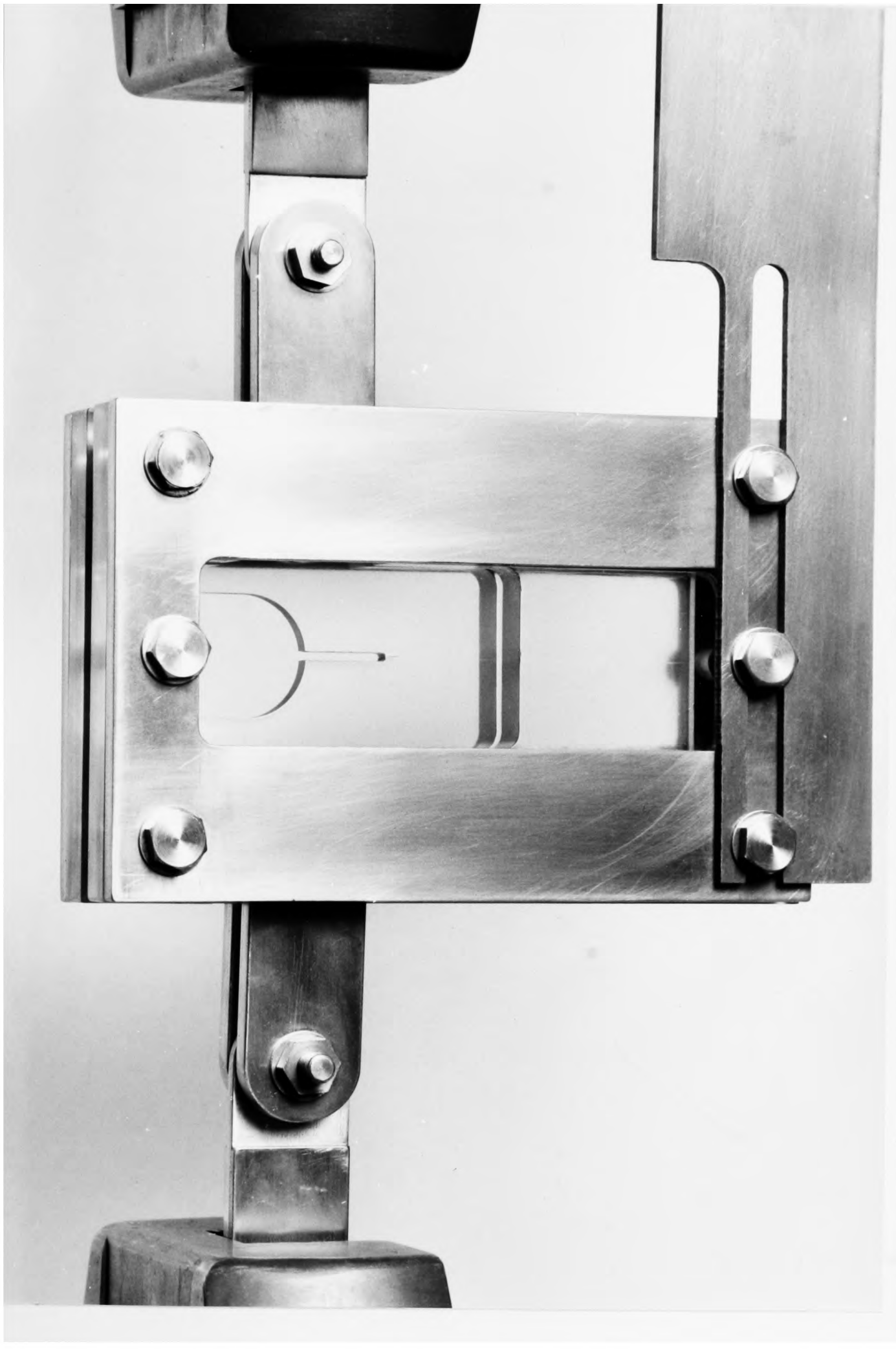


Fig. 6.3 Experimental set-up for polycarbonate plate tests

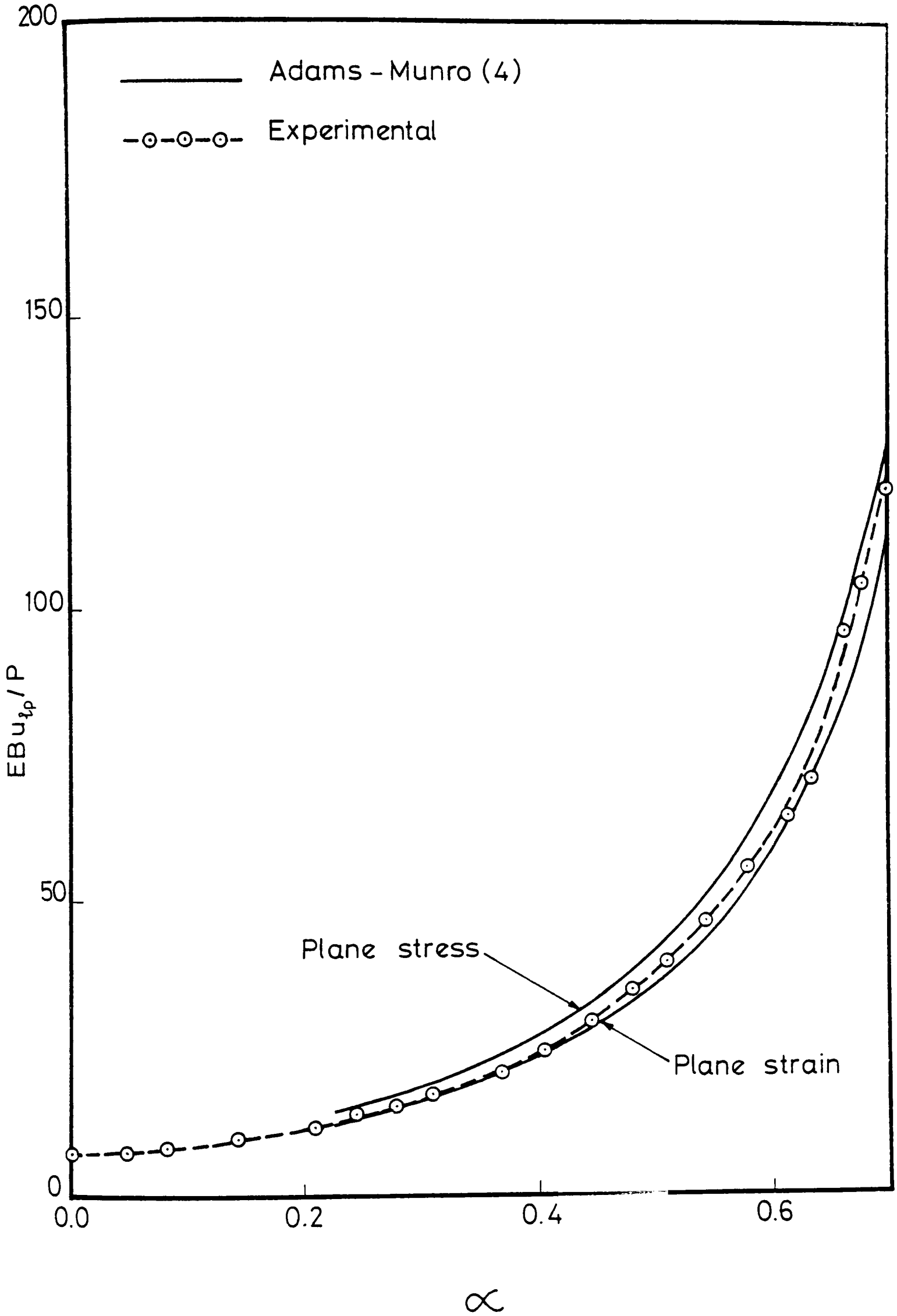
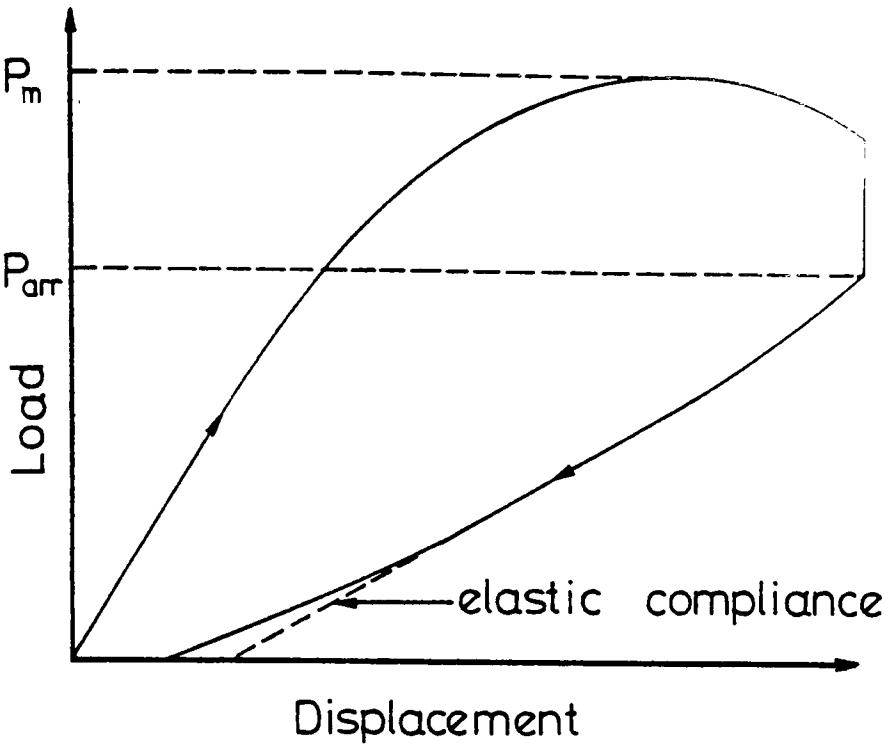
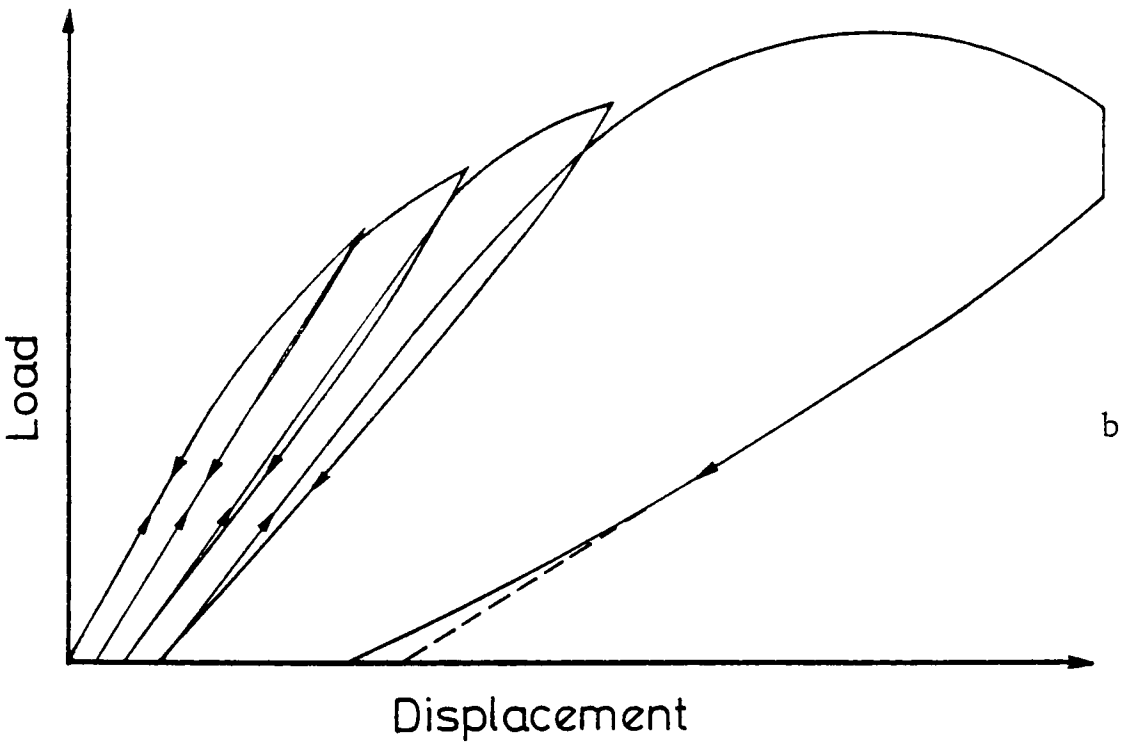


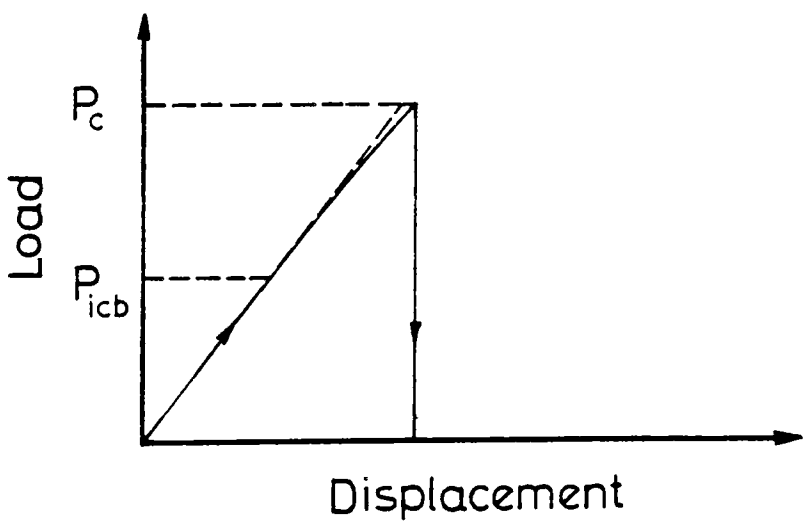
Fig. 6.4 Comparison of analytical and experimental compliance calibrations for notched polycarbonate specimen 1P



a. Finite stable crack extension

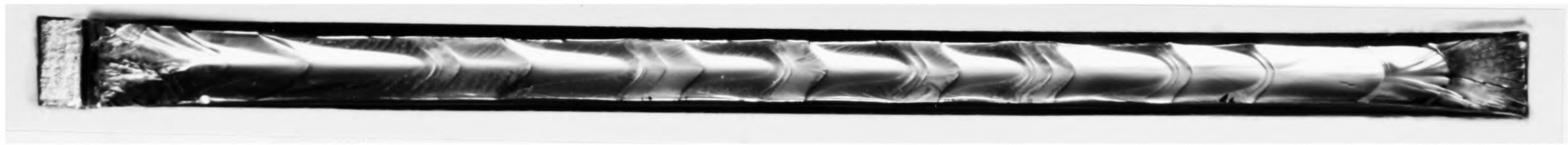


b. Incremental stable crack extension



c. Unstable crack extension

Fig. 6.5 Schematic load-displacement curves for polycarbonate compact specimens (arbitrary scale)



a. Incremental stable crack extension (3P, α_o = 0.040, x 2.4)



b. Unstable, brittle fracture (2P, α_o = 0.013, x 2.3)

Fig. 6.6 Fracture surfaces of polycarbonate compact specimens

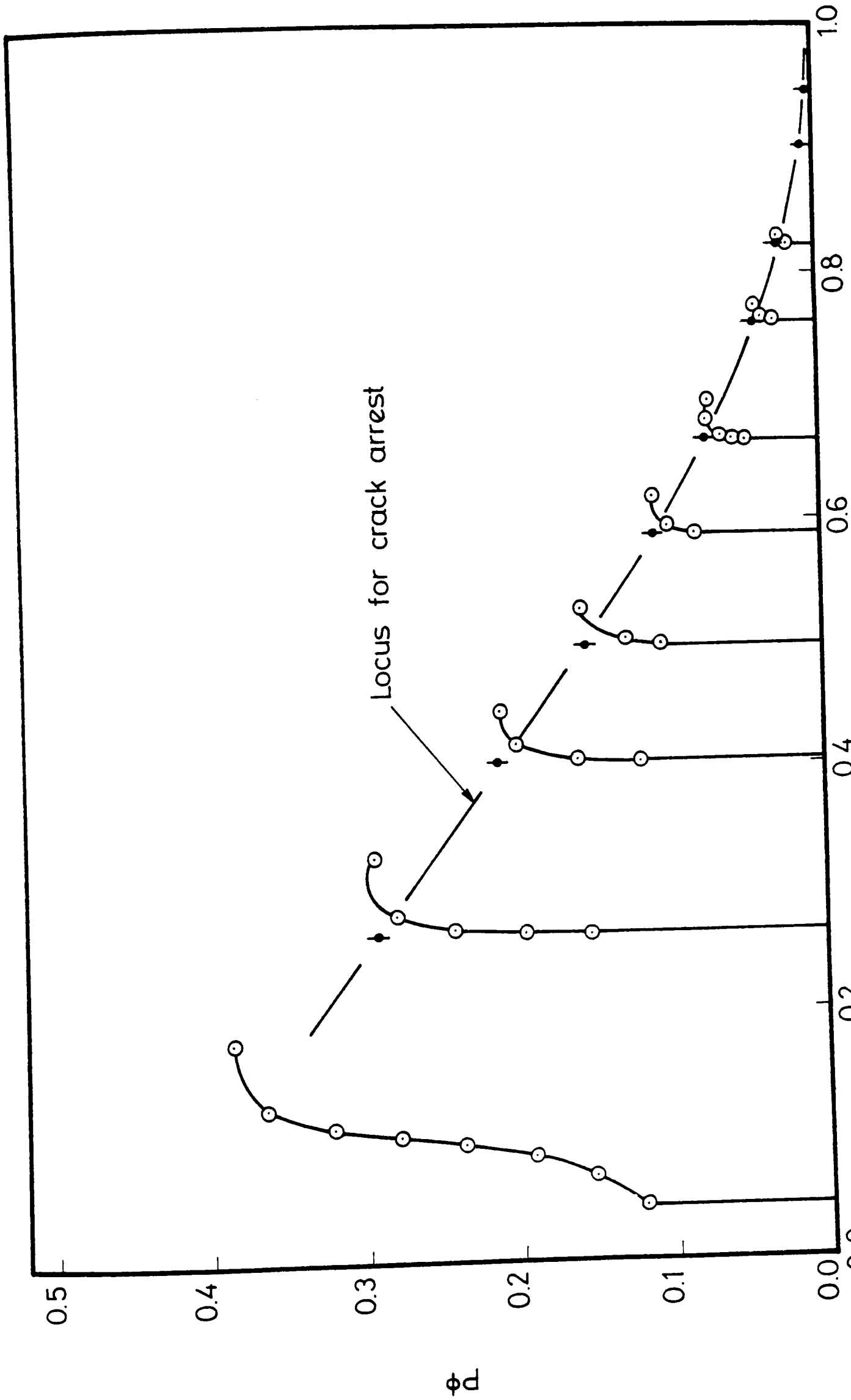


Fig. 6.7 Incremental loading sequence for polycarbonate specimen 3P

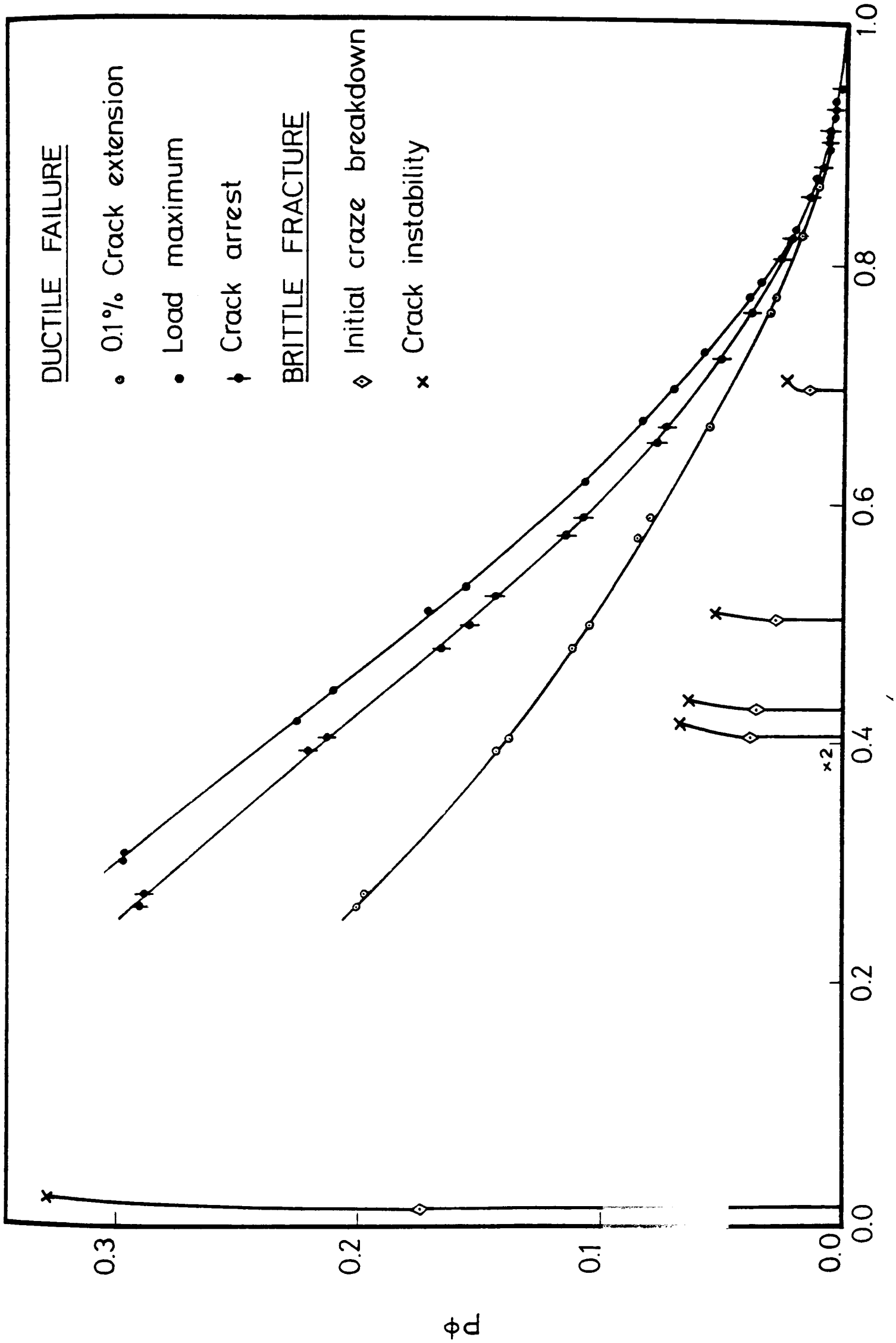


Fig. 6.8 Summary of experimental results for polycarbonate compact specimens

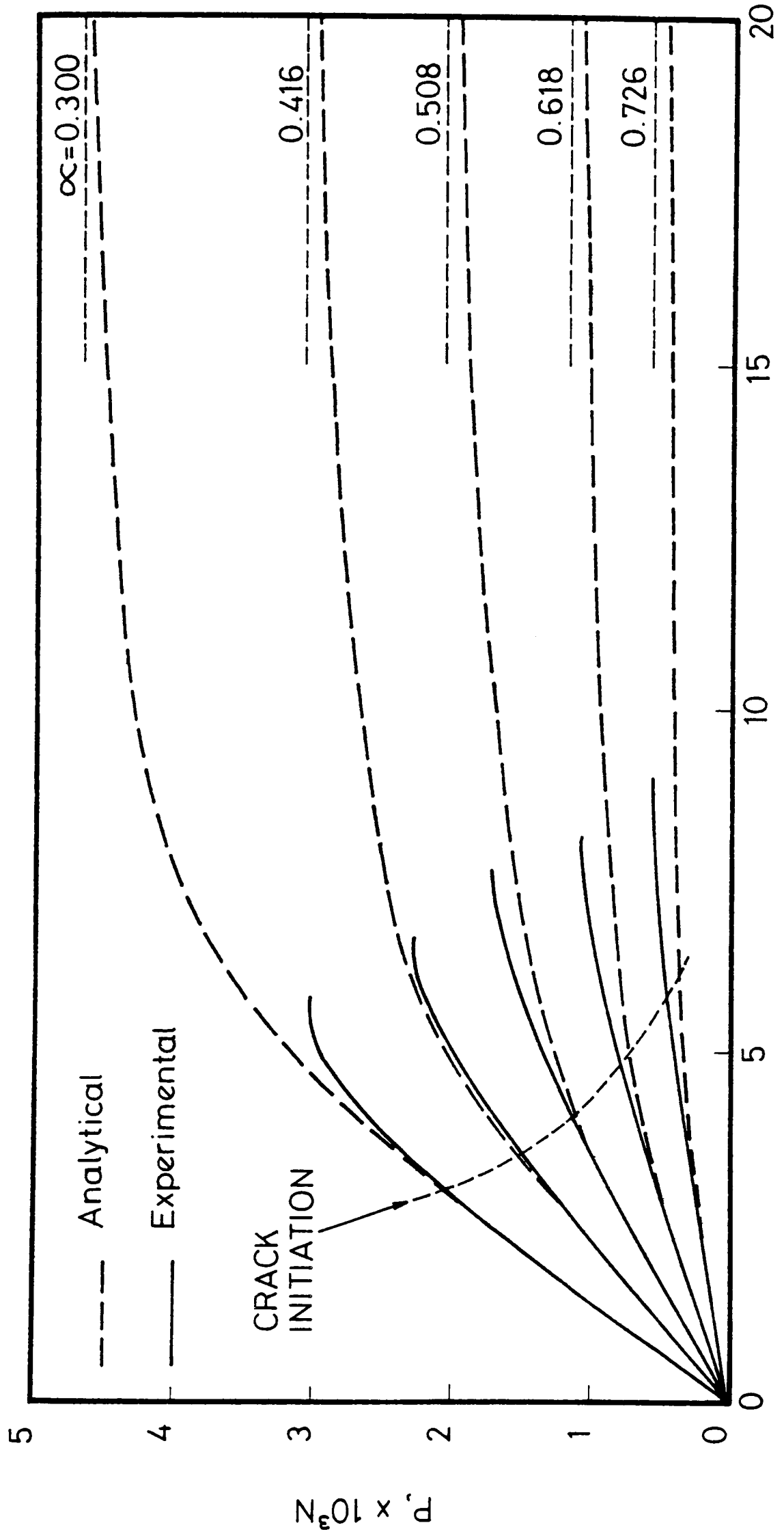


Fig. 6.9 Comparison of analytical and experimental load-displacement curves for polycarbonate compact specimens

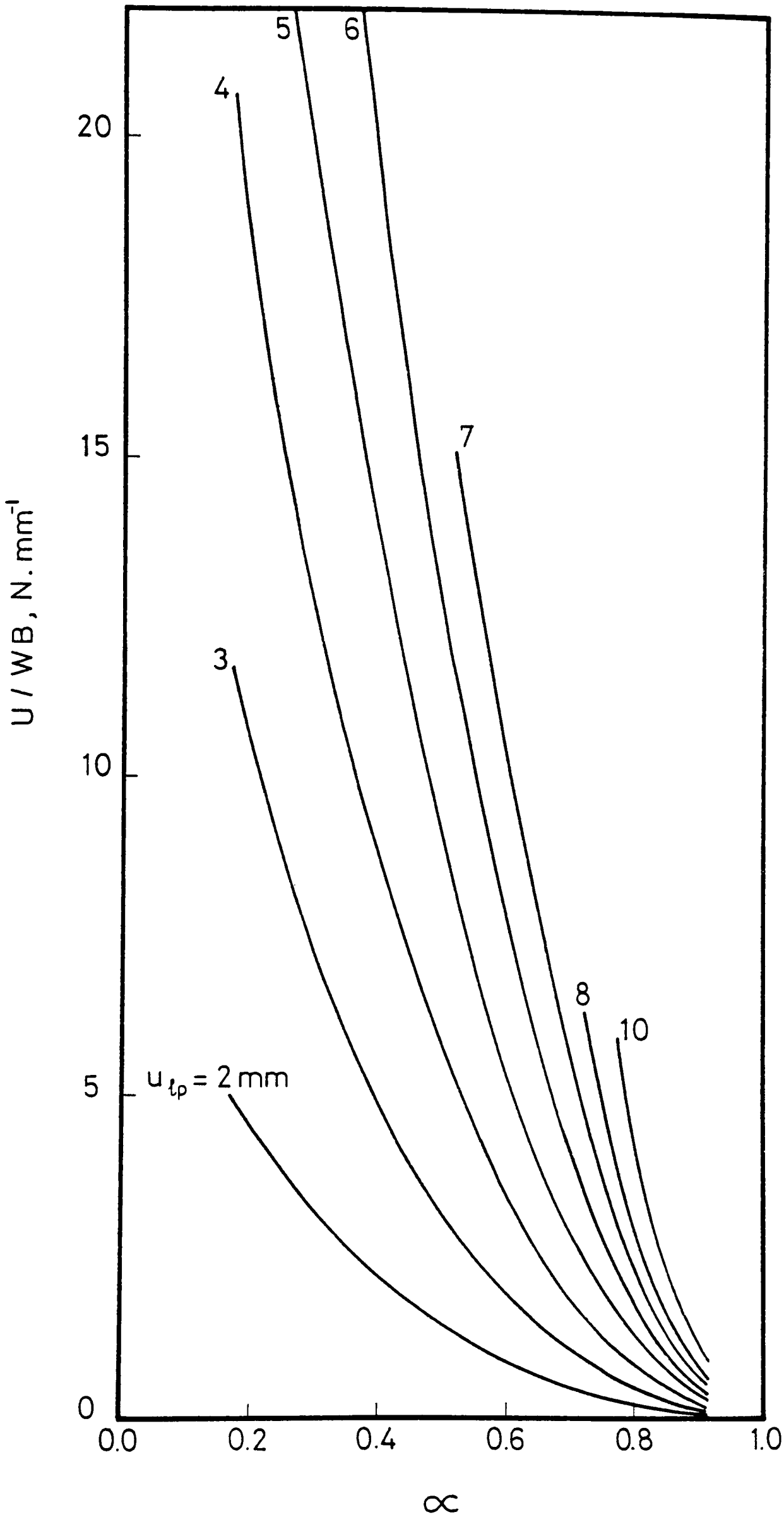


Fig. 6.10 Experimental curves of strain energy versus relative crack length for polycarbonate compact specimens

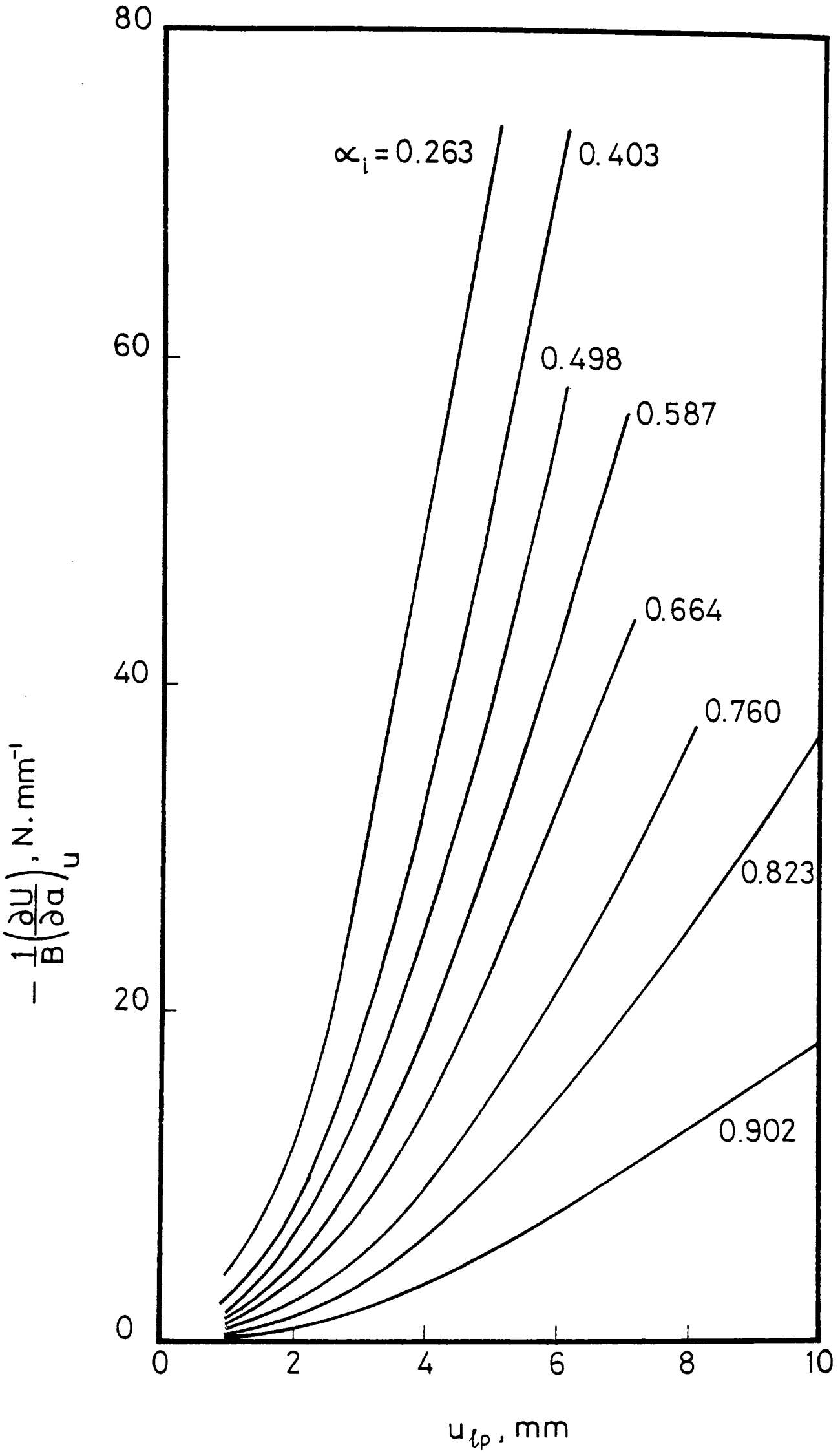


Fig. 6.11 Experimental curves of strain energy slope versus displacement for polycarbonate compact specimens

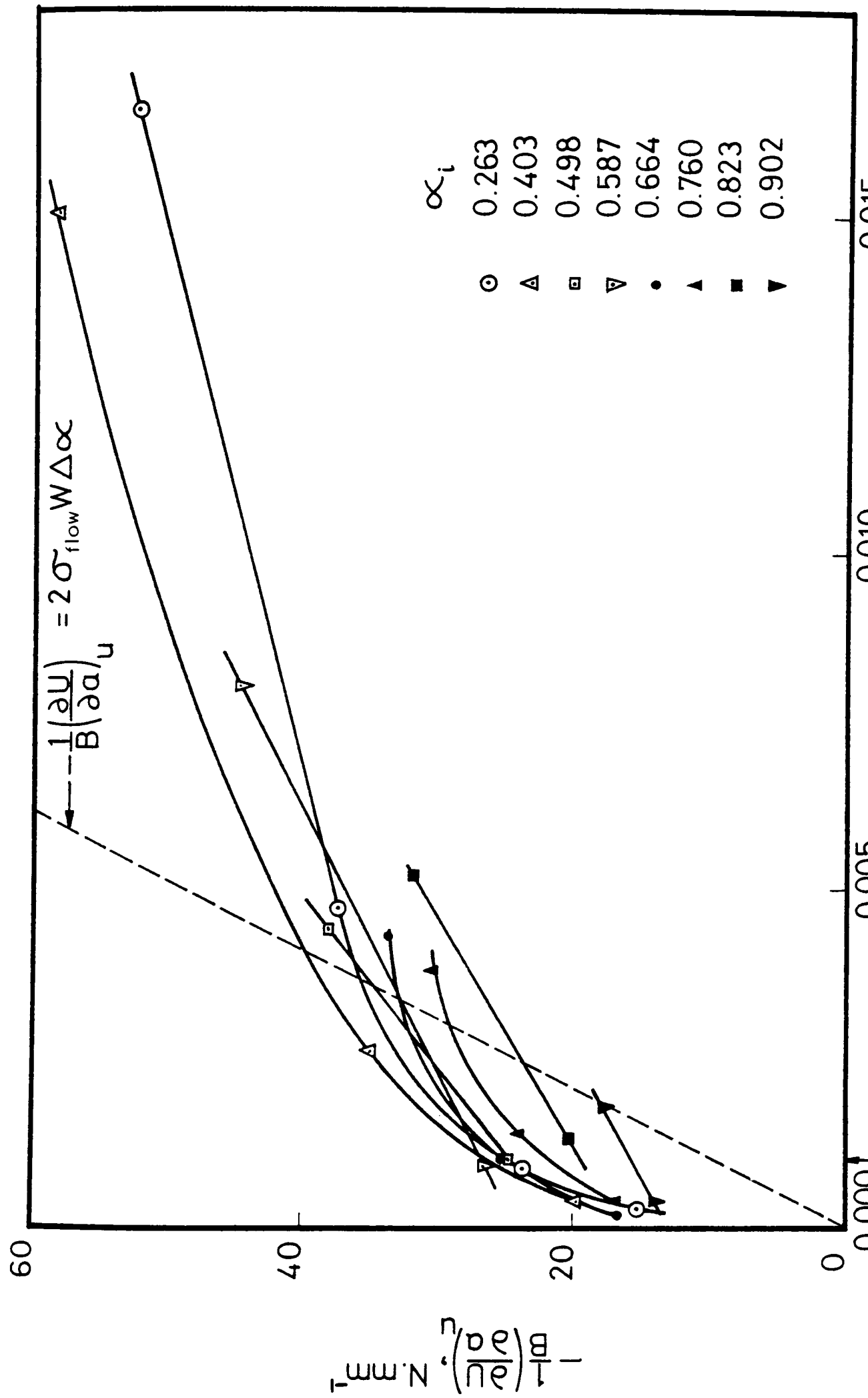


Fig. 6.12 Determination of R_i for crack initiation for polycarbonate compact specimens

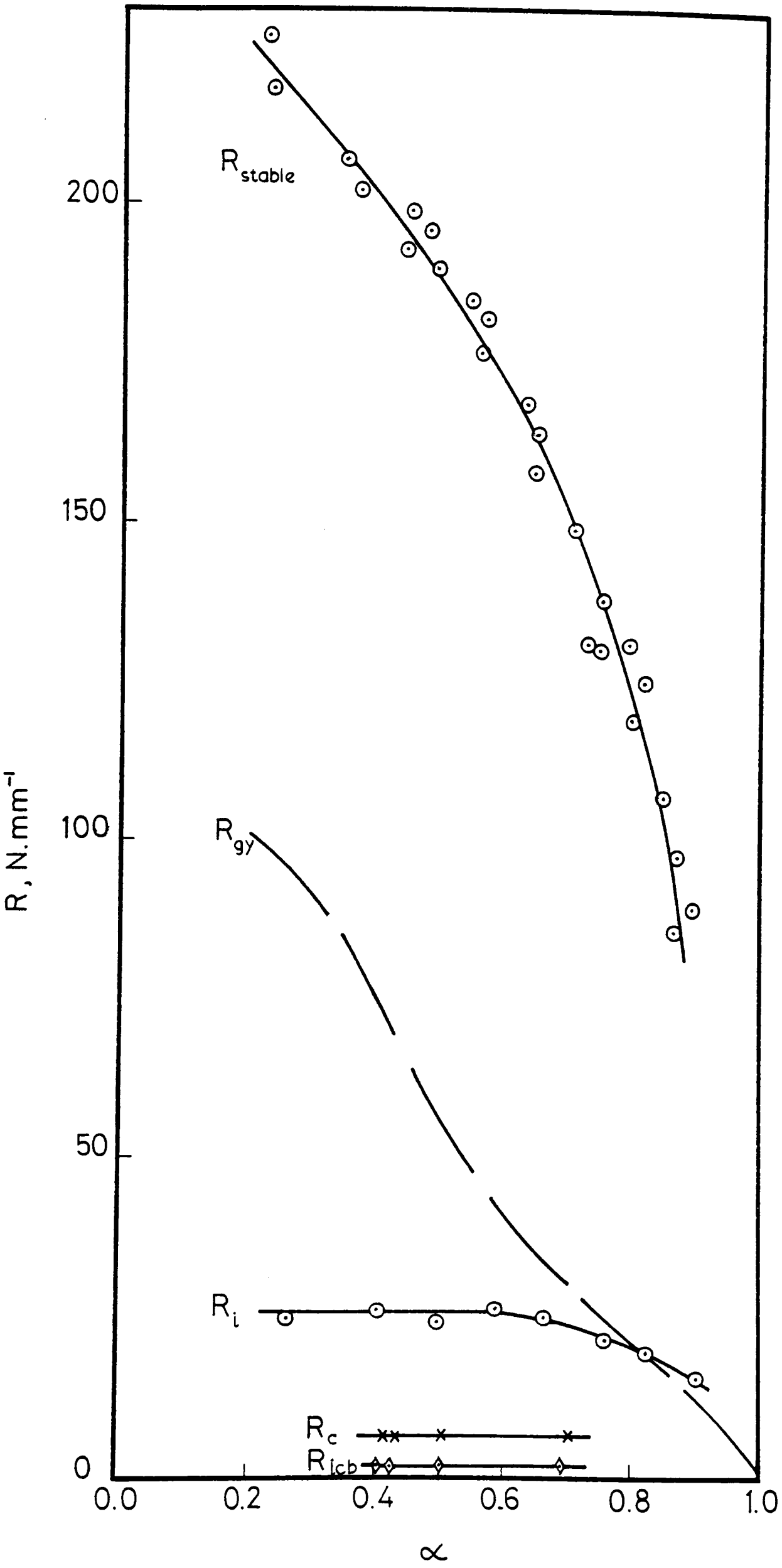


Fig. 6.13 Comparison of R values for polycarbonate compact specimens

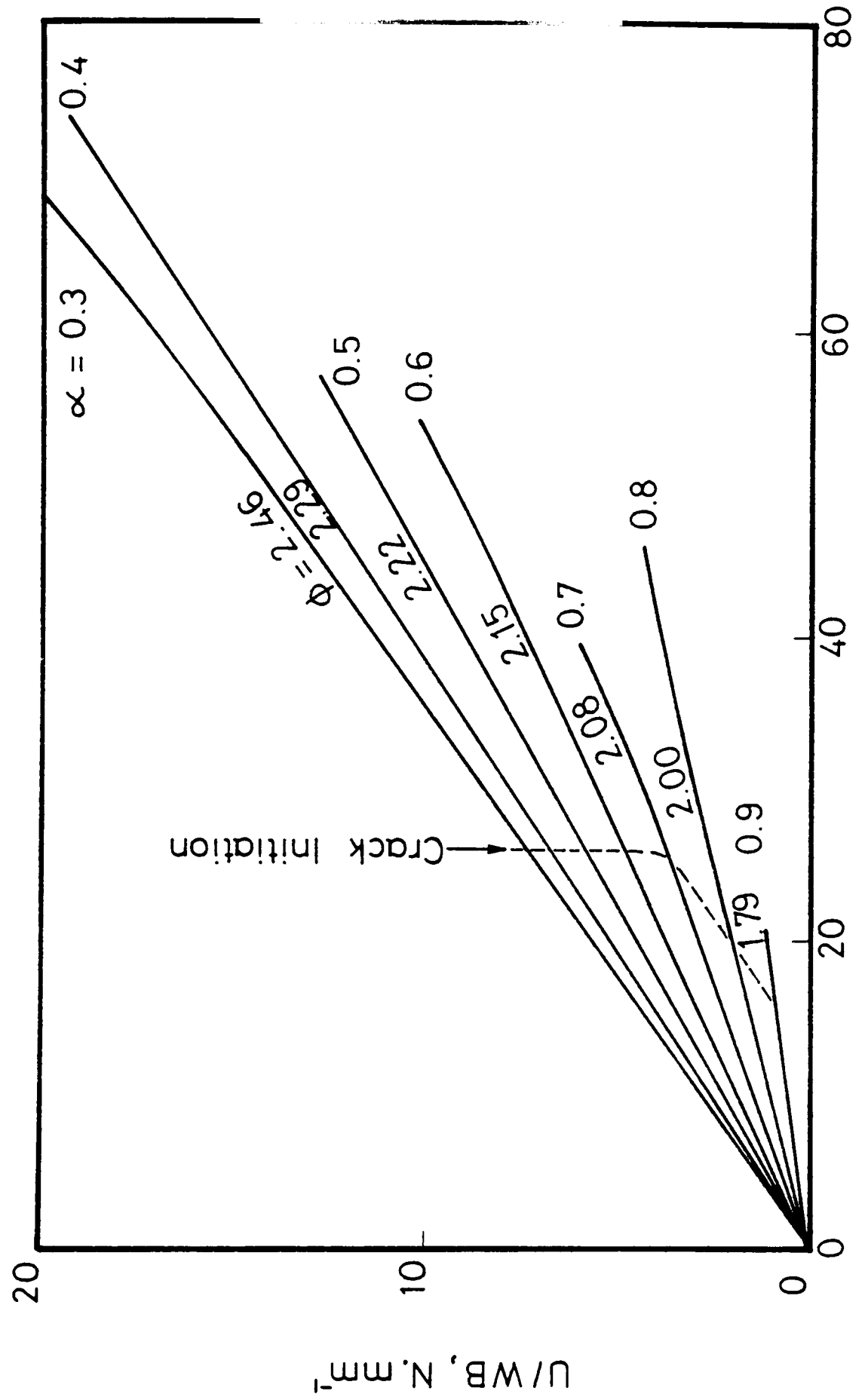


Fig. 6.14 Experimental curves of strain energy versus strain energy slope for polycarbonate compact specimens

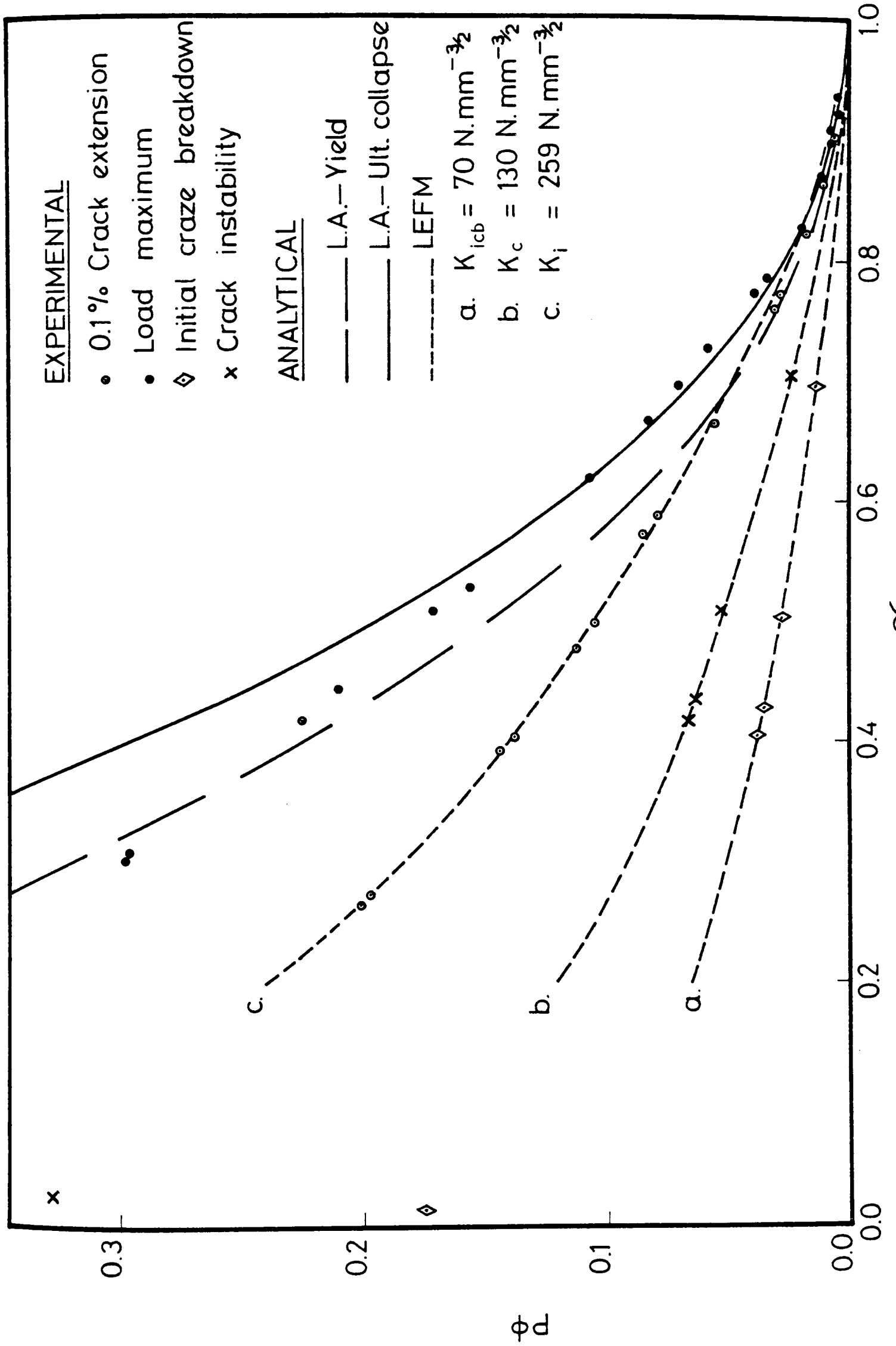


Fig. 6.15 Failure analysis diagram for polycarbonate compact specimens – comparison of analytical and experimental results

CHAPTER 7

CRACK GROWTH IN MARAGING STEEL PLATE SPECIMENS

The maraging steel was a vacuum-induction-melted, vacuum-arc-remelted 18% Ni 200-grade, supplied as 32 mm thickness bars in the solution-annealed condition (820°C air cooled). A maraging heat treatment of 3 hours at 480°C in vacuo was followed for all subsequent specimens producing Rockwell C hardness measurements between 45 and 47. No systematic variation in this hardness through-the-thickness could be detected. Chemical analysis revealed that this particular cast had a high silicon content as shown in Table 7.1.

7.1 Material Characterisation

7.1.a Structural Characterisation

Light photomicrographs of the heat treated steel, Fig. 7.1, showed an extremely uniform microstructure with elongated platelets of massive martensite. Only a small degree of banding (microsegregation of alloying elements during processing) was evident in the SL and ST planes.

7.1.b Uniaxial Tensile Properties

The mechanical properties of the steel in the longitudinal or rolling direction were determined in accordance with B.S. 18 (1) using three enlarged end uniaxial test pieces of square cross-section. These were machined in the soft solution-annealed condition to a cross-sectional area of 5 x 5 mm^2, a parallel length of 35 mm and a minimum shoulder radius of 15 mm and subsequently heat treated. The specimens were tested at room temperature in the Instron testing machine at a crosshead speed of 0.05 in. min^{-1} ($\dot{\varepsilon}_{nom}$ = 3.1 x 10^{-5} sec^{-1}), a 25.4 mm gauge length extensometer

(0-50% strain) being carefully mounted along the parallel length prior to loading in order to monitor the load versus true extension. A true stress-true strain curve for the heat treated steel up to the onset of necking is shown in Fig. 7.2.

The maraging steel exhibited little strain-hardening up to the formation of a neck and failure eventually occurred within the necked region at approximately 10% elongation of the gauge length by a ductile (cup and cone) mode. Microscopic examination of the fracture indicated that the fracture mode was microvoid coalescence accompanied by substantial stretching.

Both the 0.2% offset yield stress, σ_y and the ultimate tensile strength, σ_u were calculated and the results are shown in Table 7.2. Unfortunately, there were insufficient data to check the validity of the parabolic relationship, $\sigma = C\ \varepsilon^n$ beyond the onset of necking and thereby determine a strain-hardening exponent, n for the maraging steel and, again the true strain at plastic instability, 0.022 is quoted as a nominal strain-hardening exponent valid in the region of 2.2% strain. Finally, the static Young's modulus was measured from a single specimen by carrying out a shakedown procedure within the elastic region prior to loading to failure. After loading and unloading the test piece several times a constant slope and hence value of E was obtained; this value being checked by relocation of the extensometer at right angles to the gauge section.

7.1.c Plane Strain Fracture Toughness

Three standard compact specimens of width, 50.8 mm and thickness, 25.4 mm were prepared in accordance with B.S. 5447: 1977 (2) and A.S.T.M. E399-72 (3) for the measurement of the plane strain fracture toughness, K_{Ic}. Specimens were machined in the solution-annealed condition with chevron crack starter notches in the L-T orientation, where L is the direction normal to the crack plane and T, the expected direction of crack

propagation. After heat treatment the test pieces were fatigue precracked in an Amsler vibrophore fatigue machine at stress intensity levels permitted by the standards as shown in Appendix 5.

During a standard K_{Ic} test the edge opening displacement is measured as a function of load using a displacement gauge mounted on the front face of the specimen. In the present case this was achieved by means of attachable knife edges located 6.35 mm apart for a displacement range of 6.35-12.7 mm. A 10 ton capacity Mand servo-hydraulic testing machine was required for the 25.4 mm thick sections which were loaded to failure at a nominal stress intensity rate of approximately 6,850 N $mm^{-3/2}$ min^{-1}. Although the latter was outside the recommended limit of 1040-5200 N $mm^{-3/2}$ min^{-1} this was not felt to be a problem since the fracture toughness of maraging steel is known to be independent of loading rate (4).

A summary of results obtained from the tests is given in Appendix 5. The load-displacement records were of type I i.e. the load increased continuously up to a maximum P_m, which was less than 10% above the 5% offset load, P_Q as required by the standards. Stable ductile crack extension continued after a load maximum had been achieved, beyond the range of the displacement gauge and the specimens eventually failed by a tearing fracture mode. The resultant "mixed mode" fracture surfaces consisted of approximately 50% square fracture in the mid-thickness with 25% slant fracture at the two surfaces and met all the standard requirements with respect to crack length and crack plane orientation.

From Appendix 5 it is apparent that the specimens were marginally "invalid" according to the size requirement, a, W-a, $B \geqslant 2.5\ (K_Q/\sigma_y)^2$ as only one specimen of the three tested provided a valid K_{Ic} value. However, the mean K_Q for all three tests was calculated and is quoted in Table 7.2 as a conditional plane strain fracture toughness. Table 7.2 also includes estimates of a conditional plane strain energy release rate,

$\mathcal{G}_Q = K_Q^2 (1-\nu^2)/E$ and, for comparison, an apparent elastic strain energy release rate corresponding to a load maximum, $\mathcal{G}_m = K_m^2 (1-\nu^2)/E$ calculated on the basis of the maximum load, P_m and the initial fatigue crack length, a_o.

7.2 Experimental Procedure

The influence of through-thickness constraint on the fracture toughness of the steel was investigated using a series of modified compact specimens as shown in Fig. 7.3 and Table 7.3. All dimensions were identical to those used in the standard plane strain fracture toughness tests, the only variables being thickness, B and crack length, a_o or remaining ligament, $W-a_o$. Measurements of the fracture toughness, R_i for crack initiation were made using Landes and Begley's approximate method for a deeply cracked compact specimen, equation 5.16 (5) and, in the case of the 3.1 mm thick specimens, by evaluation of the calibration function $-\frac{1}{B}\left(\frac{\partial U}{\partial a}\right)_u$ using the method developed by Begley and Landes (6).

7.2.a Specimen Preparation

Each specimen was machined to the appropriate dimensions in the solution-annealed condition, the notches being produced in the L-T orientation with an electro-discharge machine giving notch tip radii, $r < 0.25$ mm. After heat treatment and for the purposes of the surface deformation studies later, the region of each plate immediately ahead of the notch tip was ground flat on both sides with successively finer grades of silicon carbide paper and finally polished with 6 μm and 1 μm diamond paste.

All specimens were fatigue precracked in an Amsler vibrophore fatigue machine in accordance with the standards for plane strain fracture toughness tests using a maximum stress intensity for the fatigue cycle of $0.35\ K_Q$. The minimum fatigue crack length for the 12.7 mm and 6.3 mm thick specimens was 1.27 mm. However, in order to avoid the problems associated with

excessive bowing of the fatigue crack front in the thin plates, 3.1 mm thickness, these samples were slit to a depth of approximately 0.76 mm using a wire cutting attachment to the electro-discharge machine. This produced slits with a root radius of 0.14 mm. These specimens were then fatigue cracked a further 0.51 mm so that the positions of the crack tip and the sides of the 2.38 mm wide notch encompassed a 30^{o} envelope as recommended by the British and A.S.T.M. standards (2) (3).

7.2.b Experimental Apparatus

A photograph of the experimental set-up is shown in Fig. 7.4, the linkages being positioned between the crosshead and an "F" tensile load cell (10,000 lb. capacity) in the Instron testing machine. All specimens were pin-loaded in tension with the same linkages, brass spacers being used for the thinner plates. Preliminary tests indicated that no lateral buckling occurred even with the thinnest specimens so that anti-buckling plates were not required.

Using Landes and Begley's modified compact specimen configuration (5) enabled both the load line and load pin displacement to be monitored simultaneously as a function of load. This was accomplished by means of three displacement gauges, one of which was mounted at the front of the specimen along the load line and the remaining two each side of the loading grips between attachable knife edges located 3.56 mm apart; the output of the latter being averaged to cancel any effects of misalignment. The strain gauge bridge circuit for each displacement gauge consisted of four temperature-compensated constantan foil gauges and exhibited a linear response over a displacement range of at least 2.5 mm. After amplification, the output signals from the three strain gauge bridges were recorded as a function of time by means of a multi-channel ultra-violet galvanometer recorder, the time scale allowing the output strains to be related to the

load recorded on the Instron chart. Both the load pin and load line displacements were measured to ± 0.013 mm.

7.2.c Loading Procedure

The plate tests were carried out at a room temperature of 296 ± 2°K and about 45% relative humidity ± 5%. In the first series of tests precracked specimens 1M-6M, to be used to evaluate the calibration function, $-\frac{1}{B}\left(\frac{\partial U}{\partial a}\right)_u$, were loaded at a crosshead speed of 0.05 in. min^{-1} to just beyond a load maximum. The remaining sets of specimens of identical crack size were then used to determine the crack initiation point for each initial crack length by loading to increasing displacements corresponding to various amounts of crack extension. The following experimental procedure was adopted:

a. Each specimen was loaded to a different displacement value at a crosshead speed of 0.05 in min^{-1} and then rapidly unloaded at a crosshead speed of 0.2 in min^{-1}.
b. After the surface deformation studies (see section 7.2.d), the final crack position was marked by means of secondary fatigue cracking.
c. Finally, each specimen was pulled apart in tension to reveal the extent of crack growth during monotonic loading.

In order to preserve the situation created by the monotonic load it is necessary to limit the maximum stress intensity applied initially during subsequent fatigue cracking. In the present case secondary fatigue cracking was performed in the Amsler vibrophore fatigue tester at a maximum stress intensity less than 0.6 of the final value applied to each specimen during monotonic loading, with a stress intensity range of approximately 0.9 of this maximum value. This maximum stress intensity represented the lowest limit compatible with continued crack extension from a crack tip effectively blunted by the preceding monotonic load.

7.2.d Surface Deformation Studies

During preliminary tests the surface deformation ahead of the crack tip was studied by means of photographs taken of plates in the loaded state by oblique illumination. Although quick and convenient, this method did not provide any quantitative information of the size and shape of the surface depression and required sustained loading of the specimens at the final displacement. Therefore, it was decided that quantitative measurements of the surface depression ahead of the crack tip be made by a profile measuring technique using specimens in the unloaded state.

In order to measure the large surface displacements encountered with the maraging steel a method was adopted using an optical microscope bench. Each specimen was mounted on a table having a coarse micrometer screw-feed in the x and y horizontal directions. A 0.5 mm diameter steel ball attached to the optical head was then lowered onto the specimen and using the fine displacement controls on the optical head, the surface displacement was measured along a traverse taken along the line of the crack from the crack tip. The maximum surface displacement in the through-thickness direction, w close to the crack tip was determined to $\pm$ 2.5 x 10^{-4} mm. In addition, a measure of the surface plastic zone size was obtained by defining ρ'_x, as the maximum distance along the line of the crack beyond which surface displacements were $\leqslant$ 2.5 x 10^{-4} mm i.e. the resolution of the measuring technique. Measurements taken from both sides of each specimen were averaged.

7.2.e Fractography

The initial fatigue crack length and crack extension were measured directly from the fracture surfaces using the optical microscope bench. Following the British and A.S.T.M. procedure for K_{Ic} testing (2) (3), the initial crack length, a_o was defined as the average of measurements taken at the mid-thickness and two quarter-thickness positions of each plate.

The crack extension, Δa was taken to be the maximum distance between the two regions of fatigue cracking. Measurements were made to $\pm$ 0.0025 mm using the optical microscope with a magnification of 48.

A selection of fracture surfaces were also examined by scanning electron microscopy.

7.3 Results and Analysis of Results

Fig. 7.5 and 7.6 show examples of the load-displacement curves for the maraging steel compact specimens loaded to different displacement values; all load levels being well below that necessary to cause yielding at the loading holes i.e. 55.4 x 10^3 N. Crack growth was stable in each case but for the 12.7 mm thick plates crack extension occurred in a discontinuous manner with the load-displacement records exhibiting several bursts of displacement without a corresponding increase in load, "pop-in," accompanied by audible clicks.

Some typical fracture surfaces of the various thickness maraging steel specimens tested are presented in Figs. 7.7-7.10 from which the crack growth extension areas are easily identified between the regions of fatigue cracking. The fracture surfaces for all thicknesses showed similar features. It is apparent that failure was initiated by crack extension from the mid-thickness region in the plane of the fatigue precrack, this being accompanied by the development of yield zones at the surface. With increasing crack extension the extent of surface yield increased resulting in shear lips at the surface at 45^{o} to the initial fatigue crack plane and a mixed mode or fully slant fracture.

Examination of the fractographs reveals that the extent of the transition from in-plane to out-of-plane plastic deformation up to a load maximum varied according to the plate thickness but that for a given plate thickness, such as 3.1 mm, it also depended upon the amount of slow crack

extension. Thus, the length of the region of square fracture produced up to a load maximum decreased with decreasing plate thickness until in the case of the 3.1 mm thick plates, only a triangular zone was formed close to the fatigue precrack. However, although the maximum length of this triangular zone remained approximately constant for these specimens, a fully slant fracture only developed after sufficient slow crack growth; the latter being promoted in specimens of shorter crack length or increasing remaining ligament.

The experimental test data obtained for all the maraging steel compact specimens are listed in Appendix 6 where u_{1pf} and u_{11f} refer to the final load pin and load line displacement achieved in each test, respectively. A summary of results for all the plates is shown in Fig. 7.11 where the load is plotted as the dimensionless failure parameter, $P^{\phi} = P/0.4142\ \sigma_u WB$, equation 5.11. For unambiguous presentation, the initial crack size has been plotted as the mean initial relative crack length, $\bar{\alpha}_o$ for each set of specimens, the maximum variation in $\bar{\alpha}_o$ being 0.005. In addition, the final crack size was taken as $\bar{\alpha}_o + \Delta\alpha$ i.e. the sum of the mean initial relative crack length and the maximum relative crack extension which generally occurred at the mid-section. This may or may not correspond to the real physical final crack position depending upon the curvature of the fatigue precrack and the variation of individual values of α_o from the mean. However, the maximum deviation of $\bar{\alpha}_o + \Delta\alpha$ from the real final crack length was calculated to be only 0.004, 0.006 and 0.007 for the 3.1 mm, 6.3 mm and 12.7 mm thick specimens, respectively.

The P^{ϕ} versus α curves for the 3.1 mm thick plates exhibited a similar shape with an initial steep rise in load with small increase in crack extension as the surface yield zones developed. At higher load levels close to the load maximum, however, extensive crack growth took place with further crack extension occurring rapidly under decreasing load. In

comparison, the P^{ϕ} versus α curves for the 6.3 mm and 12.7 mm thick plates showed more extensive slow crack growth prior to a load maximum and a significant reduction in the maximum load level achieved such that the load maximum for the 12.7 mm thick plates was only 1-9% above the initial pop-in value.

7.3.a Determination of R_i Using Landes and Begley's Approximate Method

The fracture toughness, R_i for crack initiation was determined for each plate thickness using the approximate relation for a deeply cracked compact specimen, equation 5.16 i.e. $-\frac{1}{B}\left(\frac{\partial U}{\partial a}\right)_u = 2U_{11}/(W-a_o)\ B$, $\alpha \geqslant 0.6$.

For the 3.1 mm and 6.3 mm thick specimens a crack initiation measurement point was obtained using the interpolation procedure suggested by Landes and Begley (5). The approximate strain energy rate corresponding to a given crack extension was calculated after measuring the total area under the appropriate load-load line displacement record with a planimeter. The crack initiation point was then taken as the intersection of the $2U_{11}/(W-a_o)\ B$ versus Δa curve with the stretch zone line defined by equation 6.1 i.e. $2U_{11}/(W-a_o)\ B = 2\sigma_{flow}\ \Delta a$. The results are shown in Fig. 7.12.a and b for the 3.1 mm and 6.3 mm thick specimens, respectively where the relative crack extension, $\Delta\alpha$ has been used. It is clear that in both cases at least one of the experimental results lies on the stretch zone line. For the 3.1 mm thick plates, the results for the two different initial crack sizes appear to define a single curve from which an interpolated crack initiation point is readily obtained. On the basis of the interpolation procedure for the 6.3 mm thick plates, the one experimental point on the stretch zone line has been taken as the crack initiation measurement point.

The load-displacement records for all four 12.7 mm thick plates, Fig. 7.6.d, showed a distinct pop-in soon after loading which resulted in an extremely large load drop in one case (34M). Pop-in is known to be

due to the abrupt advance of the crack front at the mid-section being suppressed by the out-of-plane plastic deformation at the surface and leads to the thumb-nail shaped crack arrest profile shown in Fig. 7.9.b. Assuming that the initial burst of displacement corresponded to crack initiation from the fatigue precrack, R_i for crack initiation was determined directly for each specimen from the load-load line displacement records after measuring the strain energy, U_{11} up to the critical displacement with a planimeter.

A summary of results obtained for all three plate thicknesses is given in Table 7.4.a and b which include a critical stress intensity factor, K_i for crack initiation calculated from R_i assuming plane strain crack tip conditions, as well as the crack extension, $\Delta\alpha_m$ and for comparison, an apparent fracture toughness, $\left[2U_{11}/(W-a_o)B\right]_m$ up to a load maximum.

Values of 80 N mm^{-1}, 68.9 N mm^{-1} and 103 $\pm$ 3 N mm^{-1} were obtained for R_i for the 3.1 mm, 6.3 mm and 12.7 mm thick specimens, respectively; the latter in excellent agreement with the conditional plane strain energy release rate, $\mathcal{G}_Q$ of 101 $\pm$ 7 N mm^{-1} determined for the 25.4 mm thick plates. The agreement between the measured and calculated (7) compliance of each load-load line displacement record confirms the general validity of the performance of each test.

7.3.b Determination of R_i Using the Calibration Function, $-\frac{1}{B}\left(\frac{\partial U}{\partial a}\right)_u$ For the 3.1 mm Thick Specimens

For the 3.1 mm thick specimens, R_i was also determined by evaluation of the calibration function, $-\frac{1}{B}\left(\frac{\partial U}{\partial a}\right)_u$ from the load-load pin displacement records of the precracked specimens, 1M-6M, 8M, 11M, 18M, 22M and 23M. Some examples of these experimental curves are given in Fig. 7.13 where they are compared with those derived from the simple model (see section 5.2.a.ii). Within the linear elastic regime the experimental curves appear

to deviate from those based on Adams and Munro's plane stress compliance calibration (7). This is confirmed in Table 7.5 and Fig. 7.14 which compares the measured and calculated elastic compliances for all the 3.1 mm thick specimens tested. In spite of some variation the experimental results show a similar dependence on α as the calculated values, lying approximately 9% above the analytical curve.

Considering the fully plastic regime of Fig. 7.13, as in the case for polycarbonate the analytical values were calculated on the basis of the ultimate tensile strength, σ_u to allow for some work-hardening. Again, as for the polycarbonate the experimental limit loads lie considerably below the analytical values corresponding to an infinite displacement except at longer crack lengths where the extent of slow crack growth decreased significantly.

By measuring the areas under the experimental load-load pin displacement records at constant displacement using a planimeter, the experimental curves of strain energy, U/WB versus relative crack length, α shown in Fig. 7.15 were obtained, the results covering the displacement range of 0.5-2.16 mm. The slopes of these curves were then measured graphically at selected values of α to give the required calibration function, $-\frac{1}{B}\left(\frac{\partial U}{\partial a}\right)_u$ as a function of displacement, Fig. 7.16. The values of $\bar{\alpha}_o$ selected corresponded to the five sets of specimens, 7M-26M, of identical initial crack size.

The $-\frac{1}{B}\left(\frac{\partial U}{\partial a}\right)_u$ values associated with increments of crack extension, $\Delta\alpha$ for each specimen were then computed from Fig. 7.16 according to the initial crack length, $\bar{\alpha}_o$ and the measured displacement, u_{lpf}. The resultant plot of $-\frac{1}{B}\left(\frac{\partial U}{\partial a}\right)_u$ versus crack growth increment, $\Delta\alpha$ is presented in Fig. 7.17. Although the results show some scatter at large values of $\Delta\alpha$ (estimated uncertainty in $-\frac{1}{B}\left(\frac{\partial U}{\partial a}\right)_u$ of 10% at the highest displacements) all the experimental points appear to belong to a single curve independent

of initial crack size.

Landes and Begley's interpolation procedure was used to define a crack initiation point in Fig. 7.17 although only one of the experimental results was in reasonable agreement with the equation for the stretch zone, deviations occurring at higher energy levels close to the plateau region at approximately 100 N mm^{-1}. The results are summarised in Table 7.6 where, on the basis of the five experimental results at the plateau or pop-in (a region of large increase in true crack extension), a mean value of 99 $\pm$ 2.5 N mm^{-1} has been quoted for R_i. As for the 12.7 mm thick plates, this value is in excellent agreement with the conditional plane strain energy release rate, $\mathcal{J}_Q$ of 101 $\pm$ 7 N mm^{-1} but it is 24% larger than 80 N mm^{-1} obtained for the same specimens using the approximate relation for $-\frac{1}{B}\left(\frac{\partial U}{\partial a}\right)_u$.

A comparison of R_i and $-\frac{1}{B}\left(\frac{\partial U}{\partial a}\right)_u$ corresponding to a load maximum (termed R_{mc} - see section 7.4.b) is shown in Fig. 7.18. It is apparent that while R_i is a constant independent of initial crack length for the crack size range investigated, R_{mc}, which is considerably larger than R_i, exhibits a geometry dependence at all crack lengths decreasing continuously from 432 N mm^{-1} ($\bar{\alpha}_o$ = 0.386) to 238 N mm^{-1} ($\bar{\alpha}_o$ = 0.766).

Finally, experimental curves of strain energy, U/WB versus strain energy slope, $-\frac{1}{B}\left(\frac{\partial U}{\partial a}\right)_u$ for the 3.1 mm thick maraging steel compact specimens are given in Fig. 7.19. It is clear that a linear relation does exist between the two functions within the crack initiation locus over the range $0.4 \leqslant \alpha \leqslant 0.8$, with deviations occurring only at higher energy levels. Thus, the relationship is of the form given by equation 6.2 i.e. $-\frac{1}{B}\left(\frac{\partial U}{\partial a}\right)_u = \phi\, U/(1-\alpha)WB$ with the values of ϕ shown in the figure following closely those calculated by the linear elastic—fully plastic model in Appendix 3 for α = 0.6 and 0.7. Therefore, on the basis of measurements of load pin displacement, the use of the approximate relation,

equation 5.16 i.e. $\phi = 2.0$ for $\alpha \geqslant 0.6$ should underestimate values of $-\frac{1}{B}\left(\frac{\partial U}{\partial a}\right)_u$ by 16% at $\alpha = 0.6$ and by only 5% at $\alpha = 0.7$.

7.3.c Surface Deformation Studies

Small circular surface plastic zones developed at the crack tip for all specimens soon after loading. Under rising load the size of these zones increased in the x and y directions until an equilibrium – maximum height of approximately 6-7 mm was achieved being accompanied by the onset of surface crack growth. An example of surface plastic zone development is given in Fig. 7.20. This was obtained during preliminary tests for a 3.1 mm thick specimen loaded well beyond a load maximum and shows the growing crack surface rotating into a single plane at 45° to the sheet surface. In fact, the crack trace at the surface follows closely the planes of maximum shear stress for an elastic material deforming in plane stress (compare Fig. 3.3.b).

It is known that on unloading, considerable reverse plastic flow occurs close to the crack tip as the elastic tensile stresses are replaced by compressive ones (8). However, comparison of Fig. 7.20.a and b indicates that while the depth of the surface displacement near the crack tip is substantially reduced, the plastic zone size is virtually unaltered. Thus, measurements of off-load surface plastic zones should be indistinguishable from fully loaded values. In addition, both theoretical (8) and experimental (9) (10) results indicate that good estimates of full-load through-thickness displacements may be obtained from residual measurements by multiplying the latter by a factor of 2.

The maximum surface displacement, w along the x axis occurred 0.25-1.52 mm ahead of the fatigue precrack depending upon the extent of slow crack growth and, as shown in Appendix 6, there was some variation in values obtained from each side of an individual specimen. From these

measurements, an average through-thickness strain, $\bar{\varepsilon}_z$ was calculated as 4w/B for specimens in the loaded state. The results are presented in Fig. 7.21 where $\bar{\varepsilon}_z$ has been plotted as a function of relative crack extension, $\Delta\alpha$. Although the results show considerable scatter, especially for the 3.1 mm thick plates at large $\Delta\alpha$, it is apparent that $\bar{\varepsilon}_z$ is not only a function of $\Delta\alpha$ but also of plate thickness. Thus, for a given amount of slow crack extension, the through-thickness crack tip strain increases significantly with decreasing thickness. In particular, for the 3.1 mm thick plates at small $\Delta\alpha$, $\bar{\varepsilon}_z$ appears to be independent of initial crack size and crack initiation occurs at a critical $\bar{\varepsilon}_z$ of 0.022 in the pop-in region.

In comparison, Fig. 7.22 presents the surface plastic zone size, ρ'_x as a function of the relative crack extension, $\Delta\alpha$. The boundary of the surface plastic zone along the x axis was ill-defined as surface displacements petered out gradually and measurements of ρ'_x are considered to be accurate to $\pm$ 0.1 mm. In addition, for consistency ρ'_x was defined relative to the initial fatigue precrack as shown in Fig. 7.20.c and some slow crack extension will be included at higher load levels. However, in spite of the foregoing and compared with $\bar{\varepsilon}_z$, the surface plastic zone size does not appear to depend upon plate thickness at relatively small crack extensions. In all cases the plasticity is contained and general yield across the remaining ligament did not occur. For the 3.1 mm thick plates at small $\Delta\alpha$, ρ'_x also appears to be independent of initial crack size and a critical ρ'_x of 3.4 mm is obtained for crack initiation in the pop-in region.

7.3.d Scanning Electron Microscopy

Fig. 7.23 shows some typical scanning electron micrographs of the maraging steel fracture surfaces. In addition to the regions of primary

and secondary fatigue cracking, the fractures consisted of three distinct zones; a tensile fracture region, a shear fracture region and a stretch zone separating the former from the fatigue precrack.

The characteristic dimples of microvoid coalescence in Fig. 7.23.a and b indicate that no significant change in fracture mode occurred in the tensile region at the plate mid-thickness as a result of decreasing plate thickness or increased crack tip plastic strain. However, any change in dimple size would be difficult to detect since the fracture surface in this region consisted of bands of equiaxed dimples of varying size, reflecting the slight banding of the steel in the ST fracture plane. Such fractographic evidence of microsegregation has been observed before (11). In comparison, the elongated dimples of the shear fracture region, Fig. 7.23.c, indicate considerable ductile tearing.

The transition from the fatigue precrack to ductile rupture at crack initiation occurs via the stretch zone which, as shown in Fig. 7.23.d, consisted of a series of wavy slip lines crossed by steps or striations. Precise measurements of the zone width were difficult due to variations along the leading edge of the crack but it was of the order of 70-80 μm.

7.4 Discussion

7.4.a R_i for Crack Initiation

7.4.a.i 3.1 mm Thick Specimens

The results obtained for these thickness specimens by the two different procedures indicate that Landes and Begley's approximate method can lead to considerable underestimates in R_i for crack initiation. Comparison of the two sets of results for $2U_{11}/(W-a_o)B$ (Table 7.4.a and Fig. 7.12.a) and $-\frac{1}{B}\left(\frac{\partial U}{\partial a}\right)_u$ (Table 7.6 and Fig. 7.17) shows that the 19% apparent reduction in R_i using Landes and Begley's method was due not only to the use of the approximate relation, equation 5.16 but also to the interpolation

procedure employed for determination of a crack initiation measurement point.

According to the experimental data the approximate equation 5.16 underestimates $-\frac{1}{B}\left(\frac{\partial U}{\partial a}\right)_u$ by 9% for $\bar{\alpha}_o = 0.671$, $\phi = 2.18$ and overestimates $-\frac{1}{B}\left(\frac{\partial U}{\partial a}\right)_u$ by 4% for $\bar{\alpha}_o = 0.766$, $\phi = 1.92$; these values being in excellent agreement with the results of Fig. 7.19 obtained from the load-load pin displacement records. Thus, the pop-in region which is such a prominent feature of Fig. 7.17 and is reflected in Figs. 7.21 and 7.22, remains undetected in Fig. 7.12.a with the resultant underestimate in R_i.

7.4.a.ii 12.7 mm Thick Specimens

In comparison with the 3.1 mm thick specimens, excellent agreement was obtained for the 12.7 mm thick specimens between the values of R_i determined by the approximate equation 5.16 on the basis of the initial pop-in displacement and $\mathcal{Y}_Q$, the conditional plane strain energy release rate. That such agreement is real and not fortuitous is confirmed by calculation of the stress intensity factor corresponding to the pop-in load using equation 5.2, $K = PY/\sqrt{WB}$. Values of 4440 ± 60 N mm$^{-3/2}$ are obtained for specimens 34M-38M, in excellent agreement with K_Q, the conditional plane strain fracture toughness of 4570 ± 150 N mm$^{-3/2}$. Thus, for the maraging steel studied here, the initial pop-in does correspond to crack initiation. In addition, it is apparent that the use of the approximate relation, equation 5.16 is thickness dependent; results obtained for the 12.7 mm thick maraging steel plates under plane strain conditions being within 2% of the true value i.e. $\phi = 1.96$ for $\bar{\alpha}_o = 0.646$ but significant deviations occurring under the less constrained crack tip conditions that exist in the thinner 3.1 mm thick plates.

7.4.a.iii 6.3 mm Thick Specimens

A single estimate of R_i was obtained for the 6.3 mm thick specimens

using Landes and Begley's approximate method, this value lying 32% below $\mathcal{J}_Q$, the conditional plane strain energy release rate. Unfortunately, there were insufficient experimental data to confirm the existence or not of an initial pop-in region in Fig. 7.12.b as observed for the 3.1 mm thick specimens. However, the fracture mode at crack initiation for all plate thicknesses studied was similar on both a macroscopic and microscopic level so that it is probable that R_i for the 6.3 mm thick plates is equivalent to $\mathcal{J}_Q$ as for the remaining plate thicknesses.

Considering specimen 30M, 99.3 N mm^{-1} was obtained for $2U_{11}/(W-a_o)B$ corresponding to a relative crack extension, $\Delta\alpha$ of 0.75% or $\Delta a/a_o$ of 1.2%. The latter is close to the 2% effective crack extension stipulated in a standard K_{Ic} test (2) (3) and, on this basis, an R_i value of 99.3N mm^{-1} is in excellent agreement with $\mathcal{J}_Q$ of 101 $\pm$ 7 N mm^{-1}. In addition, the stress intensity factor corresponding to the final load level for specimen 30M is 4480 N mm$^{-3/2}$ using equation 5.2, in excellent agreement with K_Q of 4570 $\pm$ 150 N mm$^{-3/2}$, confirming that for the 6.3 mm thick maraging steel specimens crack initiation occurred under essentially plane strain conditions.

Therefore, it is apparent that for the 6.3 mm thick maraging steel specimens under plane strain conditions equation 5.16 provides good estimates of $-\frac{1}{B}\left(\frac{\partial U}{\partial a}\right)_u$ within 2% of the true value i.e. $\phi = 2.04$ for $\alpha_o = 0.623$; overly conservative estimates of R_i being obtained only as a result of the interpolation procedure used to determine a crack initiation measurement point.

7.4.a.iv 5% Offset Procedure for a Crack Initiation Measurement Point

It has been demonstrated for a 1 CrMoV steel (12) that the 5% offset procedure currently used to determine a crack initiation measurement point in a standard K_{Ic} test, can be applied successfully to thinner specimens not meeting the rigid size requirements of the standards. The

present results for maraging steel compact specimens were analysed in this manner using the load-load line displacement records of specimens 10M, 11M, 18M, 22M, 23M and 32M loaded to a load maximum as well as all four of the 12.7 mm thick plates exhibiting pop-in and the results are shown in Appendix 7.

A mean K_Q of 4400 ± 70 N mm$^{-3/2}$ was obtained for the 12.7 mm thick specimens in good agreement with 4570 ± 150 N mm$^{-3/2}$ determined previously for the 25.4 mm thick plates, in spite of the fact that the 5% offset load corresponded to pop-in for only two out of the four specimens. However, for the remaining specimens the 5% offset load occurred well below a load maximum so that the remarkable agreement between the results for specimens 11M, 18M and 32M and the 12.7 mm thick plates is probably fortuitous. This is borne out by the distinct size effect exhibited by K_A (stress intensity factor corresponding to the 5% offset load but not meeting the requirement $P_m/P_Q \leqslant 1.10$ (2)(3)) for the 3.1 mm thick specimens.

The agreement between the measured and calculated (7) compliances of the records confirms the general validity of the performance of the tests. Therefore, on the basis of the results for the 12.7 mm thick plates, it is apparent that good estimates of a crack initiation measurement point and hence K_Q can be obtained from maraging steel compact specimens approximately half the section thickness stipulated in the present standards i.e. $B \geqslant 1.3\ (K_Q/\sigma_y)^2$ compared to $B \geqslant 2.5\ (K_Q/\sigma_y)^2$ (2) (3).

7.4.a.v Effect of Through-Thickness Constraint on R_i

Fig. 7.24 compares the various R_i values for the different thickness plates tested where the values in brackets are the overly conservative estimates determined by Landes and Begley's method. It is clear that R_i remains constant over a thickness range well below the recommended thickness requirement of $B \geqslant 2.5\ (K_{Ic}/\sigma_y)^2$ for a standard K_{Ic} test.

It has already been demonstrated for the 12.7 mm and 6.3 mm thick plates that crack initiation occurs under essentially plane strain conditions. However, calculating the stress intensity factor corresponding to the final load level for 3.1 mm thick specimens 7MA, 11MA, 15MA, 21M and 25M in the vicinity of the pop-in region, a mean value of 4200 ± 150 N $mm^{-3/2}$ is obtained; the latter approximately 8% less than K_Q determined for the 25.4 mm thick plates and outside the 3% measured variation in K_Q. This indicates some loss in through-thickness constraint for the 3.1 mm thick plates which is supported by the sharp increase in average through-thickness strain, $\bar{\varepsilon}_z$ at crack initiation observed for these specimens, Fig. 7.21 i.e. 0.022 compared with 0.0080 (30M) and 0.0078 (38M, just beyond pop-in) for the 6.3 mm and 12.7 mm thick plates, respectively. It should be noted that such a change in crack tip stress state with decreasing thickness is not at all apparent from the elastic compliance measurements, Table 7.4, which reflect only the deformation state of the surface regions as observed previously by others (13) (14).

It is well known that square fracture resulting from in-plane plastic deformation can occur under non-plane strain conditions (15). This is understood by considering the variation of stress through-the-thickness of a thick plate immediately ahead of a sharp crack. The change from out-of-plane plastic deformation at the surface to in-plane plastic deformation at the plate mid-thickness referred to in section 3.1, cannot occur discontinuously and there is an intermediate region where, although the maximum tensile stress, σ_{yy} is less than its full plane strain value, the smallest principal stress remains σ_{xx} below the through-thickness stress, σ_{zz}. On the basis of Tresca's criterion, yielding in this region must occur in the xy plane, resulting in a mode I type square fracture macroscopically indistinguishable from the central plane strain region. Thus, it is quite possible that the initial triangular square fracture region observed for the

3.1 mm thick plates is a non-plane strain fracture, σ_{yy} (max) not achieving a full plane strain value at the mid-section as a result of stress relaxation through-the-thickness. Furthermore, since the fracture toughness, R_i for crack initiation remained the same for this plate thickness as under fully plane strain conditions, the implication is that the reduction in stress intensification at the crack tip was fully compensated by an increase in crack tip strain as reflected in measurements of $\bar{\varepsilon}_z$.

The question arises as to the critical thickness necessary for the production of a plane strain fracture at crack initiation. Considering Fig. 7.22 the critical surface plastic zone size at crack initiation remained approximately constant at 3.4 mm for the 3.1 mm thick plates, in good agreement with 3.6 mm (30M) for the 6.3 mm thick plates although somewhat less than the 5.1 mm (38M, just beyond pop-in) for the 12.7 mm thick plates. However, assuming the critical plastic zone size to be 3.4 mm for this particular maraging steel on the basis of the pop-in measurements, this implies that for a plate thickness of 3.4 mm, crack initiation occurs under circumstances such that full through-thickness yield can just develop i.e. σ_{yy} (max) relaxes over a distance equal to half this plate thickness, 1.7 mm.

Assuming that the maximum tensile stress relaxes over a distance equal to Irwin's plane stress plastic zone size, r_{y1}, Tetelman and McEvily (16) suggested that plane strain pop-in can first be expected at a thickness of $\frac{1}{\pi}(K_{Ic}/\sigma_y)^2$ or $2r_{y1}$. For the maraging steel tested here, r_{y1} corresponds to 1.7 mm, in excellent agreement with the previous estimate of the relaxation distance for σ_{yy} (max). In addition, deviations from fully plane strain behaviour occurred at thicknesses between 6.3 mm and 3.1 mm. Thus, in the present case for maraging steel, $\frac{1}{\pi}(K_{Ic}/\sigma_y)^2$ or 3.4 mm represents a good estimate of a critical thickness for plane strain crack initiation.

7.4.a.vi Specimen Size Limitations on the Determination and Use of R_i

On the basis of the Paris (17) estimate for the achievement of full transverse constraint, equation 3.4, $25\ \delta_{Ic} \leqslant B \leqslant 50\ \delta_{Ic}$, the following specimen size requirements have been suggested by Landes and Begley (5) for the determination of R_i using their approximate method:

$$25\left(\frac{R_{Ic}}{\sigma_{flow}}\right) \leqslant a,\ W-a,\ B \leqslant 50\left(\frac{R_{Ic}}{\sigma_{flow}}\right) \qquad 7.1$$

Here R_{Ic} represents the plane strain value of R_i and $\sigma_{flow} = (\sigma_y+\sigma_u)/2$ is used to allow for a certain degree of strain-hardening since the exact form of the relation between δ_{Ic} and R_{Ic}/σ_y is not at present clear (see section 2.3.a).

According to the present results for maraging steel, significant deviations from the approximate relation, equation 5.16 occur under non-plane strain crack tip conditions i.e. at thicknesses less than approximately 3.4 mm or 49 (R_i/σ_{flow}). This is in good agreement with the upper limit of equation 7.1 suggesting a necessary thickness requirement of $B \geqslant 50\ (R_i/\sigma_{flow})$ for the maraging steel.

Unfortunately, it was not possible to check the size limits on the initial crack length, a_o or the remaining ligament, $W-a_o$ as their minimum values of 19.4 mm and 11.7 mm, respectively were well above the upper limit of equation 7.1.

It is important to realise that the above specimen size requirements are merely limitations on the use of the Landes and Begley approximate method and not on the validity of R_i as a failure parameter. This is evident from the constancy of R_i even for the 3.1 mm thick plates which exhibited a square but non-plane strain fracture at crack initiation. However, although a thickness limitation on the use of R_i is not apparent from the

present results, an indication of the crack length validity range for R_i may be obtained by comparison with the pseudo-elastic fracture toughness, R_{gy} corresponding to the general yield level, equation 6.6, $\sqrt{ER_{gy}} = \sigma_y \sqrt{W}\ Y\ [-(1+\alpha) + \sqrt{2(1+\alpha^2)}\ ]$. The variation of R_{gy} with α for the maraging steel compact specimens is shown in Fig. 7.18. It is apparent that R_i for crack initiation remains constant at energy levels considerably below R_{gy} at short and intermediate crack lengths and up to 70% R_{gy} at $\bar{\alpha}_o = 0.766$.

7.4.a.vii Physical Significance of R_i

By definition, R_i represents the energy required for the production of the crack tip stretch or process zone i.e. region dominated by the crack tip singularity and its associated plastic zone up to crack initiation. Following Green and Knott's (18) model for fibrous crack initiation, it is possible to estimate these relative energy contributions for the maraging steel.

Consider the critical plane strain thickness, $B_c = 2r_{y1}$. Assuming the process zone to be roughly triangular in shape of base, δ_i, the crack opening displacement and height, S, the stretch zone width, the volume of material in the process zone is $\frac{1}{2}\ \delta_i\ SB_c$. Then, for a material of fracture strain, ε_f, the plastic energy expended in the crack tip process zone up to initiation is approximately:

$$U_{pr} \approx \frac{1}{2}\ \delta_i\ SB_c\ \Gamma\ \sigma_u\ \varepsilon_f \qquad 7.2$$

where Γ is a constant, characterising the steep strain gradient in the process zone and σ_u is chosen as slightly greater than the ultimate tensile strength to allow for some stress intensification at the crack tip.

The volume of plastically deformed material in the crack tip plastic zone at crack initiation is easily calculated for the maraging steel at the critical thickness, $B_c = 2r_{y1}$, for which the surface plastic zone approxi-

mates to a circular area of radius, r_{y1}. Under the plane strain conditions at the plate mid-thickness it is assumed that this plastic zone reduces to a circular area of radius, r_{y2} where $r_{y2} = r_{y1}/3$, Irwin's plane strain plastic zone size. Then, for a linear variation through-the-thickness, the two conic sections contain $\frac{2}{3}\pi r_{y1}^2 B_c$ of plastically deformed material. Therefore, for a material of average plastic strain, $\bar{\varepsilon}_p$, the plastic energy expended in the crack tip plastic zone up to crack initiation is approximately:

$$U_{p1} \approx \frac{2}{3}\pi r_{y1}^2 B_c \sigma_{flow} \bar{\varepsilon}_p \qquad 7.3$$

Expressions 7.2 and 7.3 are easily evaluated for the maraging steel assuming $\delta_i \sim \mathcal{J}_Q/\sigma_y \sim 0.072$ mm, S ~ 0.075 mm, σ_u = 1.1 x 1470 N mm^{-2} (average stress intensification of 1.1), $\varepsilon_f \sim 1.14$ and $\bar{\varepsilon}_p \sim 0.01$. Ignoring the strain gradient in the process zone i.e. Γ = 1, values of 17 N mm and 296 N mm are obtained for U_{pr} and U_{p1}, respectively. This indicates that the plastic energy contribution to the process zone represents only a small percentage, approximately 6%, of the total energy expended up to crack initiation, although it is the stress distribution within the process zone which controls the size of the plastic zone (18).

The question remains as to the microstructural features which control the process zone. For several materials exhibiting fibrous crack initiation the process zone size is known to be governed by the inclusion spacing (18)-(20). No study of this was undertaken, however, the work of Webber (20) on a low toughness cast of an 18% Ni 200-grade maraging steel suggests that the stretch zone width of 70-80 μm measured here, is a measure of the average separation of inclusions; the latter being unavoidable even in a material with a high purity base such as maraging steel.

7.4.b Estimates of R after Crack Initiation

Unfortunately, the methods employed here for the determination of a critical R_i for crack initiation become invalid in the presence of large scale yielding and/or slow crack growth. However, it is interesting to discuss their use for obtaining estimates of R after crack initiation.

For example, $\mathcal{J}_m$, the apparent elastic strain energy release rate corresponding to a load maximum, always gives a conservative estimate of R_m since it ignores the influence of plasticity and slow crack growth and assumes that the material shows a linear elastic response up to a load maximum. Underestimates in R_m resulting from the use of such a parameter obviously increase with decreasing plate thickness as out-of-plane plastic deformation develops through-the-thickness.

In comparison, the use of the calibration function, $-\frac{1}{B}\left(\frac{\partial U}{\partial a}\right)_u$ as determined here provides more realistic estimates of R beyond crack initiation. Originally Begley and Landes (6) used notched specimens to determine the calibration function, $-\frac{1}{B}\left(\frac{\partial U}{\partial a}\right)_u$ but by using precracked specimens, the work rate of the applied forces, plasticity and slow crack growth are all necessarily included in $-\frac{1}{B}\left(\frac{\partial U}{\partial a}\right)_u$. The use of non-linear unloading curves and the assumption of fixed grip loading ensure that such estimates of R remain conservative.

As with some of the pseudo-elastic techniques for determining R-curves (see section 2.3.c), under conditions of contained plasticity the plot of $-\frac{1}{B}\left(\frac{\partial U}{\partial a}\right)_u$ versus $\Delta\alpha$, Fig. 7.17 consisted of a single curve independent of initial crack length in support of Krafft's (21) and Rice's (22) hypothesis (see section 4.2.a). The large increase in the plastic strain energy rate associated with shear lip formation after crack initiation, equation 4.19, $R = R_i + \frac{1}{B}\left(\frac{\Delta U_p}{\Delta a}\right)$ is apparent from the curve, being reflected in the increase in surface plastic zone size, Fig. 7.22. The continued increase of the "R-curve" even after a fully slant fracture has

developed and an equilibrium-maximum surface plastic zone size achieved has been observed previously (21) (23) and is believed to be due to the rotation of the principal strains about the x and z axes which leads to a more complex strain pattern ahead of the crack tip requiring a higher stress or strain for continued crack extension (23).

However, although values of $-\frac{1}{B}\left(\frac{\partial U}{\partial a}\right)_u$ appear to belong to a single R-curve, individual values corresponding to a load maximum, termed R_{mc} (best conservative estimate of R_m) decreased significantly with increasing crack size or decreasing remaining ligament, Fig. 7.18 in a manner directly analogous to R_{stable} for polycarbonate, Fig. 6.13. Again, this variation appears to be due to a geometry effect associated with the applied load exceeding the general yield level in narrow specimens since R_{mc} decreased in a manner similar to R_{gy}, the pseudo-elastic fracture toughness. Thus, in all cases the attainment of a load maximum corresponded to the development of local plastic instability ahead of the crack tip.

Finally, Fig. 7.24 compares the various estimates of R_m corresponding to a load maximum as a function of plate thickness for initial crack sizes in the range, $\alpha \sim 0.5 - 0.7$. The results indicate a general increase in R_m with decreasing plate thickness which would be anticipated on the basis of the increased proportion of out-of-plane plastic deformation. However, such results reveal little else for it is known that the approximate relation, equation 5.16 overestimates $-\frac{1}{B}\left(\frac{\partial U}{\partial a}\right)_u$ as a result of slow crack growth (5) and although the difference is small for short crack extensions (for example, specimens 23M-26M, $\bar{\alpha}_o = 0.766$, $\phi = 1.92$, $\left[2U_{11} \Big/ (W-a_o)B\right]_m$ overestimates R_{mc} by only 8% after a crack growth increment of 1.294 mm) for the 6.3 mm and 12.7 mm thick plates where more extensive crack extension occurred prior to a load maximum, the difference could be considerable.

7.4.c Effect of Specimen Dimensions on Slow Crack Growth Characteristics

Fig. 7.25 shows quantitatively the reduction in slow crack growth up to a load maximum, $\Delta\alpha_m$ with increasing initial crack size or decreasing remaining ligament and decreasing plate thickness for the maraging steel compact specimens.

Considering the 3.1 mm thick plates, the general decrease in $\Delta\alpha_m$ with α_o reflects the variation of R_{mc} with $\bar{\alpha}_o$ (compare Fig. 7.18) and is a direct result of the same geometrical effect i.e. the applied load exceeding the general yield level. It is interesting to note that on the basis of equation 6.6, $\sqrt{ER_{gy}} = \sigma_y \sqrt{W}\ Y \left[- (1+\alpha) + \sqrt{2\ (1+\alpha^2)} \right]$ an increase in plate width should result in an increase in R_{gy} and thereby, R_m and the extent of slow crack growth up to a load maximum.

In comparison, the effect of plate thickness on slow crack growth must have its origins in a different cause since while $\Delta\alpha_m$ increases with increasing B, $\left[2U_{11}/(W-a_o)B\right]_m$, the apparent fracture toughness, decreases. In fact, this variation in $\Delta\alpha_m$ with plate thickness merely reflects the increased proportion of square fracture across the section thickness; crack extension after crack initiation continuing at lower stress levels in the 12.7 mm thick specimens than for the predominantly out-of-plane plastic deformation and mode III slant fractures found in thinner plates.

7.4.d Failure Analysis Diagram

The two-criteria approach to failure (24) described in section 5.2.a.i was tested by constructing a failure analysis diagram for the maraging steel compact specimens based only on a knowledge of the conditional plane strain fracture toughness, K_Q and the uniaxial tensile properties, σ_y and σ_u using equations 5.12-5.14. A comparison of the analytical and experimental results are shown in Fig. 7.26.

For crack initiation for the 12.7 mm and 6.3 mm thick specimens,

agreement between the LEFM curve based on K_Q and the experimental loads is excellent, within the 3% scatter band for K_Q. However, as shown previously in section 7.4.a.v. the experimental results for the 3.1 mm thick specimens lie approximately 8% below the analytical curve for K_Q, outside its 3% scatter band. Under such circumstances the use of LEFM with a plasticity correction factor merits investigation.

In order to determine a physically based plasticity correction factor for the maraging steel, the surface plastic zone size was compared with values derived from the Irwin elastic and Dugdale elastic-plastic models (see sections 2.2 and 2.3.a, respectively). The results are shown in Fig. 7.27 where ρ'_x /a has been plotted versus $\sigma_{\infty\ plate}/\sigma_y$; for the experimental data a was taken as the instantaneous crack size and $\sigma_{\infty\ plate}$, the applied stress referred to the infinite plate models, calculated by means of the finite width correction factor or stress intensity coefficient, Y for the compact specimen. The agreement between the experimental results and Irwin's plane stress solution is remarkably good, although results obtained for $\rho'_x/a > 0.2$ should be treated with caution as the extent of slow crack growth necessarily included in the measurement of ρ'_x becomes significant. The results indicate that up to crack initiation, $\rho'_x/a < 0.2$ Irwin's plane stress solution provides a good model of the surface plastic zone for the maraging steel. At higher stress levels, it might be expected that for a low strain-hardening material the surface crack tip plastic zone would deviate from an elastic solution approaching Dugdale's elastic-perfectly plastic solution as a fully plane stress state develops (25) (26). However, this does not appear to be the case for the maraging steel.

For the 3.1 mm thick specimens at crack initiation, the crack tip stress state must be close to plane strain conditions (B_c = 3.4 mm) so that, as a first approximation, the crack tip plastic zone at the mid-thickness may be given by Irwin's plane strain model. Under such circum-

stances a plasticity correction factor of the order of $r_{y2} = \frac{1}{6\pi}\left(\frac{K_Q}{\sigma_y}\right)^2$ is appropriate. An analytical curve based on LEFM with a plasticity correction factor, r_{y2}/W has been included in Fig. 7.26 and a comparison of the experimental and calculated values of P_i^{ϕ} for crack initiation is given in Table 7.7. It is clear that with one exception the experimental results for the 3.1 mm thick plates are in extremely good agreement with the plasticity modified LEFM analysis; the same correction factor making little difference to the agreement for the thicker plates. The one exception is 15 MA which may not have achieved pop-in (see Fig. 7.17). This successful application of LEFM with a plasticity correction factor to predict crack initiation for the 3.1 mm thick plates is hardly surprising in view of the fact that crack initiation occurred well below a load maximum close to the linear elastic regime (see Fig. 7.13).

A comparison of the experimental plastic instability loads (load maxima), P_m^{ϕ} with the limit analysis solution for yield and ultimate collapse is given in Table 7.8. The experimental results for the 3.1 mm thick specimens show a marked similarity to those previously obtained for polycarbonate, Fig. 6.15. Thus, for crack lengths between $\alpha = 0.433 - 0.516$, the results are in good agreement with the limit analysis solution for yield after due allowance for slow crack growth. However, at longer crack lengths the experimental results deviate significantly from the locus for yield and are in better agreement with the limit analysis solution for ultimate collapse; the experimental loads being within 22% of the predicted values up to $\alpha = 0.789$. Again, as for the polycarbonate, this apparent variation in work-hardening capacity does not appear to be due to any significant change in the uniaxial tensile properties as a result of differences in strain rate. For example, the nominal strain rate applied to the specimens increased with decreasing crack length from 6.3×10^{-6} sec^{-1} ($\bar{\alpha}_o = 0.766$) to 9.4×10^{-6} sec^{-1} ($\bar{\alpha}_o = 0.386$) for the 3.1 mm thick

plates and such an increase should raise σ_y for maraging steel at room temperature by less than 1% (27).

In comparison, the results for the 6.3 mm and 12.7 mm thick plates show considerably greater deviation from the analytical curve; predicted values of P_m^{ϕ} underestimating experimental values by 36% and 30%, respectively. Of course, for consistency, the experimental results were based on measurements of maximum crack extension, $\alpha_o + \Delta\alpha$ which generally occurred at the plate mid-thickness. The effect of this will be to overestimate the average crack length implicit in the limit analysis calculations, particularly in cases where significant crack front tunnelling occurred such as the 6.3 mm and 12.7 mm thick plates. Thus, the experimental data for these specimens should be shifted to shorter crack lengths in closer registry with the analytical curves.

7.5 Conclusions

a. Static loading experiments on compact specimens of an 18% Ni 200 - grade maraging steel have shown that the fracture toughness R_i for crack initiation $\left(= -\frac{1}{B}\left(\frac{\partial U}{\partial a}\right)_{u_i}\right)$ is a constant independent of thickness for plane strain (6.3-25.4 mm thick plates) and non-plane strain (3.1 mm thick plates) crack tip conditions and independent of initial crack length ($\bar{\alpha}_o$ = 0.386-0.766, 3.1 mm thick plates). This value is related to the plane strain fracture toughness, K_{Ic} by the relation, $K_{Ic}^2 = ER_i/(1-\nu^2)$.

b. For the maraging steel compact specimens a linear relationship has been shown to exist between the strain energy, U/WB and its derivative with respect to crack length, $-\frac{1}{B}\left(\frac{\partial U}{\partial a}\right)_u$ as predicted by Begley and Landes (28) and Neale and Townley (29), this relationship being maintained even after initial crack extension. The approximate relation for a deeply cracked compact specimen, equation 5.16, $-\frac{1}{B}\left(\frac{\partial U}{\partial a}\right)_u$ =

$2U_{11}/(W-a_o)B$, $\alpha \geqslant 0.6$, has been shown to be applicable for maraging steel under plane strain crack tip conditions for which the size requirement, $B \geqslant \frac{1}{\pi} (K_{Ic}/\sigma_y)^2$ or $50 (R_i/\sigma_{flow})$ is met.

c. Using Landes and Begley's (5) interpolation procedure for determining a crack initiation measurement point for maraging steel resulted in considerable underestimates (up to 32%) in R_i when insufficient data were obtained close to the onset of true crack extension.

d. The 5% offset procedure currently applied in a standard K_{Ic} test, can be used to determine a crack initiation measurement point in maraging steel compact specimens approximately half the section thickness stipulated in the present standardsi.e. $B \geqslant 1.3 \left(\frac{K_{Ic}}{\sigma_y}\right)^2$ compared to $B \geqslant 2.5 \left(\frac{K_{Ic}}{\sigma_y}\right)^2$.

e. Good estimates of R beyond crack initiation have been obtained for maraging steel by means of the calibration function, $-\frac{1}{B}\left(\frac{\partial U}{\partial a}\right)_u$ obtained from precracked specimens, thus including the work rate of the applied forces, plasticity and slow crack growth; non-linear unloading curves and the assumption of fixed grip loading ensuring that such estimates of R remain conservative.

For monotonic loading, under conditions of contained plasticity, the curve of $-\frac{1}{B}\left(\frac{\partial U}{\partial a}\right)_u$ versus $\Delta\alpha$ (W, constant) for the 3.1 mm thick maraging steel plates was independent of initial crack length (α_o = 0.386 - 0.766) in support of Krafft's (21) and Rice's (22) hypothesis for R-curves. Values of $-\frac{1}{B}\left(\frac{\partial U}{\partial a}\right)_u$ corresponding to a load maximum, termed R_{mc} (best conservative estimate of R_m) exhibited a geometry dependence at all crack lengths very similar to that observed for R_{stable} for polycarbonate. This was also the result of local plastic instability ahead of the crack tip in the narrow specimens.

f. The extent of slow crack growth up to plastic instability (load

maximum) for narrow maraging steel compact specimens has been shown to increase with increasing remaining ligament and increasing plate thickness; the former as a result of finite plate width and the latter due to the increased proportion of square fracture across the section associated with thicker specimens.

g. Dowling and Townley's two-criteria approach to failure (24) has been shown to provide good estimates of crack extension loads for 3.1 mm, 6.3 mm and 12.7 mm thick maraging steel compact specimens undergoing fibrous crack initiation. Failure loads corresponding to crack initiation under plane strain conditions, 6.3 and 12.7 mm thick specimens, were within 3% of LEFM estimates. In comparison, failure loads corresponding to crack initiation under non-plane strain conditions ($B < \frac{1}{\pi} (K_{Ic}/\sigma_y)^2$), 3.1 mm thick specimens, were approximately 8% below LEFM estimates but within 3% of estimates based on LEFM with a plasticity correction factor. Physical justification for the use of a plasticity correction of the order of Irwin's plane strain plastic zone size has been presented for the maraging steel.

Finally, on the basis of the instantaneous crack size, plastic instability loads for the 3.1 mm thick plates were within 7% of the limit analysis solution for yield at crack lengths between α = 0.433 - 0.516 and within 22% of the limit analysis solution for ultimate collapse at longer crack lengths up to α = 0.789. This behaviour was very similar to that observed previously for polycarbonate. In comparison, the limit analysis solution for ultimate collapse underestimated plastic instability loads for the 6.3 mm (α = 0.691) and 12.7 mm (α = 0.729) thick plates by 36% and 30%, respectively; such large underestimates were partly the result of overestimates in instantaneous crack size due to crack front tunnelling.

References

(1) "Methods for Tensile Testing of Metals," B.S. 18: Part 2: 1971, B.S.I., London.

(2) "Methods for Plane Strain Fracture Toughness (K_{Ic}) of Metallic Materials," B.S. 5447: 1977, B.S.I., London.

(3) "Plane Strain Fracture Toughness of Metallic Materials," A.S.T.M. E399-72 Part 31, 1972.

(4) P.B. Crosley and E.J. Ripling, Nuclear Eng. and Design, 17, p. 32, 1971.

(5) J.D. Landes and J.A. Begley, A.S.T.M. S.T.P. 560, "Fracture Analysis," Am. Soc. for Testing and Materials, p. 170, 1974.

(6) J.A.Begley and J.D. Landes, A.S.T.M. S.T.P. 514, "Fracture Toughness," Am. Soc. for Testing and Materials, p. 1, 1972.

(7) N.J.I. Adams and H.G. Munro, Eng. Fract. Mechs., 6, p. 119, 1974.

(8) J.R. Rice, Proc. 1st Int. Conf. Fracture, Sendai, 1, p. 283, 1965.

(9) D.A. Bateman, F.J. Bradshaw and D.P. Rooke, R.A.E. Tech. Note No. CPM 63, March 1964.

(10) G.T. Hahn and A.R. Rosenfield, Rept. to Ship Structure Committee 191, U.S. Coast Guard H.Q., Washington D.C., 1968.

(11) J.M. Barsom and J.V. Pellegrino, Eng. Fract. Mechs., 5, p. 209, 1973.

(12) B.K. Neale, C.E.G.B. Report No. RD/B/N3787, Aug. 1976.

(13) R.J. Bucci, P.C. Paris, J.D. Landes and J.R. Rice, A.S.T.M. S.T.P. 514, "Fracture Toughness," Am. Soc. for Testing and Materials, p. 40, 1972.

(14) C.A.Griffis and G.R. Yoder, N.R.L. Report No. 7676, April 1974.

(15) J.F. Knott, "Fundamentals of Fracture Mechanics," Butterworths, London, p. 124 et seq., 1973.

(16) A.S. Tetelman and A.J. McEvily, Jr., "Fracture of Structural Materials," Wiley, New York, p. 38, 1967.

(17) P.C. Paris, A.S.T.M. S.T.P. 514, "Fracture Toughness," Am. Soc. for Testing and Materials, p. 21, 1972.

(18) G. Green and J.F. Knott, Trans. ASME, Series H, J. Eng. Mats. Tech., 98, p. 37, 1976.

(19) K-H. Schwalbe, Eng. Fract. Mechs., 9, p. 547, 1977.

(20) D. Webber, C. Roberts, N.J.I. Adams and H.G. Munro, M.V.E.E. Report No. 76504, Feb. 1976.

(21) J.M. Krafft, A.M. Sullivan and R.W. Boyle, Proc. Symp. Crack Propagation, Cranfield, p. 8, 1961.

(22) J.R. Rice, "Fracture - An Advanced Treatise," Vol. II, Ed. H. Liebowitz, Academic Press, New York, p. 191, 1968.

(23) D.P. Rooke and F.J. Bradshaw, Proc. 2nd Int. Conf. Fracture, Brighton, p. 46, 1969.

(24) A.R. Dowling and C.H.A. Townley, Int. J. Pres. Ves. and Piping, 3, p. 77, 1975.

(25) A.R. Rosenfield, P.K. Dai and G.T. Hahn, Proc. 1st Int. Conf. Fracture, Sendai, Japan, 1, p. 223, 1965.

(26) G.T. Hahn and A.R. Rosenfield, A.S.T.M. S.T.P. 432," Applications Related Phenomena in Titanium Alloys," Am. Soc. for Testing and Materials, p. 5, 1968.

(27) A.K. Shoemaker and S.T. Rolfe, Eng. Fract. Mechs., 2. p. 319, 1971.

(28) J.A. Begley and J.D. Landes, A.S.T.M. S.T.P. 536, "Progress in Flaw Growth and Fracture Toughness Testing," Am. Soc. for Testing and Materials, p. 246, 1973.

(29) B.K. Neale and C.H.A. Townley, C.E.G.B. Report No. RD/B/N3358, May 1975.

Table 7.1 Chemical Composition of 18 Ni (200) Maraging Steel

Cast VA 11169

C	Si	Mn	S	P	Cr	Ni	Mo
0.005	0.12	0.02	0.007	0.002	0.04	17.78	3.22

Co	Ti	Al	(wt. per cent)
8.30	0.32	0.069	

Nominal Si content = 0.05

Table 7.2 Mechanical Properties of Heat Treated Maraging Steel

($296^{o}K$, $\dot{\varepsilon}_{nom} = 3.1 \times 10^{-5}\ sec^{-1}$)

Hardness, Rockwell C	45-47
0.2% Offset yield stress, σ_y (L)	$1407 \pm 8\ N\ mm^{-2}$ [3] *
Ultimate tensile strength, σ_u (L)	$1470 \pm 9\ N\ mm^{-2}$ [3]
True strain at plastic instability, ε_{tm}	0.022 [3]
Static Young's modulus, E	$185 \pm 1 \times 10^{3}\ N\ mm^{-2}$ [2]
Poisson's ratio, ν	0.32 (manuf.)
Conditional plane strain fracture toughness, K_Q (L-T)	$4570 \pm 150\ N\ mm^{-3/2}$ [3]
Conditional plane strain energy release rate, $\mathcal{G}_Q$ (L-T)	$101 \pm 7\ N\ mm^{-1}$
Apparent elastic strain energy release rate corresponding to a load maximum, $\mathcal{G}_m$ (L-T)	$112 \pm 6\ N\ mm^{-1}$

* No. of measurements

± 1 Standard deviation

Table 7.3 Compact Specimen Dimensions for Heat Treated Maraging Steel

	B mm	W mm	α_o		B mm	W mm	α_o
1M	3.10	50.65	0.340	19M	3.02	50.98	0.672
2M	3.10	50.78	0.436	20M	3.02	51.13	0.673
3M	3.02	50.67	0.538	21M	3.02	51.03	0.670
4M	3.02	50.80	0.636	22M	3.02	51.08	0.669
5M	3.10	50.65	0.738				
6M	3.10	50.34	0.828	23M	3.02	50.67	0.763
				23MA	3.07	50.70	0.767
7M	3.10	50.85	0.384	24M	3.02	50.65	0.769
7MA	3.07	50.57	0.384	25M	3.10	50.65	0.769
8M	3.10	50.70	0.383	26M	3.10	50.75	0.761
9M	3.10	50.72	0.388				
10M	3.10	50.60	0.389	28M	6.34	50.57	0.626
				30M	6.34	50.57	0.623
11M	3.10	50.78	0.482	31M	6.34	50.55	0.623
11MA	3.07	50.70	0.482	32M	6.33	50.50	0.631
12M	3.18	50.85	0.484				
13M	3.02	50.83	0.481	34M	12.64	50.57	0.648
14M	3.02	50.72	0.484	35M	12.67	50.72	0.644
				37M	12.65	50.65	0.648
15M	3.02	50.80	0.580	38M	12.66	50.65	0.644
15MA	3.07	50.78	0.580				
16M	3.02	50.90	0.581				
17M	3.02	50.90	0.579				
18M	3.02	50.85	0.580				

Table 7.4 Determination of R_i for Maraging Steel Compact Specimens Using Landes and Begley's Approximate Method

a. 3.1 mm Thick Specimens

	α_o	$\Delta\alpha$	$\frac{2U_{11}}{(W-a_o)B}$ N mm^{-1}	R_i N mm^{-1}	$K_i = \sqrt{ER_i/(1-\nu^2)}$ N mm$^{-3/2}$	$\Delta\alpha_m$	$\left[\frac{2U_{11}}{(W-a_o)B}\right]_m$ N mm^{-1}	$\frac{EBu_{11}}{P}$ Expt.	$\frac{EBu_{11}}{P}$ Adams-Munro (7) plane stress	$\frac{C_{exp}}{C_{A,M}}$
19M	0.672	0.0117	121			-	-	99.2	100.4	0.99
20M	0.673	0.0200	178			-	-	95.2	100.7	0.95
21M	0.670	0.0038	90.0			-	-	99.4	99.55	1.00
22M	0.669	0.0305	318			0.0305	318	98.4	98.27	1.00
23M	0.763	0.0255	256	80	4060	0.0255	256	216	205.5	1.05
23MA	0.767	0.0011	80.7			-	-	215	212.6	1.01
24M	0.769	0.0156	160			-	-	220	216.9	1.01
25M	0.769	0.0071	102			-	-	220	216.9	1.01
26M	0.761	0.0003	57.3			-	-	202	201.5	1.00

Table 7.4 (cont.) b. 6.3 mm and 12.7 mm Thick Specimens

	α_o	$\Delta\alpha$	$\frac{2U_{11}}{(W-a_o)B}$ N mm^{-1}	R_i N mm^{-1}	$K_i = \sqrt{ER_i/(1-\nu^2)}$ N mm$^{-3/2}$	$\Delta\alpha_m$	$\left[\frac{2U_{11}}{(W-a_o)B}\right]_m$ N mm^{-1}	$\frac{EBu_{11}}{P}$ Expt.	$\frac{EBu_{11}}{P}$ Adams-Munro (7) plane stress	$\frac{C_{exp}}{C_{A,M}}$
28M	0.626	0.0005	68.9	68.9	3770	-	-	72.7	74.76	0.97
30M	0.623	0.0075	99.3			-	-	71.5	73.04	0.98
31M	0.623	0.0203	158			-	-	69.8	73.04	0.96
32M	0.631	0.0598	371			0.0598	371	76.2	77.40	0.98
34M	0.648	pop-in	104	104	4640	-	-	85.6	85.80	1.00
35M	0.644	pop-in	97.8	97.8	4500	0.0652	233	84.1	83.64	1.01
37M	0.648	pop-in	105	105	4650	0.1012	267	86.9	85.80	1.01
38M	0.644	pop-in	105	105	4650	-	-	83.0	83.64	0.99
Mean				103 ± 3	4610 ± 60					

Table 7.5 Comparison of Measured and Calculated Elastic Compliances for 3.1 mm Thickness Maraging Steel Compact Specimens

	α_o, $\bar{\alpha}_o$	$\frac{EBu_{1p}}{P}$		
		Expt.	Adams-Munro (7) plane stress	$\frac{C_{exp}}{C_{A,M}}$
1M	0.340	23.8	20.68	1.15
2M	0.436	31.0	30.42	1.02
3M	0.538	50.0	48.17	1.04
4M	0.636	93.7	81.79	1.15
5M	0.738	184	168.1	1.09
6M	0.828	425	382.9	1.11
7M-10M	0.386	27.9	24.66	1.13
11M-14M	0.483	40.8	37.47	1.09
15M-18M	0.580	62.1	59.68	1.04
19M-22M	0.671	111	102.1	1.09
23M-26M	0.766	225	212.8	1.06

Table 7.6 Determination of R_i for Crack Initiation for 3.1 mm Thickness Maraging Steel Compact Specimens Using the Calibration Function, $-\frac{1}{B}\left(\frac{\partial U}{\partial a}\right)_u$

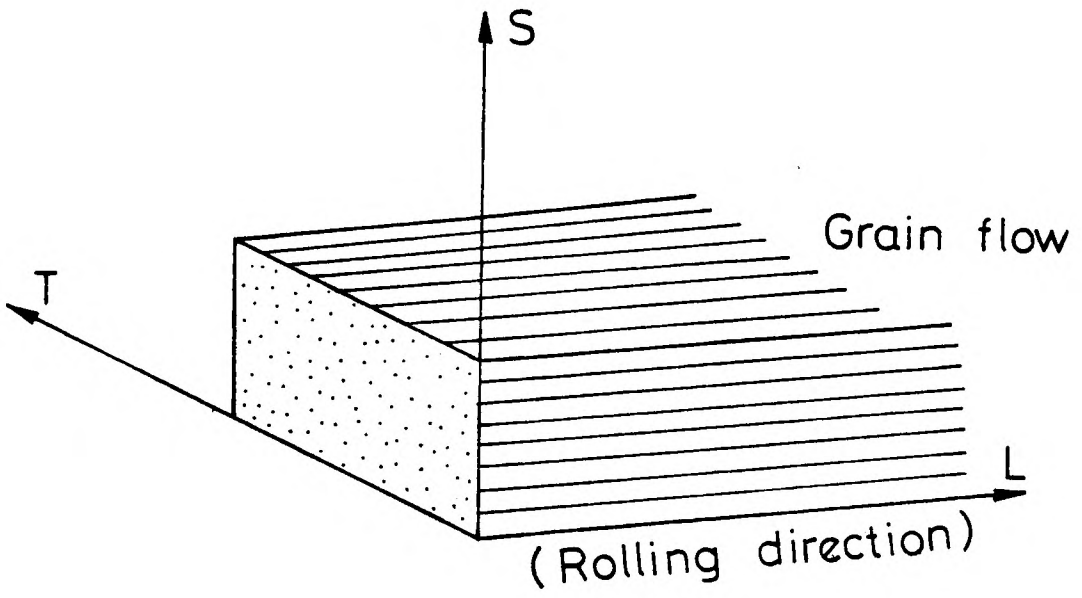
	$\bar{\alpha}_o$	$\Delta\alpha$	$-\frac{1}{B}\left(\frac{\partial U}{\partial a}\right)_u$	R_i	$K_i = \sqrt{ER_i/(1-\nu^2)}$
			N mm^{-1}	N mm^{-1}	N mm$^{-3/2}$
7M	0.386	0.0329	394	100	4540
7MA		0.0057	100		
8M		0.0671	513		
9M		0.0240	335		
10M		0.0589	470		
11M	0.483	0.0394	417	102.5	4600
11MA		0.0035	102.5		
12M		0.0271	329		
13M		0.0227	295		
14M		0.0212	258		
15M	0.580	0.0093	115	95	4430
15MA		0.0016	95		
16M		0.0279	266		
17M		0.0185	197		
18M		0.0356	371		
19M	0.671	0.0117	138	98	4490
20M		0.0200	200		
21M		0.0038	98		
22M		0.0305	335		
23M	0.766	0.0255	238	99	4520
23MA		0.0011	78		
24M		0.0156	159		
25M		0.0071	99		
26M		0.0003	55		
Mean				99 ± 2.5	4520 ± 60

Table 7.7 Comparison of Experimental and Calculated Values of the Failure Parameter, P_i^{ϕ} for Crack Initiation

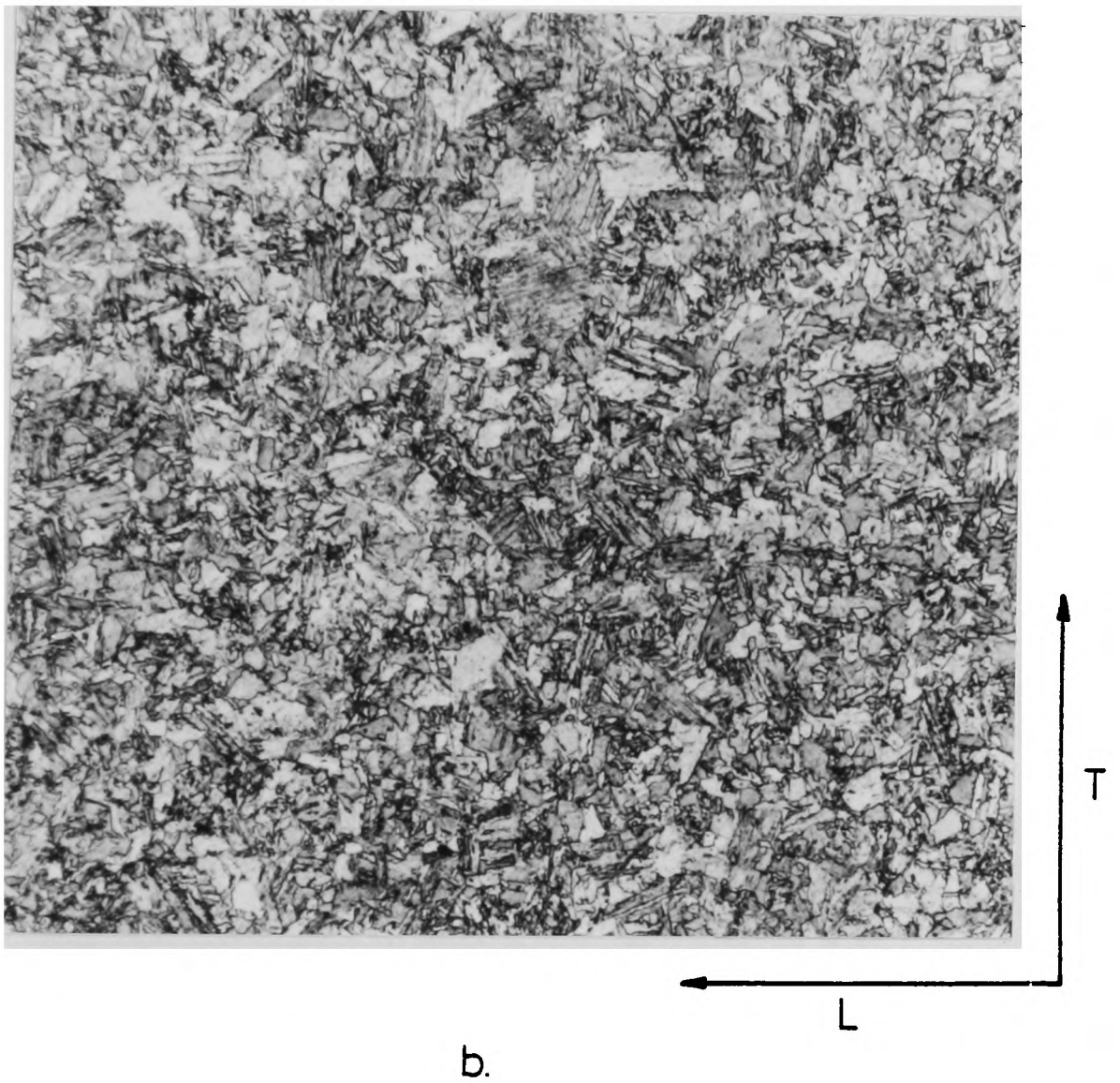
	α_o	P_i^{ϕ}				
		a. Expt.	b. LEFM α_o	c. LEFM $\alpha_o + \frac{r_{y2}}{W}$	$\frac{a}{b}$	$\frac{a}{c}$
7MA	0.384	0.1450	0.1510	0.1470	(0.96)	0.99
11MA	0.482	0.1090	0.1150	0.1110	(0.95)	0.98
15MA	0.580	0.0721	0.0833	0.0799	(0.87)	0.90
21M	0.670	0.0527	0.0568	0.0538	(0.93)	0.98
25M	0.769	0.0290	0.0322	0.0298	(0.90)	0.97
30M	0.623	0.0691	0.0704	0.0672	0.98	1.03
34M	0.648	0.0625	0.0632	0.0601	0.99	1.04
35M	0.644	0.0611	0.0642	0.0611	0.95	1.00
37M	0.648	0.0613	0.0631	0.0600	0.97	1.02
38M	0.644	0.0624	0.0643	0.0611	0.97	1.02

Table 7.8 Comparison of Experimental and Calculated Values of the Failure Parameter, P_m^{ϕ} for Load Maximum

	$\alpha_o + \Delta\alpha_m$		P_m^{ϕ} a. Expt.	b. L.A.-Yield	c. L.A.-U.C.	$\frac{a}{b}$	$\frac{a}{c}$
7M	0.417	0.433	0.2320	0.2500	0.2610	0.93	(0.89)
10M	0.448						
12M	0.511	0.516	0.1670	0.1740	0.1820	0.96	(0.92)
11M	0.521						
18M	0.616		0.1200	0.1040	0.1090	(1.15)	1.10
22M	0.700		0.0748	0.0608	0.0635	(1.23)	1.18
23M	0.789		0.0365	0.0286	0.0299	(1.28)	1.22
32M	0.691		0.0918	0.0647	0.0676	(1.42)	1.36
35M	0.709	0.729	0.0664	0.0488	0.0509	(1.36)	1.30
37M	0.749						

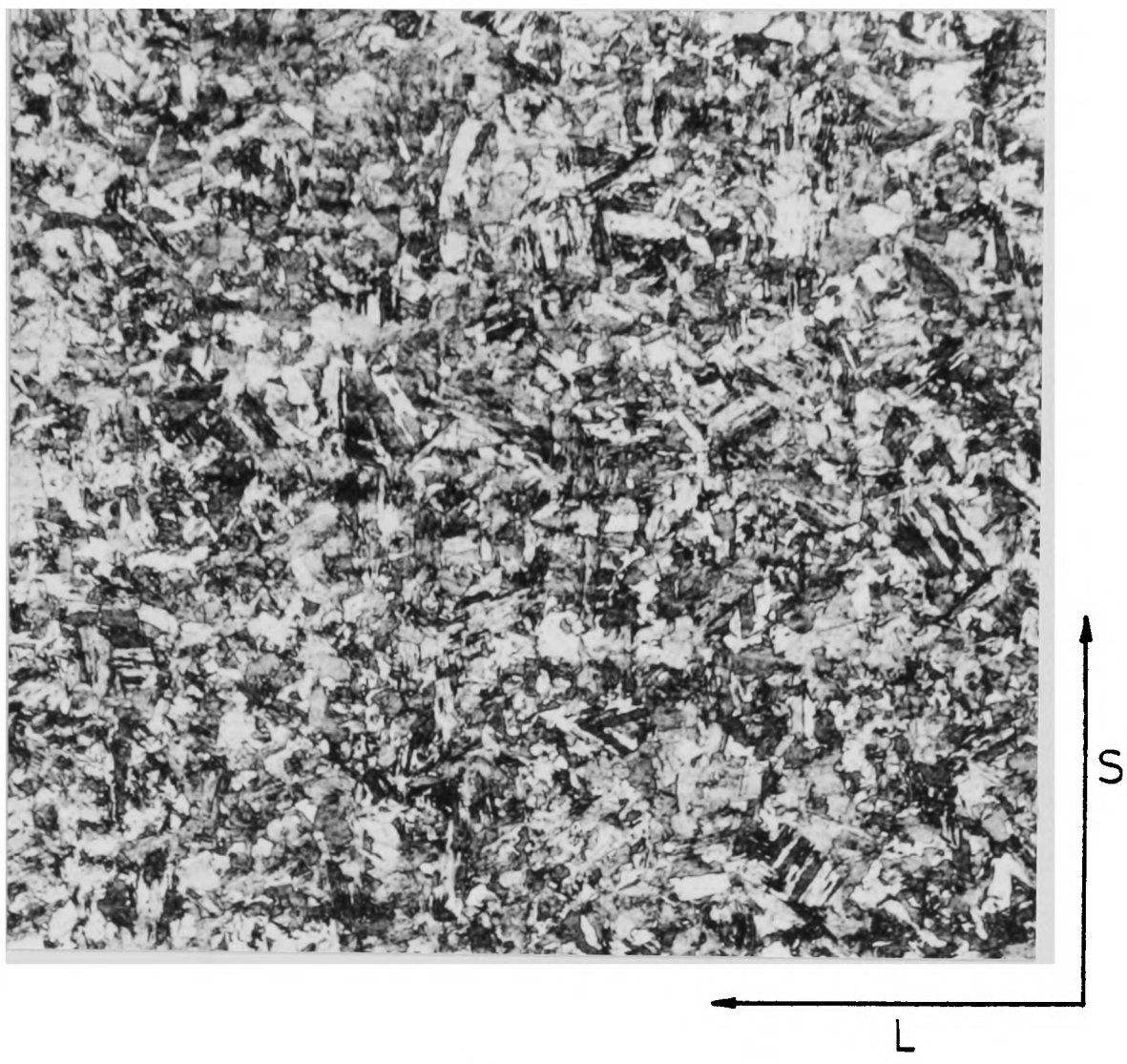


a.

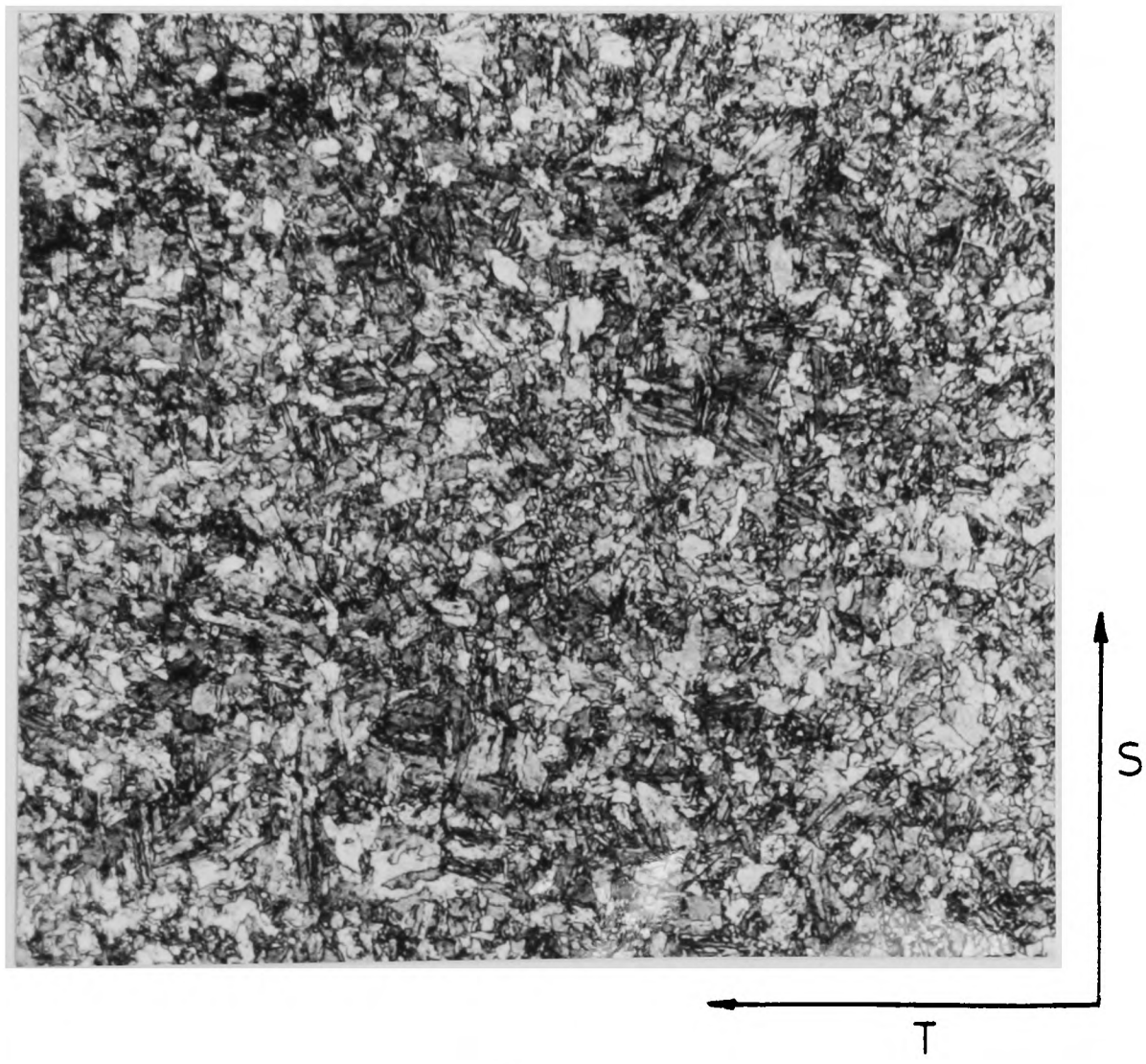


b.

Fig. 7.1 Optical micrographs of maraging steel after heat treatment for 3 hours at 480°C (x87)
(Etchant, modified Fry's reagent — 30 ml hydrochloric acid, 10 ml nitric acid, cupric chloride added to saturation and diluted to twice the volume with water)



c.



d.

Fig. 7.1 (cont.)

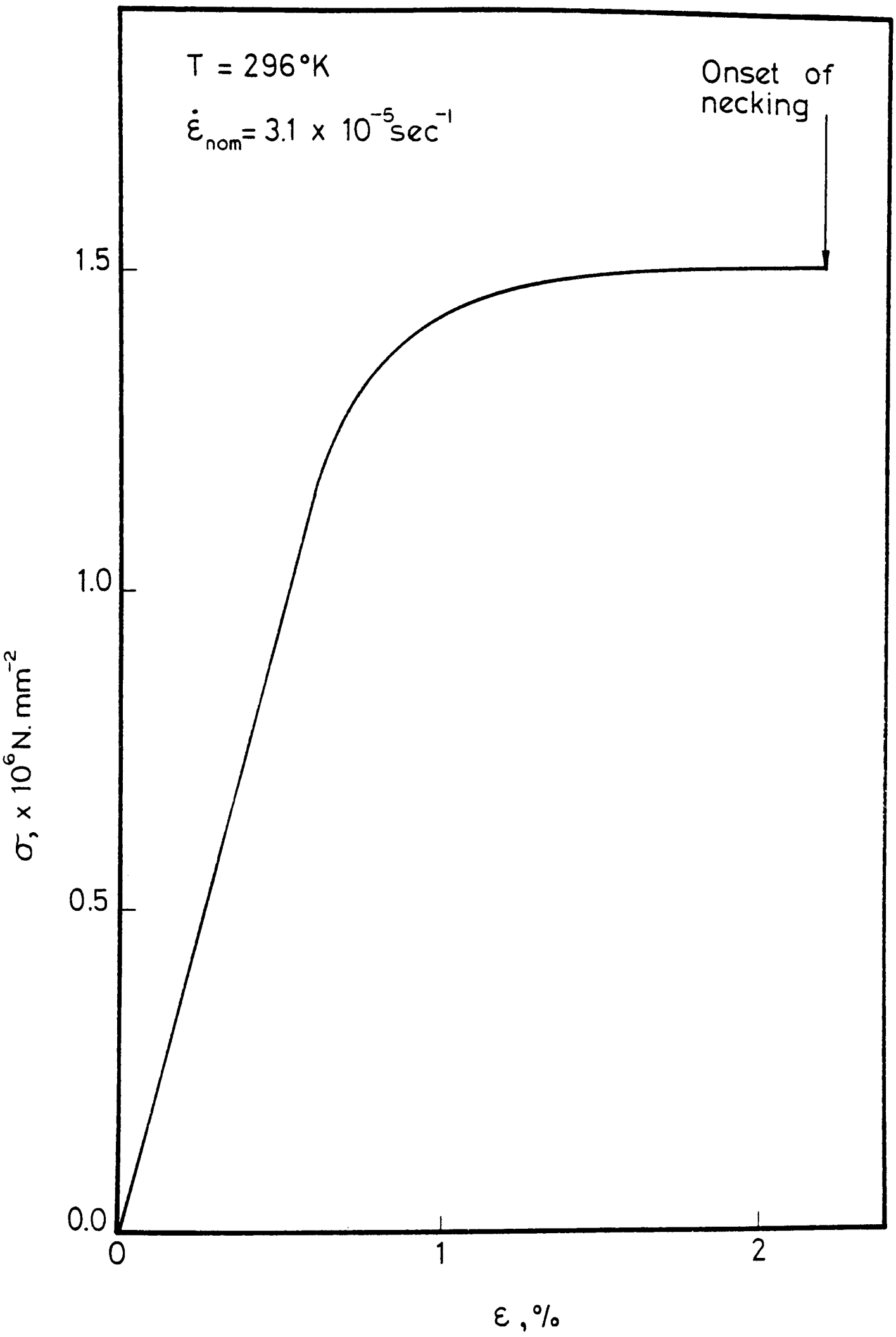
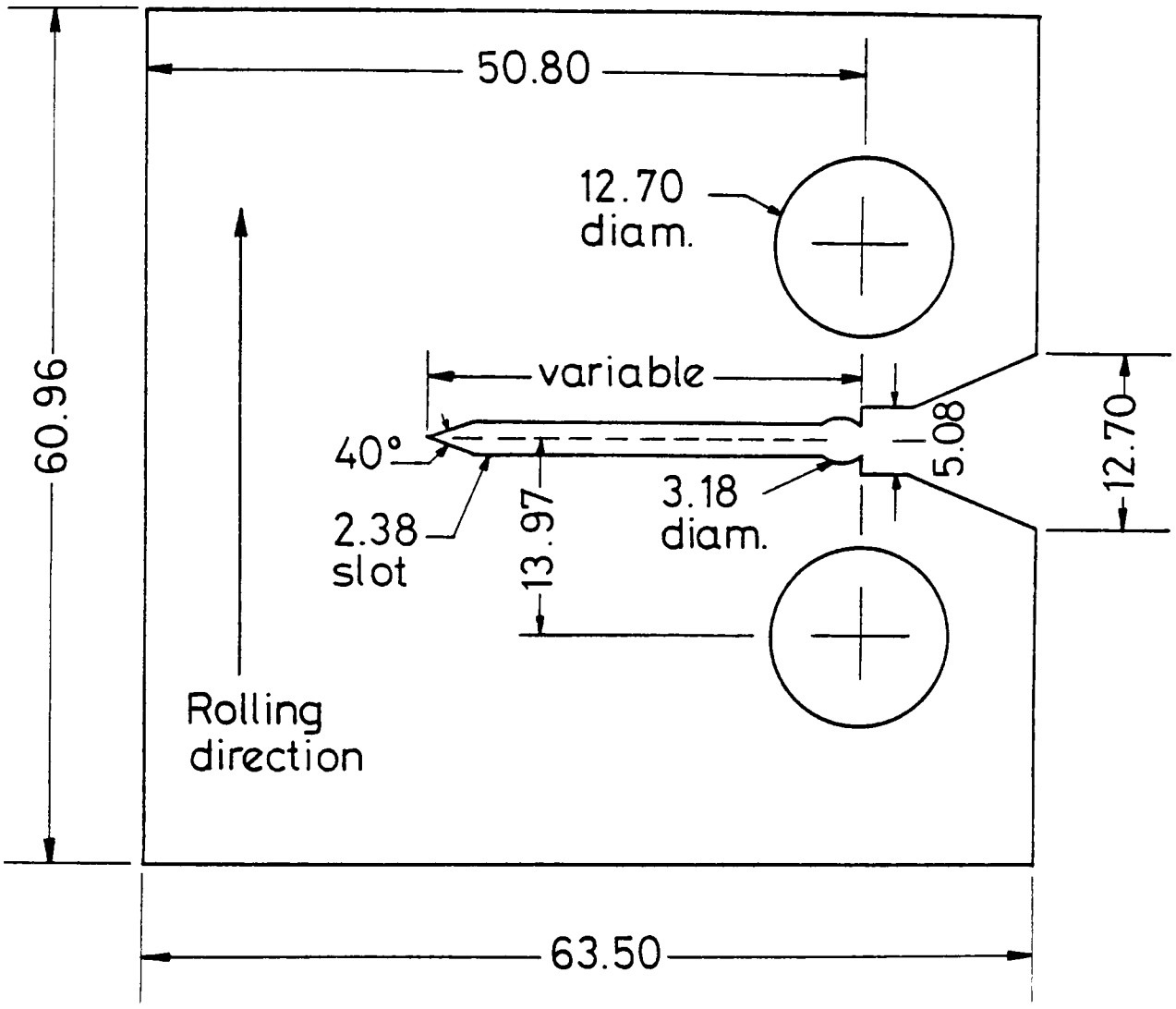
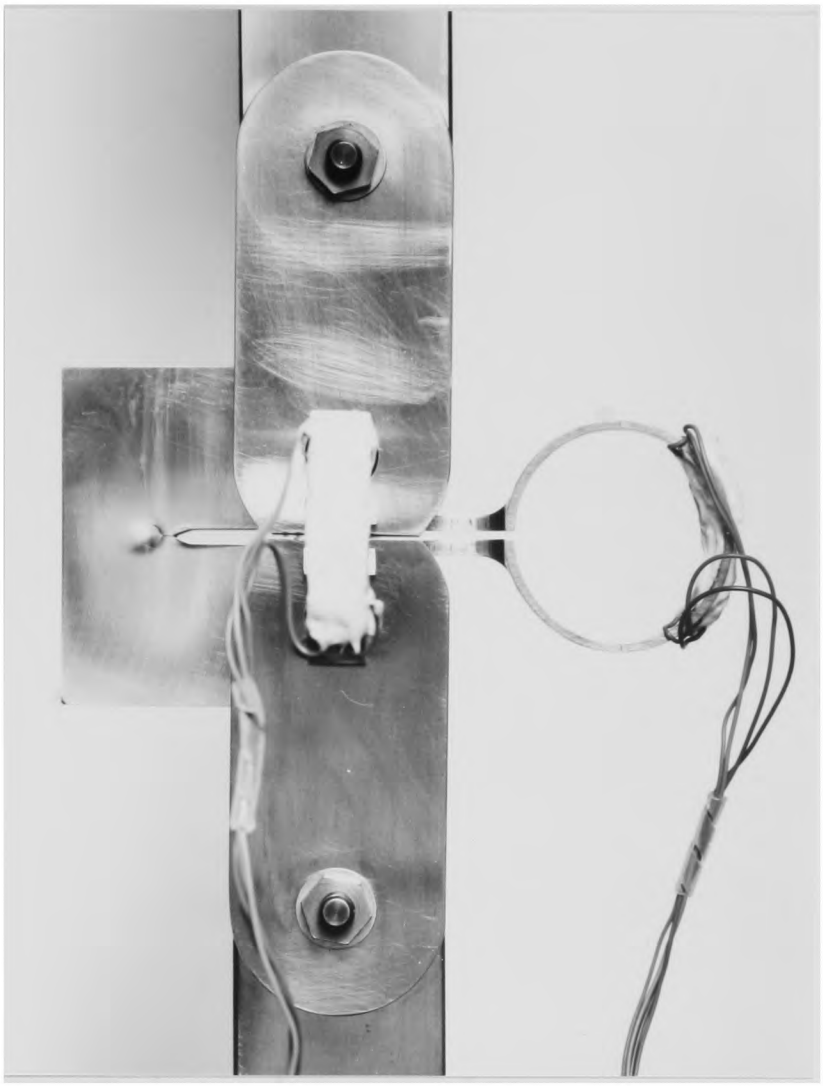


Fig. 7.2 True stress versus true strain for heat treated maraging steel at room temperature

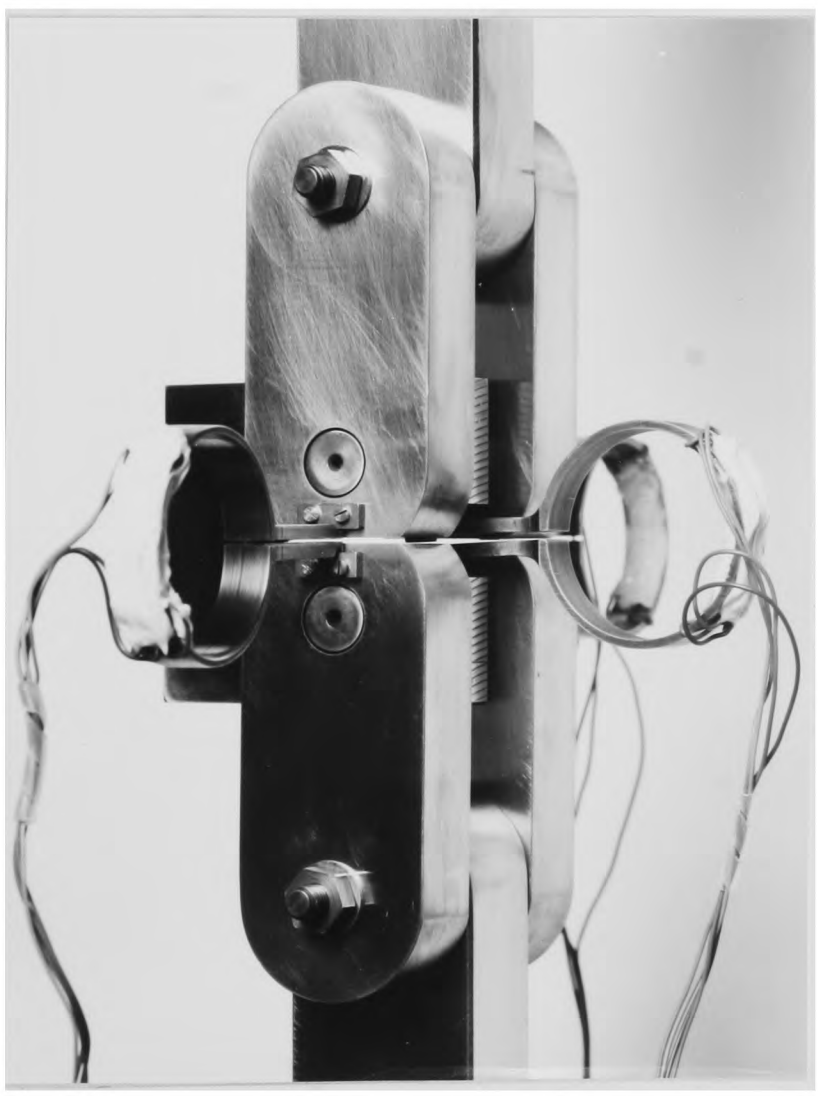


(Dimensions in mm.)

Fig. 7.3 Modified compact specimen configuration for maraging steel plate tests



a. Front view



b. Side view

Fig. 7.4 Experimental set-up for maraging steel plate tests

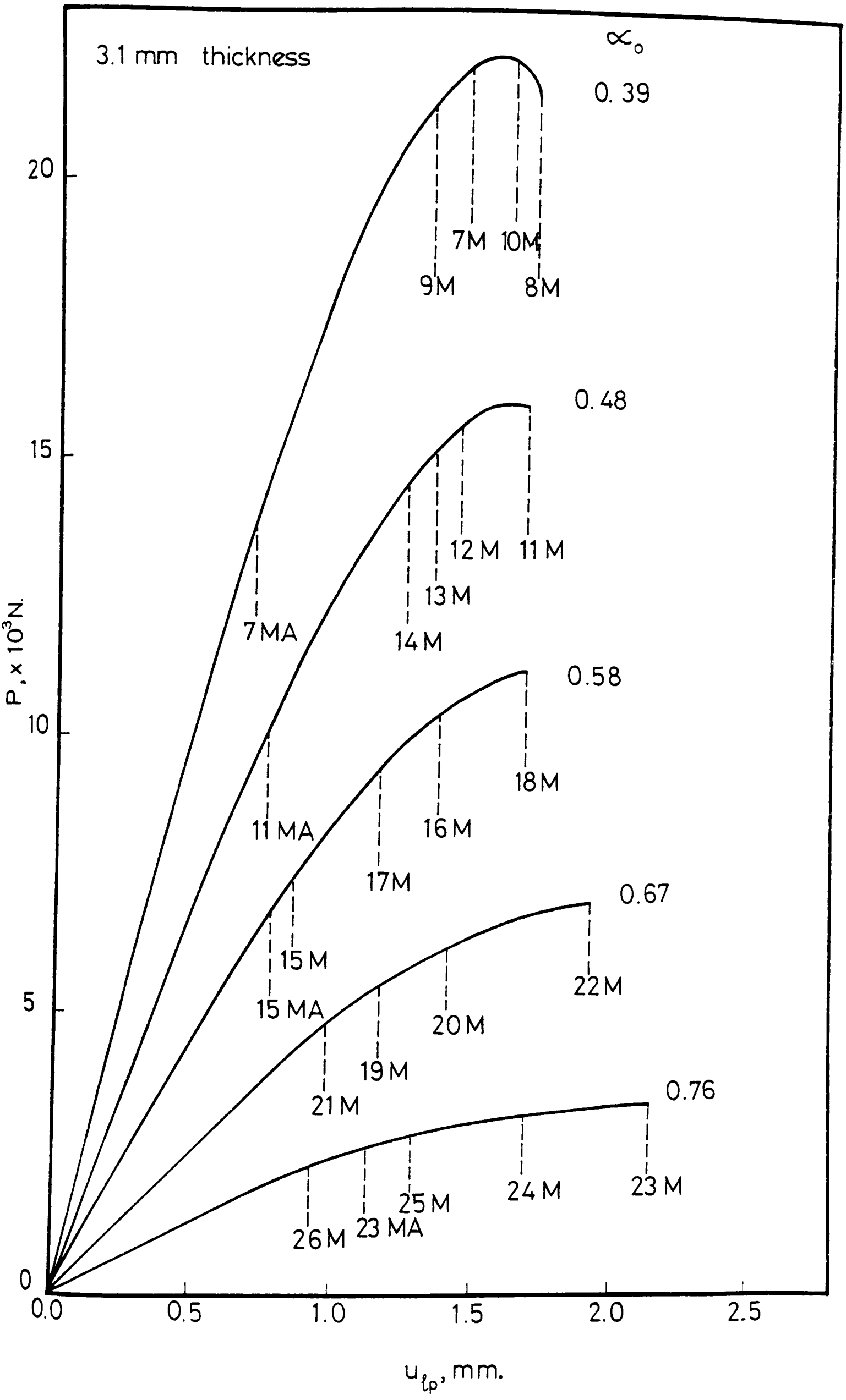


Fig. 7.5 Experimental load-load pin displacement curves for 3.1 mm thickness maraging steel compact specimens

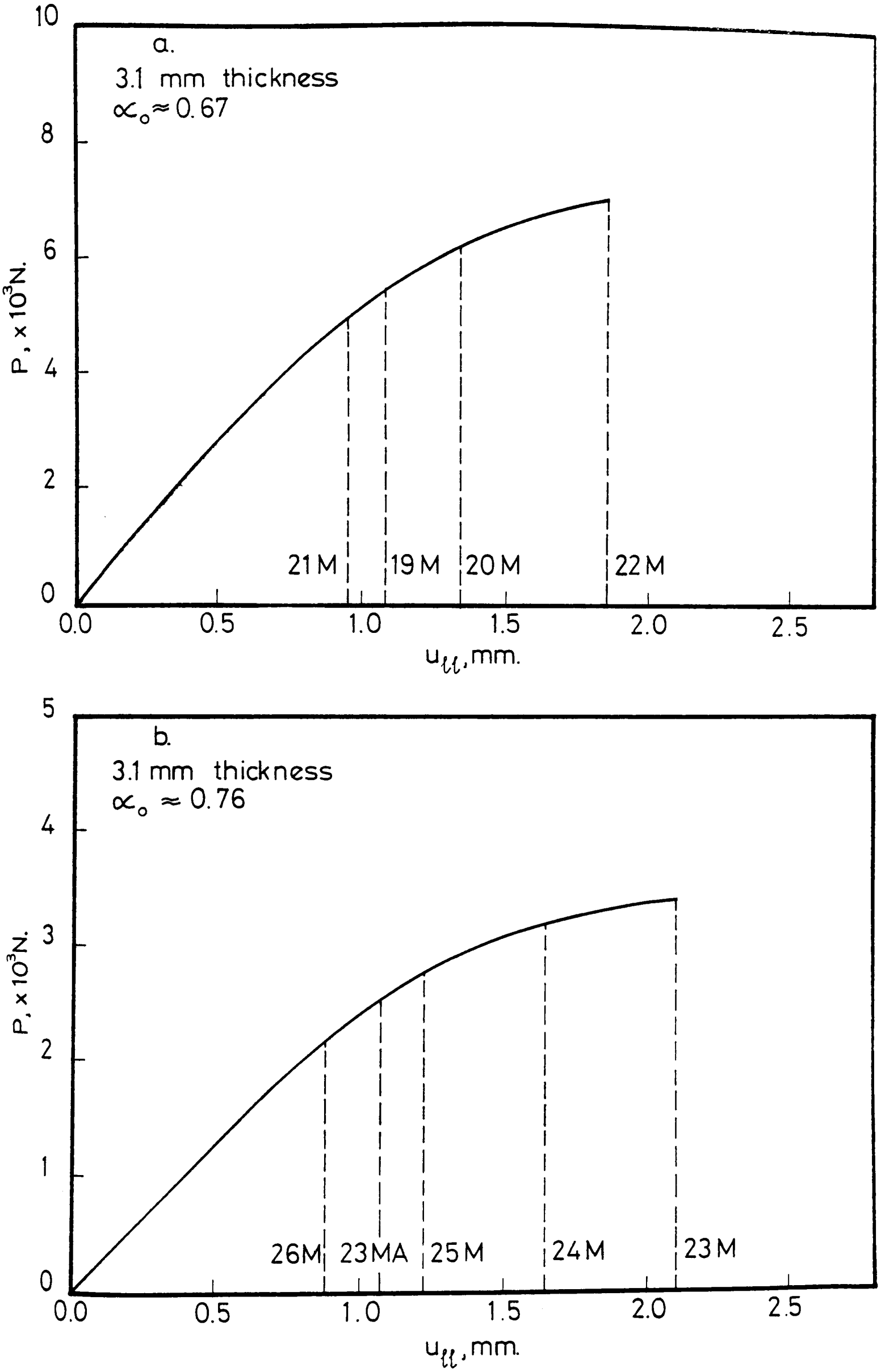


Fig. 7.6 Experimental load-load line displacement curves for maraging steel compact specimens a. and b. 3.1 mm thickness

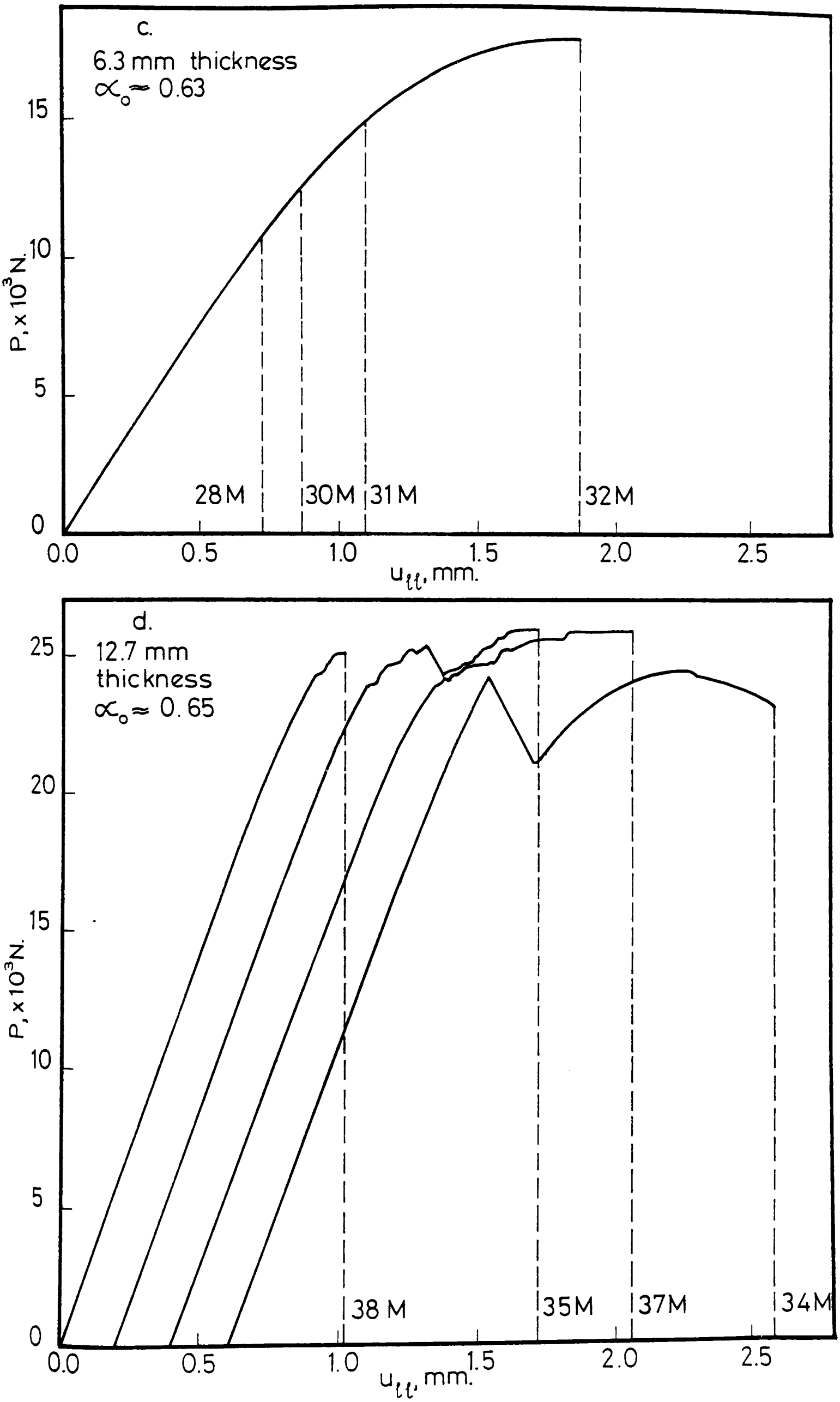


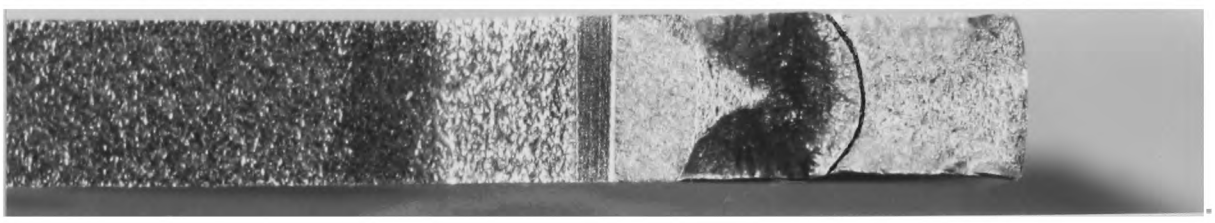
Fig. 7.6 (cont.) c. 6.3 mm thickness and d. 12.7 mm thickness



a. Crack initiation (25M, α_o = 0.769, x 5.6)



b. Load maximum (23M, α_o = 0.763, x 5.7)

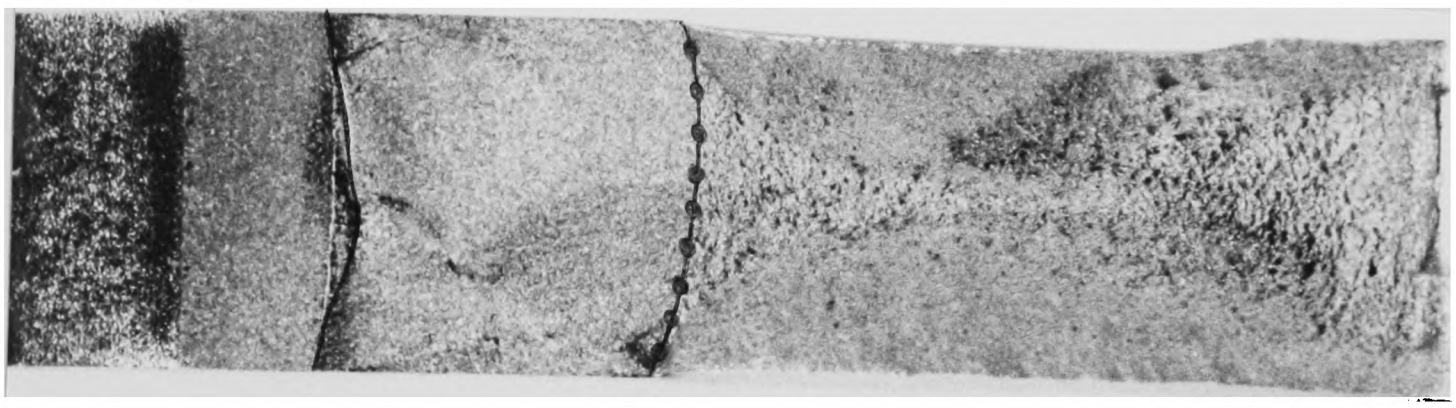


c. Load maximum (10M, α_o = 0.389, x 5.4)

Fig. 7.7 Typical fractures of 3.1 mm thickness maraging steel compact specimens

——— Limit of crack extension

—•—•— Limit of secondary fatigue cracking



a. Crack initiation (30M, α_o = 0.623, x 5.7)

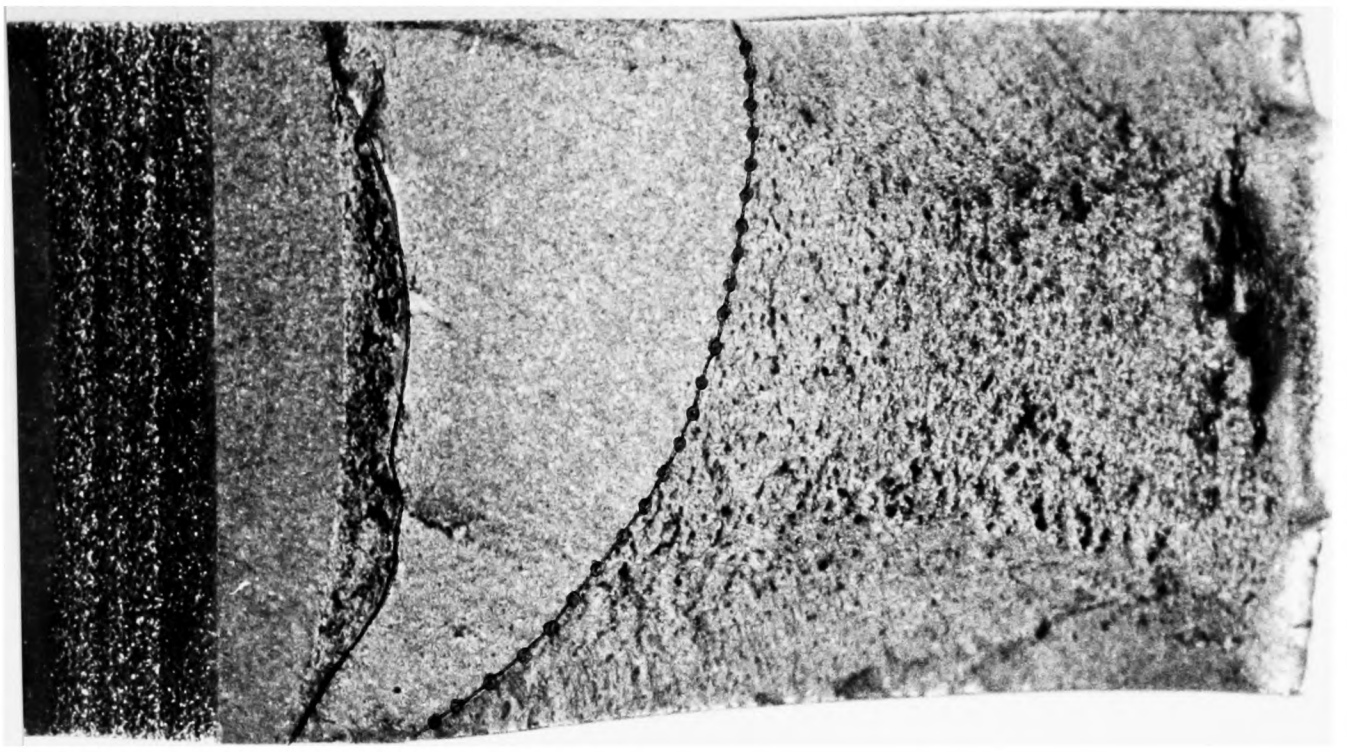


b. Load maximum (32M, α_o = 0.631, x 5.7)

Fig. 7.8 Typical fractures of 6.3 mm thickness maraging steel compact specimens

——— Limit of crack extension

—•—•— Limit of secondary fatigue cracking



a. Crack initiation (38M, α_o = 0.644, x 5.7)



b. Load maximum (34M, α_o = 0.648, x 5.7)

Fig. 7.9 Typical fractures of 12.7 mm thickness maraging steel compact specimens

——— Limit of crack extension

—•—•— Limit of secondary fatigue cracking



(Specimen 3, α_o = 0.551, x 5.1)

Fig. 7.10 Typical fracture of 25.4 mm thickness maraging steel compact specimen

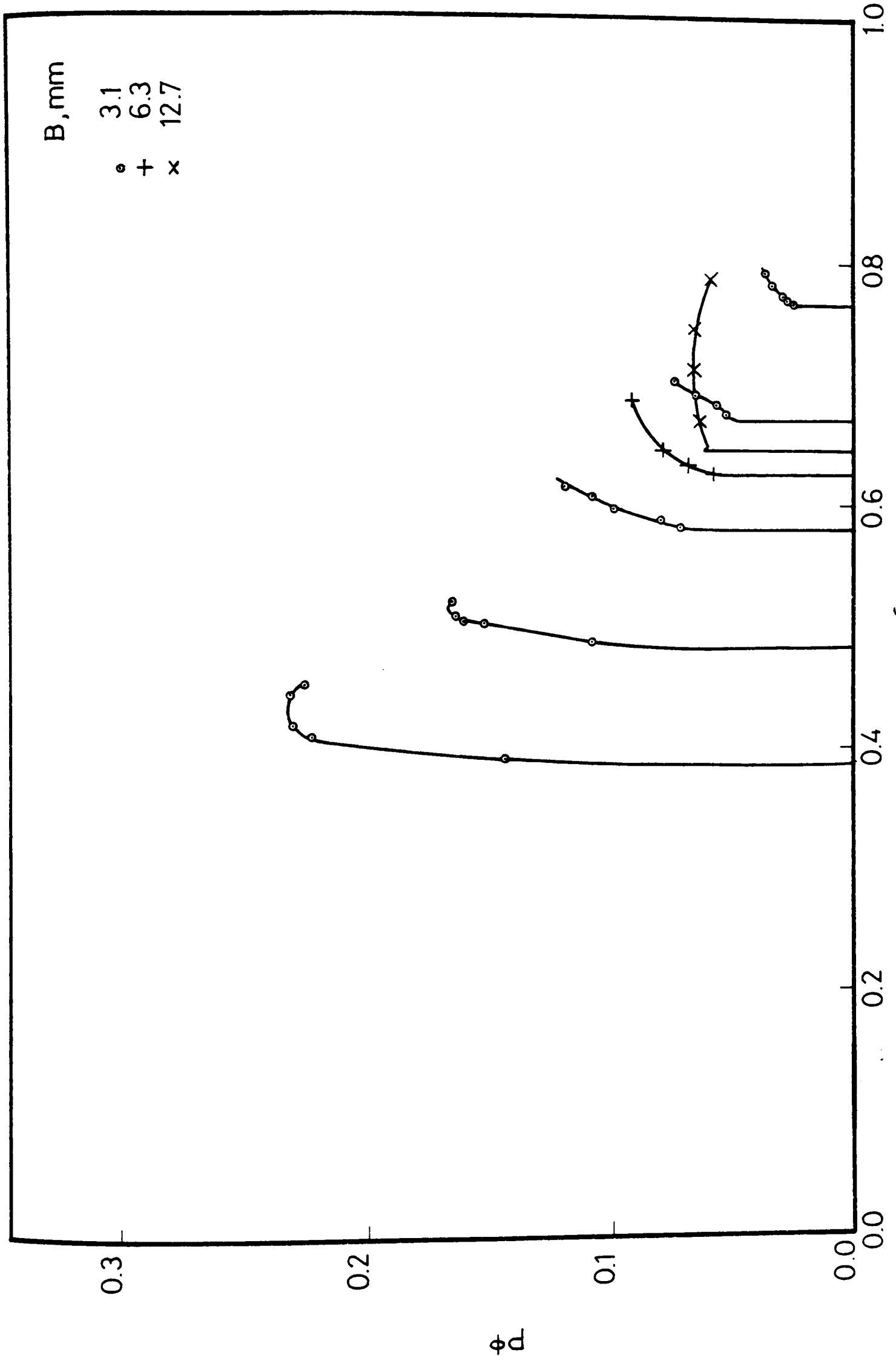


Fig. 7.11 Summary of experimental results for maraging steel compact specimens

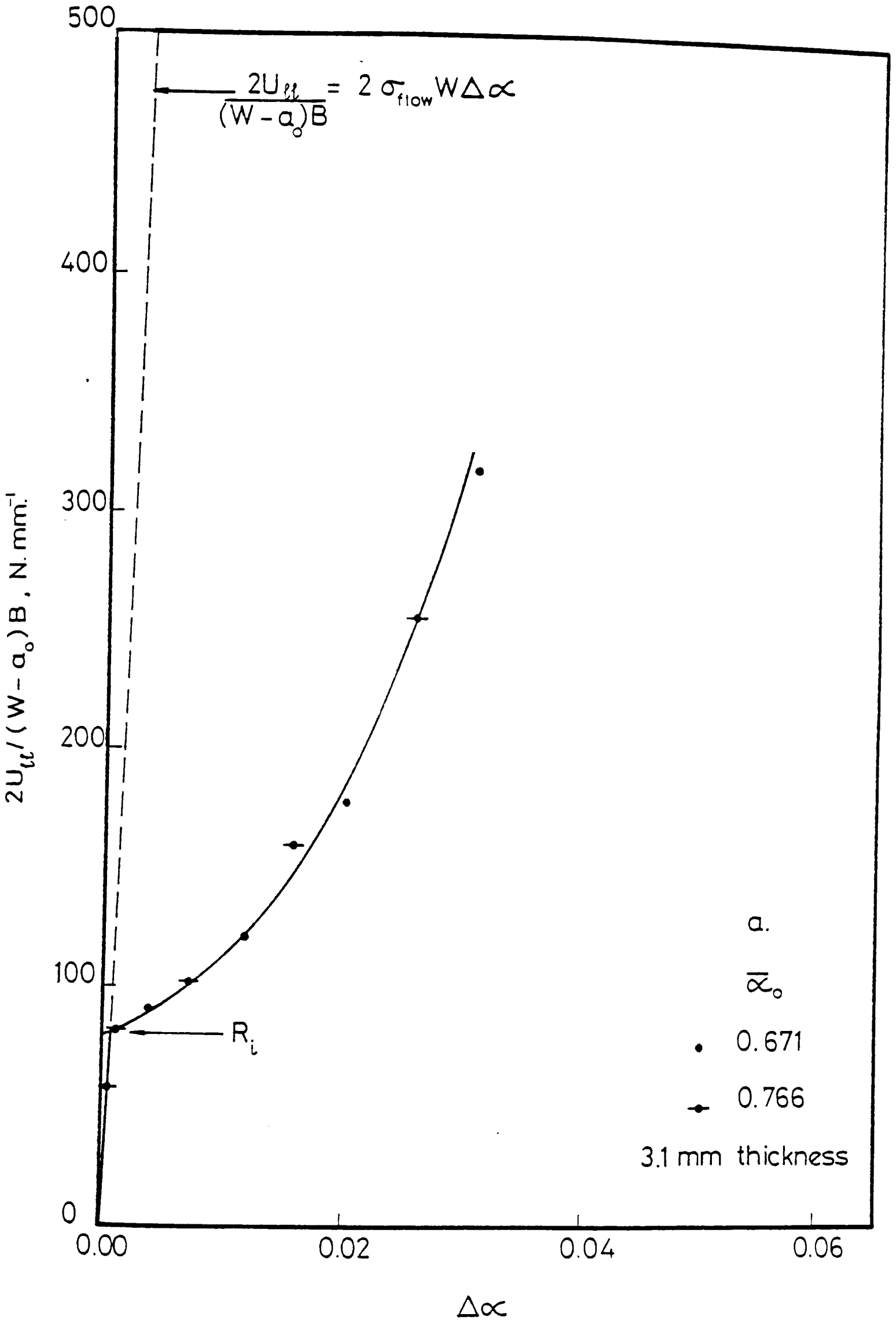


Fig. 7.12 Determination of R_i for crack initiation for maraging steel using Landes and Begley's approximate method
a. 3.1 mm thickness

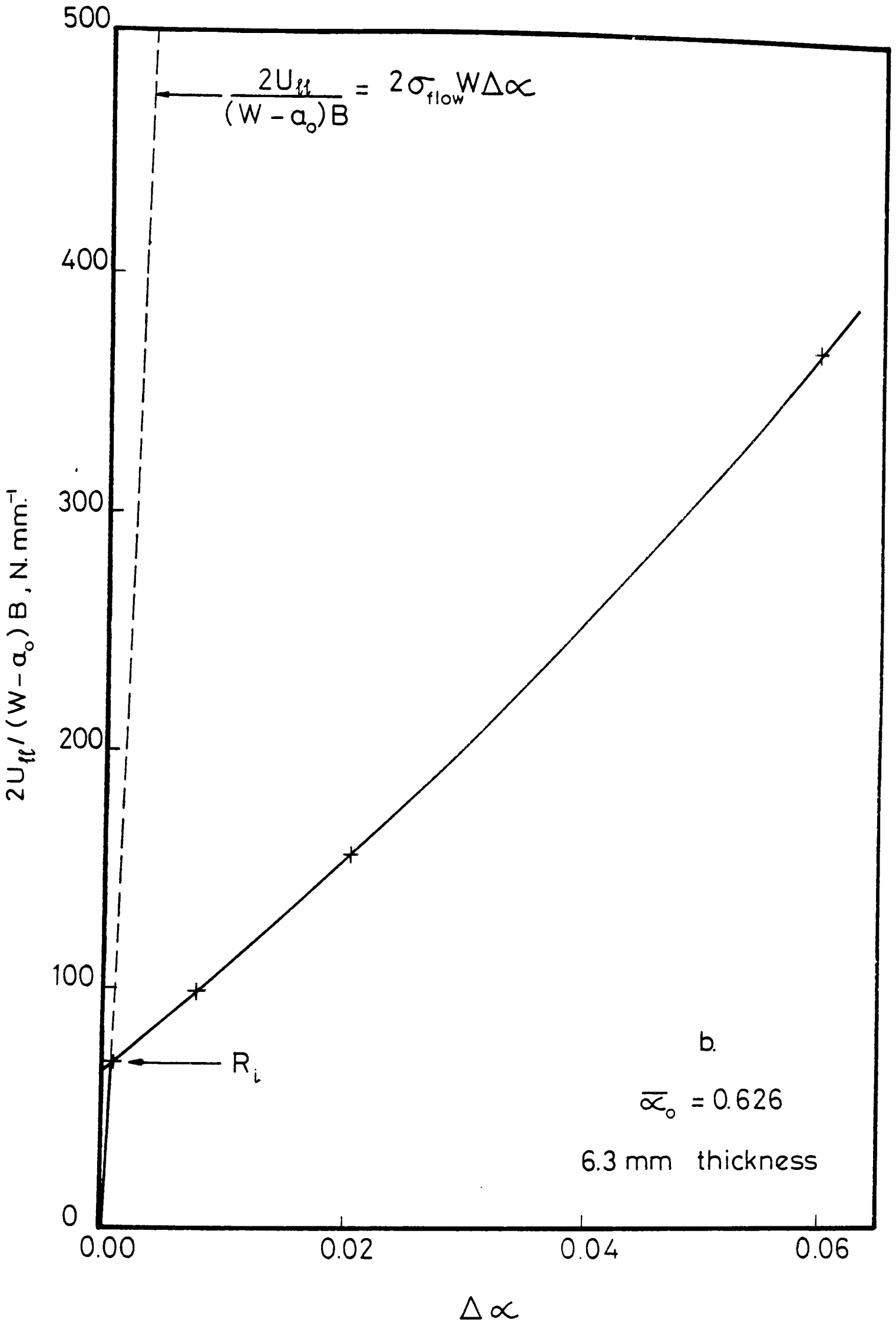


Fig. 7.12 (cont.) b. 6.3 mm thickness

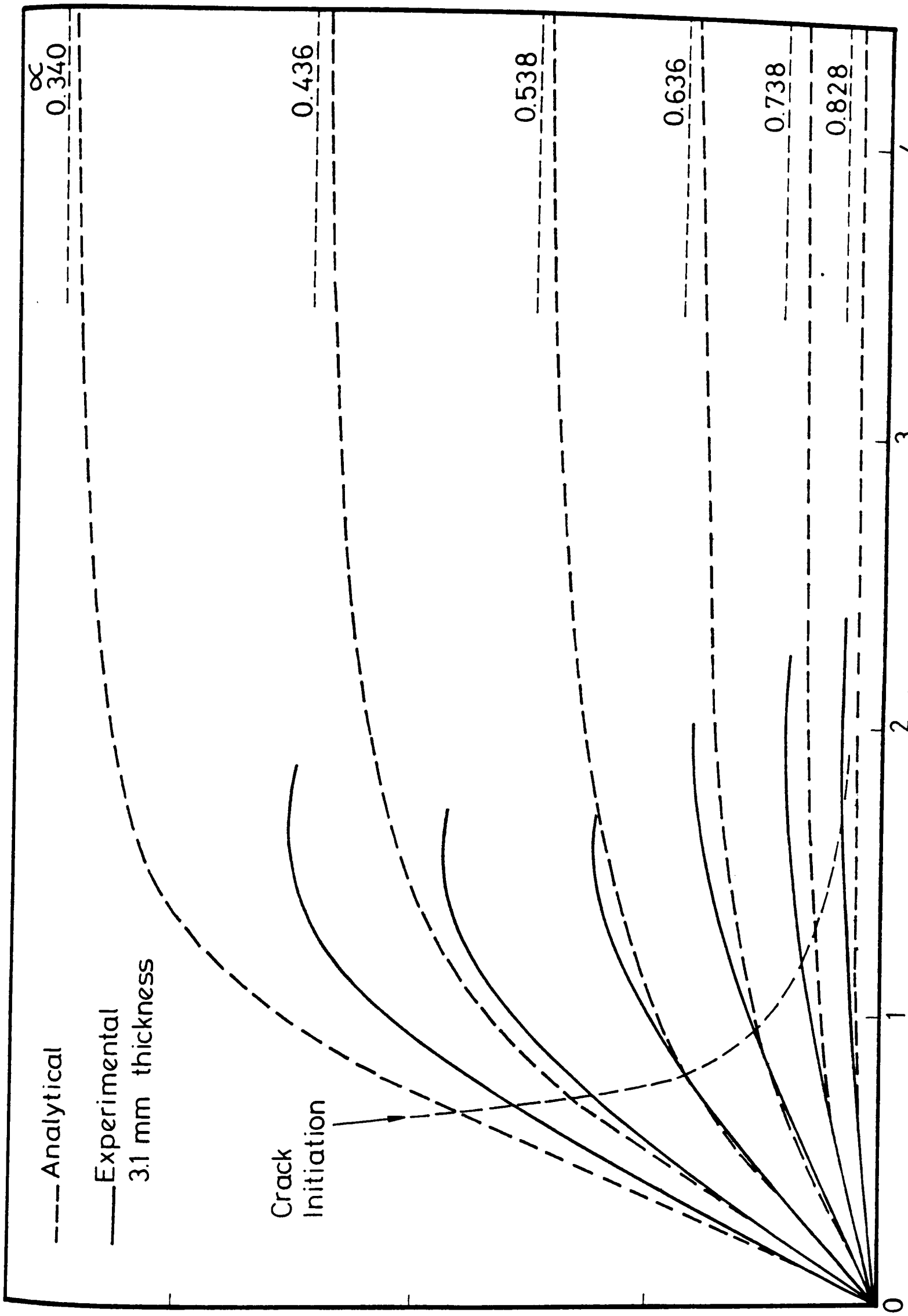


Fig. 7.13 Comparison of analytical and experimental load-load pin displacement curves for 3.1 mm thickness maraging steel compact specimens

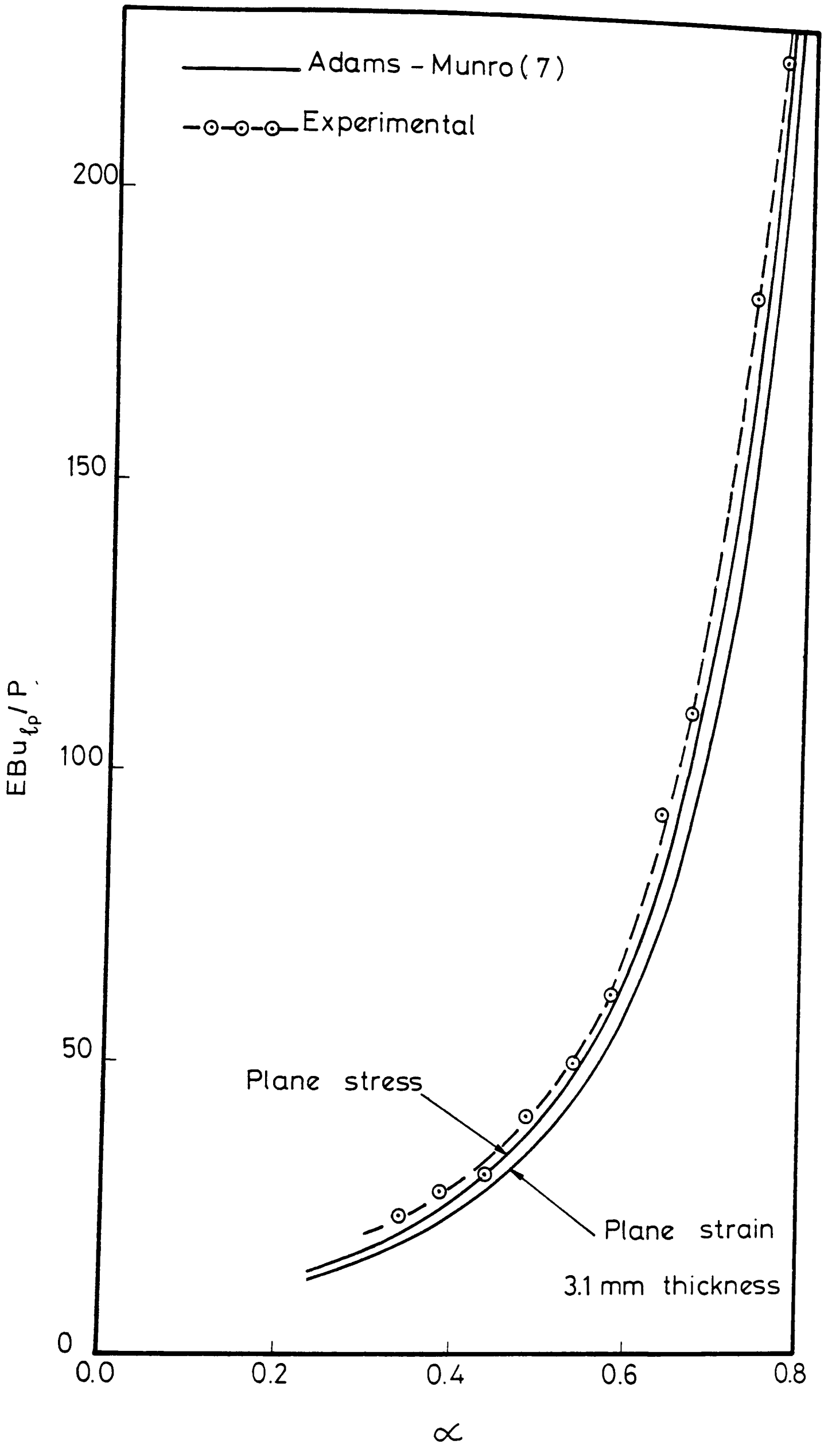


Fig. 7.14 Comparison of analytical and experimental elastic compliances for 3.1 mm thickness maraging steel compact specimens

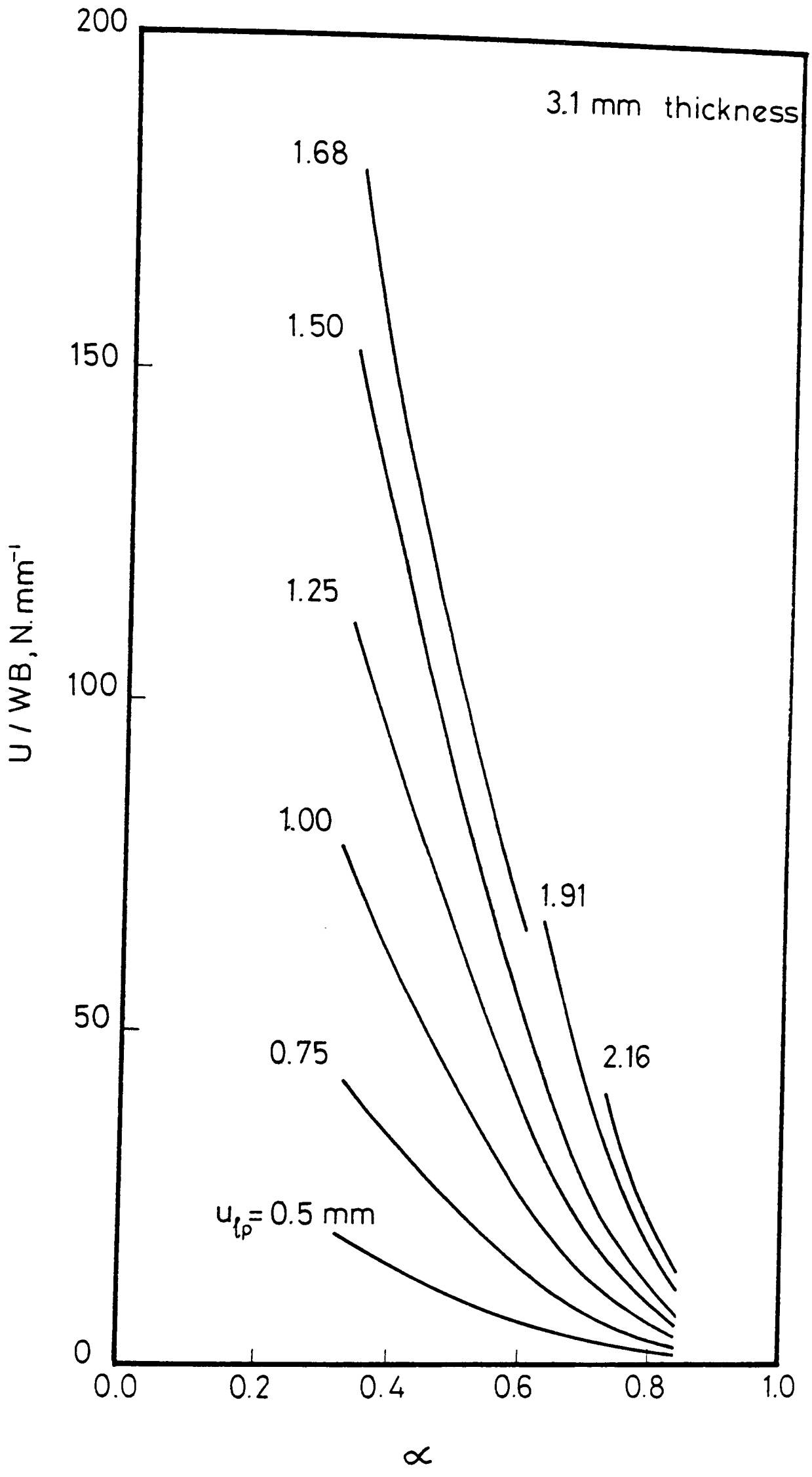


Fig. 7.15 Experimental curves of strain energy versus relative crack length for 3.1 mm thickness maraging steel compact specimens

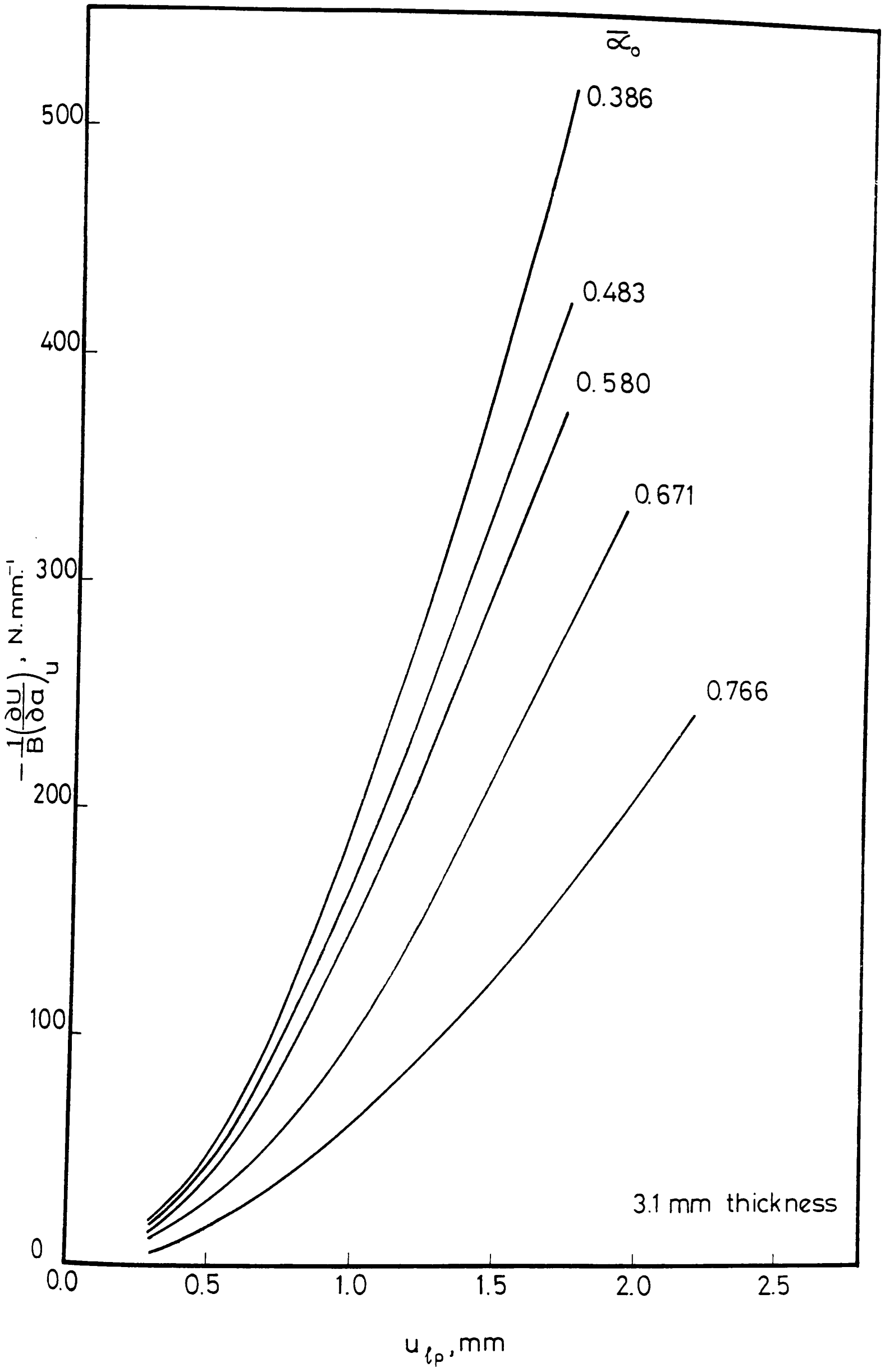


Fig. 7.16 Experimental curves of strain energy slope versus displacement for 3.1 mm thickness maraging steel compact specimens

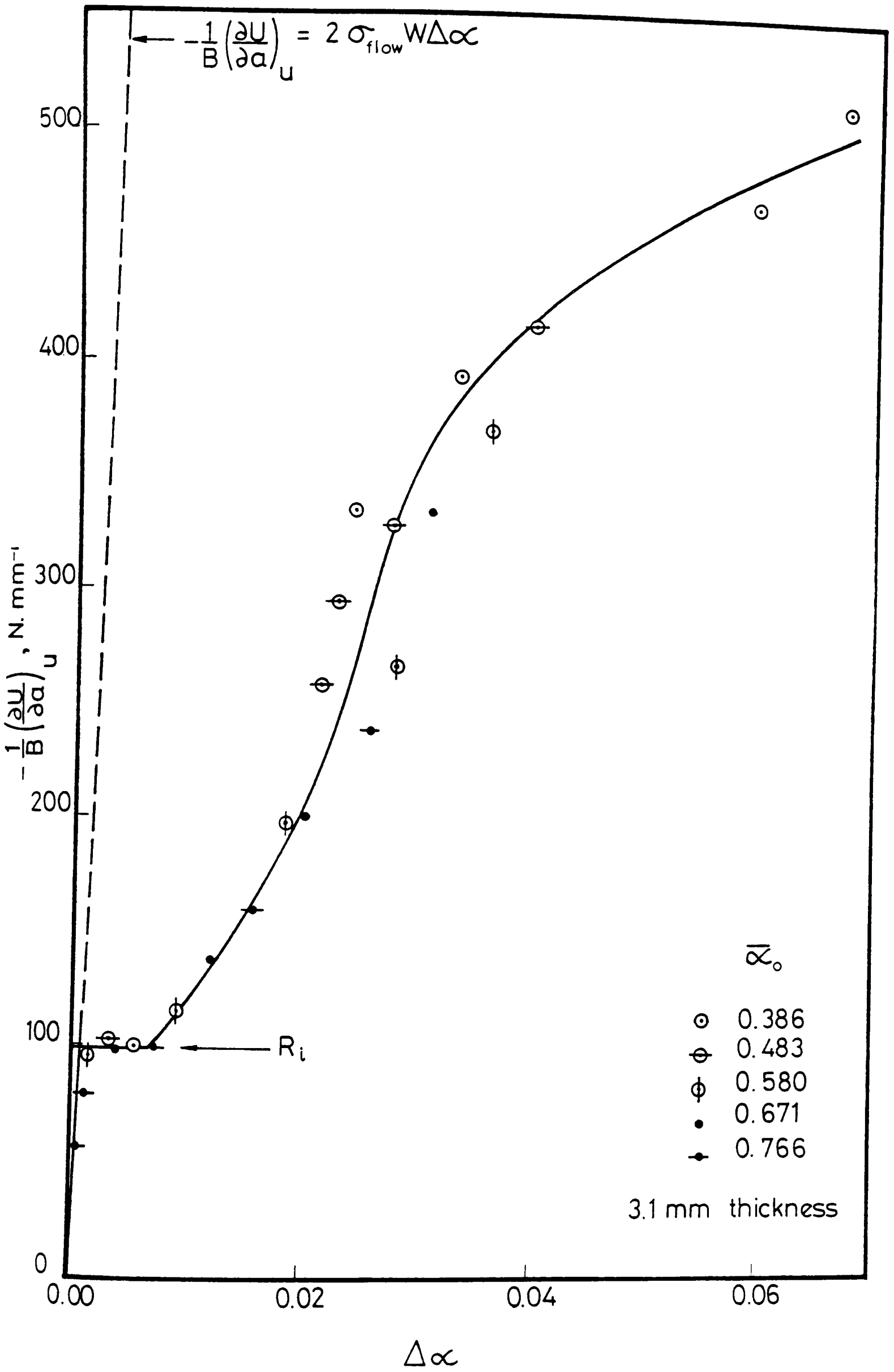


Fig. 7.17 Determination of R_i for crack initiation for 3.1 mm thickness maraging steel compact specimens using the calibration function, $-\frac{1}{B}\left(\frac{\partial U}{\partial a}\right)_u$

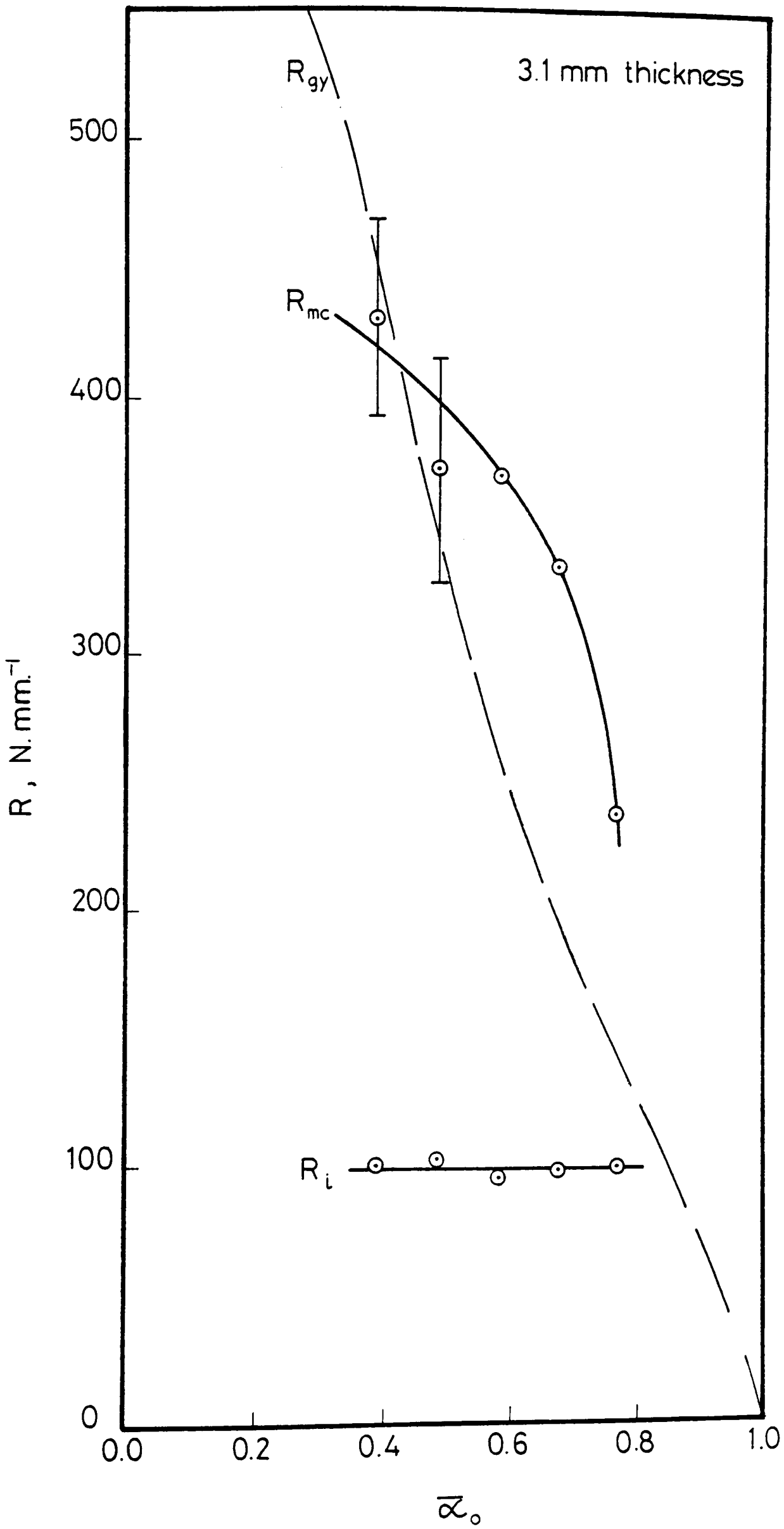


Fig. 7.18 Comparison of R values for 3.1 mm thickness maraging steel compact specimens

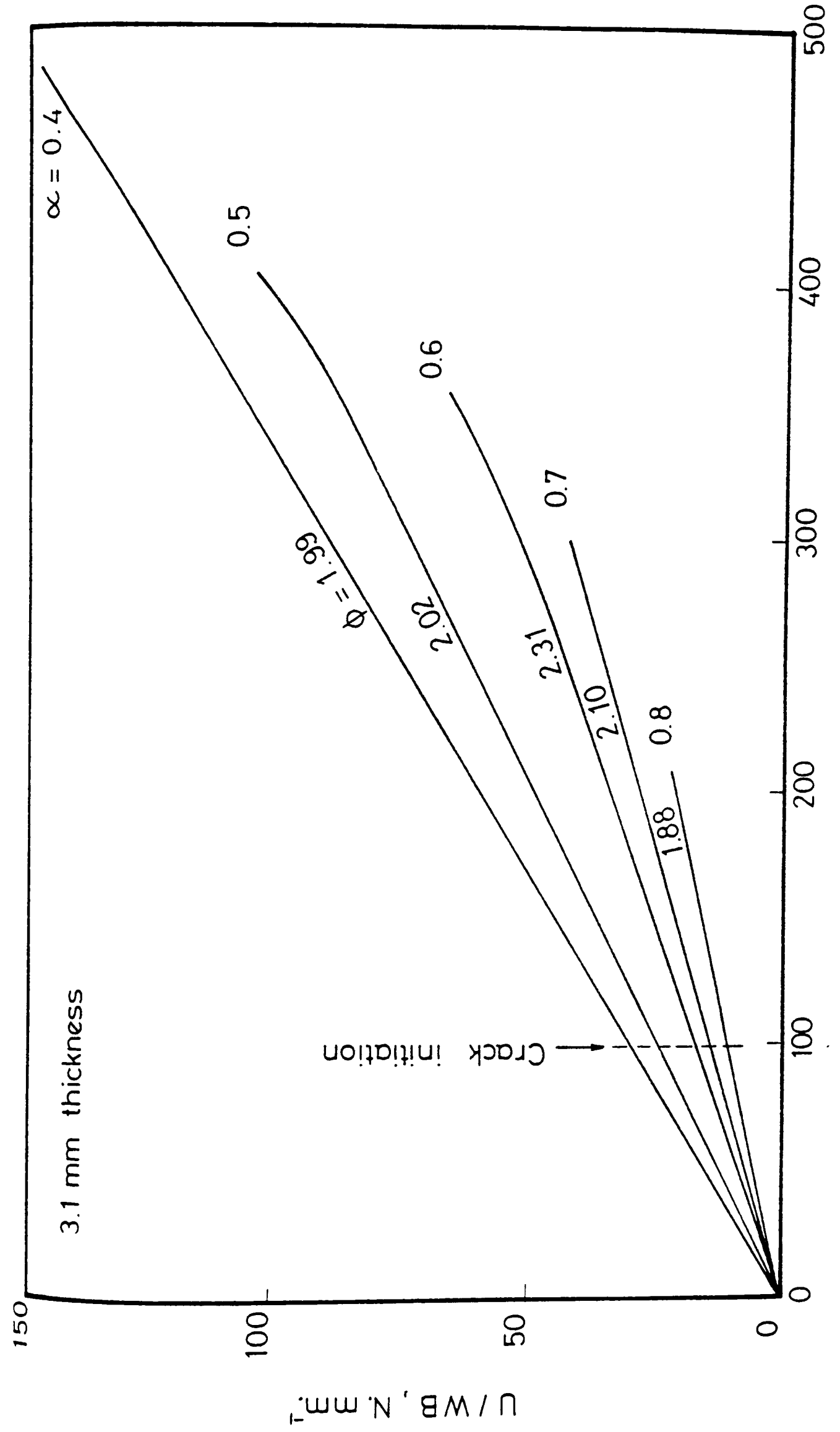
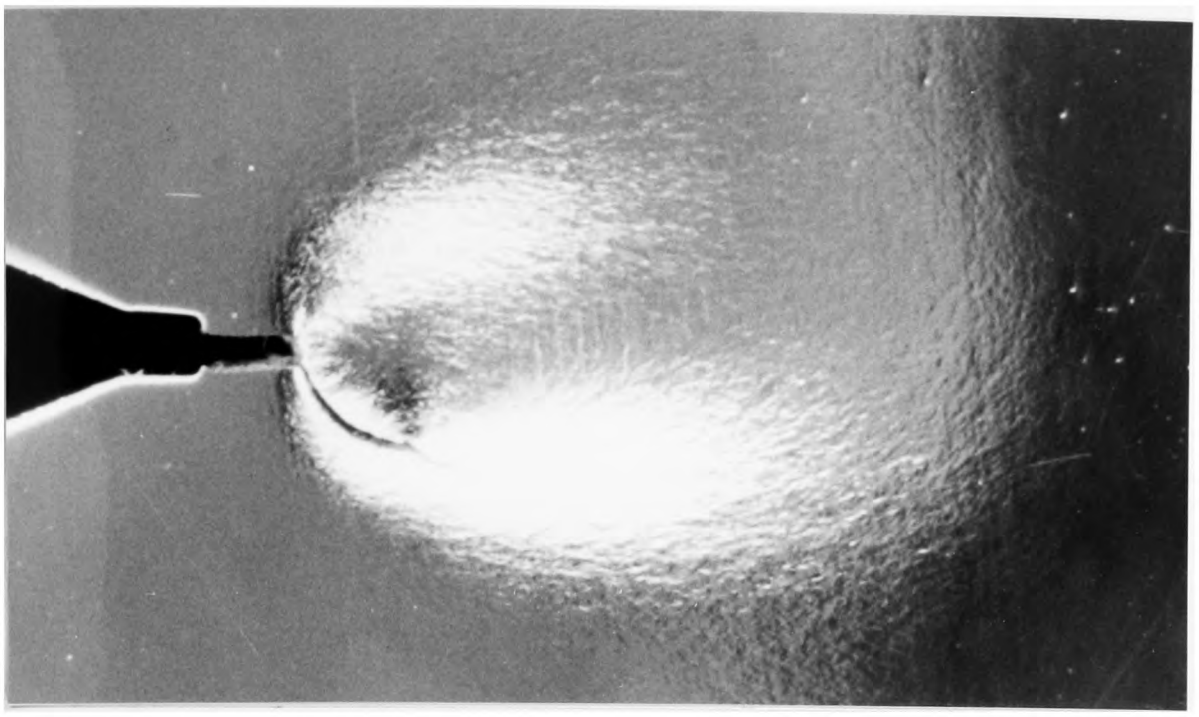
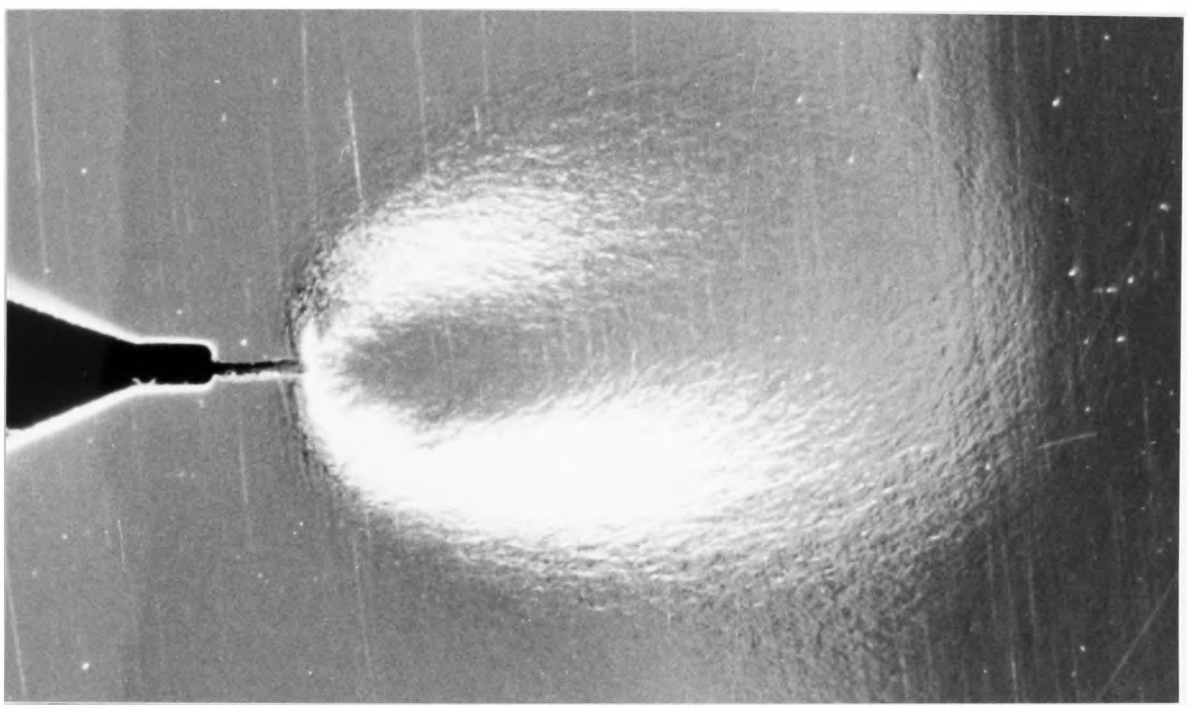


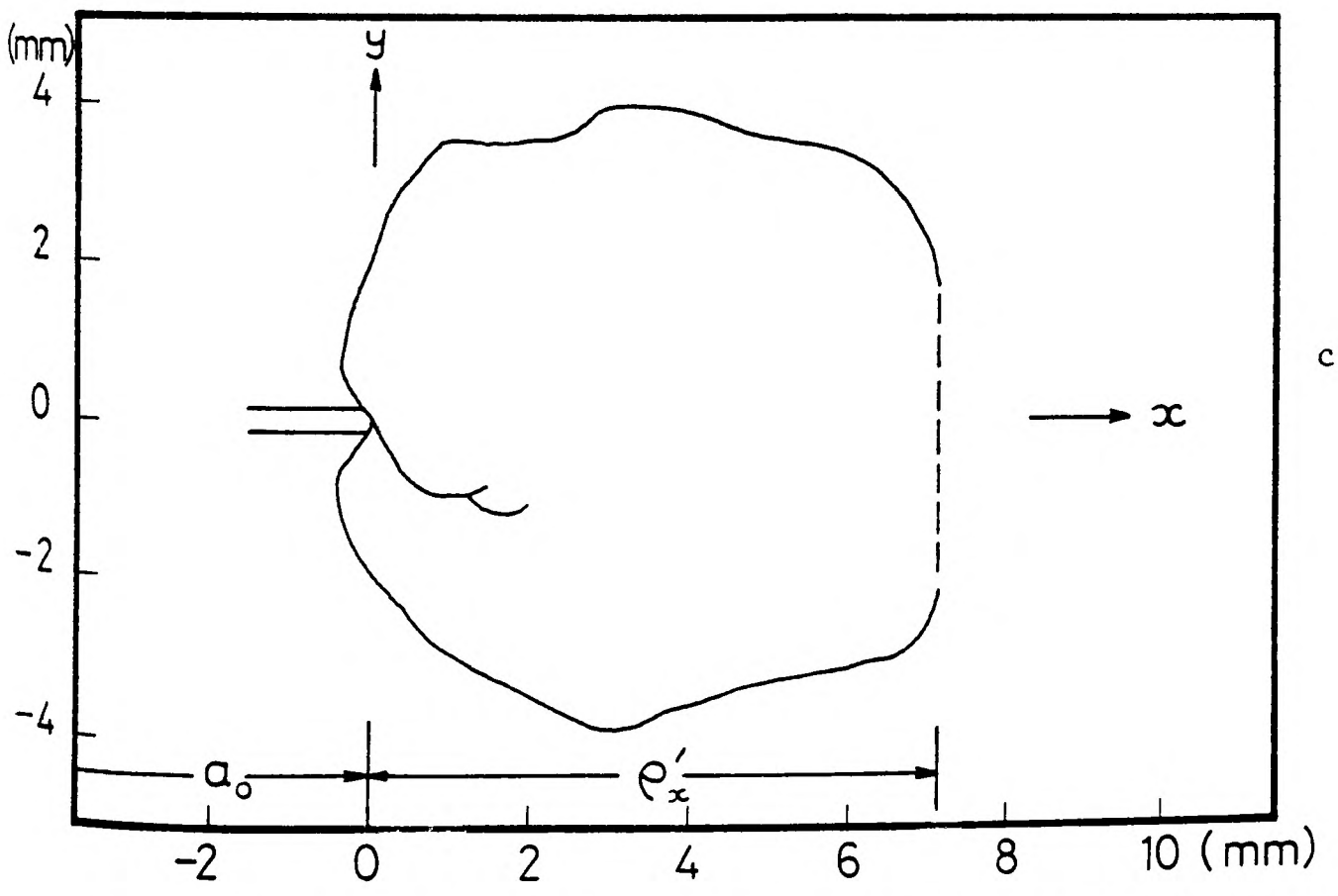
Fig. 7.19 Experimental curves of strain energy versus strain energy slope for 3.1 mm thickness maraging steel compact specimens



a. Loaded (x9.1) oblique illumination



b. Unloaded (x9.1) oblique illumination



c. Unloaded-contour of $w = 2.5 \times 10^{-4}$mm

Fig. 7.20 Typical surface plastic zone development for 3.1 mm thick maraging steel compact specimen ($\alpha_o = 0.604$, $P = 9.3 \times 10^3$N)

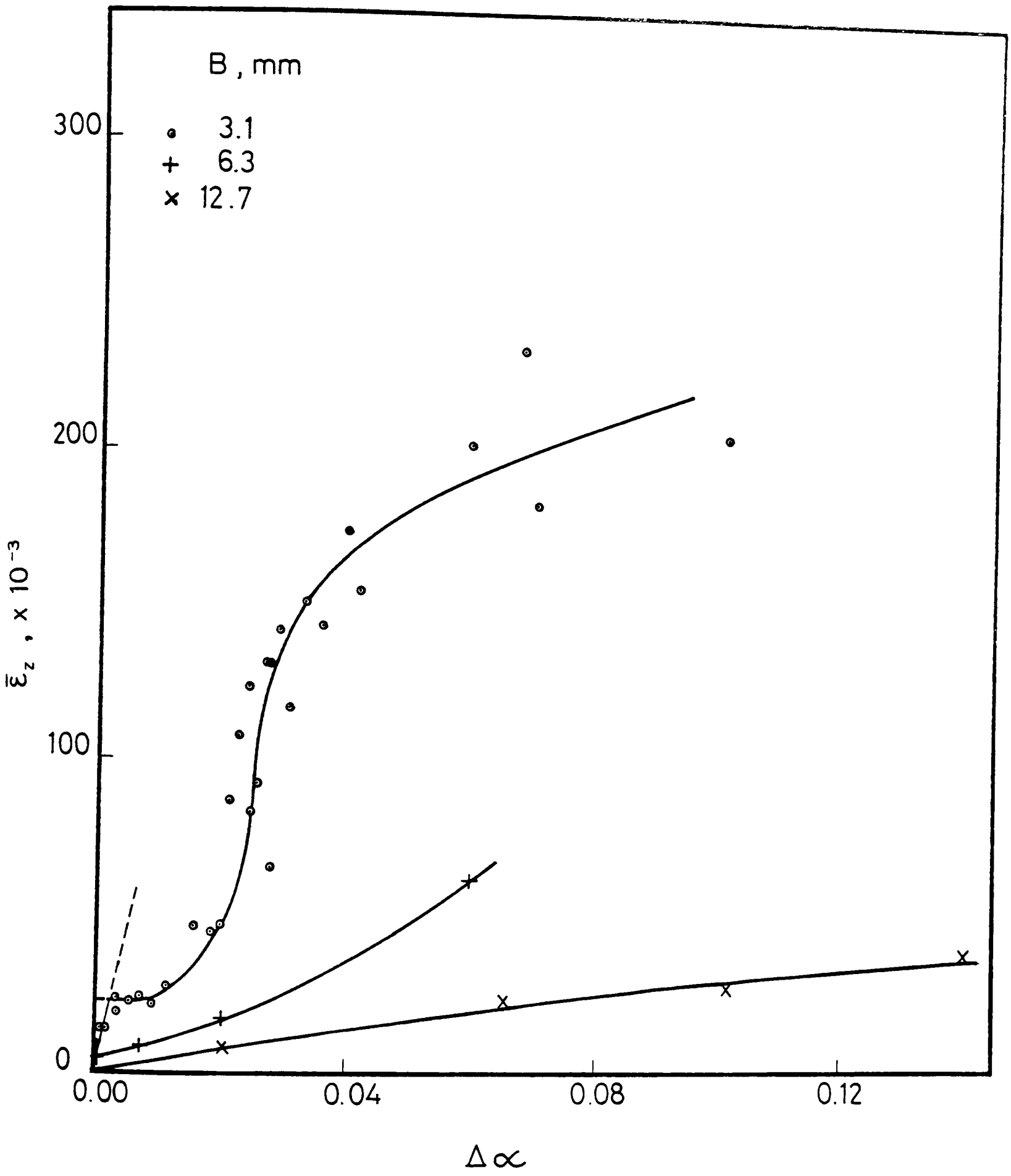


Fig. 7.21 Average through-thickness strain versus relative crack extension for maraging steel compact specimens

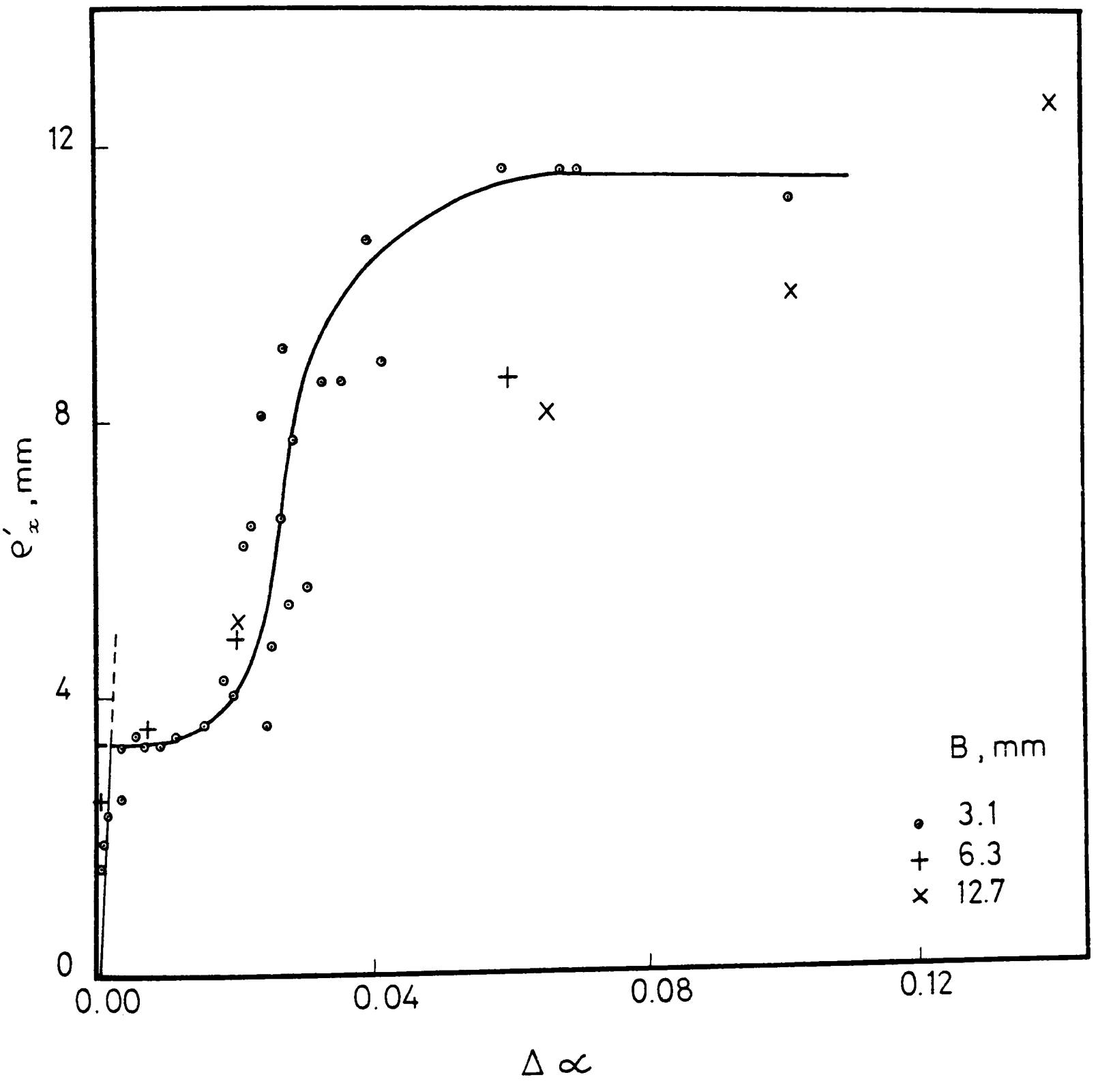
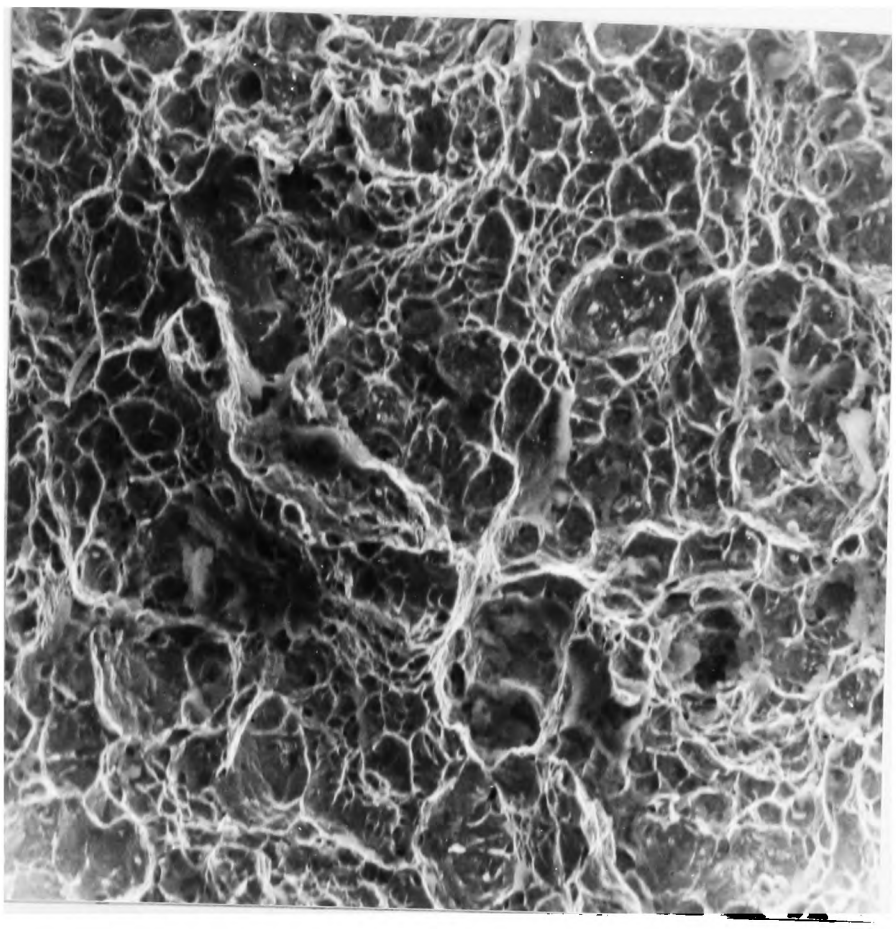
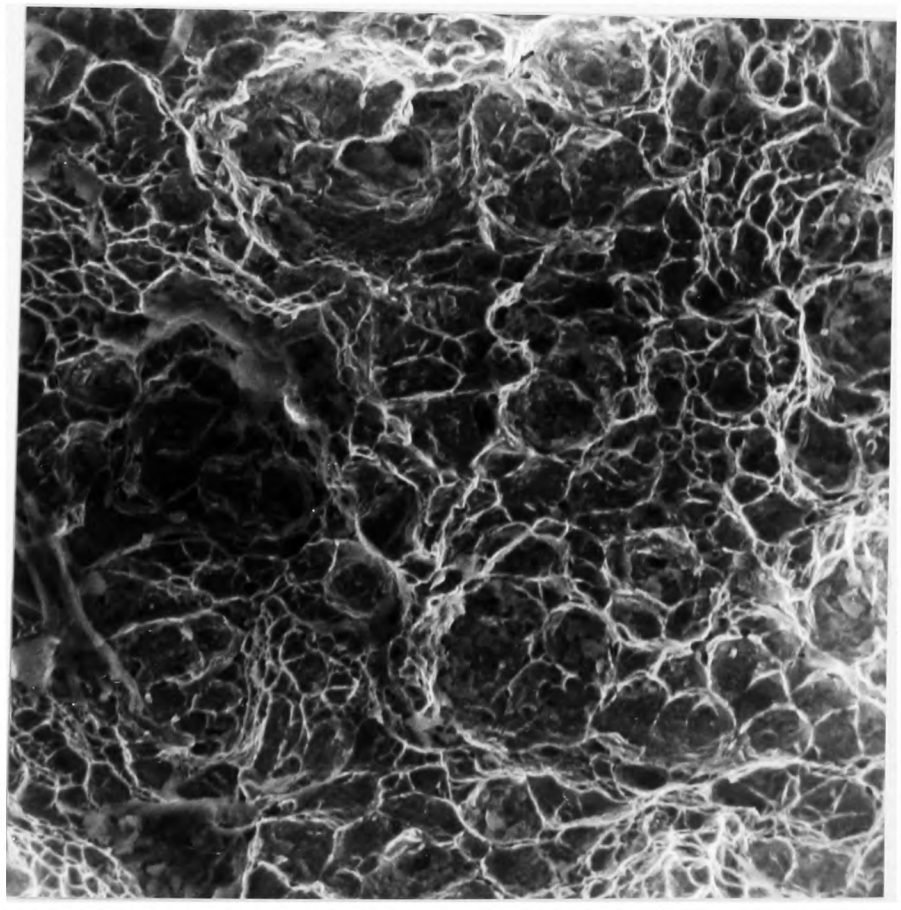


Fig. 7.22 Surface plastic zone size versus relative crack extension for maraging steel compact specimens

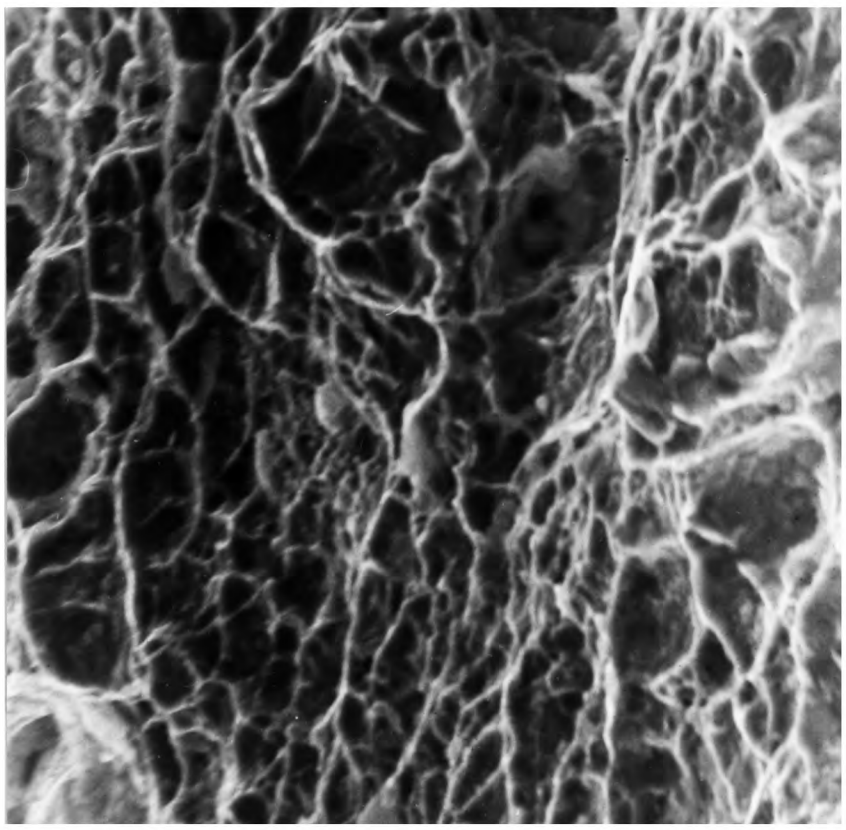


a. Equiaxed dimples in tensile fracture region of 3.1 mm thick plate (x600)



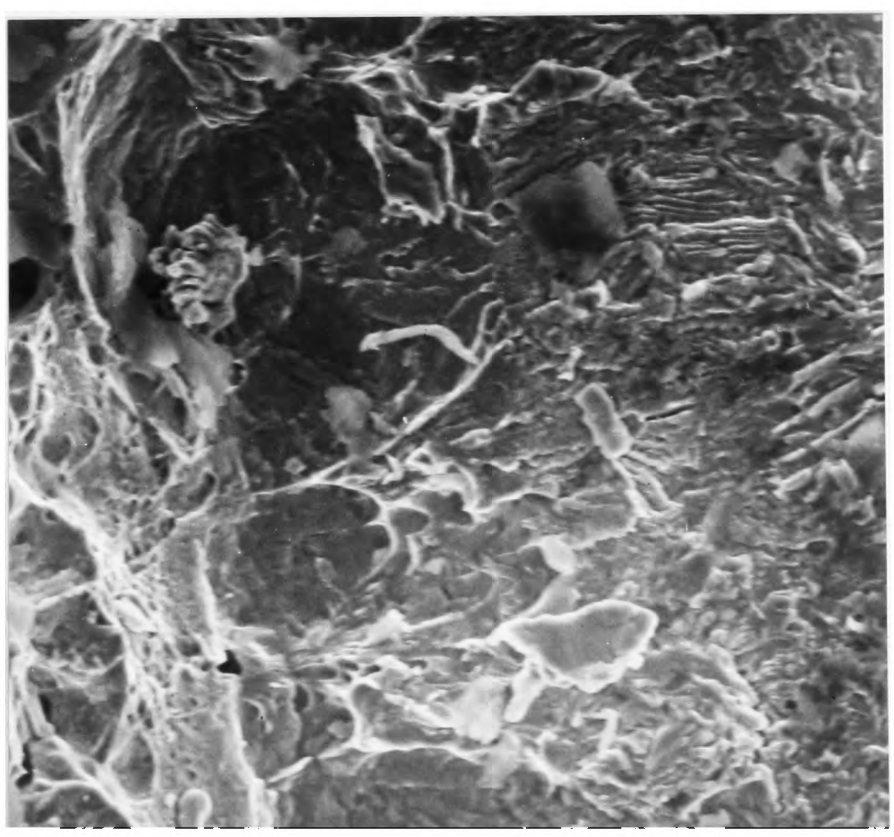
b. Equiaxed dimples in tensile fracture region of 6.3 mm thick plate (x600)

Fig. 7.23 Typical scanning electron micrographs of fractured maraging steel compact specimens



c. Elongated dimples in shear fracture region (x1600)

tensile fracture	stretch zone	fatigue precrack



d. Stretch zone (x1000)

Fig. 7.23 (cont.)

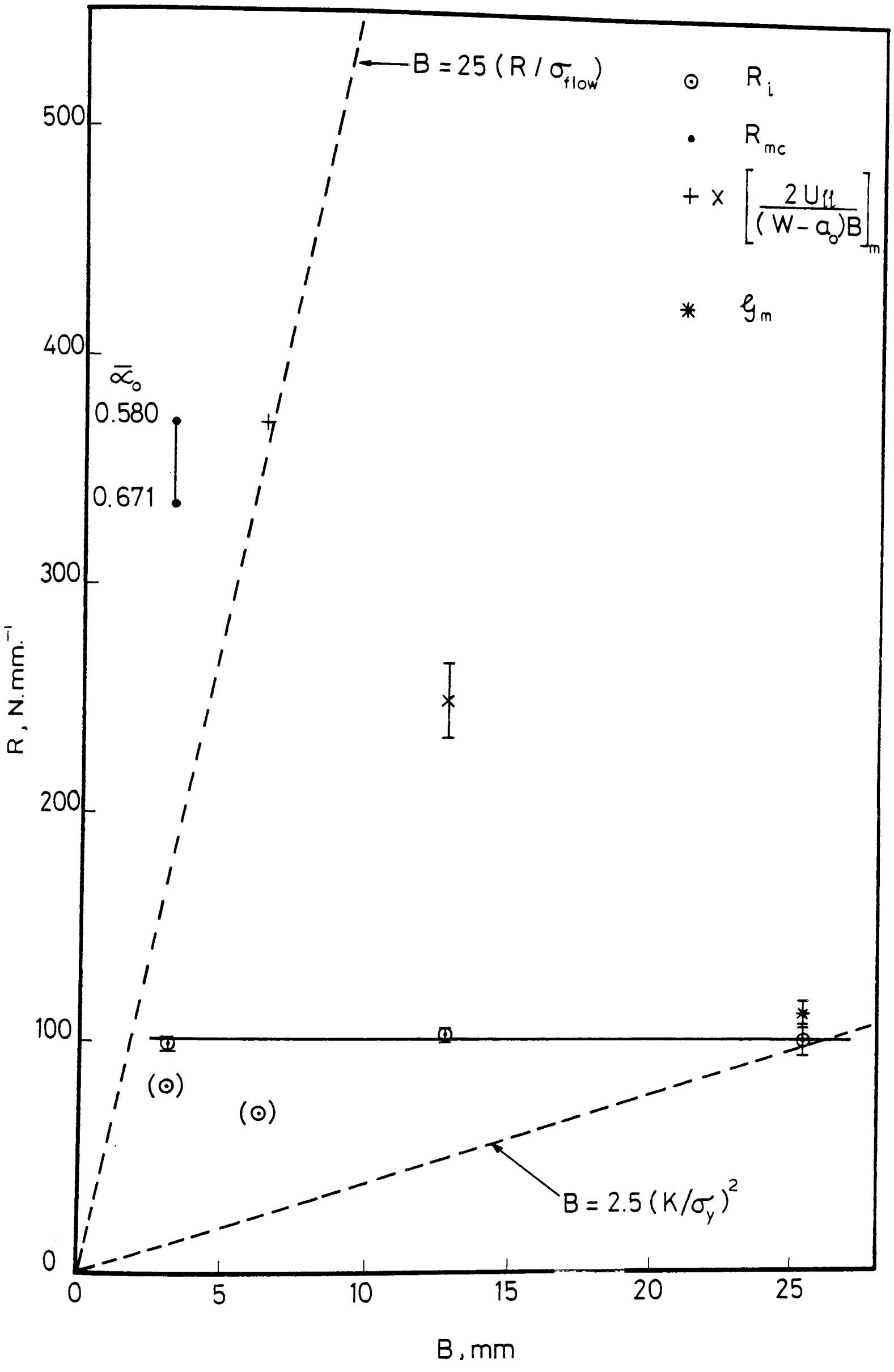


Fig. 7.24 Comparison of R values for different thickness maraging steel compact specimens

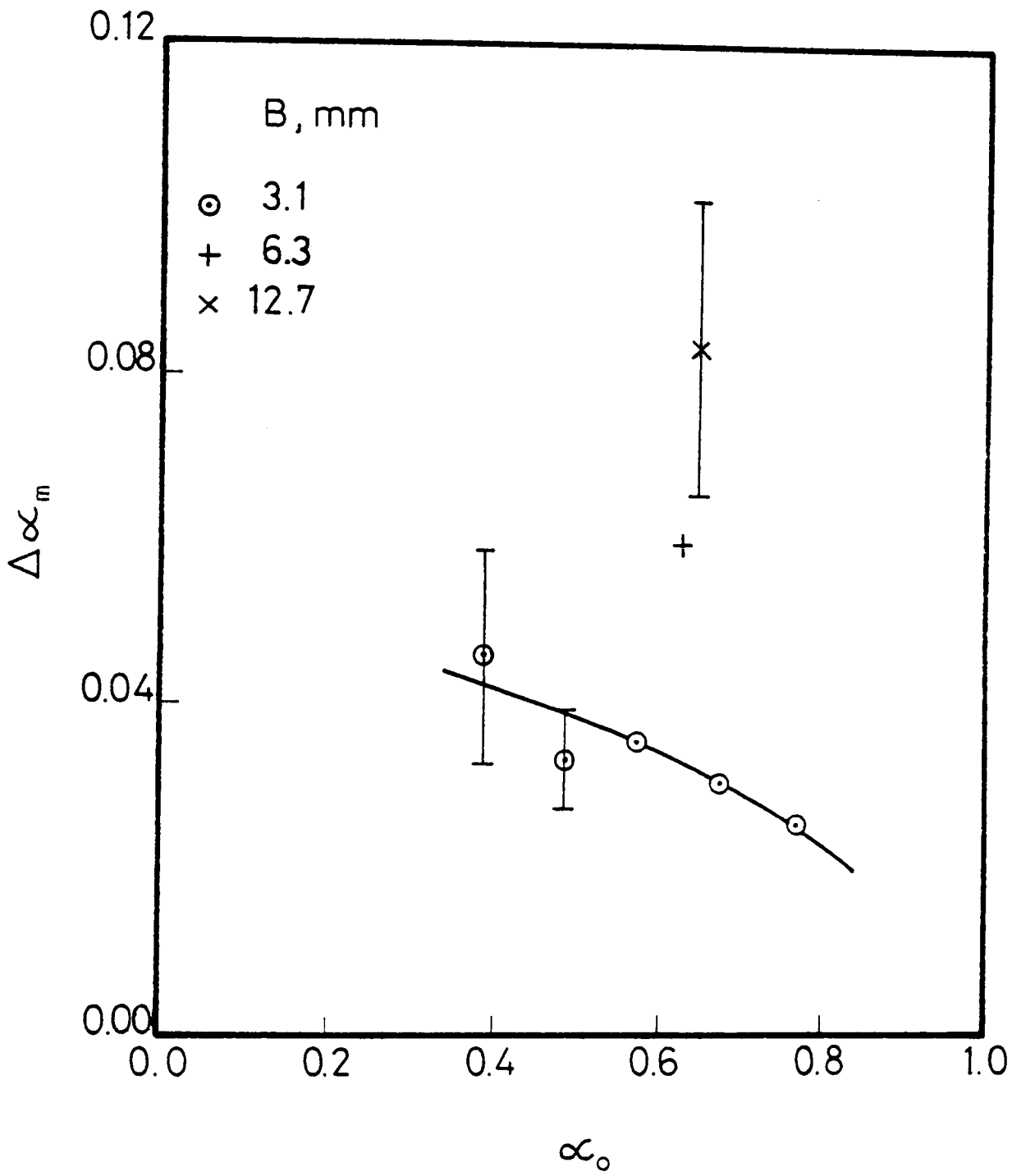


Fig. 7.25 Slow crack growth characteristics of maraging steel compact specimens

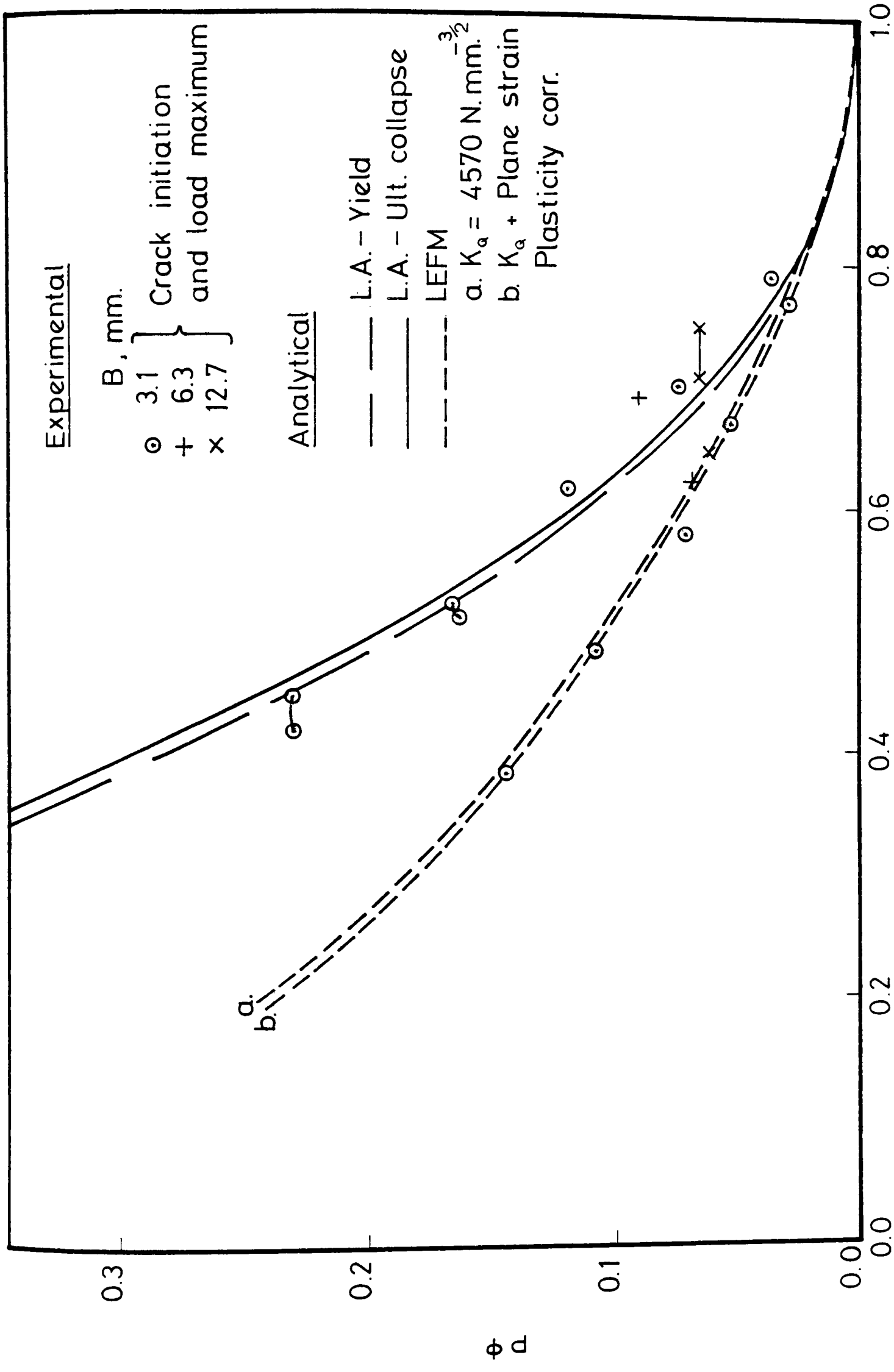


Fig. 7.26 Failure analysis diagram for maraging steel compact specimens — comparison of analytical and experimental results

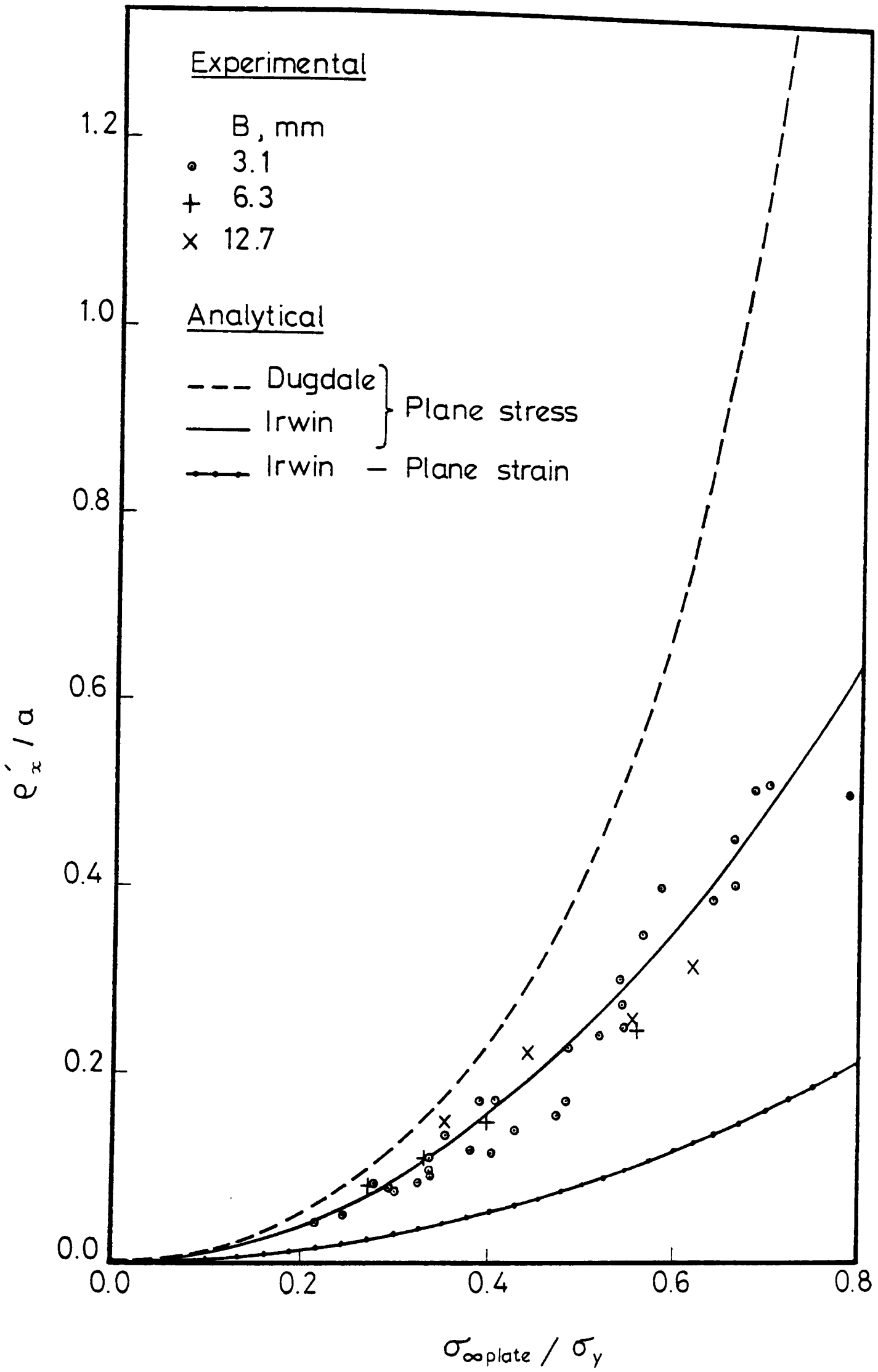


Fig. 7.27 Comparison of surface plastic zone size for maraging steel compact specimens with the Irwin and Dugdale models

CHAPTER 8

CRACK GROWTH IN MODEL VESSELS OF POLYCARBONATE

Room temperature tests were performed on model cylindrical vessels of polycarbonate made from the Bayer "Makrolon" 3203 grade used in the previous study. The dimensions were restricted by the ability to fabricate the models in the laboratory since this particular material was not available as tube. Both 50.8 mm and 102 mm internal diameter cylinders could be formed from the 5 mm thick sheet. In addition, for the part-through-thickness defects 102 mm diameter cylinders were made from 6 mm thick sheet of the same grade material. Characterisation of the heat treated polycarbonate was carried out afterwards.

8.1 Preparation of Model Vessels

Model vessels of polycarbonate were fabricated from 152 mm long sections of the 5 mm and 6 mm thickness transparent sheet. After drying in an air circulating oven at 120°C for 24 hours, the sheet and associated former were heated to 150°C at which temperature the polycarbonate could be easily rolled between the former and two rollers as shown in Fig. 8.1. The result was an almost complete cylinder, the final arc being made from a separate formed sheet sealed with dichloroethane solvent. In order to attach end caps later, the last 25 mm of each model was machined to remove any out-of-roundness. Finally, internal and external reinforcements of 1 mm thick polycarbonate sheet, previously formed, were made across the solvent joints, these being sealed to the model with a warm-set Araldite epoxy adhesive, AY105 resin and HY951 hardener. The dimensions of the polycarbonate models are listed in Table 8.1 where D refers to the mean diameter, $(I.D. + O.D.)/_2$ and values for the out-of-roundness were acceptable according to Bickell and Ruiz (1) i.e. < 1-2% depending on the

thickness-to-diameter ratio.

After curing for 3 hours at 60°C, the cylinders were stress-relieved for 24 hours at 65°C. On examination of each cylinder in a polariscope very few small order fringes were apparent indicating that no appreciable residual stresses were present as a result of the fabrication procedure. This was later confirmed when it was noted that those models failing by a brittle fracture mode in the longitudinal direction retained their original shape on removal of the end sections.

Longitudinal through-thickness defects were introduced at mid-length in the outside wall of models A1-A5, B1-B5 and C3 by means of a fine slitting wheel, 19.1 mm diameter and 0.10 mm thick. The remaining curved profile was removed with a fine fret-saw blade ground down to a thickness of 0.10 mm, as indicated in Fig. 8.2.a.

Two single tooth cutters of tapered profile were used to introduce the longitudinal part-through-thickness defects at mid-length in the outside walls of models C1 and C2. These cutters were made from 0.64 mm thick cutting wheels, ground down to a 30° cutting angle with a cutting tip profile of 0.01 mm radius, as shown in Fig. 8.2.b. The radii of the single tooth cutters used were 9.7 mm and 8.4 mm for models C1 and C2, respectively.

After introducing the slits, the inside of each cylinder was sealed with room temperature curing silicone rubber to prevent leakage through the openings during testing and water up-take by the polycarbonate. The flexibility of the rubber was such that no reinforcement to the defect should be introduced by this procedure.

Finally, each model vessel was completed by affixing two Dural end caps, again using the warm-set Araldite epoxy adhesive, AY105 resin and HY951 hardener. A releasing agent was coated around the inside of each end cap prior to glueing for easy removal after testing. Epoxy adhesive

was also coated around the outside of the cylinder-end cap junction and glass fibre embedded in the adhesive to produce a tapered profile, thus reducing the stress concentration at the end cap junction. The geometric configuration of polycarbonate models A1-A5 is shown in Fig. 8.3.a and b, a different pair of end caps being used for each set of specimens A, B and C.

Fig. 8.4 points out the various stages in the preparation of the model vessels. Preliminary tests indicated that in order to prevent leakage through the end caps during testing a complete silicone rubber bladder was required. Subsequent tests were therefore performed on vessels in which the rubber seal was completed by introducing silicone rubber to both ends of each vessel through the water inlet. Slow leakage through the end caps continued to be a problem with some of the large vessels as these proved more difficult to seal effectively. The significance of this is discussed later.

8.2 Experimental Procedure

The experimental set-up for testing the polycarbonate cylinders is shown in Fig. 8.5.a and b. Each model was lightly clamped by means of external tie bars between the top and bottom platens so that the end caps were not required to support the end load, thereby preventing any longitudinal stresses. After filling with water, the models were pressurised hydraulically with water at room temperature using a hand pump, pressures being measured with a Budenberg standard test gauge accurate to $\pm$ 0.5 bar (0.05 N mm^{-2}). The pressure was applied in steps of 1 bar at a rate of 10 bar min^{-1} (corresponding to a nominal hoop strain rate of 3.7 x 10^{-5} sec^{-1}, 7.5 x 10^{-5} sec^{-1} and 6.2 x 10^{-5} sec^{-1} for the A, B and C models, respectively) until crack initiation occurred. On subsequent pressure steps the crack extension was monitored by means of a travelling

microscope (x14) set up in front of each vessel, measurements being made at each crack tip to ± 0.03 mm. After each 1 bar pressure step the pressure would drop slightly due to stress relaxation, the maximum pressure drop for those vessels for which no leakage occurred being 2.5 bar at 30 bar after a 5 minute period between pressure steps. However, this method of test procedure was felt to be preferable to testing under continuously increasing pressure, a situation in which it is difficult to measure the crack extension accurately.

Pressurising continued until either the vessel failed due to unstable crack propagation or due to failure of the silicone rubber bladder at the crack opening with subsequent leakage.

8.3 Results and Analysis of Results

Considering the small diameter vessels, A1-A5. In all cases crack growth was entirely stable throughout each test. No leakage from the end caps occurred in any of the experiments and failure was either by leakage through the crack opening (A3, A4, A5) or by failure at a solvent joint (A1, in a preliminary test prior to reinforcement of the cylinder-end cap junction with glass fibre and epoxy adhesive; A2, at the highest pressure achieved in any of the tests, 44 bar).

Initial crack extension took place in a manner identical to that previously observed for the polycarbonate plates. Thus, crazes formed ahead and in the plane of the precrack tip from which a crack developed with a roughly elliptical shape. With increasing crack extension under increasing pressure, the surface plastic zone increased in size resembling the Dugdale wedge model and of equilibrium height approximately equal to the wall thickness, 5 mm. Fig. 8.6 shows one of the models, A4 after testing, together with photographs of the crack tunnelling forward through the mid-section and a view of the considerable through-thickness yield which accompanied such crack extension. Crack growth behaviour at the two crack tips

was very similar.

Considering the large diameter models, B1-B5 with the same wall thickness as models A1-A5, four out of five of these vessels failed by an unstable,brittle fracture mode following an initial region of craze breakdown or subcritical crack growth. An example is given in Fig. 8.7, together with the fracture surface showing the tongue-shaped regions of craze material left behind when the crack accelerated rapidly to produce a square fracture with negligible surface yield. Again, the crack growth behaviour at the two crack tips was very similar with crack initiation from the two ends occurring at pressures within 1 bar of each other. However, considerably more subcritical crack growth took place in the case of model B3 than for any of the other models failing by brittle fracture as exemplified by the fracture surface for vessel C3, Fig. 8.8.c. In sharp contrast, stable crack growth occurred for model B5 in a manner identical to that observed for the smaller vessels with failure eventually by leakage at the crack opening.

Finally, fractographs for models C1-C3 are presented in Fig. 8.8. Quantitative measurements of the extension of the part-through defects in the radial direction could not be made. However, the transparency of the plastic allowed observation of the crack growth process during testing. For models C1 and C2 crazes were first observed all around the crack front perimeter except at the outside surface. Under increasing pressure a crack front developed from the crazes with maximum crack extension occurring preferentially at the positions of maximum crack front curvature. Eventually a small amount of craze/crack growth was observed at the outer surface when the crack front profile in the longitudinal direction was almost planar. Model C2 finally failed by an unstable,brittle fracture mode with the crack accelerating rapidly in the radial and longitudinal directions, Fig. 8.8.b.

In comparison, the initial relative crack depth for model C1 was such that "snap-through" was observed after a small amount of crack extension. With increasing pressure a stable crack front developed from the initial region of craze material, extending in the longitudinal direction in a manner similar to that observed previously for the through-thickness defects of models A2-A5 and B5. The test terminated only when the silicone rubber bladder ruptured with subsequent leakage at the crack opening. The photograph of Fig. 8.8.a was obtained after sectioning the vessel and breaking open the crack front plane under impact. It can be clearly seen how crack extension was accompanied by considerable through-thickness yield on the inside surface of the model vessel.

Slow leakage from one end cap occurred prior to final failure during the testing of models B1, B2, B4, C2 and C3. The instantaneous effect of such leakage was to decompress the models to a greater extent between incremental pressure steps than simply as a result of stress relaxation. The interrupted loading tests carried out by Broek (2) on thin centre-cracked sheets of aluminium alloys have been mentioned previously in section 6.3. Broek demonstrated that if the plastic zone size is sufficiently large then after unloading from a given stress level, crack extension will be reinitiated at a lower stress level on reloading due to reversed plastic flow. However, in the present situation all models which underwent slow leakage prior to failure, failed by an unstable, brittle fracture mode for which the plastic zone size must be extremely small. Thus, it is believed that leakage from the end caps had no significant influence upon the experimental results for models B1, B2, B4, C2 or C3.

8.3.a Material Characterisation

In order to analyse the polycarbonate cylinder results a material characterisation of the thermally treated polycarbonate was performed. Four enlarged end uniaxial specimens and four compact specimens (of

identical dimensions as used previously, see section 6.1 and 6.2) were heat treated in a manner similar to the polycarbonate sheet formed into cylinders, one specimen being cut in each of the two principal sheet directions for the 5 mm and 6 mm sheet. The polycarbonate plates were dried in an air circulating oven at 120°C for 24 hours, heated to 150°C for 30 minutes while supported between glass plates and then cooled rapidly to room temperature with compressed air whilst still being supported between the glass plates to prevent buckling. The plates were tested after conditioning for a minimum of one week at room temperature.

The resultant room temperature mechanical properties of the heat treated polycarbonate are listed in Table 8.2. A crosshead speed of 0.1 in. min^{-1} was used in all tests corresponding to nominal strain rates, $\dot{\varepsilon}_{nom}$ of 4.8×10^{-4} sec^{-1} (uniaxial plates) and 2.9×10^{-5} sec^{-1} (compact specimens).

For the uniaxial tensile specimens deformation occurred in a manner identical to that observed previously for the as-received material, with a highly localised neck forming across the section width accompanied by a significant load drop. As before, the variation in the plastic instability stress, $\dot{\sigma}_u$ measured in the x and y directions, 0.7% was less than the experimental uncertainty of the measurements, 1.3% so that the heat treated polycarbonate was reasonably isotropic. Comparison of the room temperature properties of the heat treated and as-received material, Tables 8.2 and 6.2, respectively, indicates that the general effect of the heat treatment was a small increase in plastic instability stress, σ_u together with a slight reduction in ductility as measured by the true strain at plastic instability, ε_{tm}. This occurred in spite of differences in nominal strain rate since according to Bauwens-Crowet (3) decreasing the strain rate by a factor of five reduces the plastic instability stress, σ_u of polycarbonate at room temperature by 1.5 N mm^{-2}.

No unstable brittle fractures took place with any of the 5 mm or 6 mm thick compact specimens ($\alpha_o \sim 0.5$) but in all cases a pop-in mode was observed on the load-displacement record after approximately 1 mm of initial crack front bowing followed by increasing crack extension under rising load. Values of the critical stress intensity factors corresponding to initial craze breakdown, K_{icb} and pop-in, $K_{pop\text{-}in}$ were calculated from the critical loads and crack lengths using equation 5.2, $K = PY/\sqrt{W}\,B$ and the appropriate calibration function, Y.

Mean values of 70.5 ± 0.7 N mm$^{-3/2}$ and 145 ± 1 N mm$^{-3/2}$ were obtained for K_{icb} and $K_{pop\text{-}in}$, respectively for the four specimens indicating that K_{icb} and $K_{pop\text{-}in}$ for the heat treated polycarbonate are independent of section thickness for plates at least 5 mm thick. In addition, since K_{icb} and $K_{pop\text{-}in}$ are known to be independent of loading rate (4), it is apparent that, although the heat treatment had no effect on the stress intensity level for initial craze breakdown (K_{icb} = 70.5 N mm$^{-3/2}$ and 70 N mm$^{-3/2}$ for the heat treated and as-received materials, respectively) it increased the stress intensity level for potential crack instability [a] by 12% ($K_{pop\text{-}in}$ = 145 N mm$^{-3/2}$ and K_c = 130 N mm$^{-3/2}$ for the heat treated and as-received materials, respectively).

8.3.b Analysis of Results

Experimental results for the three sets of model vessels A, B and C are presented graphically in Fig. 8.9.a, b and c, respectively where the dimensionless failure parameter, $P^{\phi} = \sigma_{h/\sigma_u}$ is plotted versus the dimensionless crack length, $\rho = c / \sqrt{DT/2}$. In addition, a plot of P^{ϕ} versus

---

[a] Results obtained by Parvin and Williams (4) and Key and Katz (5) indicate that for polycarbonate the stress intensity factor corresponding to pop-in, $K_{pop\text{-}in}$ is a measure of the critical stress intensity factor for crack instability, K_c.

relative crack depth, $d/_T$ is given for models C1-C3 in Fig. 8.10. With pressure measurements accurate to $\pm$ 0.5 bar (0.05 N mm^{-2}), the experimental uncertainty in P^{ϕ} is considered to be $\pm$ 0.004, $\pm$ 0.008 and $\pm$ 0.006 for the A, B and C models, respectively together with the approximate 1% variation in mean diameter, D and 1.3% uncertainty in ultimate tensile strength, σ_u.

8.3.b.i Longitudinal Through-Thickness Defects

With a knowledge of K_{icb} and K_{pop-in} for the heat treated polycarbonate, analytical curves corresponding to initial craze breakdown and pop-in were determined from the linear elastic stress analysis for longitudinal through-thickness cracks in cylindrical shells (6) (7) using equation 5.23. Analytical solutions for the attainment of a limiting pressure corresponding to yield and ultimate collapse were calculated from the lower bound limit analysis for a thin cylindrical shell with a circular cutout (8) on the basis of the uniaxial tensile properties, σ_y and σ_u using equations 5.24 and 5.25. Both sets of curves are presented in Fig. 8.9.a, b and c for models A, B and C, respectively.

For the small diameter models A1-A5 excellent agreement is obtained between the theoretical curve for initial craze breakdown and the experimental results, Fig. 8.9.a. Under increasing pressure curves A2-A5 pass through a plateau in the general region of the analytical curve for pop-in although no distinct pop-in pressure is evident. At higher pressures when the surface plastic zones developed, the experimental curves steepen until in the case of models A3-A5 the results appear to approach a limiting pressure in the vicinity of the limit analysis solutions for yield and ultimate collapse.

In comparison, initial craze breakdown occurred at slightly lower pressure levels for the large diameter models B1-B5 than those predicted by the analytical curve, Fig. 8.9.b but agreement is still reasonably

good. The critical failure pressures for models B1-B4 and C3 (Fig. 8.9.c) failing by an unstable, brittle fracture mode all lie close to the analytical curve corresponding to pop-in. This is confirmed in Table 8.3 which compares experimental and calculated values of the dimensionless failure parameters, P^{ϕ}_{icb} for initial craze breakdown and P^{ϕ}_{c} for crack instability. A certain variation in the experimental results is to be expected considering any slight differences in thermal treatment during fabrication. However, mean values of the experimental parameters for all vessels are within 1% of the predicted values with standard deviations of 6% and 5% for P^{ϕ}_{icb} and P^{ϕ}_{c}, respectively. Thus, the stress intensity factor corresponding to pop-in, K_{pop-in} is a measure of the critical stress intensity factor for crack instability, K_c for polycarbonate.

Considering Fig. 8.9.b again, the experimental results for model B5 are similar to those for the smaller models although less stable, ductile crack extension occurred at higher pressure levels and the limiting pressure appears to lie considerably below the limit analysis solution for ultimate collapse. However, at longer crack lengths the possibility of constraint due to the proximity of the end caps cannot be discounted. Estimates of the maximum ρ at which significant interaction of the crack tip stress field and the stress field in the vicinity of the end caps might occur were made for each set of models using $\rho_{max} = (F-2\sqrt{DT/2}) / \sqrt{DT/2}$ where F is the free cylindrical half-length and $2\sqrt{DT/2}$ is a measure of the interaction distance [b]. Mean values of ρ_{max} are indicated in Fig. 8.9.a, b and c for the A, B and C models, respectively. Although selection of $2\sqrt{DT/2}$ as the interaction distance was somewhat arbitrary since it neglects the size of the crack tip stress field, the similarity in crack growth

---

[b] Consideration of the edge bending solutions and the flexibility matrix of a thin cylindrical shell (9) indicates that the stress field interaction of the two ends decays rapidly over $3\sqrt{DT/2}$ and becomes insignificant for cylindrical shells $\geqslant 4\sqrt{DT/2}$ in length i.e. approximately $2\sqrt{DT/2}$ from each end.

behaviour for the small diameter models, A2-A5 with differing initial crack lengths, suggests that it is of the correct order; no significant deviations in limit pressure from the analytical curves occurring for ρ up to 1.920 i.e. approximately 2.5 $\sqrt{DT/_2}$ from the ends. In comparison, the value of ρ_{max} for the large diameter models, B1-B5 indicates that end cap interaction effects probably occurred for model B5 at longer crack lengths and for this reason the experimental results obtained for this vessel at high pressures are not considered further.

8.3.b.ii Longitudinal Part-Through-Thickness Defects

The results for models C1 and C2 with longitudinal part-through-thickness defects are shown in Fig. 8.9.c and Fig. 8.10 and summarised in Table 8.4.

For model C2 which failed by an unstable, brittle fracture mode after an initial region of subcritical crack growth, it was assumed that failure corresponded to the attainment of the critical stress intensity factor, K_c taken as 145 N mm$^{-3/2}$ for the heat treated polycarbonate i.e. K_{pop-in} in Table 8.2. A theoretical estimate of the dimensionless failure parameter, P_c^{ϕ} for crack instability was then determined on the basis of the final critical crack length, $2c_c$ (mid-section) and depth, d_c using the Paris-Sih (10) equation for a semi-elliptical surface flaw in a tension plate, equation 5.35. The result is given in Table 8.4.b where for comparison, estimates of P_c^{ϕ} were also obtained from the Irwin (11) and Kobayashi-Moss (12) equations for which the product of the front and back free surface magnification factors in the denominator of equation 5.35 is now replaced by 1.2 and M_e (function of $d/_c$ and $d/_T$), respectively. It is clear that the Paris-Sih equation gives a conservative estimate of P_c^{ϕ} within 10% of the experimental value but that the Irwin and Kobayashi-Moss equations overestimate the failure pressure by 52% and 37%, respectively. This appears to support Derby's (13) suggestion that the Paris-

Sih equation be used for deep cracks because of its conservatism.

Table 8.4.b also includes values of the dimensionless failure parameters, P^{ϕ}_{gy} for yield and P^{ϕ}_{u} for ultimate collapse calculated from the Ruiz (14) solution on the basis of the instantaneous crack length, $2c_c$ and depth, d_c using equations 5.36 and 5.37. These values clearly represent much higher pressure levels than the LEFM value of P^{ϕ}_{c} obtained using the Paris-Sih approximate solution. Both the Paris-Sih and Ruiz equations are indicated in Fig. 8.10 where it is apparent that the experimental failure pressure for model C2 failing by an unstable, brittle fracture mode lies well below the limit analysis solution for yield and ultimate collapse in support of Dowling and Townley's two-criteria approach to failure (15).

Considering model C1, owing to the complex nature of the craze/crack growth and yield process it was not immediately clear how an analytical equation could be used to predict failure if the latter is defined as the "snap-through" pressure, P_{s-t}. Therefore, equations 5.35-5.37 were used to predict the dimensionless failure parameters, P^{ϕ}_{icb} for initial craze breakdown, P^{ϕ}_{gy} for yield and P^{ϕ}_{u} for ultimate collapse on the basis of the initial surface crack length, $2c_o$ and depth, d_o. The results are shown in Table 8.4.a. Assuming that the Paris-Sih (10) equation underestimates the actual pressure level by 10%, a failure level for initial craze breakdown, P^{ϕ}_{icb} of approximately 0.16 is consistent with subsequent "snap-through" at P^{ϕ}_{s-t} of 0.235 after 0.73 mm of subcritical crack growth; P^{ϕ}_{icb} being reduced by only 7% if allowance is made for a plane strain plastic zone ahead of the crack equal to $r_{y2} = \frac{1}{6\pi}\left(\frac{K_{icb}}{\sigma_y}\right)^2$ or 0.10 mm. On the other hand, the extremely high values of P^{ϕ}_{gy} for yield and P^{ϕ}_{u} for ultimate collapse obtained using the Ruiz (14) equation indicates that a plane stress yield criterion has little relevance in this case.

After "snap-through" subsequent crack growth behaviour for model C1

was similar to that of a through-thickness defect extending in a stable, ductile manner with the experimental curve approaching a limiting pressure level, Fig. 8.9.c. However, the latter appears to lie considerably below the limit analysis solution for a through-thickness defect. This may be due to the increased yield on the inner wall of the model during longitudinal crack extension although end cap interaction is also a possibility at longer crack lengths.

In spite of the foregoing, it is clear that for very deep cracks in polycarbonate, $\frac{d}{T} \geqslant 0.88$ stabilisation of the crack occurs as a result of subcritical crack growth and yield across the remaining ligament and failure of such a model may be classified as a "leak" compared with the "rupture" of model C2.

8.4 Discussion

8.4.a Longitudinal Through-Thickness Defects

All the models containing longitudinal through-thickness defects (A1-A5, B1-B5 and C3) exhibited initial craze breakdown at pressure levels close to the LEFM K_{icb} analysis, Table 8.3. Subcritical crack growth was then followed by either unstable, brittle fracture or a pop-in mode and stable, ductile crack extension; both failure levels being well predicted by the LEFM K_{pop-in} or K_c analysis independent of the extent of subcritical crack growth. The latter is exemplified by the results for model B3 undergoing 4.4 mm subcritical crack extension prior to crack instability, approximately twice that observed for any other model. A failure to allow for this crack extension, however, would have resulted in an overestimate in the predicted failure level for model B3, P_c of 18% i.e. 14% above the actual experimentally measured failure pressure.

The agreement between experimental results and LEFM theoretical predictions using Erdogan and Kibler's (7) numerical solution may seem surprising in view of the fact that the assumptions of thin shell theory

were obviously not met for the polycarbonate cylinders. For example, Folias (6) recommends that $\frac{2T}{D} \leqslant 0.01$ compared to $\frac{2T}{D} = 0.18$, 0.10 and 0.12 for the A, B and C models, respectively. However, it is probable that the Erdogan and Kibler stress intensity coefficients are still applicable for dimensions outside the stipulated size when the curvature correction is relatively small i.e. $1 < A_e \leqslant 1.89$ for all models.

Of particular interest in the present tests was the variation in crack growth behaviour observed for the different size polycarbonate models with longitudinal through-thickness defects. For example, unstable, brittle fracture occurred only with the large diameter cylinders (B1-B4, C3) whilst all the small diameter models (A2-A5) exhibited stable, ductile crack extension. Such duplex behaviour was observed before with the 5 mm thick polycarbonate plates and was ascribed to differences in crack tip acuity resulting from slight variations in precracking procedure (see section 6.4.a). However, ductile-brittle fracture transitions in polycarbonate are also known to be strain rate and thickness dependent (4). In the present case the nominal hoop strain rate for the large diameter models was approximately twice that for the small diameter models i.e. 3.7×10^{-5} sec^{-1}, 7.5×10^{-5} sec^{-1} and 6.2×10^{-5} sec^{-1} for the A. B and C models, respectively. In addition, the stored elastic strain energy of the large vessels is considerably greater than that of the small vessels for the same nominal crack length and applied internal pressure [c]. Both effects increase the probability of unstable, brittle fracture of the larger models.

For those models undergoing stable, ductile crack extension considerable bulging of the crack faces occurred at the higher pressures accompanied by the development of surface plastic zones ahead of the crack tip.

---

[c] The elastic strain energy release rate, $\mathcal{G}$ is proportional to K^2 or σ_h^2 A_e^2 πc, equation 5.18 with the influence of vessel diameter, D through the extensional component of the stress intensity, A_e being secondary to its influence through the hoop stress, $\frac{PD}{2T}$.

These yield zones were extremely large so that it is reasonable to assume that failure of these models was governed by the load-bearing capacity of the crack tip regions deforming under plane stress conditions. Under such circumstances the application of a plane stress limit analysis solution would appear to have some validity. In fact, the experimental results for models A3-A5 do approach the limit pressures calculated using Goodall's (8) lower bound analysis, Fig. 8.9.a.

The difficulty of sealing long cracks against pressure loss without strengthening the vessel wall is a considerable problem in experimental studies of through-thickness defects. In the present tests internal patches were not used and the main problem associated with the use of an internal silicone rubber bladder was the transmission of the internal pressure to the crack walls when bulging became significant at high pressures. The increase in applied stress arising from this effect may be calculated simply by the addition of the internal pressure, P to the hoop stress, $\frac{PD}{2T}$ i.e. rewriting equation 5.22:

$$P_p^{\phi} = \frac{\sigma_h}{\sigma_u}\left(1 + \frac{2T}{D}\right) \qquad \text{crack faces pressurised} \qquad 8.1$$

Thus, allowing for the pressurisation of the crack faces of the A models results in an increase in the experimental failure parameter, P^{ϕ} of approximately 18% at the highest pressures.

In comparison, the influence of loading rate on the plastic instability stress, σ_u of the polycarbonate is of secondary importance. The nominal hoop strain rate for the A models, 3.7×10^{-5} sec^{-1}, was an order of magnitude less than the nominal strain rate used to determine σ_u, 4.8×10^{-4} sec^{-1}. However, an order of magnitude reduction in strain rate reduces the plastic instability stress for polycarbonate by only 2.9 N mm^{-2} (3) or 4% σ_u.

Consideration of these two effects implies that the experimental

results for the A models should be increased by a maximum of 22% at the highest pressures, shifting the experimental curves away from the limit analysis solution for yield and into closer agreement with the solution for ultimate collapse.

Finally, it is of interest to compare Goodall's (8) lower bound solution to a semi-empirical "flow-stress criterion" proposed by Hahn (16) for use at high stress levels and successfully applied to the large scale yielding of line pipe with axial through-thickness defects (17):

$$\left.\begin{aligned} \frac{\sigma_h}{\sigma_{flow}} &= \frac{1}{A_e} \\ \text{or} \quad P^{\phi}_{flow} &= \frac{\sigma_{flow}}{\sigma_u} \cdot \frac{1}{A_e} \end{aligned}\right\} \quad \begin{array}{l}\text{semi-empirical}\\ \text{flow-stress}\\ \text{criterion}\end{array} \qquad 8.2$$

where $\sigma_y < \sigma_{flow} < \sigma_u$ and A_e is the LEFM curvature correction factor defined previously. Taking an average $\sigma_{flow} = (\sigma_y + \sigma_u)/2$, equation 8.2 is represented in Fig. 8.9.a for the polycarbonate. Given the uncertainty in the definition of σ_{flow}, it is apparent that the semi-empirical equation predicts failure at pressure levels in the same region as those given by the limit analysis solution for ultimate collapse. Therefore, on the basis of the instantaneous crack length, the present results for polycarbonate cylinders undergoing large scale yielding would appear to be consistent with those of Kiefner (17) obtained for line pipe.

8.4.b Longitudinal Part-Through-Thickness Defects

As for the through-thickness defects, it is apparent that crack extension for the part-through flaws was initiated by the breakdown of thick craze material formed at the precrack front. However, although models C1 and C2 contained longitudinal defects of similar length, subsequent crack growth behaviour in each case was very different.

For example, model C2 exhibited unstable crack propagation when the

pressure reached the critical level for crack instability of the instantaneous configuration, P_c^{ϕ}. Examination of Fig. 8.9.c reveals that this pressure level was well above that necessary for unstable, brittle fracture of the through-thickness defect so that on popping through the wall, the crack had more than enough energy to continue its rapid propagation along the entire length of the vessel.

In comparison, the pressure level at "snap-through", P_{s-t}^{ϕ} for model C1 was similar to that required for unstable, brittle fracture of the through-thickness defect. Given that P_c^{ϕ} for the full depth through crack represents a conservative estimate of the rupture condition (no allowance being made for the instantaneous crack shape at "snap-through" nor for any through-thickness yield) it is clear that after growing through the wall, the crack had insufficient energy for rapid propagation and arrest occurred.

It has been demonstrated that good conservative estimates of failure levels for deep part-through-thickness defects, $\frac{d}{T} = 0.87 - 0.88$ may be obtained using the Paris-Sih (10) expression for a surface-flawed tension plate. The relative success of this LEFM approximate solution compared with the Irwin (11) and Kobayashi-Moss (12) equations, Table 8.4, appears to be in its prediction of the strong influence of the back free surface, the latter overriding any effects due to bending or curvature. In fact, the inadequacy of the Irwin and Kobayashi-Moss equations at large d/T merely reflects underestimates in the back free surface magnification factors known to occur at $\frac{d}{T} > 0.5$ and 0.7, respectively.

For part-through flaws initial plastic deformation generally occurs under plane strain conditions since the effective material thickness is, in fact, the cylindrical length rather than the ligament. In addition, there is a high degree of constraint associated with a curved crack profile. Under such circumstances the application of a LEFM analysis for

predicting initial craze breakdown (model C1) and crack instability (model C2) has some validity although the application of a plane stress limit analysis solution for determining the onset of yield is open to question. All that can be said is that for models C1 and C2, the Ruiz (14) equation predicts widespread yielding at pressure levels very much higher than that required for initial craze breakdown, Table 8.4, so that on this basis subcritical crack extension would be anticipated prior to general yield.

For comparison, Kiefner (17) has proposed an empirical formula for extending Hahn's "flow-stress criterion" to part-through defects:

$$\frac{\sigma_h}{\sigma_{flow}} = \frac{(1 - \frac{d}{T})}{(1 - \frac{d}{A_e T})}$$

$$\text{or} \quad P^{\phi}_{flow} = \frac{\sigma_{flow}}{\sigma_u} \cdot \frac{(1 - \frac{d}{T})}{(1 - \frac{d}{A_e T})}$$

empirical flow-stress criterion — 8.3

where $\sigma_y < \sigma_{flow} < \sigma_u$ and A_e is the LEFM curvature correction factor for an equivalent through-thickness defect of length, $2c_{eq} = A/d$ where A is the actual profile area of the part-through defect. Assuming an average $\sigma_{flow} = (\sigma_y + \sigma_u)/2$, equation 8.3 predicts a dimensionless failure parameter, P^{ϕ}_{flow} for model C1 of 0.399 compared with 0.454 and 0.603 for P^{ϕ}_{gy} and P^{ϕ}_{u}, respectively using the Ruiz (14) equation. If the latter are also corrected for the machined flaw shape, this difference is increased as values of 0.499 and 0.663 are now obtained for P^{ϕ}_{gy} and P^{ϕ}_{u}, respectively. Thus, it is apparent that a "flow-stress" or "yield criterion" is not applicable to the failure of model C1 and that a "toughness-dependent criterion", LEFM analysis (with the possibility of a plasticity correction factor) has more relevance.

Of course, for $\frac{d}{T} > 0.88$, even the usefulness of the Paris-Sih (10)

linear elastic analysis must be limited as the stress intensity coefficient rapidly approaches an infinite value as $\frac{d}{T} \rightarrow 1.0$. More realistic estimates of load-bearing capacity may then be obtained by treating a part-through defect as a fully penetrating flaw. For example, examination of Fig. 8.10 reveals that the limit of applicability of the LEFM Paris-Sih equation for a part-through flaw of length, $\rho = 0.749$ is $\frac{d}{T} \lesssim 0.9$; predicted failure pressures, P_c for part-through defects having $\frac{d}{T} > 0.9$ lying below that necessary for a through-thickness defect of the same length.

8.5 Conclusions

a. Static loading experiments on 5 mm and 6 mm thick compact specimens of heat treated polycarbonate at room temperature have shown that the critical stress intensity factors, K_{icb} for initial craze breakdown and K_{pop-in} for pop-in are independent of section thickness for plates at least 5 mm thick.

b. Room temperature, static loading experiments on heat treated polycarbonate cylinders containing longitudinal defects have shown that the stress intensity factor at pop-in, K_{pop-in} is a measure of the critical stress intensity factor for crack instability, K_c for polycarbonate.

c. Dowling and Townley's two-criteria approach to failure (15) has been shown to give good estimates of failure pressures for 50.8 mm and 102 mm diameter, 5 mm and 6 mm thick model cylindrical vessels of polycarbonate with longitudinal through-thickness defects undergoing both unstable, brittle fracture and stable, ductile crack extension.

The mean experimental pressure for initial craze breakdown for all vessels was within 1% of the LEFM estimate with a standard deviation of 6%. For those models failing by an unstable, brittle fracture mode, the mean experimental pressure at crack instability was within 1% of the LEFM estimate with a standard deviation of 5% after

due allowance for subcritical crack growth.

On the basis of the instantaneous crack length, experimental pressures for models exhibiting stable, ductile crack extension approached a limiting value in the vicinity of the limit analysis solution for yield and ultimate collapse, agreement with the latter being improved after allowance had been made for pressurisation of the crack faces at high pressures.

d. Finally, Dowling and Townley's two-criteria approach to failure has been shown to provide good conservative estimates of the failure pressures for two 102 mm diameter, 6 mm thick model cylindrical vessels of polycarbonate with longitudinal part-through defects which exhibited "leakage" ($\frac{d_o}{T} = 0.878$) and "rupture" ($\frac{d_o}{T} = 0.700$).

On the basis of the instantaneous crack size, the experimental pressure at crack instability for the model failing by an unstable, brittle fracture mode ($\frac{d_o}{T} = 0.700$) after 1.02 mm subcritical crack growth was within 10% of the LEFM estimate using the Paris-Sih (10) approximate solution.

For the model exhibiting "leakage" ($\frac{d_o}{T} = 0.878$) after 0.73 mm of subcritical crack extension, the pressure for initial craze breakdown calculated using the Paris-Sih linear elastic equation provided a realistic conservative estimate of the "snap-through" pressure; extremely large non-conservative estimates being obtained on the basis of Ruiz's (14) limit analysis solution and Kiefner's (17) empirical "flow-stress criterion".

References

(1) M.B. Bickell and C. Ruiz, "Pressure Vessel Design and Analysis", MacMillan, London, p. 64, 1967.

(2) D. Broek, Aerospace Proc., p. 811, 1966.

(3) C. Bauwens-Crowet, J.C. Bauwens and G. Homès, J. Polymer Sci., Part A-2, 7, p. 735, 1969.

(4) M. Parvin and J.G. Williams, Int. J. of Fracture, 11, p. 963, 1975.

(5) P.L. Key and Y. Katz, Int. J. of Fract. Mechs., 5, p. 63, 1969.

(6) E.S. Folias, Int. J. of Fract. Mechs., 1, p. 20, 1965.

(7) F. Erdogan and J.J. Kibler, Int. J. of Fract. Mechs., 5, p. 229, 1969.

(8) I.W. Goodall, "On the Design of Intersections in Pressure Vessels," Ph.D. dissertation, University of Cambridge, 1967.

(9) Ref. (1), p. 131.

(10) P.C. Paris and G.C. Sih, A.S.T.M. S.T.P. 381, "Fracture Toughness Testing and its Applications", Am. Soc. for Testing and Materials, p. 30, 1965.

(11) G.R. Irwin, J. Appl. Mech., 29, p. 651, 1962.

(12) A.S. Kobayashi and W.L. Moss, Proc. 2nd Int. Conf. Fracture, Brighton, p. 31, 1969.

(13) R.W. Derby, A.S.T.M. S.T.P. 536, "Progress in Flaw Growth and Fracture Toughness Testing", Am. Soc. for Testing and Materials, p. 482, 1973.

(14) C. Ruiz, O.U.E.L. Report No. 1200, 1977, to be published in Int. J. of Mech. Sci.

(15) A.R. Dowling and C.H.A. Townley, Int. J. Pres. Ves. and Piping, 3, p. 77, 1975.

(16) G.T.Hahn, M. Sarrate and A.R. Rosenfield, Int. J. of Fract. Mechs., 5, p. 187, 1969.

(17) J.F. Kiefner, W.A. Maxey, R.J. Eiber and A.R. Duffy, A.S.T.M. S.T.P. 536, "Progress in Flaw Growth and Fracture Toughness Testing", Am. Soc. for Testing and Materials, p. 461, 1973.

Table 8.1 Dimensions of Polycarbonate Cylinders with Longitudinal Through-Thickness and Part-Through-Thickness Defects

	D mm	T mm	2F mm	$2c_o$ mm	d_o mm	c_o/F	ρ_o	d_o/T	d_o/c_o	Out-of-roundness * %
A1	55.1	4.95	101.8	17.49	-	0.172	0.749	-	-	0.64
A2	55.0	4.95	101.9	18.68	-	0.183	0.801	-	-	0.76
A3	54.7	4.95	101.7	25.12	-	0.247	1.079	-	-	0.76
A4	54.9	4.95	102.0	33.44	-	0.328	1.434	-	-	0.42
A5	54.6	4.95	101.9	29.71	-	0.292	1.278	-	-	0.72
B1	103.7	4.95	103.1	19.87	-	0.193	0.620	-	-	1.12
B2	105.3	4.95	103.2	24.66	-	0.239	0.764	-	-	0.65
B3	103.7	4.95	103.8	22.92	-	0.221	0.715	-	-	0.89
B4	104.8	4.95	102.1	29.82	-	0.292	0.926	-	-	0.49
B5	104.0	4.95	101.6	27.72	-	0.273	0.864	-	-	1.04
C1	106.1	6.00	101.8	25.01	5.27	0.246	0.701	0.878	0.421	1.00
C2	105.9	6.00	103.2	25.83	4.20	0.250	0.725	0.700	0.325	1.02
C3	104.7	6.00	106.0	24.96	-	0.236	0.704	-	-	1.05

* Out-of-roundness = 2 (Max. diam. - Min. diam.) / (Max. diam. + Min. diam.) < 1 - 2% (1)

Table 8.2 Mechanical Properties of Heat Treated Polycarbonate

(293°K, $\dot{\varepsilon}_{nom} = 4.8 \times 10^{-4}$ sec^{-1} for uniaxial tensile properties)

Uniaxial yield stress, σ_y	51 N mm^{-2} [1]*
Ultimate tensile strength, σ_u	
"x" direction	68.20 ± 0.03 N mm^{-2} [2]
"y" direction	67.26 ± 0.02 N mm^{-2} [2]
mean	67.7 ± 0.5 N mm^{-2} [4]
True strain at plastic instability, ε_{tm}	0.064 [2]
Static Young's modulus, E	2.27 x 10^3 N mm^{-2} [2]
Poisson's ratio, ν	0.37 (manuf.)
Critical stress intensity factors, K_{icb}	70.5 ± 0.7 N mm$^{-3/2}$ [4]
K_{pop-in}	145 ± 1 N mm$^{-3/2}$ [4]

* No. of measurements

± 1 Standard deviation

Table 8.3 Comparison of Experimental and Calculated Values of the Failure Parameters, P^{ϕ}_{icb} and P^{ϕ}_{c} for Polycarbonate Cylinders with Longitudinal Through-Thickness Defects

	$2c_o$	P_{icb}	P^{ϕ}_{icb}			$2c_c$	P_c	P^{ϕ}_{c}	$P^{\phi}_{pop\text{-}in}$		$\Delta c/c_o$
			a.	b.	$\frac{a}{b}$			a.	b.	$\frac{a}{b}$	
	mm	N mm^{-2}	Expt.	LEFM		mm	N mm^{-2}	Expt.	LEFM		
A1	17.49	1.90	0.156	0.149	1.05	–	–	–	–	–	–
A2	18.68	1.75	0.144	0.141	1.02	–	–	–	–	–	–
A3	25.12	1.30	0.106	0.105	1.01	–	–	–	–	–	–
A4	33.44	0.85	0.070	0.076	0.92	–	–	–	–	–	–
A5	29.71	1.10	0.090	0.087	1.03	–	–	–	–	–	–
B1	19.87	0.85	0.132	0.150	0.88	21.57	1.70	0.263	0.287	0.92	0.086
B2	24.66	0.80	0.126	0.124	1.02	26.50	1.65	0.258	0.240	1.08	0.075
B3	22.92	0.80	0.124	0.133	0.93	27.32	1.55	0.240	0.232	1.03	0.192
B4	29.82	0.65	0.102	0.104	0.98	31.39	1.35	0.211	0.203	1.04	0.053
B5	27.72	0.70	0.109	0.111	0.98	–	–	–	–	–	–
C3	24.96	1.05	0.135	0.128	1.06	26.54	1.90	0.245	0.248	0.99	0.063
Mean					0.99 ± 0.06					1.01 ± 0.05	

Table 8.4 Analysis of Results for Polycarbonate Cylinders with Longitudinal Part-Through-Thickness Defects

a. Model C1

	$2c_o$ Surface mm	d_o mm	$d_o/_T$	$2c_f$ Mid-section mm	d_f mm	$d_f/_T$	P_{s-t} N mm^{-2}	P^{ϕ}_{s-t} Expt.	P^{ϕ}_{icb} Paris-Sih (10)	P^{ϕ}_{gy} Ruiz (14)	P^{ϕ}_{u} Ruiz (14)
C1	25.01	5.27	0.878	30.03	6.00	1.00	1.95 Stable, ductile failure → LEAK	0.255	0.144	0.454	0.603

b. Model C2

	$2c_o$ Surface mm	d_o mm	$d_o/_T$	$2c_c$ Mid-section mm	d_c mm	$d_c/_T$	P_c N mm^{-2}	P^{ϕ}_{c} Expt.	Paris-Sih (10)	Irwin (11)	Kobayashi-Moss (12)	P^{ϕ}_{gy} Ruiz (14)	P^{ϕ}_{u} Ruiz (14)
C2	25.83	4.20	0.700	27.02	5.22	0.870	2.55 Unstable, brittle fracture → RUPTURE	0.332	0.300	0.503	0.454	0.440	0.584

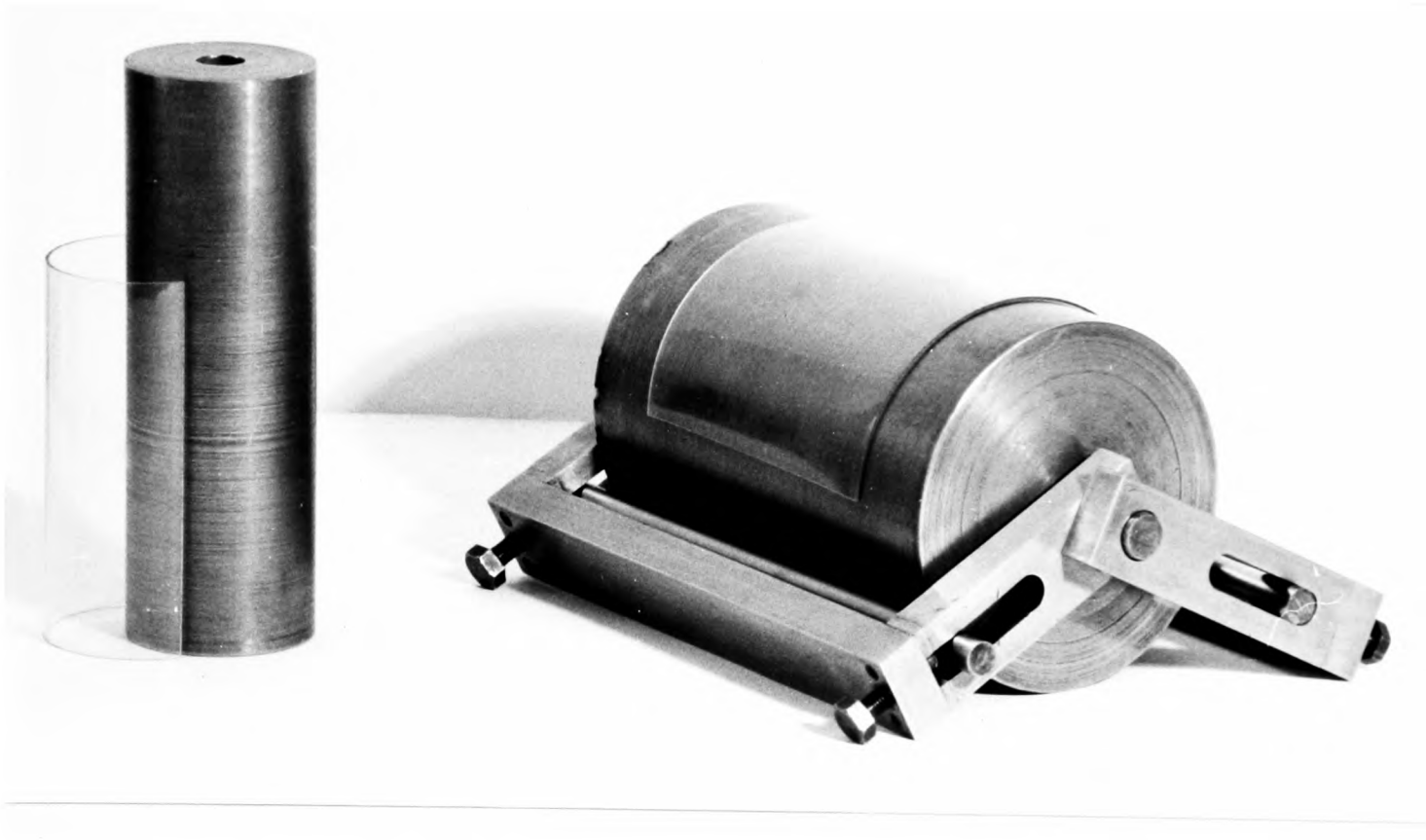
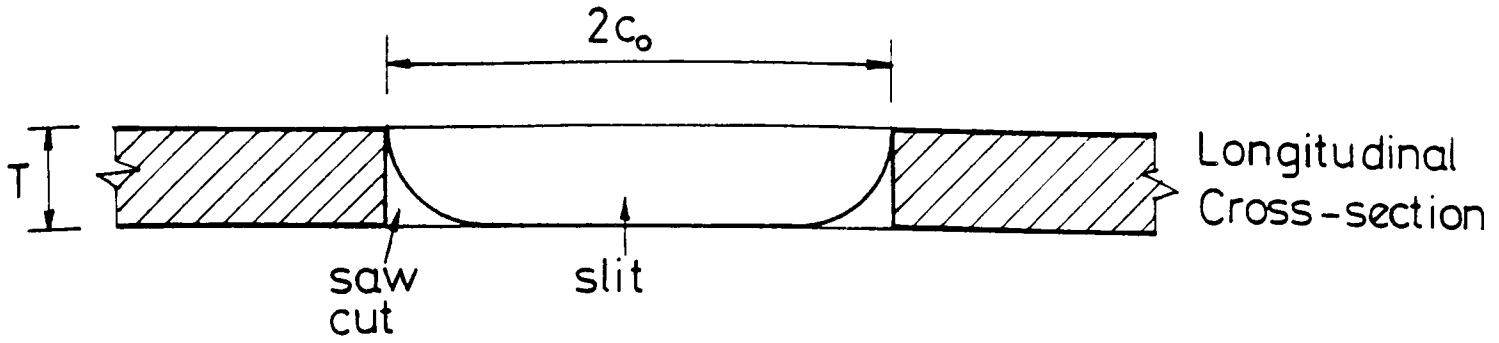
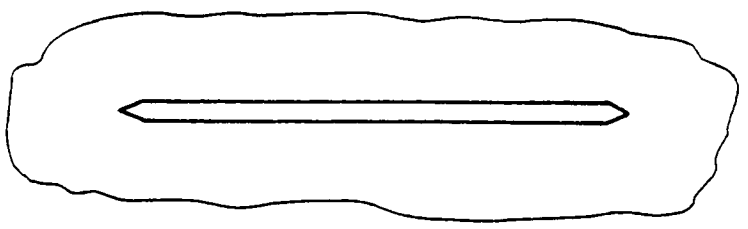


Fig. 8.1 Forming of polycarbonate sheet

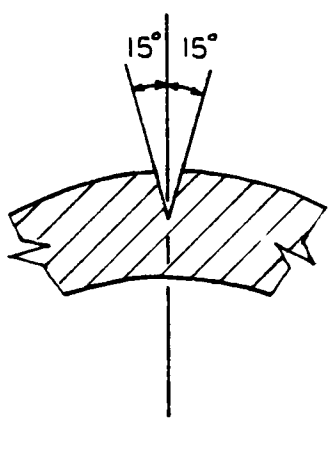


Fig. 8.4 Model vessels in various stages of preparation

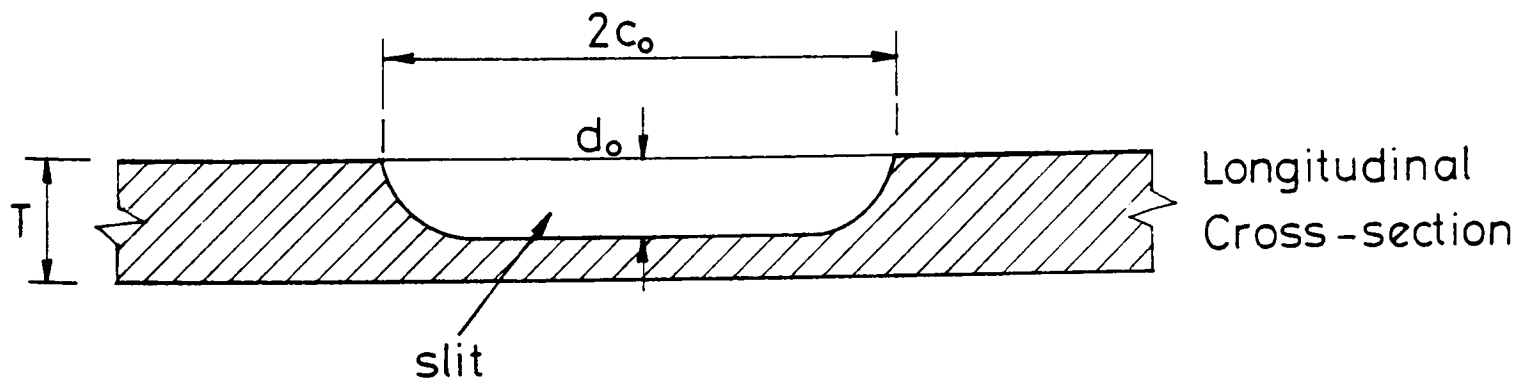


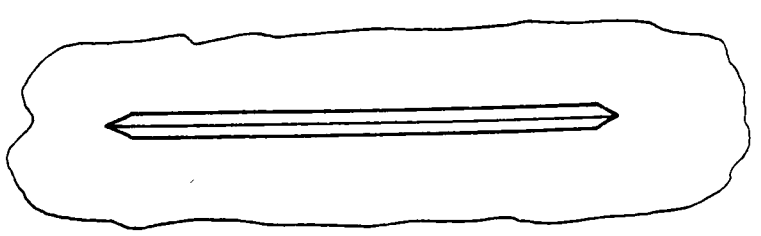


a. Through-thickness defect



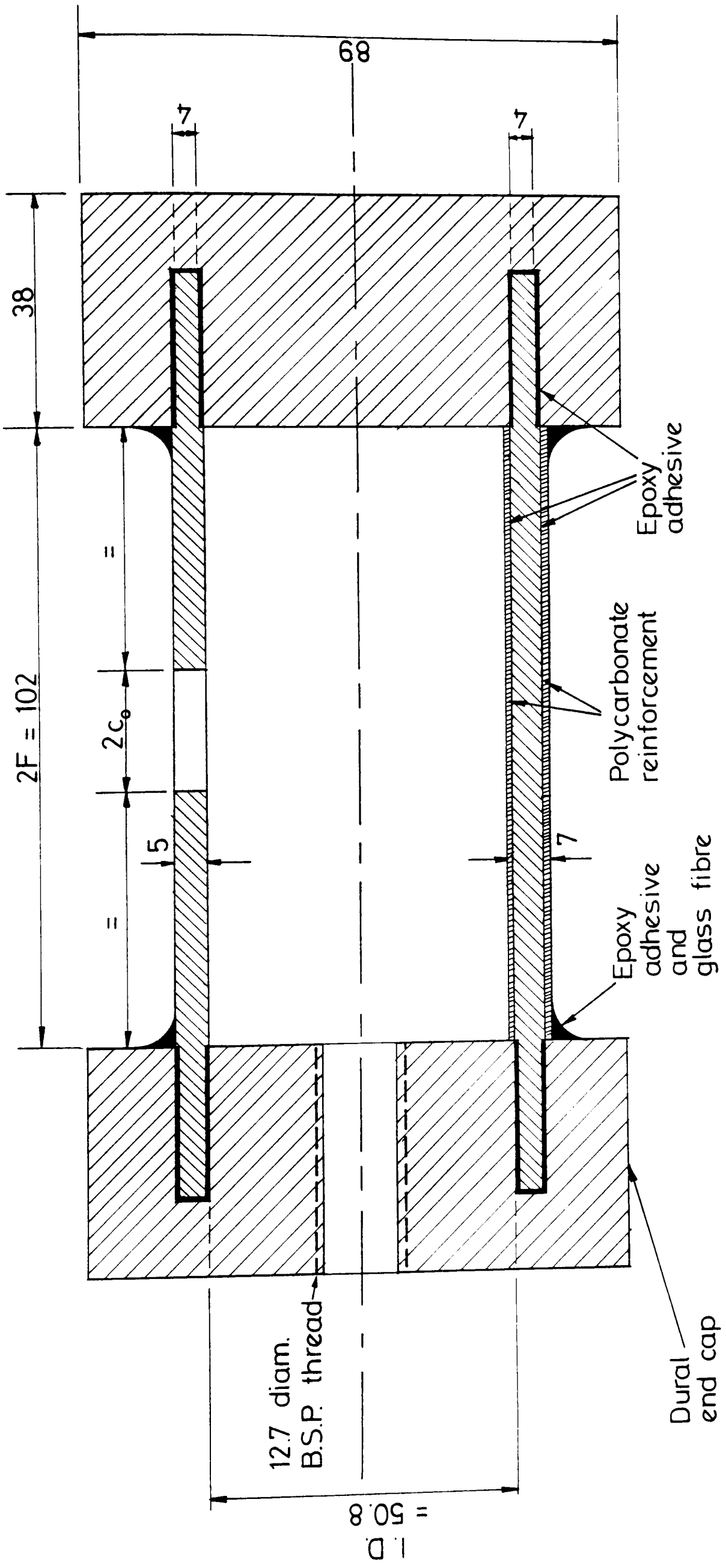
Tip radius = 0.01 mm.





b. Part-through-thickness defect

Fig. 8.2 Geometric configuration of longitudinally-oriented defects



a. Longitudinal cross-section

Fig. 8.3 Geometric configuration of polycarbonate models A1-A5 with Dural end caps

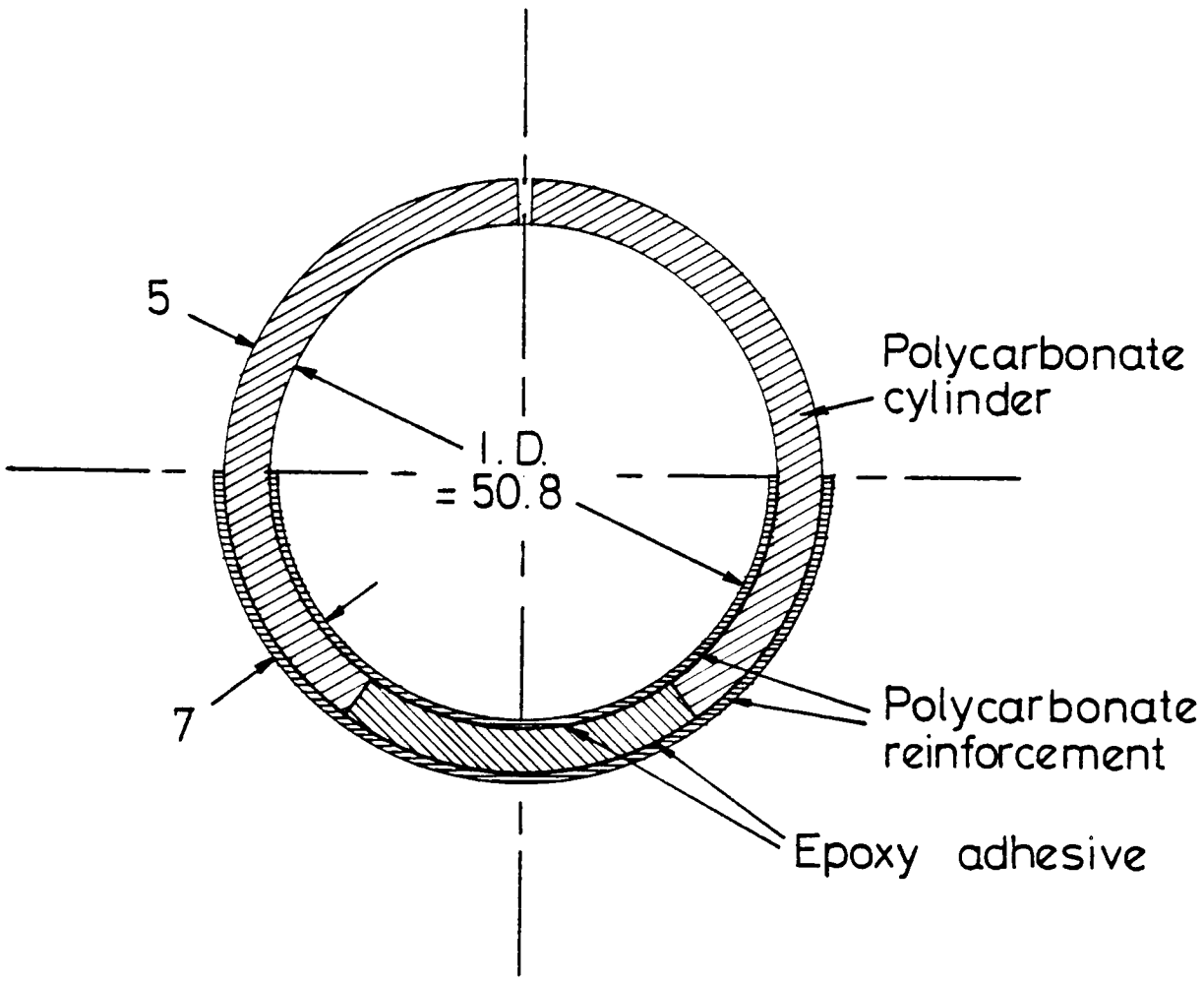
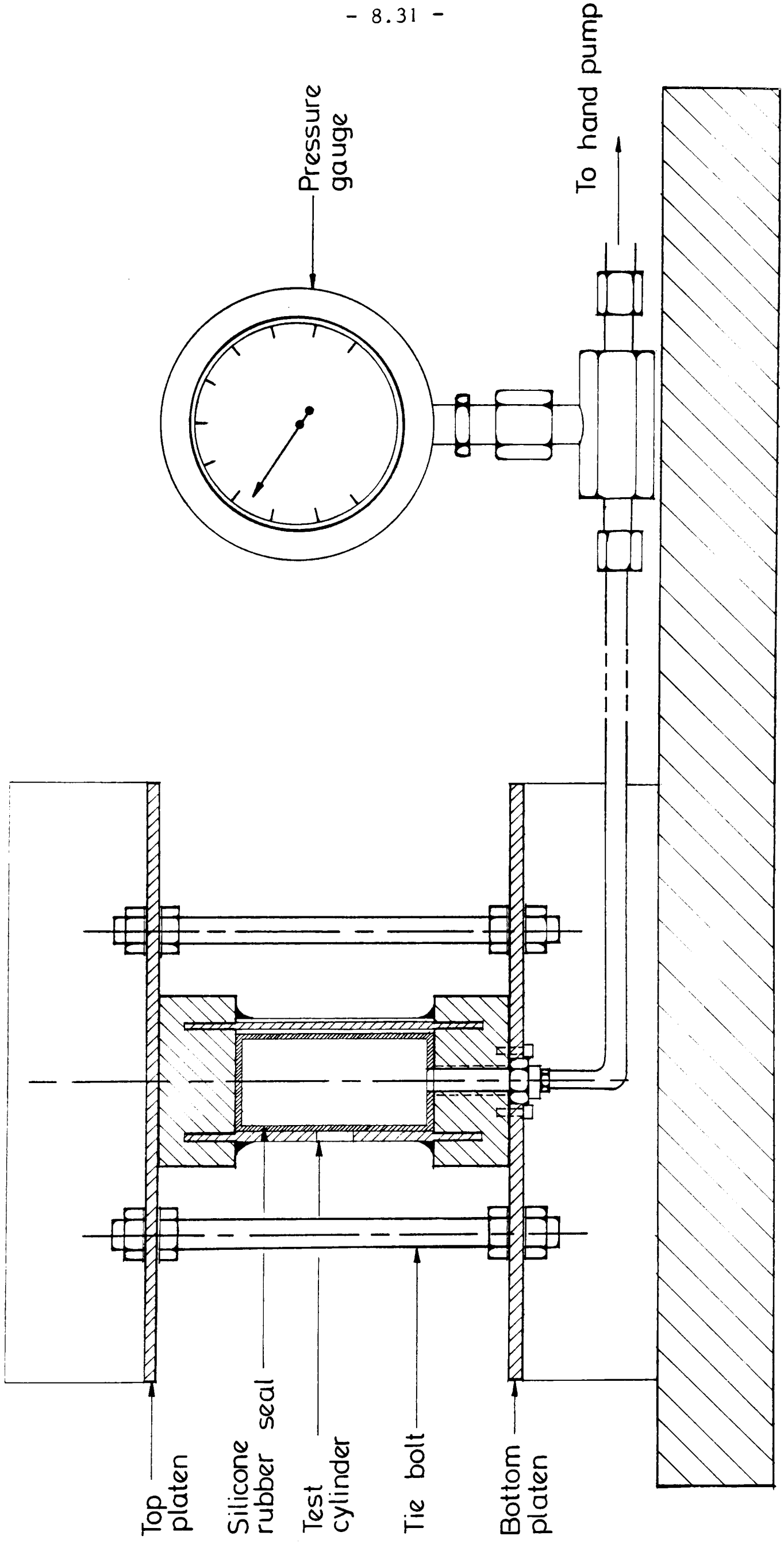


Fig. 8.3 (cont.) b. Circumferential cross-section

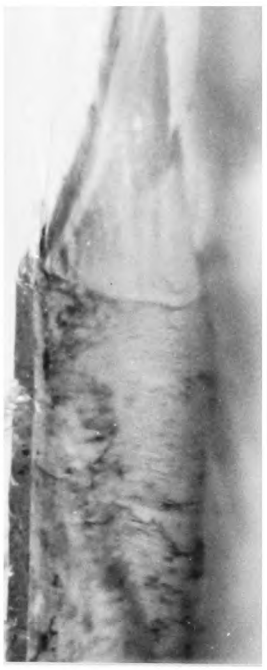


a. Schematic diagram

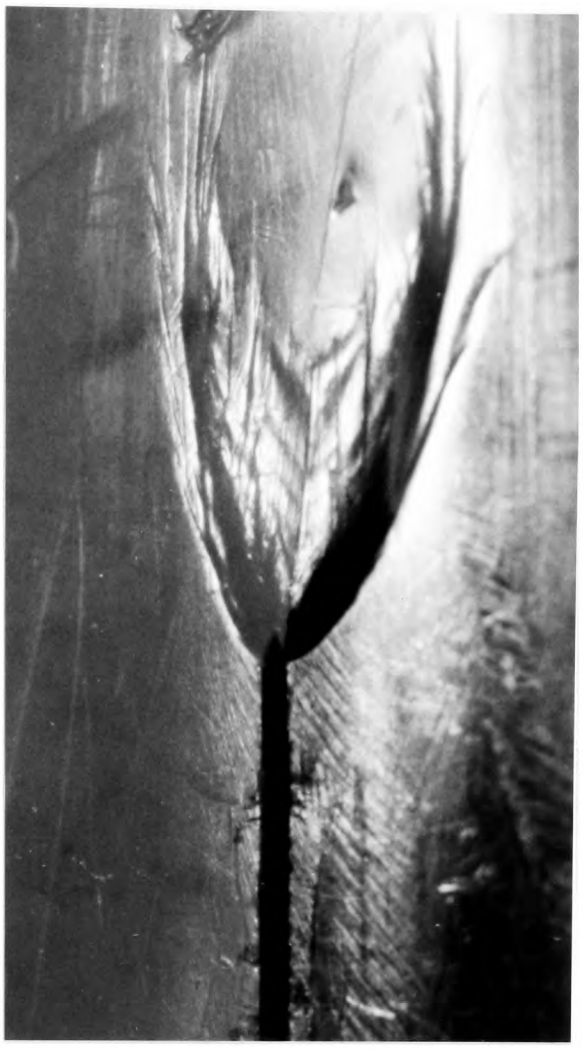
Fig. 8.5 Experimental set-up for polycarbonate cylinder tests



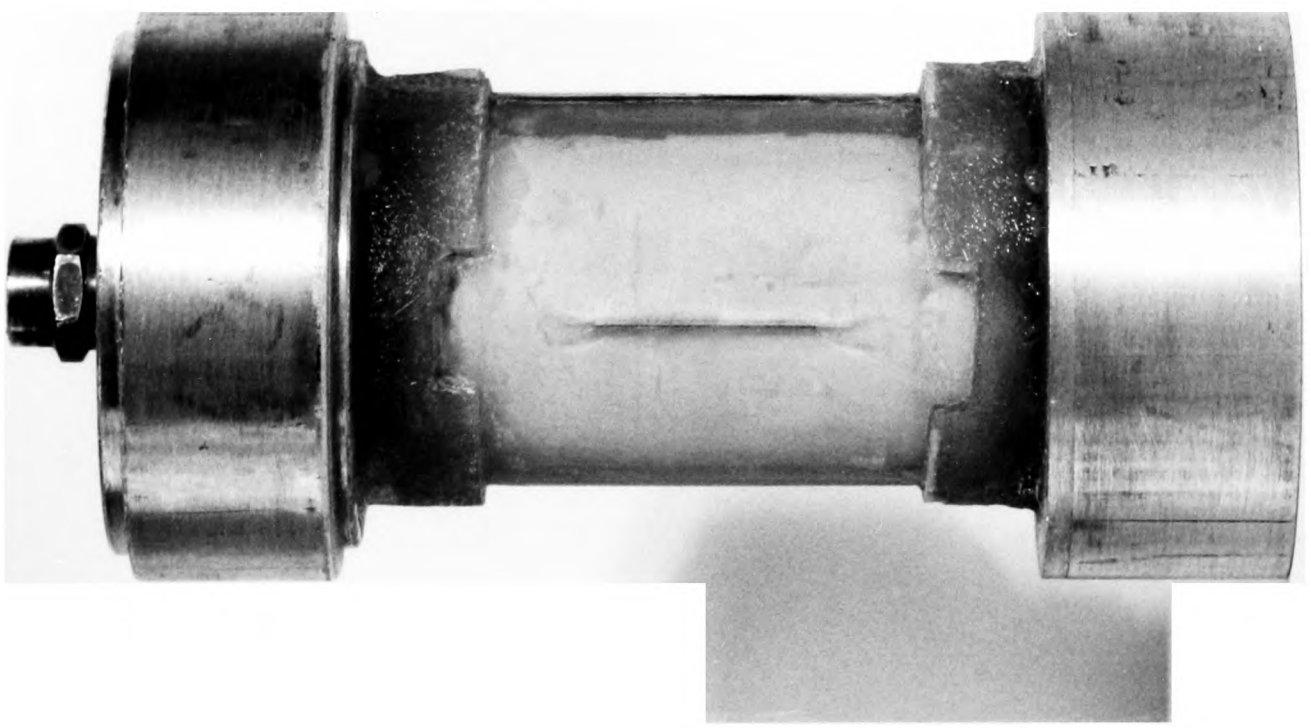
Fig. 8.5 (cont.) b. Photograph



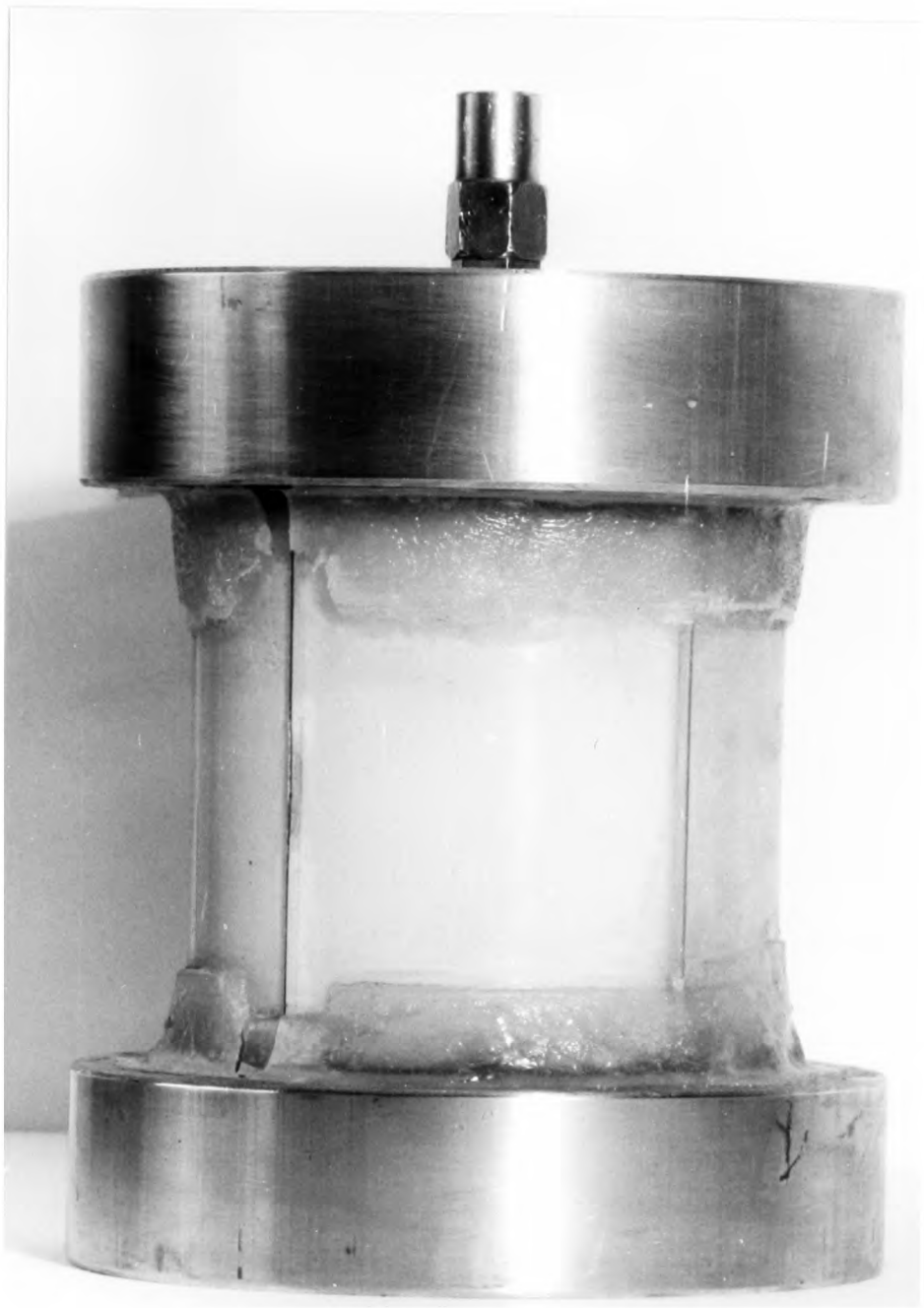
b.



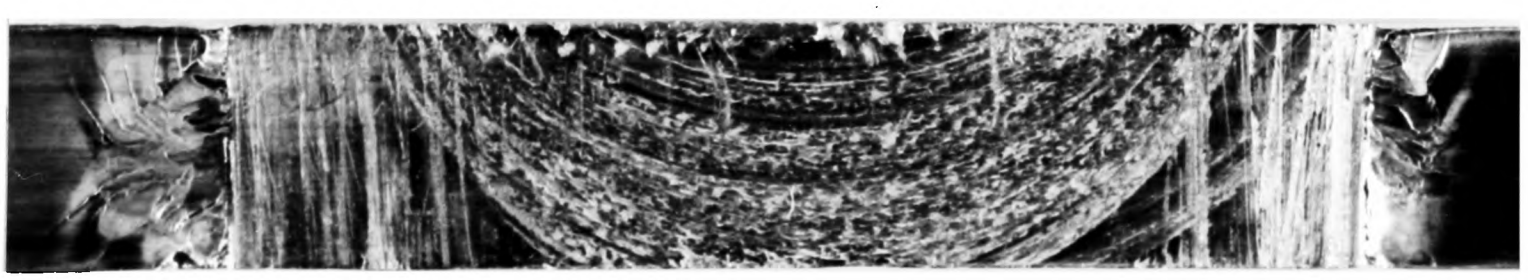
c. x 6.1



a.

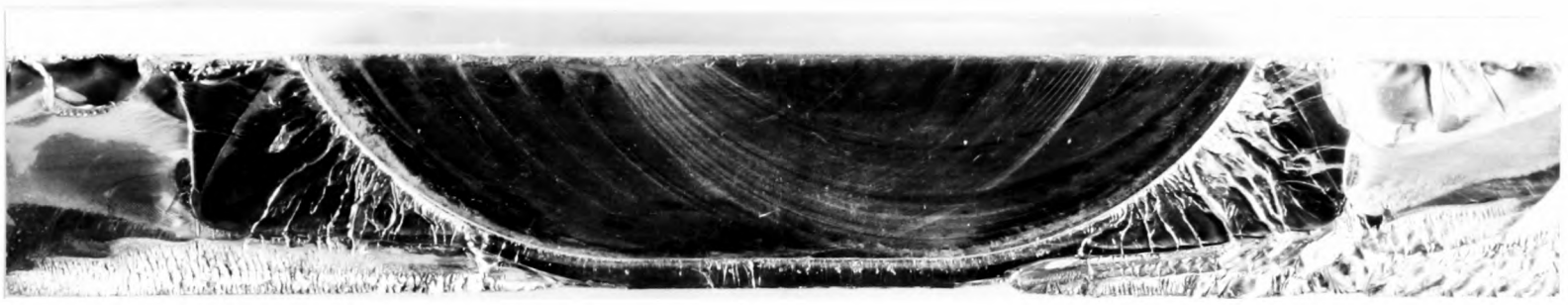


a.

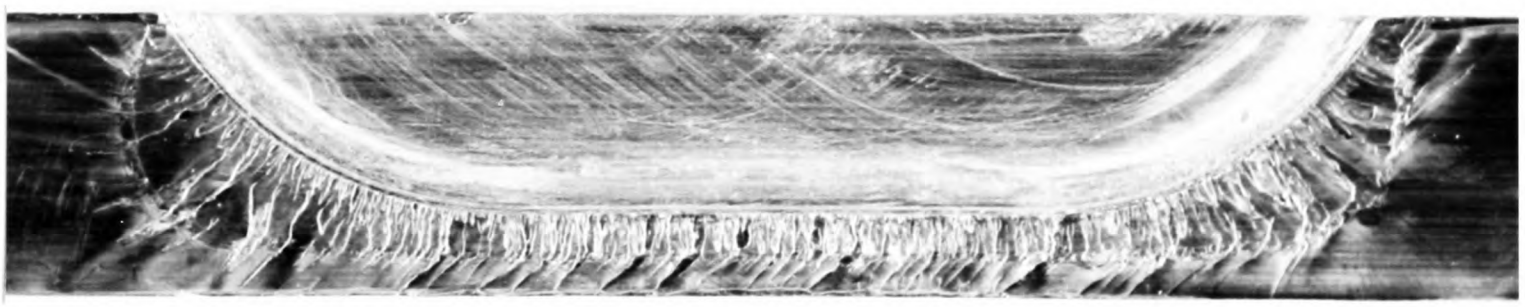


b. x 4.8

Fig. 8.7 Model vessel B3 after testing a. Overall model and b. Fracture surface showing initial region of craze material and resultant brittle fracture



a. x 3.9



b. x 4.7



c. x 4.2

Fig. 8.8 Fracture surfaces for model vessels C1, C2 and C3

a. C1 showing initial region of craze material and stable crack growth with accompanying yield zones on internal surface of model

b. C2 and c. C3 showing initial region of craze material and resultant brittle fracture

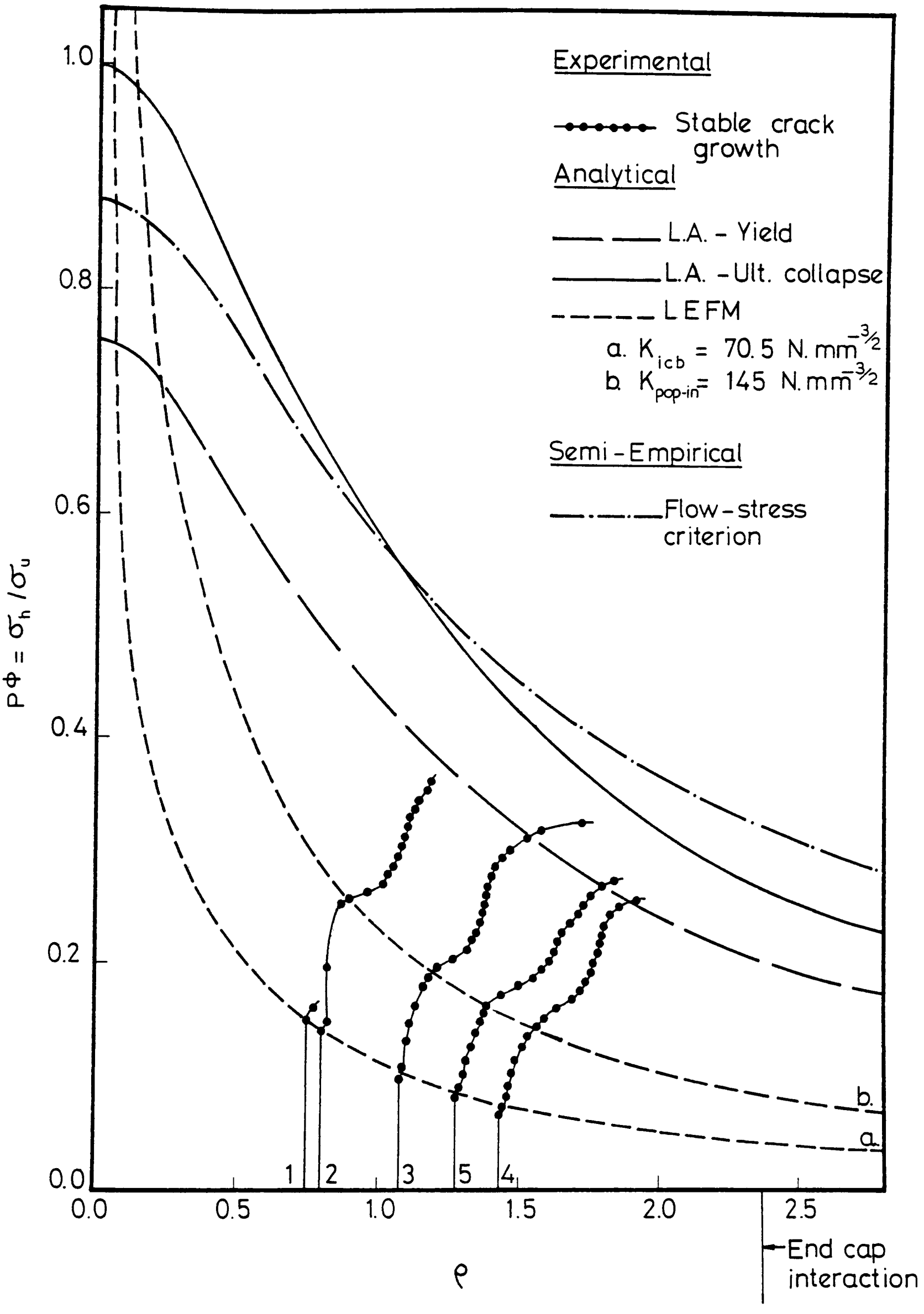


Fig. 8.9 Failure analysis diagram for polycarbonate cylinders with longitudinal through-thickness defects a. A1-A5

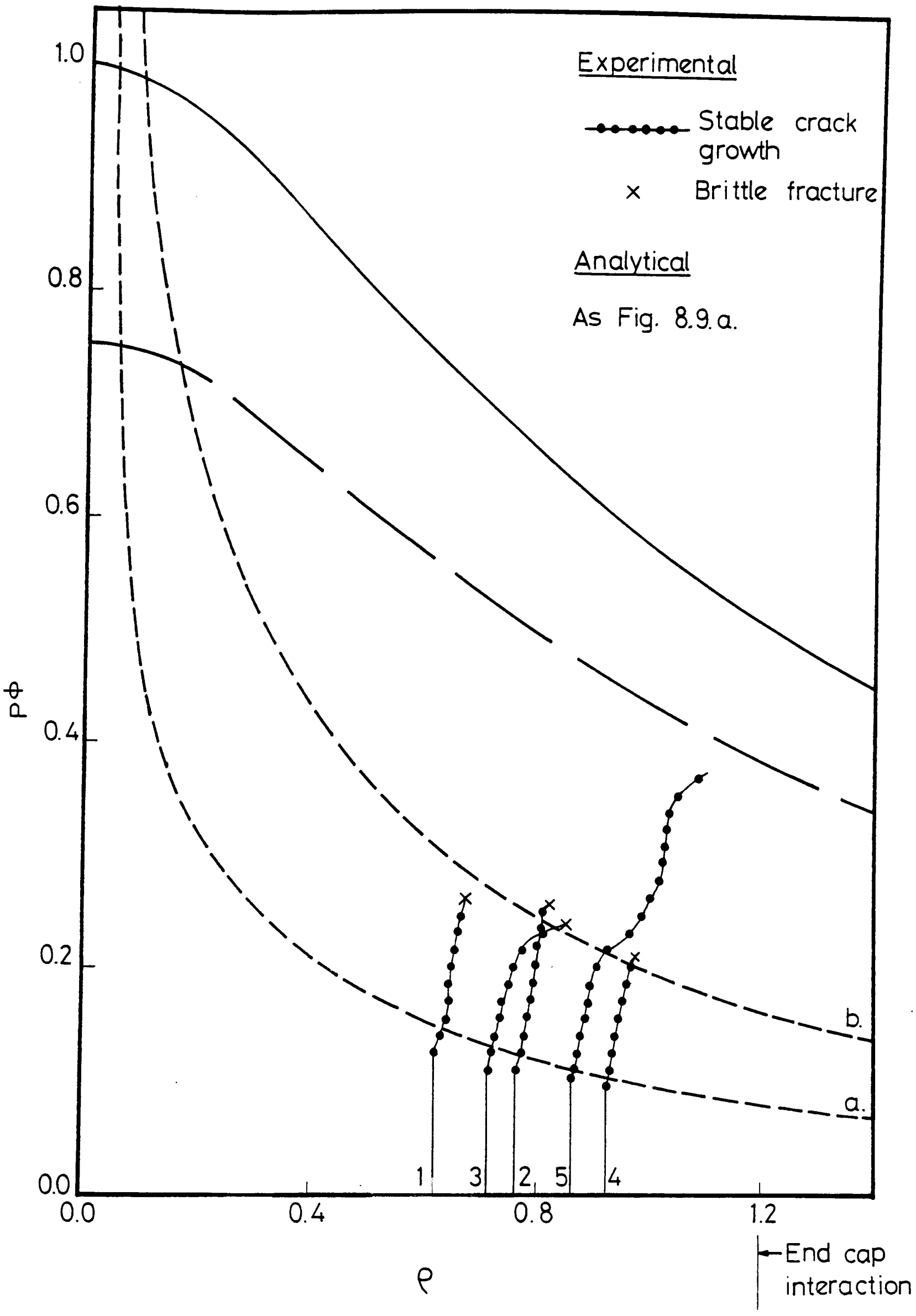


Fig. 8.9 (cont.) b. B1-B5

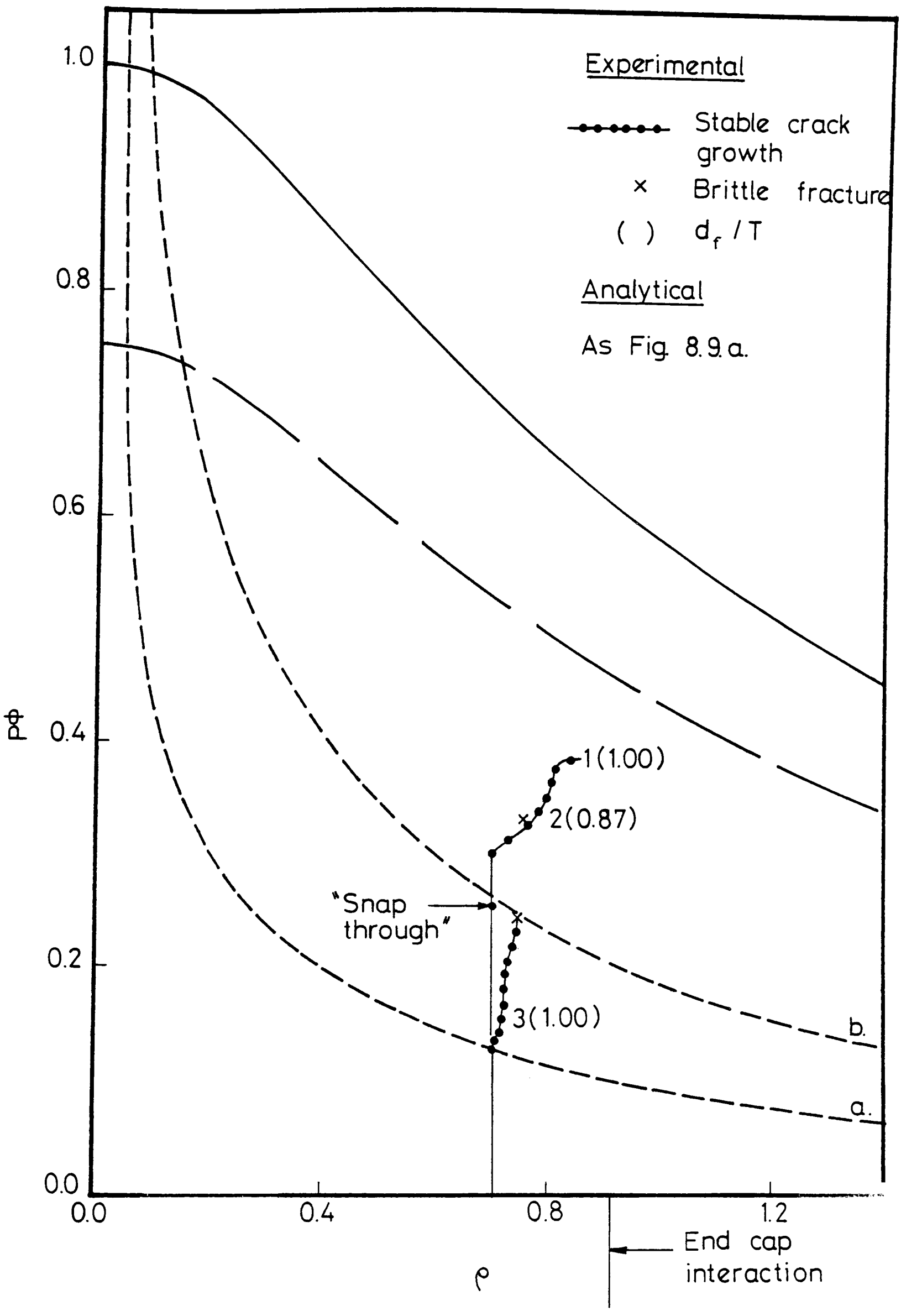


Fig. 8.9 (cont.) c. C1-C3

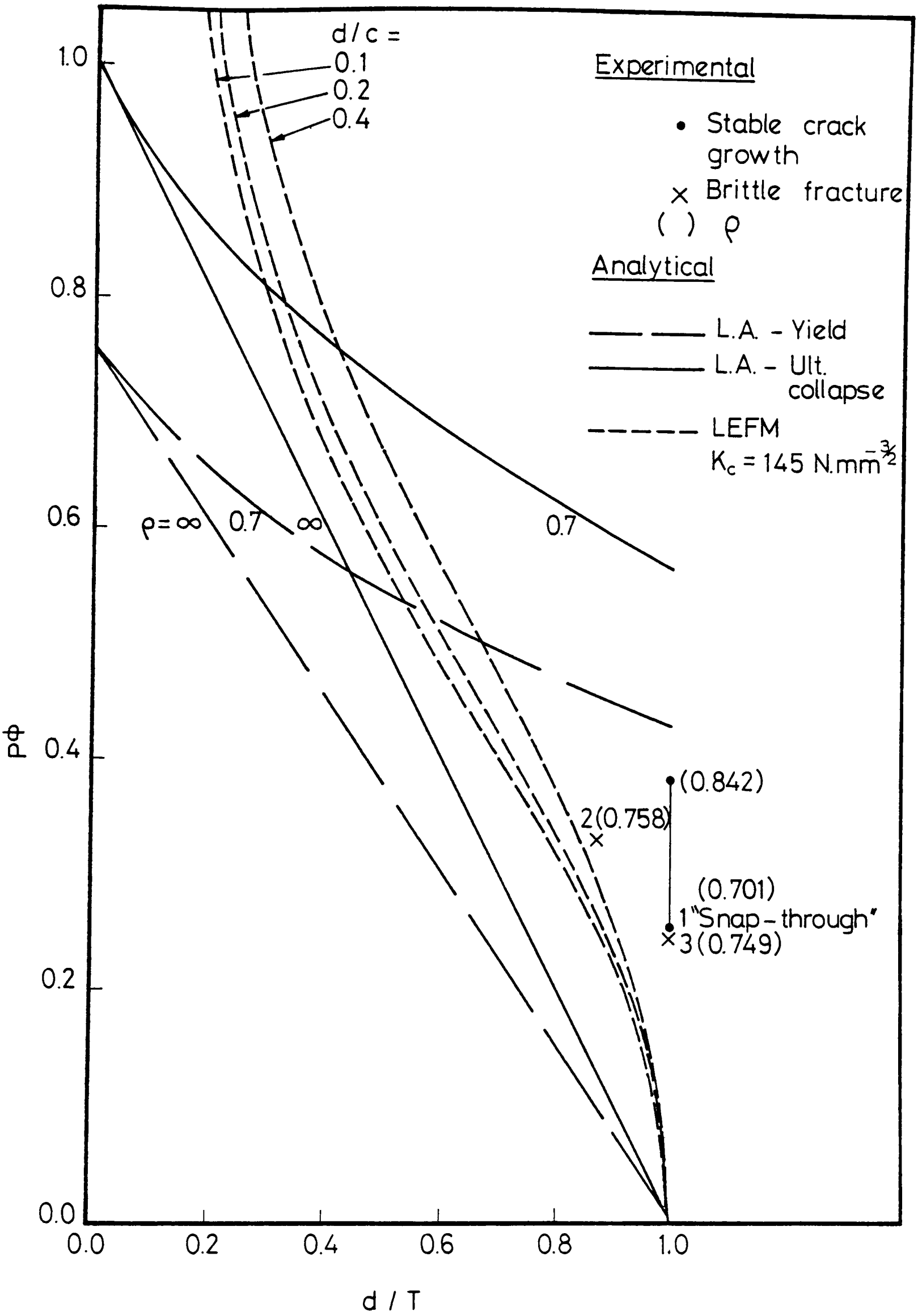


Fig. 8.10 Failure analysis diagram for polycarbonate cylinders with longitudinal part-through-thickness defects

CHAPTER 9

SUMMARY AND CONCLUSIONS

The experimental study has clearly demonstrated that in spite of slight differences in thermal treatment and loading procedure, the crack growth behaviour of the 5 mm thick polycarbonate sheet was very similar to that of the 5 mm and 6 mm thick polycarbonate model vessels. Both compact specimens and model cylinders containing longitudinal through-thickness and deep part-through-thickness cracks failed either by unstable, brittle fracture or by stable, ductile crack extension. In the former case failure was successfully predicted by means of LEFM using two critical stress intensity factors, K_{icb} and K_c corresponding to initial craze breakdown and crack instability respectively, which under static loading conditions were shown to be material constants. In comparison, stable, ductile crack extension in polycarbonate could only be characterised by means of an LEFM material parameter during the initial stages of crack extension i.e. K_{icb} for initial craze breakdown, K_{pop-in} at meta-instability and K_i for crack initiation in the presence of prior plasticity. However, provided due allowance was made for slow crack growth reasonable estimates of final load-bearing capacity were obtained using limit analysis techniques.

Results for the 18% Ni 200-grade maraging steel compact specimens also bore a marked similarity to those obtained for the polycarbonate model plates undergoing mixed mode failure. For example, crack initiation was characterised by means of the fracture toughness parameter, $R_i = \frac{1}{B} \left(\frac{\partial U}{\partial a}\right)_{u_i}$. This was shown to be essentially constant for both materials independent of thickness for plane strain (6.3 - 25.4 mm thick plates of maraging steel) and non-plane strain (3.1 mm thick plates of maraging steel) crack tip conditions, initial crack length and prior plasticity; these corresponding to energy levels up to at least 70% (maraging steel) and up to 76% (polycar-

bonate) of the pseudo-elastic general yield level, R_{gy}.

For both sets of specimens a linear relationship was found to exist between the strain energy, U/WB and its derivative with respect to crack length, $-\frac{1}{B}\left(\frac{\partial U}{\partial a}\right)_u$. The relationships were maintained even after initial crack extension. Such relationships are important since they simplify considerably the determination of the crack initiation parameter, R_i which in the case of maraging steel has been shown to be directly related to the plane strain fracture toughness, K_{Ic} by the relation, $K_{Ic}^2 = ER_i/(1-\nu^2)$.

The experimental work has clearly shown the importance of a knowledge of the plane strain fracture toughness, K_{Ic} in failure analysis. For example, it has been demonstrated by means of the model elastic-plastic material polycarbonate, that LEFM can be used to predict crack initiation even in the presence of prior plasticity. For maraging steel plate specimens deforming under plane strain crack tip conditions ($B \geqslant \frac{1}{\pi}\left(K_{Ic/\sigma_y}\right)^2$) the relevant parameter for crack initiation was shown to be K_{Ic}. However, failure loads corresponding to crack initiation in maraging steel under non-plane strain conditions ($B < \frac{1}{\pi}\left(K_{Ic/\sigma_y}\right)^2$) were also well predicted by K_{Ic} when used with a plasticity correction factor for which there was physical justification. Thus, K_{Ic} appears to have relevance in the failure analysis of cracked sections even when deformation occurs under non-plane strain crack tip conditions.

Further support for the use of polycarbonate as a model elastic-plastic material was provided by the behaviour of the fracture toughness parameter, R_{stable} for finite stable crack extension. This exhibited a geometry dependence at all crack lengths as a result of local plastic instability ahead of the crack tip in the narrow specimens; behaviour analogous to that of the parameter, R_{mc} corresponding to a load maximum in maraging steel compact specimens. Unfortunately, such parameters are of little value in the failure analysis of wide sections undergoing significant stable, ductile crack

extension. However, in keeping with the polycarbonate plates and cylinders, reasonable estimates of final load-carrying capacity were obtained for the maraging steel compact specimens by means of limit analysis. Such values were calculated on the basis of the instantaneous crack size, although large underestimates occurred with the thicker plates (36% and 30% for the 6.3 mm and 12.7 mm thick plates, respectively) partly as a result of overestimates in crack length due to crack front tunnelling.

These various aspects of the macroscopic fracture behaviour of polycarbonate model plates and vessels overlapping with the maraging steel plates, indicate that the underlying failure criteria discussed critically in chapters 2-4 have relevance in the quantitative assessment of the severity of defects in structural components. Therefore, on the basis of this combined theoretical and experimental study, the following are presented as the relevant criteria for the failure analysis of a pressure vessel with defects:

a. In situations where limited plasticity ahead of the crack tip is fully contained by an outer elastic field i.e. not general yield, the linear elastic fracture mechanics parameter, K_{Ic} (with the possibility of a plasticity correction factor for thin sheet) can be used to predict crack initiation. For a low strain-hardening maraging steel Irwin's plane strain plasticity correction, $\frac{1}{6\pi}\left(K_{Ic/\sigma_y}\right)^2$ is applicable to sheet thicknesses comparable to $\frac{1}{\pi}\left(K_{Ic/\sigma_y}\right)^2$ i.e. twice Irwin's plane stress plastic zone radius.

b. For materials where subcritical crack growth is known to occur care should be taken in basing estimates of load-carrying capacity on linear elastic solutions using K_{Ic}. Static loading tests on model plates and cylindrical vessels of polycarbonate have shown that crack instability does not occur at stress intensity levels significantly below the critical value, K_c for polycarbonate; under such circum-

stances linear elastic fracture mechanics based on K_c is applicable if due allowance is made for subcritical crack extension.

c. Crack initiation may or may not correspond to crack instability since the latter is governed by the general energy balance conditions:

$$\left.\begin{aligned} -\frac{1}{B}\frac{\Delta U_e}{\Delta a} &= R \\ \text{and } -\frac{1}{B}\frac{\Delta^2 U_e}{\Delta a^2} &> \frac{1}{B}\frac{\Delta R}{\Delta a} \end{aligned}\right\} \quad \text{crack instability}$$

Results for 3.1 mm thick plates of a strain rate-insensitive maraging steel indicate that, for monotonic loading under conditions of contained plasticity, curves of R versus absolute crack extension, Δa may be a material parameter, independent of initial crack length for a given plate thickness.

d. If extensive plastic deformation accompanies slow crack extension failure may occur by plastic instability due to localised yield in the region immediately ahead of the moving crack tip; this may lead to the onset of general yield across the remaining ligament with negligible crack extension. Static loading tests on maraging steel plates and model plates and cylindrical vessels of polycarbonate have shown that limit analysis techniques can provide reasonable estimates of the onset of plastic instability and general yield on the basis of the instantaneous crack size i.e. allowance must be made for any prior slow crack extension.

e. Dowling and Townley's two-criteria approach to failure i.e. linear elastic fracture mechanics on the one hand and limit analysis on the other, provides a useful method for assessing the relative importance of crack initiation, in the presence of limited crack tip plasticity and general yield as failure criteria for a given sized defect.

CHAPTER 10

SUGGESTIONS FOR FUTURE WORK

a. Compact specimens ($\alpha \geqslant 0.6$) of pressure vessel steels having intermediate and high strain — hardening exponents should be tested over the thickness range $\frac{1}{2\pi} (K_{Ic}/\sigma_y)^2 - \frac{2}{\pi} (K_{Ic}/\sigma_y)^2$ in order to determine the conditions governing crack initiation e.g. stress intensity factor, fracture toughness, plastic zone size. This should confirm whether or not the minimum thickness for plane strain crack initiation of maraging steel, $\frac{1}{\pi} (K_{Ic}/\sigma_y)^2$ with a low strain-hardening exponent is applicable to other materials with entirely different plastic flow properties.

b. Single-edge-cracked and/or centre-cracked tension plates of pressure vessel steel with a high strain-hardening exponent should be tested in order to determine the conditions governing the failure of short, shallow defects ($\alpha \sim 0\text{-}0.2$) in the absence of yielding at regions remote from the crack tip. Such experiments should reveal the boundaries of applicability of LEFM on the one hand and limit analysis based on yield and ultimate collapse on the other for the important transition region which occurs at short crack lengths.

c. The latter should also be performed on specimens of variable width for a quantitative assessment of the influence of section width or remaining ligament on the size of the transition region for short, shallow defects. On the basis of the two-criteria approach to failure, an increase in section width should reduce the extent of the transition region increasing the probability of brittle fracture at shorter crack lengths.

d. Further experiments are necessary to determine the influence of loading history and through-thickness constraint on subcritical crack

growth. Sustained load tests on polycarbonate compact specimens of varying thickness should prove useful in providing a qualitative study of the phenomenon.

APPENDICES

APPENDIX 1

Limit Analysis of the Compact Specimen

A.1.a Elastic Region

With reference to Fig. 5.2.a it is assumed that a linear elastic stress distribution exists across the remaining ligament, W-a of the compact specimen, thickness, B such that the elastic stress at a distance x from the crack tip is:

$$\sigma_x = \sigma_t \frac{(W-a-x)}{(W-a)} + \sigma_c \frac{x}{(W-a)} \qquad A.1$$

where σ_t and σ_c are the maximum tensile and compressive stresses at the crack tip and the far free surface, respectively.

Static equilibrium of the top half of the specimen requires that:

$$\int_{o}^{W-a} \sigma_x \, dx = \frac{P}{B} \qquad A.2$$

Substituting for σ_x from equation A.1 and integrating:

$$\sigma_t + \sigma_c = \frac{2P}{(W-a)B} \qquad A.3$$

Taking moments about A:

$$\int_{o}^{W-a} \sigma_x \, (a+x) \, dx = 0 \qquad A.4$$

Substituting for σ_x from equation A.1 and integrating:

$$\sigma_t = - \sigma_c \frac{(2W+a)}{(W+2a)} \qquad A.5$$

The maximum tensile and compressive elastic stresses are then obtained from equations A.3 and A.5:

$$\sigma_t = \frac{P}{WB} \, 2 \frac{(2+\alpha)}{(1-\alpha)^2} \qquad A.6$$

$$\text{and} \quad \sigma_c = -\frac{P}{WB} \, 2 \frac{(1+2\alpha)}{(1-\alpha)^2} \qquad A.7$$

where $\alpha = a/W$.

Thus, the elastic limit load, P_{el} is reached when yielding occurs in the vicinity of the crack front:

$$\left.\begin{aligned} \sigma_t &= \sigma_y \\ \text{or } \frac{P_{el}}{\sigma_y WB} &= \frac{(1-\alpha)^2}{2(2+\alpha)} \end{aligned}\right\} \quad \text{A.8}$$

where σ_y is the uniaxial yield stress for a material obeying Tresca's yield criterion. Assuming that C acts as a hinge, the elastic strain at the point of loading, A at the onset of yielding may be given by:

$$\left.\begin{aligned} \varepsilon_{el} &= \frac{\sigma_y}{E} \cdot \frac{(a+BC)}{BC} \\ \text{or } \frac{E\varepsilon_{el}}{\sigma_y} &= \frac{(2+2\alpha+2\alpha^2)}{(1-\alpha)(2+\alpha)} \end{aligned}\right\} \quad \text{A.9}$$

A.1.b Elastic-Plastic Region

Elastic-perfectly plastic material response is assumed such that at higher load levels a stress state represented by Fig. 5.2.b is achieved. Let β be the distance from the crack tip over which fully plastic yielding has occurred and let x represent the half-width of the internal stress block required to equilibrate the applied load.

The force equilibrium equation is:

$$\sigma_y\beta + \sigma_y \frac{x}{2} - \sigma_y \frac{(W-a-\beta-x)^2}{2x} = \frac{P}{B} \quad \text{A.10}$$

Taking moments about C:

$$\sigma_y\beta \left(x + \beta/2\right) + \sigma_y \frac{x}{2} \cdot \frac{2x}{3} + \sigma_y \frac{(W-a-\beta-x)^3}{2x} \cdot \frac{2}{3} = \frac{P}{B}(a+\beta+x) \quad \text{A.11}$$

Yielding in compression at the back surface occurs when:

$$x = W-a-\beta-x \quad \text{A.12}$$

and substituting into equations A.10 and A.11 gives:

$$\beta = \frac{P_{by}}{\sigma_y B} \quad \text{A.13}$$

$$\text{and} \quad \beta x - \beta^2/2 + \frac{2x^2}{3} = \frac{P_{by}}{\sigma_y B} \quad (a+\beta+x) \qquad \text{A.14}$$

where P_{by} is the load corresponding to yield at the back surface.

Equation A.14 is then solved by substituting for $P_{by}/\sigma_y B$ from equation A.13 and for x from equation A.12:

$$\left.\begin{aligned} \beta &= -\left(\frac{W}{2} + a\right) + \frac{1}{2}\sqrt{3(W^2 + 2a^2)} \quad \text{since } \beta > 0 \\ \text{or } \frac{P_{by}}{\sigma_y WB} &= -\left(\frac{1}{2} + \alpha\right) + \frac{1}{2}\sqrt{3\,(1 + 2\alpha^2)} \end{aligned}\right\} \qquad \text{A.15}$$

Again, assuming C acts as a hinge, a notional elastic strain at the point of loading may be estimated:

$$\left.\begin{aligned} \varepsilon_{by} &= \frac{\sigma_y}{E} \cdot \frac{(a + \beta + x)}{x} \\ \text{or } \frac{E\varepsilon_{by}}{\sigma_y} &= \frac{1 + \sqrt{3(1 + 2\alpha^2)}}{3 - \sqrt{3(1 + 2\alpha^2)}} \end{aligned}\right\} \qquad \text{A.16}$$

After yielding at the back surface the width of the internal stress block, 2x decreases until eventually fully plastic failure occurs. The half-width, x during this transition may be determined from the new force equilibrium equation for the stress state represented by Fig. 5.2.d:

$$\left.\begin{aligned} \sigma_y \beta + \sigma_y \frac{x}{2} - \sigma_y \frac{x}{2} - \sigma_y (2n - \beta - 2x) &= \frac{P_p}{B} > \frac{P_{by}}{B} \\ \text{or } \beta &= \frac{P_p}{2\sigma_y B} + n - x \end{aligned}\right\} \qquad \text{A.17}$$

where $n = (W-a)/2$ and P_p is the applied load corresponding to this stress state.

Taking moments about C:

$$\left.\begin{aligned} &\sigma_y \beta\left(x + \frac{\beta}{2}\right) + \sigma_y \frac{2x}{2} \cdot \frac{2x}{3} + \sigma_y (2n - \beta - 2x)\left(n - \frac{\beta}{2}\right) = \frac{P_p}{B}(a + \beta + x) \\ \text{or } &3\beta^2 + 2x^2 + 6n^2 + 6\beta x - 6\beta n - 6xn = \frac{3P_p}{\sigma_y B}(a + \beta + x) \end{aligned}\right\} \qquad \text{A.18}$$

Substituting for β from equation A.17 and solving for x:

$$x = \sqrt{3n^2 - \frac{3}{4}\left(\frac{P_p}{\sigma_y B}\right)^2 - 3\left(\frac{P_p}{\sigma_y B}\right)} \; (a + n)$$

$$\text{or} \quad x = \sqrt{\frac{3}{4}(W-a)^2 - \frac{3}{4}\left(\frac{P_p}{\sigma_y B}\right)^2 - \frac{3}{2}\left(\frac{P_p}{\sigma_y B}\right)} \; (W + a) \qquad \text{A.19}$$

A notional elastic strain at the loading point is then given by:

$$\varepsilon_p = \frac{\sigma_y}{E} \; \frac{(a + \beta + x)}{x} \qquad \text{A.20}$$

Substituting for $(\beta + x) = P_p/2\sigma_y B + (W-a)/2$ and for x from equation A.19:

$$\varepsilon_p = \frac{\sigma_y}{E} \; \frac{\left(\frac{W+a}{2}\right) + \left(\frac{P_p}{2\sigma_y B}\right)}{\sqrt{\frac{3}{4}(W-a)^2 - \frac{3}{4}\left(\frac{P_p}{\sigma_y B}\right)^2 - \frac{3}{2}\left(\frac{P_p}{\sigma_y B}\right)} \; (W-a)} \qquad \text{A.21}$$

$$\text{or} \quad \frac{E\varepsilon_p}{\sigma_y} = \frac{\left[1 + \alpha + (P_p/\sigma_y WB)\right]}{\sqrt{3(1-\alpha)^2 - 3\,(P_p/\sigma_y WB)^2 - 6\,(P_p/\sigma_y WB)\,(1+\alpha)}}$$

A.1.c Fully Plastic Region

Under fully plastic conditions the stress state, Fig. 5.2.e, consists of a region immediately beneath the crack and the hinge, C subjected to a uniform tension, σ_y and a region between the hinge, C and the back surface subjected to a uniform compression, $-\sigma_y$.

A lower bound solution can be determined immediately from equation A.21 i.e. the applied load, P_p tends to the general yield load, P_{gy} as $\varepsilon_p \to \infty$:

$$(1-\alpha)^2 - (P_{gy}/\sigma_y WB)^2 - 2\,(P_{gy}/\sigma_y WB)\,(1+\alpha) \to 0$$

$$\text{or} \quad \frac{P_{gy}}{\sigma_y WB} = -(1+\alpha) + \sqrt{2(1+\alpha^2)} \qquad \text{A.22}$$

$$\left(\text{since } \frac{P_{gy}}{\sigma_y WB} > 0\right)$$

APPENDIX 2

Comparison of the Dimensionless Compliance Expressions for the Simple Model with Adams and Munro's Calibration for the Standard Compact Specimen

α	$\frac{EBW\varepsilon_{el}}{P_{el}}$	$\frac{EBW\varepsilon_{by}}{P_{by}}$	$\frac{EBu_{el}}{P_{el}}$	$\frac{EBu_{by}}{P_{by}}$	$\frac{EBu_{lp}}{P}$
			gauge length = 0.55W		plane stress (1)
0.3	16.21	18.33	8.92	10.08	17.73
0.4	28.89	31.16	15.89	17.14	26.33
0.5	56.00	58.69	30.80	32.28	40.50
0.6	122.5	124.9	67.38	68.70	66.72
0.7	324.4	330.0	178.4	181.5	125.7
0.8	1220	1252	671.0	688.6	293.0

APPENDIX 3

Estimation Procedure for $-\frac{1}{B}\left(\frac{\partial U}{\partial a}\right)_u$ from a Single Load-Displacement Record for the Compact Specimen

Under linear elastic loading, the strain energy is given by:

$$U_e = \frac{1}{2}\,\frac{u^2}{C} \qquad \text{A.23}$$

where C is the elastic compliance, u/p. Differentiating with respect to a under fixed grip conditions:

$$-\frac{1}{B}\left(\frac{\partial U_e}{\partial a}\right)_u = -\frac{1}{2}\,\frac{u^2}{B}\left(\frac{\partial\, 1/C}{\partial a}\right)_u \qquad \text{A.24}$$

$$\left.\begin{aligned} \text{which leads to } -\frac{1}{B}\left(\frac{\partial U_e}{\partial a}\right)_u &= -\frac{U_e}{(W-a)B}\,(1-\alpha).\,C\,.\left(\frac{\partial\, 1/C}{\partial \alpha}\right)_u \\ \text{or } -\frac{1}{B}\left(\frac{\partial U_e}{\partial a}\right)_u &= \phi_e \cdot \frac{U_e}{(W-a)B} \end{aligned}\right\} \qquad \text{A.25}$$

where ϕ_e is a geometrical parameter, $-(1-\alpha).\,C\left(\frac{\partial\, 1/C}{\partial \alpha}\right)_u$.

For rigid-perfectly plastic material behaviour, the strain energy is given by:

$$U_p = u\,P_{gy} \qquad \text{A.26}$$

where u is the displacement of the general yield load, P_{gy}. Differentiating with respect to a under fixed grip conditions:

$$-\frac{1}{B}\left(\frac{\partial U_p}{\partial a}\right)_u = -\frac{u}{B}\left(\frac{\partial P_{gy}}{\partial a}\right)_u \qquad \text{A.27}$$

$$\left.\begin{aligned} \text{which leads to } -\frac{1}{B}\left(\frac{\partial U_p}{\partial a}\right)_u &= -\frac{U_p}{(W-a)B}\cdot\frac{(1-\alpha)}{P_{gy}}\left(\frac{\partial P_{gy}}{\partial \alpha}\right)_u \\ \text{or } -\frac{1}{B}\left(\frac{\partial U_p}{\partial a}\right)_u &= \phi_p \cdot \frac{U_p}{(W-a)B} \end{aligned}\right\} \qquad \text{A.28}$$

where ϕ_p is a geometrical parameter, $-(1-\alpha)/P_{gy}\cdot\left(\frac{\partial P_{gy}}{\partial \alpha}\right)_u$

Equation A.25 is valid both in terms of the load pin displacement

(total) and the load line displacement (due to the crack) provided U_e is defined accordingly, since the displacement due to the uncracked specimen is independent of a. Values of ϕ_e based on the load pin and load line displacement are easily calculated for the standard compact specimen from the dimensionless compliance expression of Adams and Munro (1) and the results are listed below.

Values of ϕ_e and ϕ_p for the Standard Compact Specimen

α	ϕ_{ell}	ϕ_{elp}	ϕ_p
	plane stress		
0.3	2.86	2.50	2.36
0.4	2.63	2.41	2.32
0.5	2.42	2.29	2.27
0.6	2.31	2.23	2.22
0.7	2.26	2.22	2.18
0.8	2.33	2.31	2.12

For the case of rigid-perfectly plastic behaviour there is no distinction between load pin and load line displacement and ϕ_p may be calculated directly from the lower bound general yield solution, equation A.22. The results are compared with ϕ_e.

It is apparent that ϕ_e and ϕ_p are similar at all crack lengths but that the agreement is particularly good for deeply cracked specimens, $\alpha \geqslant 0.6$, for which the elastic contribution due to the uncracked specimen is negligible. Thus, assuming a similar relationship holds in the transitional elastic-plastic region for real materials, the total strain energy function $-\frac{1}{B}\left(\frac{\partial U}{\partial a}\right)_u$ for a deeply cracked compact specimen may be obtained from an

expression of the form:

$$-\frac{1}{B}\left(\frac{\partial U}{\partial a}\right)_u = \phi \cdot \frac{U_{11}}{(W-a)B} \qquad \alpha \geqslant 0.6 \qquad \text{A.29}$$

where U_{11} is the total strain energy (elastic and plastic) measured from a single load-load line displacement record and a conservative estimate of the geometrical parameter, ϕ would be 2.0.

APPENDIX 4

Approximate Expression for the Crack Tip Strain Rate

Studying the elastic stress distribution about an elliptically shaped crack of length, 2a in a uniform tensile stress field, σ Inglis (2) showed that the major principal stress at the crack tip may be given by:

$$\sigma_{yy} = \sigma \left[1 + 2 \sqrt{\frac{a}{r}} \right] \approx 2\sigma \sqrt{\frac{a}{r}} \quad \text{for} \quad r << a \qquad \text{A.30}$$

where r is the radius of curvature at the crack tip. Restating this in terms of the elastic stress intensity factor, $K = \sigma \sqrt{\pi a}$ for an infinite sheet:

$$\sigma_{yy} \approx \frac{2K}{\sqrt{\pi r}} \qquad \text{A.31}$$

Differentiating with respect to time and assuming r remains constant, an approximate expression for the crack tip strain rate is:

$$\dot{\varepsilon}_{tip} \approx \frac{2\dot{K}}{E \sqrt{\pi r}} \qquad \text{A.32}$$

where $\dot{K}$ is the rate of increase of stress intensity and E, Young's modulus.

For application to the compact specimen configuration, a finite width correction is required and the resulting equation is:

$$\dot{\varepsilon}_{tip} \approx \frac{2\dot{K}}{E \sqrt{r}} \qquad \text{A.33}$$

where $\dot{K}$ is now defined for the compact specimen by $\dot{P}Y/\sqrt{W}\,B$. Therefore, an estimate of the initial crack tip strain rate for the polycarbonate compact specimens can be obtained using equation A.33, assuming an initial crack tip radius of curvature of 0.05 mm i.e. half the width of the razor blade.

APPENDIX 5

Summary of Results for Plane Strain Fracture Toughness Tests of Heat Treated Maraging Steel

(L-T orientation, 296°K, 40% relative humidity)

	W	B	a_o	α_o	$\frac{\Delta K}{K_f(max)}$	$\frac{K_f(max)}{K_Q}$	$\frac{P_m}{P_Q}$	K_Q	$2.5\left(\frac{K_Q}{\sigma_y}\right)^2$	Valid	Fraction oblique
	mm	mm	mm		fatigue precracking			N mm$^{-3/2}$	mm		
1	50.80	25.43	25.00	0.492	0.91	0.13	1.07	4350	23.9	Yes	0.45
2	50.80	25.30	25.53	0.503	0.91	0.12	1.05	4690	27.8	No	0.49
3	50.80	25.40	27.99	0.551	0.91	0.14	1.04	4660	27.4	No*	0.43
Mean								4570 ± 150	26.4		

* Invalid due to preloading to 0.86 P_Q in addition to specimen size requirement not met

APPENDIX 6

Experimental Test Data for Maraging Steel Compact Specimens

(L-T orientation, 296 ± 2°K, 45 ± 5% relative humidity)

	a_o mm	Δa mm	w mm		ρ'_x mm		u_{lpf} mm
1M	17.24	5.105	0.1532 0.1641	0.1587	10.3 12.3	11.3	1.83
2M	22.13	3.539	0.1417 0.1415	0.1416	12.2 11.2	11.7	1.70
3M	27.26	2.089	0.1204 0.1140	0.1172	8.9 8.9	8.9	1.68
4M	32.29	1.461	0.1092 0.1052	0.1072	6.9 8.6	7.75	2.01
5M	37.36	1.364	0.1008 0.1016	0.1012	6.1 7.1	6.6	2.24
6M	41.68	1.250	0.0587 0.0711	0.0649	3.9 3.3	3.6	2.38
7M	19.53	1.674	0.0991 0.1341	0.1166	9.1 8.1	8.6	1.46
7MA	19.43	0.290	0.0160 0.0188	0.0174	2.8 4.1	3.45	0.71
8M	19.43	3.401	0.1862 0.1753	0.1808	11.7 11.7	11.7	1.70
9M	19.68	1.219	0.0965 0.0950	0.0958	8.1 8.1	8.1	1.33
10M	19.66	2.979	0.1549 0.1580	0.1565	12.2 11.2	11.7	1.62
11M	24.50	1.999	0.1491 0.1201	0.1346	12.2 9.1	10.65	1.68
11MA	24.42	0.179	0.0173 0.0185	0.0179	3.0 3.6	3.3	0.76
12M	24.59	1.379	0.1024 0.1064	0.1044	9.1 9.1	9.1	1.44
13M	24.43	1.156	0.0795 0.0831	0.0813	6.4 6.6	6.5	1.35

	a_o mm	Δa mm	w mm	ρ'_x mm	u_{lpf} mm	u_{llf} mm
14M	24.54	1.073	0.0640, 0.0678 ← 0.0659	5.8, 6.6 ← 6.2	1.25	-
15M	29.45	0.470	0.0173, 0.0145 ← 0.0159	3.3, 3.3 ← 3.3	0.86	-
15MA	29.43	0.083	0.0097, 0.0114 ← 0.0106	2.3, 2.3 ← 2.3	0.78	-
16M	29.57	1.419	0.0508, 0.0483 ← 0.0496	5.0, 5.7 ← 5.35	1.37	-
17M	29.45	0.940	0.0363, 0.0310 ← 0.0337	3.9, 4.6 ← 4.25	1.16	-
18M	29.48	1.810	0.1067, 0.1100 ← 0.1084	9.1, 8.1 ← 8.6	1.68	-
19M	34.28	0.599	0.0216, 0.0196 ← 0.0206	2.8, 4.1 ← 3.45	1.17	1.08
20M	34.40	1.021	0.0305, 0.0406 ← 0.0356	4.3, 3.8 ← 4.05	1.41	1.34
21M	34.19	0.196	0.0152, 0.0130 ← 0.0141	2.3, 2.8 ← 2.55	0.98	0.95
22M	34.18	1.560	0.0826, 0.0945 ← 0.0886	4.8, 6.4 ← 5.6	1.92	1.85
23M	38.68	1.294	0.0729, 0.0668 ← 0.0699	4.4, 5.1 ← 4.75	2.14	2.10
23MA	38.90	0.056	0.0102, 0.0109 ← 0.0106	1.5, 2.3 ← 1.9	1.13	1.07
24M	38.95	0.789	0.0391, 0.0310 ← 0.0351	3.4, 3.8 ← 3.6	1.69	1.64
25M	38.94	0.359	0.0180, 0.0191 ← 0.0186	4.1, 2.5 ← 3.3	1.29	1.22
26M	38.62	0.017	0.0056, 0.0076 ← 0.0066	1.1, 2.0 ← 1.55	0.93	0.88
28M	31.68	0.025	0.0076, 0.0089 ← 0.0083	2.3, 2.8 ← 2.5	-	0.72
30M	31.49	0.381	0.0102, 0.0152 ← 0.0127	2.8, 4.3 ← 3.55	-	0.86

	a_o mm	Δa mm	w mm	ρ'_x mm	u_{1pf} mm	u_{11f} mm
31M	31.48	1.026	0.0254, 0.0279 ← 0.0267	5.1, 4.6 ← 4.85	-	1.09
32M	31.86	3.020	0.1041, 0.0914 ← 0.0978	10.2, 7.1 ← 8.65	-	1.87
34M	32.77	7.104	0.1151, 0.1234 ← 0.1193	12.2, 13.2 ← 12.7	-	1.99
35M	32.68	3.310	0.0686, 0.0757 ← 0.0722	8.4, 7.9 ← 8.15	-	1.52
37M	32.84	5.126	0.0787, 0.0912 ← 0.0850	8.6, 11.2 ← 9.9	-	1.66
38M	32.60	1.044	0.0239, 0.0254 ← 0.0247	5.1, 5.1 ← 5.1	-	1.02

APPENDIX 7

Determination of Critical Stress Intensity Factors from Load-Load Line Displacement Records Using 5% Offset Procedure*

	B	α_o	P_Q	$\frac{P_m}{P_Q}$ †	K_Q	K_A	$\frac{1}{B}\left(\frac{K_Q}{\sigma_y}\right)^2$ ‡	$\frac{1}{B}\left(\frac{K_A}{\sigma_y}\right)^2$	$\frac{C_{exp}}{C_{A,M}}$
	mm		x 10^3 N.		N $mm^{-3/2}$	N $mm^{-3/2}$			
10M	3.10	0.389	14.5	1.53	-	4650	-	3.52	0.95
11M	3.10	0.482	10.7	1.50	-	4430	-	3.20	1.00
18M	3.02	0.580	7.56	1.48	-	4440	-	3.30	1.02
22M	3.02	0.669	4.54	1.55	-	3870	-	2.51	1.00
23M	3.02	0.763	2.32	1.47	-	3390	-	1.92	1.05
32M	6.33	0.631	13.0	1.38	-	4480	-	1.60	0.98
34M	12.64	0.648	24.3 (pop-in)	1.01	4520	-	0.82	-	1.00
35M	12.67	0.644	23.9 (pop-in)	1.09	4350	-	0.75	-	1.01
37M	12.65	0.648	23.5	1.10	4360	-	0.76	-	1.01
38M	12.66	0.644	24.0	-	4370	-	0.76	-	0.99
Mean					4400 ± 70		0.77		

* 5% offset load corresponds to 2% effective crack extension for $0.45 < \alpha < 0.55$

† $\frac{P_m}{P_Q} \leqslant 1.10$ (3) (4)

‡ $\frac{1}{B}\left(\frac{K_Q}{\sigma_y}\right)^2 \leqslant 0.4$ (3) (4)

References

(1) N.J.I. Adams and H.G. Munro, Eng. Fract. Mechs., 6, p. 119, 1974.

(2) C.E. Inglis, Trans. Inst. Nav. Arch. (London), 55, p. 219, 1913.

(3) "Methods for Plane Strain Fracture Toughness (K_{Ic}) of Metallic Materials," B.S. 5447: 1977, B.S.I., London.

(4) "Plane Strain Fracture Toughness of Metallic Materials," A.S.T.M. E399-72 Part 31, 1972.